Thermodynamics of the Spin-Chain Compounds Cs_2CoCl_4 and $Cu(C_4H_4N_2)(NO_3)_2$

Inaugural-Dissertation

zur

Erlangung des Doktorgrades
der Mathematisch-Naturwissenschaftlichen Fakultät
der Universität zu Köln

vorgelegt von
Oliver Breunig
aus Köln

Köln, 2015

Berichterstatter: Prof. Dr. Thomas Lorenz
Prof. Dr. Achim Rosch
Prof. Dr. Xenophon Zotos

Vorsitzender der Prüfungskomission: Prof. Dr. Ladislav Bohatý

Tag der mündlichen Prüfung: 24.6.2015

Contents

1 Introduction

In the field of solid state physics many exciting phenomena emerge from the interactions between individual particles and from the competition of processes with similar energy scales. Some of them are only understood by taking into account the quantum nature of matter. Due to the high complexity of interacting quantum many-body systems, often it is more instructive to identify the relevant processes in a simplified model system. A transfer of the gained fundamental insights to more involved systems is the key for the design of new materials. One exemplary field, where the joint theoretical and experimental efforts have led to the development of new methods and materials, is that of low-dimensional spin systems. The fundamental research in this field is commonly motivated by its relation to the physics of high-temperature superconductors that reveal a huge potential for application.

Reducing the dimension, quantum effects are enhanced and in some cases the ground state can be derived analytically. In some one-dimensional spin chains the ground state changes non-analytically as a function of a non-thermal control parameter, known as a quantum phase transition. Prominent examples are the Ising-spin chain compounds $LiHoF_4$ and $CoNb_2O_6$, where a quantum phase transition arises as a function of the transverse magnetic field [1, 2]. In these systems close to the critical field quantum fluctuations are dominant and the finite-temperature dynamics is governed by the strong entanglement of the ground state.

Another type of models, where quantum criticality is induced by the magnetic field are the easy-plane type *XXZ* models. Here, the rotational symmetry around z is broken by an applied magnetic field in the transverse direction, i. e., perpendicular to z and within the easy planes. However, experimental realizations of this type are comparably rare. A promising candidate is the effective spin-$1/2$ chain compound Cs_2CoCl_4 that is isostructural to the intensely studied Cs_2CuCl_4, but with an additional easy-plane anisotropy of the magnetism. In Cs_2CoCl_4, a crystal field anisotropy of the order of 7 K splits the spin-$3/2$ states of the magnetic Co^{2+} into Kramers doublets and at low temperature a description in terms of an effective spin-$1/2$ arises. Several thermodynamic properties indicate a strongly one-dimensional magnetism of the easy-plane type below about 2 K [3–7]. However, the influence of symmetry-breaking magnetic fields on the one-dimensional magnetism of Cs_2CoCl_4 has not been investigated previously. Below $T_{\mathrm{N}} \simeq 0.22\,\mathrm{K}$ antiferromagnetic order is reported and a spin-liquid phase is suggested to arise close to 2 T based on a single study of the magnetic order for fields along the a axis [8]. Field directions other than a are not covered in literature and the presence of a spin-liquid state has not been confirmed by other means.

To address the question if there is a quantum phase transition in Cs_2CoCl_4 and if the one-dimensional magnetism is fully described by the *XXZ* model, in this thesis measurements of thermodynamic properties at temperatures down to 50 mK and in magnetic fields up to 4 T are compared to numerical calculations of the *XXZ* model in a transverse field. Furthermore, the application of an effective spin-$1/2$ model to the compound is revised and the contribution of the parent spin-3/2 states on the magnetism is analyzed. The influence of magnetic fields on the low-temperature phases is studied for fields applied along the different crystallographic axes as well as along non-principal directions. The magnetic phase diagrams are derived and possible microscopic origins of the various observed phases are discussed.

The magnetic exchange in Cs_2CoCl_4 is mediated by chlorine ions via superexchange. Thus, a change of the magnetism is expected when exchanging the chlorine ions in Cs_2CoCl_4 with bromine. In the isostructural Cs_2CuCl_4 the doping is site-selective, resulting in a non-linear change of the low-temperature properties as a function of the doping and in magnetic frustration [9]. In this thesis, in analogy crystals of the $Cs_2CoCl_{4-x}Br_x$ series are synthesized and characterized with respect to their structure and low-temperature magnetism.

Among the numerous spin chain models the isotropic spin-1/2 Heisenberg model stands out due its intriguing low-temperature characteristics and the exact solubility. As a function of an applied magnetic field, it also shows a quantum phase transition at $h_c = 2\,J$, where J is the exchange constant between spins. It ranges from a few Kelvin to several thousands of Kelvin among the known compounds. Thus, within the magnetic-field range accessible with standard laboratory magnets, quantum criticality may be investigated only in systems with coupling constants of few Kelvin and at low temperatures $T \ll J$. Most corresponding compounds which realize the Heisenberg model in a wide temperature range base on the isotropic magnetism of copper ions in a crystal field. They are comparably rare due to the tendency of spin-1/2 chains to either perform a Spin-Peierls transition or to show long-range magnetic order due to finite interchain couplings. One established compound with an adequate coupling constant of about 10 K and an absence of magnetic order down to 107 mK is the semi-organic copper pyrazine dinitrate, $Cu(C_4H_4N_2)(NO_3)_2$ [10, 11]. Several individual investigations of the system indicate quantum critical behavior and a high level of agreement with the Heisenberg model [12–17]. Yet, the thermodynamics of CuPzN have not been quantitatively compared to the model in the full quantum critical regime. Here, exact results of the Heisenberg model are compared to several thermodynamic properties measured in a temperature range from 0.25 K to 30 K and in magnetic fields up to 17 T. The quantum criticality of CuPzN is investigated by analyzing the finite-temperature signatures.

The thesis is structured as follows. In Chapter 2 the employed theoretical methods and concepts are outlined, with special focus on the properties of spin models and the numerical simulation of their thermodynamics. In the next introductory Chapter 3 the experimental techniques and the developed setups are presented. The established properties of Cs_2CoCl_4 are summarized in the first part of Chapter 4, followed by the results on the one-dimensional magnetism and the magnetic order of Cs_2CoCl_4. The crystal growth of the mixed systems $Cs_2CoCl_{4-x}Br_x$ as well as structural and thermodynamic investigations are discussed in Chapter 5. The thermodynamic properties of $Cu(C_4H_4N_2)(NO_3)_2$ are compared to the spin-1/2 Heisenberg model and analyzed with respect to quantum criticality in Chapter 6.

2 Theory

In this chapter some basic concepts and models are introduced that are employed in the discussion of the experimental results on Cs_2CoCl_4 and $Cu(C_4H_4N_2)(NO_3)_2$ in Chapters 4 and 6. Starting from the physics of isolated local moments described by the crystalline electric field, the concept of magnetic exchange is introduced which leads to the formation of more complex interacting systems. After the derivation of an effective spin-$1/2$ model for the application to the compound Cs_2CoCl_4, the thermodynamic properties of different one-dimensional models are compared and the finite-size effects of numerical simulations of the models are estimated. Selected simulation results are compared to experimental data. Last, the concepts of quantum phase transitions and magnetic order in low-dimensional systems are summarized.

2.1 Crystal electric field

In 1929 Bethe introduced a theory [18] to describe how the degenerate energy levels of a free atom split upon placing it in a crystal environment consisting of electrically charged ions. The splitting depends on the shape of the electric field generated by the surrounding ions. Applying group theory it was found that the type of splitting is determined by the potential's symmetry and thus, very general statements of the electronic and associated magnetic properties can be deduced for different coordinations.

In the following, a summary of the theoretical treatment of the interaction of a transition metal's d and f-electrons with the surrounding ligands is given. More detailed introductions and discussions exceeding an effective electrostatic "point charge model" are found in text books [19, 20]. In the Hamiltonian of a free atom,

$$\mathcal{H}_0 = \sum_i \frac{p_i^2}{2m} - \frac{Ze^2}{r_i} + \sum_{i,j} \frac{1}{2} \frac{e^2}{\mid r_i - r_j \mid}, \tag{2.1}$$

the first two terms account for the kinetic energy and the Coulomb interaction of the ion's electrons with the nucleus of charge Ze. The last term describes the electron-electron interaction between more than one single electron in a shell. Considering interactions only within s, p, d or f-orbitals they can be expressed by the numerically calculated Slater integrals [21]. In addition the spin-orbit coupling of strength ζ and the potential of the crystal field enter in the full crystal field Hamiltonian,

$$\mathcal{H} = \mathcal{H}_0 + \zeta \sum_i l_i \cdot s_i + V_{CF}. \tag{2.2}$$

As the eigenfunctions of the undisturbed Hamiltonian $\mathcal{H}_0$ are commonly expressed in terms of spherical harmonics $Y_{\ell m}$ it is convenient to rewrite the crystal field potential V_{CF} in this basis, as well. A general solution to the Laplace equation $\nabla^2 V_{CF} = 0$, describing the electrostatic potential of point charges distributed in space, relates to the spherical harmonics

$$Y_\ell^m(\vartheta, \phi) = \sqrt{\frac{(2\ell+1)(\ell-m)!}{4\pi(\ell-m)!}} \cdot P_\ell^m(\cos\vartheta) \cdot e^{im\phi} \tag{2.3}$$

with the Legendre polynomials $P_\ell^m(x)$. Thus a general crystal field potential is characterized by the crystal field coefficients $a_{k,m}$,

$$V_{CF} = \sum_{k=0}^{\infty} \sum_{m=-k}^{k} a_{k,m} \sqrt{\frac{4\pi}{2k+1}} r^k Y_k^m(\vartheta, \phi). \tag{2.4}$$

The number of different coefficients $a_{k,m}$ contributing is restricted by the symmetry of the crystal environment around the central ion. The non-vanishing coefficients $a_{k,m}$ and their symmetry relations can be derived by solving the eigenvalue equation $R\,V_{CF} = V_{CF}$, where R represents a rotational or mirror symmetry at the atom's site. In this thesis a MATHEMATICA notebook written by M. Haverkort [22, 23] was employed which provides definitions of the crystal field Hamiltonian and the operators in a basis suitable for a full diagonalization.

2.2 Magnetic exchange

In the context of complex materials with multiple degrees of freedom like spin, charge and orbitals especially the competition between them leads to interesting phenomena. A prominent example is the field of multiferroics, where a coupling of two ferroic properties yields a high potential for possible application in electronics. Responsible for the emerging collective phenomena are the interactions between the contained charged or magnetic particles. Different theories were developed to understand for example the spontaneous ordering of magnetic moments in a ferromagnet. One important concept, introduced in 1908 by P. Weiss, is that of an exchange (or mean-)field which is proportional to the macroscopic magnetization. Due to a gain of internal energy by the coupling of individual moments to the exchange field, a spontaneous magnetization arises below a critical temperature T_C and the well-known Curie-Weiss law for the susceptibility,

$$\chi(T) = \frac{C}{T - T_C}, \tag{2.5}$$

can be derived, that successfully describes many simple magnets. However, the microscopic origin and the coupling to the exchange field was not covered by these early descriptions.

Dipolar interactions between magnetic moments arise from the potential energy of two magnetic dipoles in their mutual magnetic field. In some materials with large magnetic moments, like the spin-ice compounds [24–26], they rule the low-temperature magnetism. However, in most solid state materials they are very small due to the cubic dependence of the energy on the inverse distance between the dipoles.

The magnetism of most materials is explained only by the quantum nature of electrons and the overlap of their wave functions. In a simple system of just two electrons the product wave function of the spatial and the spin part must be antisymmetric to fulfill the Pauli principle, which leads to the formation of a singlet and a triplet state described by the wave functions Ψ_S and Ψ_T, which can be written as products of the spatial parts $\psi_a(\boldsymbol{r})$, $\psi_b(\boldsymbol{r})$ of electron a and b and the singlet and triplet spin states χ_S and χ_T,

$$\Psi_S = \frac{1}{\sqrt{2}} \left(\psi_a(\boldsymbol{r}_1)\psi_b(\boldsymbol{r}_2) + \psi_a(\boldsymbol{r}_2)\psi_b(\boldsymbol{r}_1)\right) \chi_S \tag{2.6}$$

$$\Psi_T = \frac{1}{\sqrt{2}} \left(\psi_a(\boldsymbol{r}_1)\psi_b(\boldsymbol{r}_2) - \psi_a(\boldsymbol{r}_2)\psi_b(\boldsymbol{r}_1)\right) \chi_T \,. \tag{2.7}$$

The difference between the singlet and triplet energy,

$$J = \frac{E_S - E_T}{2} = \int \psi_a^*(\mathbf{r}_1)\phi_b^*(\mathbf{r}_2)\mathcal{H}\phi_a(\mathbf{r}_2)\phi_b(\mathbf{r}_1) d\boldsymbol{r}_1 d\boldsymbol{r}_2 \,, \tag{2.8}$$

is given by integration over the spatial wave functions, where $\mathcal{H}$ is the Hamiltonian of the two-electron system. The integral can be understood as the matrix element between two states that only differ in the exchange of the two particle's coordinates and, thus, is referred to as the *exchange integral.* It describes the electrostatic interaction of the electrons and allows to formulate an effective Hamiltonian for their spins,

$$\bar{\mathcal{H}} = \frac{1}{4}(E_s + 3E_t) - (E_s - E_t)\, \boldsymbol{S}_1 \cdot \boldsymbol{S}_2 \tag{2.9}$$

$$= const. - 2J\boldsymbol{S}_1 \cdot \boldsymbol{S}_2. \tag{2.10}$$

Depending on the geometry and the resulting integrals the effective coupling J between spins can be either positive or negative. In case of a positive (negative) value the interaction leads to a ferromagnetic (antiferromagnetic) ground state with spins parallel (antiparallel). Furthermore, the results can be generalized also to systems with many electrons, described by the Hamiltonian of the Heisenberg model,

$$\mathcal{H} = -\sum_{i,j} J_{i,j}\, \mathbf{S_i} \cdot \mathbf{S_j}, \tag{2.11}$$

where $J_{i,j}$ is the exchange integral between spins i and j. Its precise value depends on microscopic details like the shape of orbitals and the crystal structure.

Various exchange mechanisms between two spins can be effectively expressed in the exchange constant. A direct overlap of the electronic wave functions like in the textbook example of a covalent bond, namely the H_2 molecule [27], cannot account for the magnetism, e. g., of the strongly localized $4f$ or most $3d$ moments. In these systems the exchange often is mediated by an intermediate non-magnetic ion and thus referred to as superexchange. Hopping of electrons from the magnetic ion to the unoccupied states of the intermediate ion allows them to lower their kinetic energy in second order perturbation theory and depending on the geometric and orbital details a ferro- or antiferromagnetic spin alignment is favored [28, 29].

2.3 Spin models

The magnetism of many insulating transition-metal and rare-earth compounds can be related to the physics of spin models. In some copper-based systems the electronic properties of Cu^{2+} allow a description in terms of isotropic spin-$^1/_2$ models similar to that of Eqn. (2.11). The anisotropic magnetism, e. g., of Co^{2+}, arises from the spin-orbit coupling of crystal-field states. Due to an anisotropy of the crystal field degenerate orbital states may split. The details of the splitting depends on the symmetry of the crystal field and can be analyzed in detail by considering the full interacting electron system by crystal field theory, which typically, however, does not account for magnetic exchange (cf. Chapter 4.1.2). Irrespective of the electronic details, a lifting of the orbital degeneracy may lead to a population of only a subset of states at low temperatures. Neglecting the high-energy states thus yields a simplified description within a subspace of the parent Hamiltonian by an effective spin system. In the following the derivation of an effective spin-$^1/_2$ system is demonstrated, followed by a discussion of different one-dimensional spin models and their thermodynamic properties as obtained by numerical simulations.

2.3.1 Effective spin models

Crystal field effects are responsible for the magnetic anistropy of the Co^{2+} ions in Cs_2CoCl_4. According to Hund's rules the orbital ground state of Co^{2+} ($3d^7$) has $S = 3/2$ and $L = 3$. In a cubic tetrahedral crystal field the orbital moment is quenched due to fully occupied t_2 and e levels and the electrons couple to a four-fold degenerate spin state with $|S_z = \pm{}^3/_2, \pm{}^1/_2\rangle$. Their splitting by the crystal field can be effectively described by the single-ion Hamiltonian using the spin-$^3/_2$ operator $\mathcal{S}$,

$$\mathcal{H}_{s.i.} = \mathcal{D}\left[\mathcal{S}_z^2 - \frac{1}{3}\mathcal{S}(\mathcal{S}+1)\right] , \tag{2.12}$$

with the crystal field anisotropy $\mathcal{D}$. The four-fold degeneracy is lifted by the anisotropy $\mathcal{D}$ and according to the Kramers theorem two doublets remain [30]. They correspond to states $\mathcal{S}_z = \pm 3/2$ and $\mathcal{S}_z = \pm 1/2$, which have energies that differ by $2\mathcal{D}$ in energy due to the different $\mathcal{S}_z^2$ expectation values. At low temperatures $T \ll \mathcal{D}$ one can restrict to the lower-lying states, which gives rise to a simplified representation of the system by an effective spin $1/2$. In extension to the single-ion problem, the reduced basis has consequences for the exchange of spins as well. This can be demonstrated for two spin $3/2$ interacting via an exchange J by considering the pair Hamiltonian

$$\mathcal{H}_{3/2} = \mathbf{J}\vec{\mathcal{S}}_1 \cdot \vec{\mathcal{S}}_2 + D(\mathcal{S}_{1,z}^2 + \mathcal{S}_{2,z}^2). \tag{2.13}$$

In the limit of $\mathcal{D} \gg J$ and $\mathcal{D} > 0$ the non-vanishing matrix elements of $\mathcal{H}_{3/2}$ can be given explicitely for the lower-lying $|\mathcal{S}_{1,z} = \pm 1/2, \mathcal{S}_{2,z} = \pm 1/2\rangle =: |{\uparrow/\downarrow}{\uparrow/\downarrow}\rangle$ states.

$$\begin{array}{c|cccc}
\mathcal{H}_{3/2} & |\uparrow\uparrow\rangle & |\uparrow\downarrow\rangle & |\downarrow\uparrow\rangle & |\downarrow\downarrow\rangle \\
\hline
\langle\uparrow\uparrow| & 1/4(J+2\mathcal{D}) & & & \\
\langle\uparrow\downarrow| & & 1/4(-J+2\mathcal{D}) & 2J & \\
\langle\downarrow\uparrow| & & 2J & 1/4(-J+2\mathcal{D}) & \\
\langle\downarrow\downarrow| & & & & 1/4(J+2\mathcal{D})
\end{array} \tag{2.14}$$

Neglecting an energy shift of $\mathcal{D}/2$ the eigenvalues of $\mathcal{H}_{3/2}$ can be calculated by diagonalization of $\mathcal{H}_{3/2}$.

$$\frac{J}{4}, \quad \frac{J}{4}, \quad \frac{-9J}{4}, \quad \frac{7J}{4} \tag{2.15}$$

The two-fold energy corresponds to states $|\uparrow\uparrow\rangle$, $|\downarrow\downarrow\rangle$ with parallel spins, while the others are the mixed states $|\downarrow\uparrow\rangle \mp |\uparrow\downarrow\rangle$. The low-energy Hamiltonian and the energies can be reproduced by an effective spin-$1/2$ system with anisotropic couplings J_{xy} and J_z. In the spin-$1/2$ Hamiltonian

$$\begin{aligned}
\mathcal{H}_{1/2} &= J_{xy}\left(S_{1,x}S_{2,x} + S_{1,y}S_{2,y}\right) + J_z S_{1,z}S_{2,z} \\
&= \tfrac{J_{xy}}{2}\left(S_{1,-}S_{2,+} + S_{1,+}S_{2,-}\right) + J_z S_{1,z}S_{2,z}
\end{aligned} \tag{2.16}$$

the operators S_i differ from the previous spin-$3/2$ operators $\mathcal{S}$ in Eqn. (2.13) by having $S_z = \pm 1/2$, only. Furthermore, the anisotropy $\mathcal{D}$ does not appear in this model any longer, but is represented by the different values of the in- and out-of-plane couplings. The matrix form in the same four-state basis

$$\mathcal{H}_{1/2} = \begin{pmatrix} J_z/4 & 0 & 0 & 0 \\ 0 & -J_z/4 & J_{xy}/2 & 0 \\ 0 & J_{xy}/2 & -J_z/4 & 0 \\ 0 & 0 & 0 & J_z/4 \end{pmatrix} \tag{2.17}$$

reveals the same shape and symmetry as $\mathcal{H}_{3/2}$. The eigenvalues

$$\frac{J_z}{4}, \quad \frac{J_z}{4}, \quad \frac{-2J_{xy} - J_z}{4}, \quad \frac{2J_{xy} - J_z}{4} \tag{2.18}$$

reproduce those of $\mathcal{H}_{3/2}$ when choosing the couplings J_z and J_{xy} in relation to the spin-$^3/_2$ coupling J,

$$J_z = J, \qquad J_{xy} = 4\,J. \tag{2.19}$$

In general, the technique to obtain an effective Hamiltonian for the low-energy states is known as Schrieffer-Wolff transformation [31, 32]. The same results presented above for two interacting spins are also obtained via this technique for a spin chain with an infinite number of spins. The resulting transformation of the exchange constants can be illustrated in a semiclassical picture. Due to the anisotropy terms $\propto \mathcal{D}\mathcal{S}_z^2$ in Eqn. (2.13) the z component of the primary spin $^3/_2$ is suppressed. Thus, a spin orientation within the xy plane is favored. In consequence more energy can be gained by a coupling of the x and y components, which illustrates the increase of J_{xy} over J_z by increasing $\mathcal{D}$. Interestingly, J_z remains finite even though $\mathcal{D} \to \infty$, which is due to the finite fluctuations of the z component. As a function of $\mathcal{D}$ a full suppression of J_z therefore can not be realized, but only the limit of $J_z/J_{xy} = {}^1/_4$.

In the opposite case of large negative crystal field anisotropies $\mathcal{D} \to -\infty$ one obtains the Ising model as an effective spin model, where only the z components of the spins are coupled and $J_z = 9J, J_{xy} = 0$. The ratio J_z/J_{xy} is often referred to as anisotropy parameter $\Delta = 1/\epsilon$, which allows to finally rewrite the effective spin Hamiltonian in different ways.

$$\begin{aligned} \mathcal{H}_{XXZ} &= J \sum_i \left(S_x^i S_x^{i+1} + S_y^i S_y^{i+1} + \Delta S_z^i S_z^{i+1} \right) && (2.20) \\ &= J \sum_i \left(\epsilon (S_x^i S_x^{i+1} + S_y^i S_y^{i+1}) + S_z^i S_z^{i+1} \right) && (2.21) \end{aligned}$$

2.3.2 Model systems

Many linear spin chains can be written in the general form of Eqn. (2.20) and depending on the value of Δ different anisotropies are realized. The resulting models are generally referred to as depicted in Fig. 2.1. In case of $\Delta = 0$ only the x and y components of the spins are coupled, which is known as the XY model. Values of $0 < \Delta < 1$ are still considered as easy-plane type anisotropies, but due to the additional coupling of S_z the model often is referred to as XXZ model. If $\Delta = 1$ the exchange is isotropic in spin space, which yields the famous Heisenberg model. Values of Δ larger than 1 lead to Ising-type models where the exchange along z is largest. This case may be depicted as $\Delta \to \infty$ or as $\epsilon = 0$.

The fundamentals of these spin models are theoretically investigated since the evolution of quantum theory about a century ago. A very comprehensive overview of the properties with reference to thermodynamics will be given in the following. For simplicity, only the zero-field properties are discussed.

None of the models shows magnetic order at finite temperature. However, most systems can be solved exactly and in the following the results are summarized. In Fig. 2.2 the dispersion of excitations and selected thermodynamic properties of the XY, the Heisenberg and the Ising model are plotted for comparison.

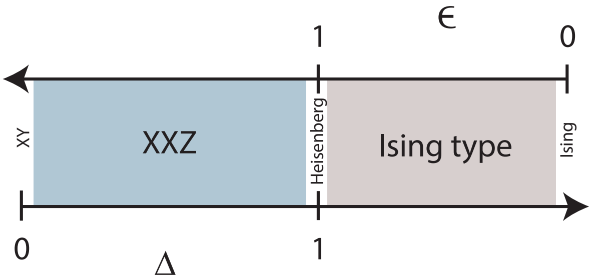

Figure 2.1: Spin chain models as a function of the anisotropy parameters Δ and ϵ.

XY model

The XY model is obtained from Eqn. (2.20) by considering only the exchange of the x and y component of the spin,

$$\mathcal{H}_{XY} = J \sum_i (S_x^i S_x^{i+1} + S_y^i S_y^{i+1}). \tag{2.22}$$

The algebra of spin operators allows to rewrite the Hamiltonian in terms of the ladder operators $S_\pm = S_x \pm i S_y$,

$$\mathcal{H}_{XY} = \frac{J}{2} \sum_i (S_-^i S_+^{i+1} + S_+^i S_-^{i+1}). \tag{2.23}$$

Via a Jordan-Wigner transformation the model is mapped to that of spinless fermions hopping on a chain and is solved exactly [33, 34]. In contrast to finite Δ, in the XY model the fermions are free and do not interact. The magnetic excitations form a cosine dispersion $\epsilon(k, h) = J \cos k - h$ and can be understood as the creation and annihilation of fermions. At $k = \pm\pi/2$ the excitations are gapless at zero field, which is also reflected in the linear specific heat and the finite value of the susceptibility at low temperature as described by the analytic solutions, plotted in Fig. 2.2 (a).

$$\frac{C}{R} = \frac{1}{\pi} \left(\frac{J}{2k_\mathrm{B}T}\right)^2 \int\limits_0^\pi \frac{\cos^2 \omega}{\cosh^2\left(\frac{J}{2k_\mathrm{B}T}\cos\omega\right)} d\omega \overset{T \ll J}{\approx} \frac{\pi}{3}\frac{T}{J} \tag{2.24}$$

$$\frac{k_\mathrm{B}\chi_z}{Ng^2\mu_\mathrm{B}^2} = \frac{1}{\pi}\frac{1}{T} \int\limits_0^\pi \frac{d\omega}{\cosh^2\left(\frac{J}{2k_\mathrm{B}T}\cos\omega\right)}. \tag{2.25}$$

The transverse susceptibility χ_{xy} can be calculated exactly as well [35]. However, no simple analytic form can be given. The transverse susceptibility, i. e., for the field within the XY plane, is about half as large as the longitudinal susceptibility.

XXZ and Heisenberg models

The XXZ models, obtained for intermediate $0 < \Delta < 1$, show properties very similar to that of the XY model. The excitations remain gapless [36]. The thermodynamic quantities, like the specific heat plotted in Fig. 2.2 (a.1), continuously evolve with increasing

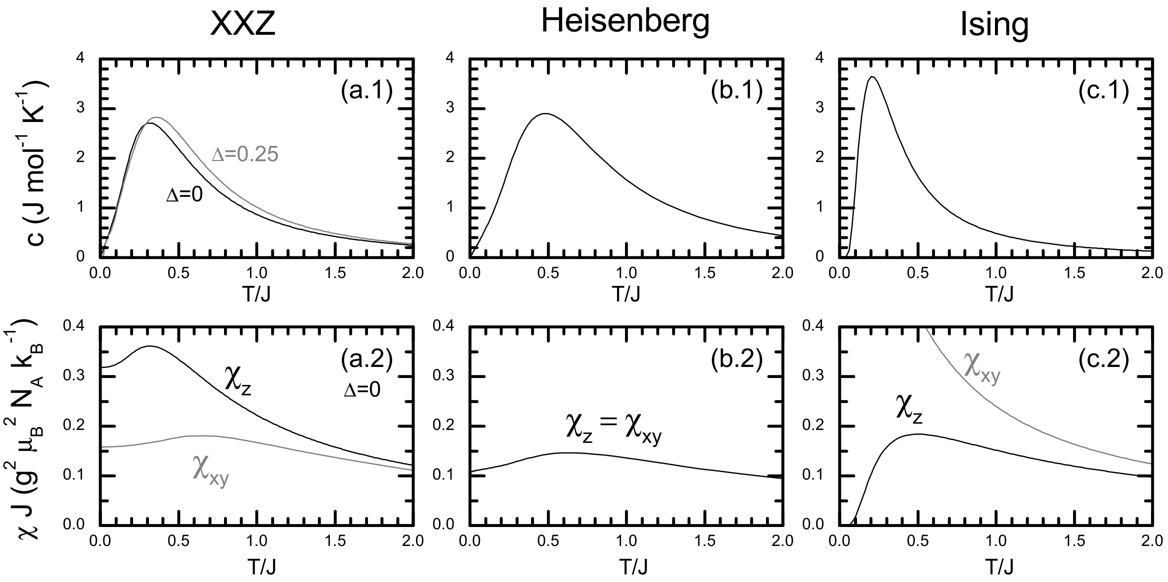

Figure 2.2: Heat capacity and magnetic susceptibilities of selected one-dimensional antiferromagnetic spin models. The longitudinal (black lines) and transverse susceptibilities (gray lines) are calculated assuming $g = 2$.

Δ. In the Heisenberg model ($\Delta = 1$) the exchange is isotropic. The fundamental excitations of the Heisenberg model are described by the dispersion $\epsilon(k) = \frac{\pi}{2} J |\sin k|$ [37]. Just like in the *XXZ* models they form an excitation continuum [38] which is intensely studied in Heisenberg systems [12, 39]. Although the Heisenberg model is exactly solvable via the Bethe ansatz [40], the finite temperature properties have been subject of many theoretical works [37, 38, 41–44] and show surprisingly complex details like a logarithmic correction in the temperature dependence of the susceptibility [45],

$$\chi = \frac{1}{\pi^2 J} \left(1 + \frac{1}{2 \ln(T_0/T)} + ... \right), \tag{2.26}$$

which is not described by a simple analytical equation in the full temperature range. The specific heat, shown in Fig. 2.2 (b.1), was calculated based on a method described in Ref. 46. The influence of a magnetic field on the thermodynamic properties is discussed in Chapter 6 by a comparison to experimental results on the Heisenberg system $\mathrm{Cu(C_4H_4N_2)(NO_3)_2}$.

Ising models

Increasing $\Delta > 1$ an easy axis is established and the magnetic excitations develop a gap. In the limit of $\epsilon = \Delta^{-1} = 0$, the dispersion is constant. Starting from a Néel state, flipping a single spin always costs an energy $\propto J$. For finite anisotropies ϵ a continuum,

$$\omega(k) = J \left(1 - 2\epsilon \cos k \cos(k + \Phi)\right), \quad -\pi < \Phi \leq \pi, \tag{2.27}$$

evolves due to the propagation of two domain walls that develop from a single excitation due to the transverse spin operators [47]. The specific heat in consequence of the gapped excitation shows an exponential temperature dependence at low temperature and a shift of the maximum position to smaller temperature than in the XXZ models, see Fig. 2.2 (c.2). The analytical expression was derived in the original work of Ising [48] and translates to the present convention of Eqn. (2.21) as

$$\frac{C}{R} = \left(\frac{J}{4k_\mathrm{B}T}\right)^2 \frac{1}{\cosh^2\left(\frac{J}{4k_\mathrm{B}T}\right)}. \tag{2.28}$$

A strong anisotropy arises between the longitudinal susceptibility [49],

$$\frac{k_\mathrm{B}\chi_z}{Ng^2\mu_\mathrm{B}^2} = \frac{1}{k_\mathrm{B}T} \cdot e^{-\frac{J}{2k_\mathrm{B}T}}, \tag{2.29}$$

and the transverse susceptibility [50],

$$\frac{k_\mathrm{B}\chi_{xy}}{Ng^2\mu_\mathrm{B}^2} = \frac{1}{2T}\left(\frac{1}{\cosh^2\frac{J}{4k_\mathrm{B}T}} + \frac{\tanh\frac{J}{4k_\mathrm{B}T}}{\frac{J}{4k_\mathrm{B}T}}\right). \tag{2.30}$$

As plotted in Fig. 2.2 (c.3), χ_z goes to zero with the formation of a Néel type ground state for $T \to 0$, while the transverse susceptibility χ_{xy} shows a temperature dependence similar to a Curie-Weiss law.

2.3.3 Numerical simulations

Some of the spin chain models introduced in the previous chapter can be solved exactly and analytical expressions can be given for the finite-temperature properties. Models that additionally show a phase transition as a function of a model parameter other than the temperature, i. e., a quantum phase transition, are of special interest. Two textbook examples of this kind are the transverse field Ising model (TFIM) and the XY model in a longitudinal magnetic field. The existence of analytical functions, for example, allows to directly obtain information on the magnetic correlations from a comparison to experimentally obtained data. Yet, the complexity of most real quantum magnets which show new and exciting phenomena, some of them with a potential for commercial application, extends above these simplified models [51–56]. For example, already a tilt of the magnetic field in the XY model to the transverse direction, i. e., into the XY plane, yields a model whose ground state at finite field is not explicitly known. Many techniques have been developed to find approximate solutions by considering systems of reduced size.

The Alps (Algorithms and Libraries for Physics Simulations) project [57] allows to perform calculations based on various of these methods. It is an open source project that provides libraries and a common framework to simulate strongly correlated electron systems. The source code as well as binary packages and pre-configured virtual machines are available on the web page of the project [58]. One main concept of the project lies in the separation of the lattice from the model and the algorithm.

The geometry of the system is defined based on a finite size lattice using a unit cell that is repeated in one or more dimensions. Within each unit cell an arbitrary number of sites can be defined. Interactions between the sites can be defined within a single unit cell, or extend to sites in neighboring cells. For each site and interaction a type number can be given, which allows to model also complex systems with different interaction types and inequivalent sites. The full geometry is then represented by a finite graph of vortices and edges of different types. A large number of common lattices is included in the project. Custom graphs can be defined in an XML file, as given in Appendix A for the magnetic lattice of Cs_2CoCl_4.

On each vortex of the graph one of the available models is placed. The edges represent the interactions between the sites. In addition to the default models (spin, bosonic and fermionic Hubbard models) custom models can be defined. For the calculations performed during this thesis the spin model was extended to include fully anisotropic couplings and anisotropies, see the code listings in Appendix A. Finally, the system can be analyzed using one of the implemented algorithms: Monte Carlo methods (classical, looper [59], directed loop [60], QWL [61]), DMRG [62], diagonalization (full and sparse [63]). For each method a varying number of parameters can be given.

In the following, results on the thermodynamic quantities of some selected models are shown. A comparison of experimental data of Cs_2CoCl_4 and $Cu(C_4H_4N_2)(NO_3)_2$ to model calculations will be drawn in Chapters 4 to 6. In the following, the main focus lies on the analysis of finite-size effects, the magnetic anisotropy of an effective spin system and on the calculation of the thermal expansion and the magnetostriction.

Finite size effects

Due to the finite system size, the thermodynamic data obtained from the numerical calculations do not represent the true properties of the considered models, which in most cases are defined based on an infinitely large number of sites. Thus, numerical data have to be carefully analyzed in how far they are influenced by the finite size of the system. Only in few cases, like the segmentation of spin chains by non-magnetic impurities, the properties with reduced system sizes are of experimental relevance. In most cases one, however, strives to minimize the finite size effects by either increasing the system size within the computational limits, or by restricting to a temperature range where they are negligible. In most spin systems, the correlation length decreases with increasing the temperature. Therefore, the high-temperature properties are dominated by single sites and hardly depend on the system size or the boundaries of the system. The scaling behavior of systems also is subject of more involved techniques like the renormalization group [64].

In the following the finite size effects in the exact diagonalization results for the XXZ model in transverse field are analyzed. This model is compared to experimental data in Chapter 4 for different values of the anisotropy parameter $\Delta = J_z/J_{xy}$. Here, an exemplary value of $\Delta = 1/4$ is assumed, which represents a strong XY anisotropy. For

L	6	8	10	14	16	18	20
spin-1/2							
number of states	64	256	1024	16384	65536	262144	1048576
memory consumption	4 kB	64 kB	1 MB	256 MB	4 GB	65 GB	1 TB
spin-3/2							
number of states	4096	65536	1048576	268435456			
memory consumption	16 MB	4 GB	1 TB	65 PB			

Table 2.1: Scaling of the number of states and the estimated memory required to store the full Hamiltonian of a spin-1/2 and a spin-3/2 chain of size L.

simplicity, the temperature and the magnetic field h_x are given in units of the exchange constant $J = 1$. The Hamiltonian of the system,

$$\mathcal{H} = \sum_{i=1}^{L} \left[S_x^i S_x^{i+1} + S_y^i S_y^{i+1} + \frac{S_z^i S_z^{i+1}}{4} - h_x S_x^i \right], \tag{2.31}$$

cannot be solved exactly for $L \to \infty$ due to the non-commuting transverse field term and the finite coupling of S_z^i. Yet, for finite system sizes L the full Hamiltonian can be diagonalized. Due to the exponential growth of the number of states, a full diagonalization without symmetry-based simplifications is possible only up to $L = 16$ in case of spin-1/2. In that case a total number of $2^{16} = 65536$ product states enter the wave function of the system. The Hamiltonian describing this system consists of 2^{16^2} matrix elements. Assuming that each element requires 1 byte of storage, a total of 4 GB of memory is required to treat the full system. In Tab. 2.1 the scaling of the number of states and the approximate memory requirements are given for spin-1/2 and spin-3/2 systems. Due to the larger number of states per site in the spin-3/2 system, here only up to 8 sites can be solved by a simple-minded full diagonalization. In case the system reveals certain symmetries, associated with a conserved quantity, the Hamiltonian can be described by a block matrix. Then, the diagonalization process is simplified and may be extended to larger L. In the present case $\mathcal{H}$ at zero field ($h_x = 0$) reveals a rotational symmetry around z, respectively a conserved quantum number S_z. Thus, system sizes up to $L = 18$ can be realized using a standard workstation.

In Fig. 2.3 (a) the specific heat, calculated by exact diagonalization of Eqn. (2.31), is shown. The system size L was varied from 9 to 18 sites. The high-temperature behavior is identical for all chain lengths. For comparison, at zero field also Quantum Monte Carlo (QMC) simulations of the specific heat were performed for a chain length $L = 100$, shown as green symbols in Fig. 2.3 (a). Although the QMC results show an increasing noise at low temperature, they confirm the overall shape of the specific heat calculated by the full diagonalization method. Due to the long computation time of about 50 hours for the temperature dependence at a fixed field via QMC, this method could not be applied for the magnetic-field dependence using the available desktop computers. Instead, full diagonalization is used which takes less than one hour to complete. As discussed in the following, the finite size effects are comparably small in the temperature range of interest. At zero field ($h_x = 0$) all simulations show a

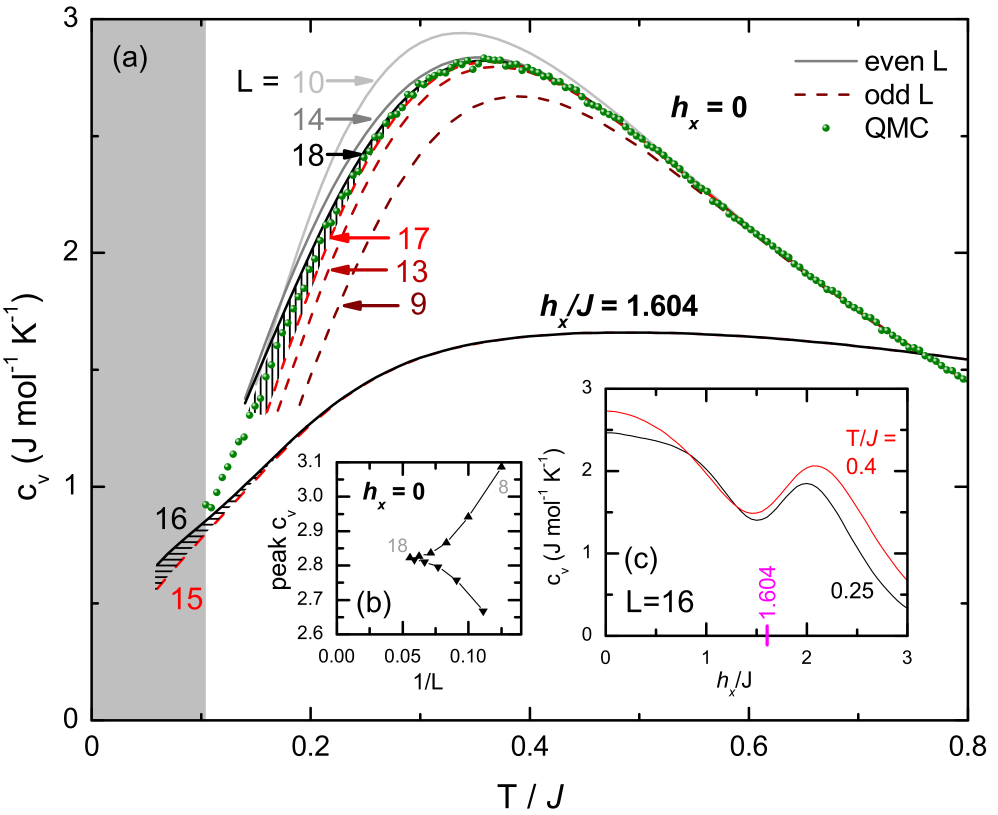

Figure 2.3: Finite size analysis of the specific heat of the *XXZ* model ($\Delta = 1/4$). The main panel shows exact diagonalization results for different chain lenghts L at zero field and at the critical field of the spin chain. The striped area marks the estimated error due to finite size effects below $T/J \lesssim 0.4$. Symbols represent Quantum Monte Carlo results for a system size $L = 100$. In (b) the field dependence of c_v is displayed. Panel (c) shows how the specific heat peak at zero field scales with the inverse system size $1/L$.

maximum between 0.3 and $0.4\,T/J$. Yet, the exact position and the height depend on the chain length L. A systematic difference between chains with even and odd number of sites is seen. This is explained by the possible formation of a singlet ground state in systems with even L, whereas in systems with odd L a two-fold degeneracy remains, illustrated as an excited state at one site in a classical picture [65]. Thus, for antiferromagnetic spin chains even numbers of sites are more advisable to approximate the true ground state of the infinite system. Yet, in the limit of $L \to \infty$ both even- and odd-sized systems should approach each other. As the main comparison to experimental data is to be drawn close to the maximum (cf. Chapter 4), the scaling is analyzed by plotting the specific heat peak height versus the inverse chain length $1/L$ in Fig. 2.3 (b). In this representation the infinite chain limit is realized for $1/L = 0$. As indicated by the converging lines for odd and even sites, the expected change of the peak specific heat for $L > 18$ of below 1% is negligible. At lower temperature the finite size effects strongly increase as approximated by the difference between the results for $L = 17$ and for $L = 18$, shown as striped area in Fig. 2.3 (a). In fact, the QMC data lie within this area with a slight tendency towards the diagonalization results for $L = 18$. Down to $0.2\,T/J$ the finite size errors are in a range from 5 to 10 % and strongly increase for smaller T/J. Thus, the calculations cannot be quantitatively compared to experiment below that temperature and are cut off at $T/J \approx 0.2$.

In a finite transverse magnetic field the rotational symmetry of the model is broken and, thus, the calculations can only be performed up to $L = 16$. However, the single-site magnetic field term reduces the significance of spin correlations and introduces a gap in the excitation spectrum [66]. In consequence, the finite size effects are reduced, which overcomes the reduced system size. The field dependence of the specific heat, shown in Fig. 2.3 (c) for two selected temperatures, indicates the critical field of the spin chain, $h_c/J = 1.604$ in case of $\Delta = 1/4$ [67], by a double peak structure around h_c. As the correlation length ξ in general diverges when approaching the quantum critical point, one may expect that the finite size effects at the critical field arise similar to those at zero field. As shown in Fig. 2.3 (a) for $h_x = h_c$ the calculations surprisingly reveal no significant finite size effects down to $T/J = 0.2$. This may be explained by a different temperature dependence of $\xi(T)$ at zero field and at the critical field. While at zero field the coupling J defines the dominant energy scale, in contrast the physics at the critical field is governed by quantum fluctuations.

Effective spin-1/2 chain

Many striking properties of spin models originate from the quantum nature of the spins that is most prominent in spin-1/2 systems. Fortunately, these are easier to treat with numerical methods than systems with a larger spin quantum number. Most compounds with correlated spin-1/2 moments are based on Cu^{2+}. In a crystal field the angular momentum of the $3d^7$ electron system is suppressed and the magnetism in most cases is highly isotropic. Experimental realizations of anisotropic spin-1/2 Ising systems instead usually base on the splitting of the states of a spin with a higher quantum number and on the application of an effective spin-1/2 model as outlined in Chapter 2.3.1. Often these compounds contain Co^{2+} with a spin 3/2 that in an anisotropic crystal field can give rise to a description as an effective spin 1/2. Nevertheless, the true parent system remains a spin-3/2 system and at a temperature of the order of the crystal field anisotropy the effective spin-1/2 system fails to describe its properties. In the following the formation of an effective spin system is discussed by the example of the compound $BaCo_2V_2O_8$. Spin-1/2 and spin-3/2 model calculations are compared to experimental data at different temperature, particularly with regard to magnetic anisotropies emerging in the calculations.

The compound $BaCo_2V_2O_8$ at low temperature can be described as an antiferromagnetic effective spin-1/2 Ising chain compound with an anisotropy parameter $\Delta^{-1} = \epsilon = 0.46$ [68–74]. The susceptibility of the compound is reported in Refs. 75 and 73. Here, it is compared to the exact diagonalization results for a spin-1/2 chain's susceptibility, shown in Fig. 2.4 (a). It was obtained numerically from the expectation values $\langle S_z \rangle$ and $\langle S_x \rangle$ calculated for small magnetic fields along z, respectively along x. The numerical output is given as an energy χJ in units of $g^2 \mu_B^2 N_A / k_B \simeq g^2 \cdot 1.5\,\text{emu mol}^{-1}$ and thus scales with the coupling constant and with the g factor which is fixed to 2 in the ALPS code. Close to $0.5\,T/J$ both parallel and perpendicular susceptibilities show a broad peak that is typical for one-dimensional magnetism. The perpendicular

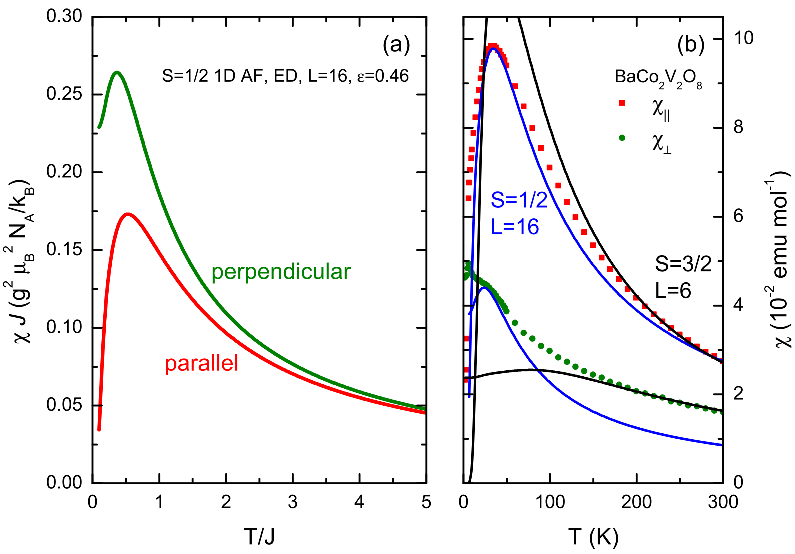

Figure 2.4: (a) Susceptibilities of an antiferromagnetic spin-1/2 chain with an Ising anisotropy $\epsilon = 0.46$ parallel and perpendicular to the Ising axis. (b) The experimental data of $BaCo_2V_2O_8$ are compared to a spin-1/2 (blue lines) and to a spin-3/2 chain (black lines).

susceptibility, i. e., where the field is applied perpendicular to the easy axis z, exceeds the parallel susceptibility in the whole temperature range. In the experimental data, shown in Fig. 2.4 (b) as symbols, this order is inverted. The origin of this inversion lies in the anisotropy of the g factor. In the spin-1/2 calculations, an isotropic electronic g factor of 2 is assumed. Upon the application of an effective spin-1/2 system, the g factors in the spin-1/2 basis, however, become highly anisotropic. For a comparison of the model to the data, therefore the anisotropy of the g factor has to be considered by using different values $g_{\|}$ for the longitudinal and $g_{\perp}$ for the transverse susceptibility when fitting the data by

$$\chi_{\|,\perp}(T) = \frac{[\chi J]_{\text{calc}}(T/J)}{J} \cdot \frac{g^2_{\|,\perp} \cdot 1.5\,\text{emu mol}^{-1}}{4} \cdot 2\ . \tag{2.32}$$

Here, $(g_{\|,\perp}/2)^2$ transforms the g factor and the factor 2 takes into account that the experimental data are given per formula unit, each containing two cobalt ions. The fit, shown as solid blue lines in Fig. 2.4 (b), yields an exchange constant $J/k_B = 65\,\text{K}$ and the g factors $g_{\|} = 7$, $g_{\perp} = 3.8$, exactly matching with the value of the exchange constant and close to the g factors $g_{\|} = 6.3$, $g_{\perp} = 3.2$ derived from the low-temperature magnetization in Ref. 75. It gives a reasonable description close to the maximum of the susceptibility. The high-temperature behavior, however, is hardly reproduced. While the experimental data show the tendency to merge, the calculations for high temperature extrapolate to the ratio of $g_{\|}/g_{\perp}$.

This fundamental difference originates from the neglected spin-3/2 states of the parent Co^{2+}. At high temperature, i. e., when $k_B T$ is comparable to the crystal field anisotropy D, the effective spin-1/2 model is no more applicable (cf. Chapter 4.2) and finally a continuous crossover to an almost isotropic spin-3/2 magnetism is in fact expected. To investigate the emergence of the effective spin system simulations of the susceptibility of spin-3/2 chains with different anisotropies D from -40 to 40 have been performed. Exact diagonalization was applied to system sizes up to $L = 6$. The results are summarized in Fig. 2.5. Due to the small size, severe finite size effects arise at low temperature,

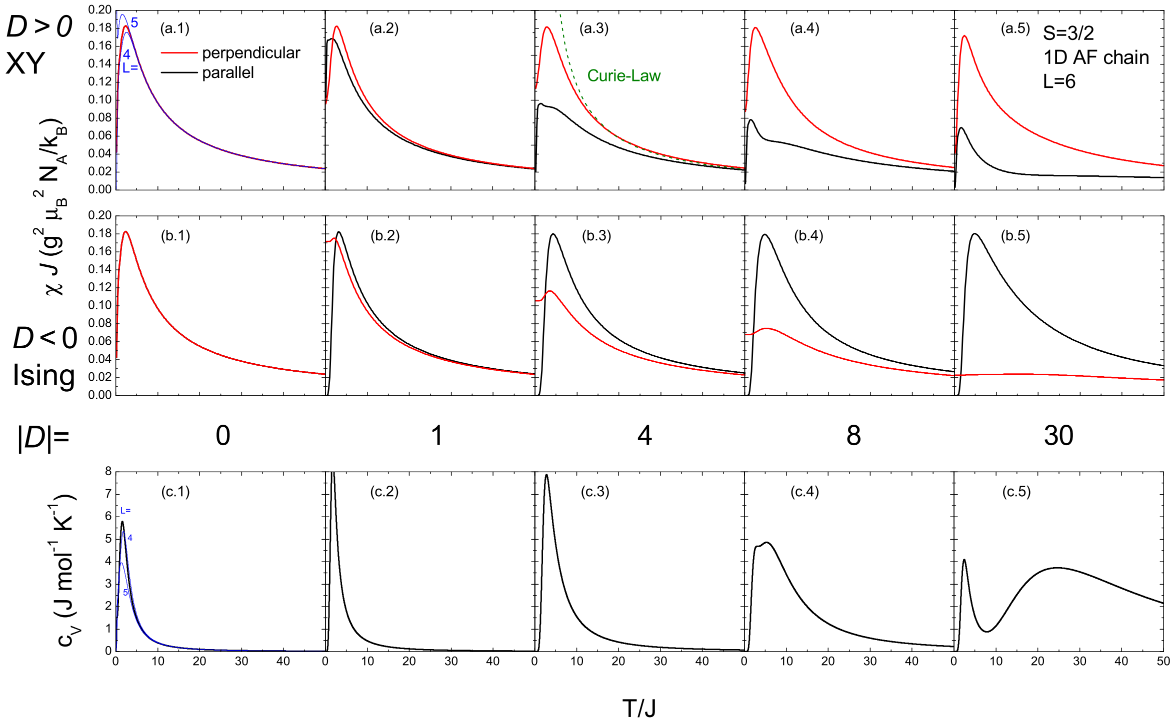

Figure 2.5: Susceptibility and specific heat of a spin-$^3/_2$ chain with 6 sites calculated for different single ion anisotropies D. In (a) positive D are used that lead to an XY type anisotropy. The dashed line in (a.3) represents a S=3/2 free ion's susceptibility. In (b) Ising anisotropies are formed by $D < 0$. Black (red) lines in panels (a) and (b) refer to the susceptiblities parallel (perpendicular) to the anisotropy axis z. In (c) the respective specific heat is shown. In (a.1) and (c.1) the calculations for smaller system sizes $L = 4, 5$ are shown as blue lines.

as shown exemplary for $D = 0$ in panel (a.1) and (c.1) by comparing the results for $L = 6$ (red and black lines) to those for $L = 5$ and $L = 4$, shown as thin blue lines. Nevertheless, the overall splitting of the parallel and the perpendicular susceptibilities by the anisotropy D can be resolved. In the Ising case of $D < 0$, shown in the panels (b) of Fig. 2.5, the parallel susceptibility increases, explaining the g factor anisotropy discussed above. In the easy-plane systems with $D > 0$, instead the susceptibility within the XY plane is larger than the out-of-plane susceptibility. Note, that the magnetic anisotropy follows from the full inclusion of the crystal field acting on the spin-$^3/_2$ system without any further assumptions.

Another consequence of fully considering the spin of $^3/_2$ concerns the high-temperature behavior. Irrespective of the anisotropy D, all susceptibilities approach a simple Curie Law at high temperature, shown as a dashed green line for a selected anisotropy in Fig. 2.5 (a.3). This explains the deviation of the effective spin-$^1/_2$ model from the experimental data in the high-temperature range. Instead, the susceptibility of $BaCo_2V_2O_8$ above 100 K can be well understood on a basis of spin $^3/_2$. Fitting both longitudinal and transverse susceptibilities with the spin-$^3/_2$ calculations yields a reasonable description of the high-temperature data, shown in Fig. 2.4 (b) by black lines. The fit yields an isotropic spin-$^3/_2$ exchange constant $J_{3/2}/k_B = 8\,K$, an anisotropy $D/k_B = -142\,K$ and an isotropic g factor of 2.65. As expected the exchange constant is smaller than for the

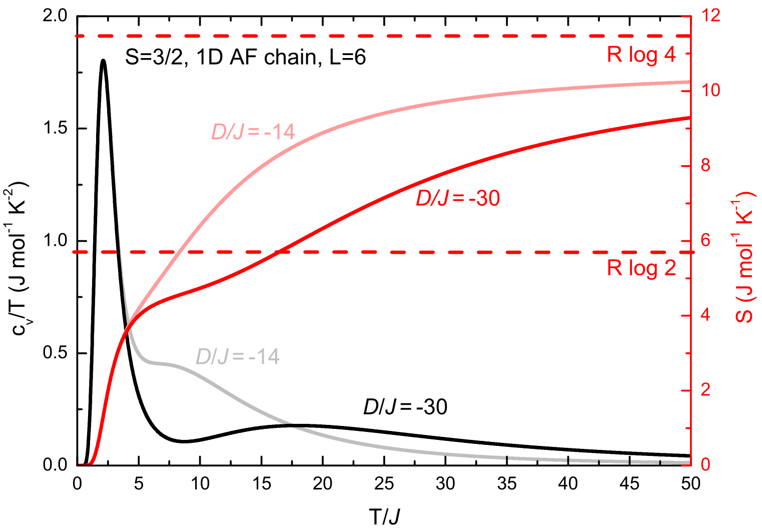

Figure 2.6: Calculated specific heat divided by temperature (black lines) and the entropy S (red lines) of a spin-$^3/_2$ chain ($L = 6$) for two different anisotropies $D = -30$ and $D = -14$ (light colors). Dashed lines mark the entropies expected from a spin-$^1/_2$ and a spin-$^3/_2$.

spin-$^1/_2$ system. In the Ising limit a ratio of $J_{1/2}/J_{3/2} = 9$ is found (cf. Chapter 2.3.1). However, here the anisotropy is only Ising-like, characterized by $\epsilon = 0.46$, explaining the slightly smaller ratio $J_{1/2}/J_{3/2} \approx 8$. While the high-temperature regime is convincingly described by these calculations, the agreement becomes worse with decreasing the temperature. The position of the maximum of the susceptibility is reproduced, but the absolute value is not. This may originate from the small system size of the spin-$^3/_2$ calculations of only 6 sites. Approaching the maximum the finite size effects increase. Yet, their approximate size is smaller than the deviation from the data. In addition, neither of the present calculations takes into account that the true structure of the compound reveals an alternating tilt of the easy axes which strongly influences the low-temperature magnetism [72, 73, 76].

The different temperature regimes of predominantly one-dimensional magnetism and of local paramagnetic behavior are also reflected in the specific heat, shown in panels (c) of Fig. 2.5. For $D/J = 30$ the splitting $2D$ of the spin-$^3/_2$ states (cf. Chapter 2.3.1) is large enough to induce a separation of the specific heat into a low-temperature feature of the one-dimensional magnetism and a high-temperature Schottky-like contribution. This separation is also reflected in the temperature dependence of the entropy, shown in Fig. 2.6 together with the specific heat divided by temperature. The dashed lines represent the expected full entropy $R\log 2$ of a two-level system, respectively $R\log 4$ of the four states of a spin-$^3/_2$. For $D = -30$ a step-like increase of $S(T)$ to these two values arises. Yet, the shape is strongly broadened, which suggests that despite the large D the spin-$^3/_2$ states contribute in a wide temperature range. Similar conclusions are drawn for the effective spin-$^1/_2$ system applied to Cs_2CoCl_4 in Chapter 4.

Thermal expansion and magnetostriction

In Chapter 4 the magnetism of the compound Cs_2CoCl_4 is compared to a spin-$1/2$ model. Besides the common thermodynamic quantities of specific heat, magnetization and energy, that are straightforwardly obtained from numerical simulations, also the thermal expansion and the magnetostriction are analyzed. In statistical physics the volume expansion coefficient,

$$\beta = \frac{1}{V}\frac{\partial^2 G}{\partial T \partial p}, \tag{2.33}$$

relates to the Gibbs free energy G, which apart from temperature may depend on various other parameters, $G = G(T, x_1, x_2, ..)$. In case of a spin system the additional parameters are the exchange constants J_α between spins. Assuming that each of them depends on the pressure p, the pressure derivative of them enters in Eqn. (2.33) via[1]

$$\beta = \frac{1}{V}\frac{\partial}{\partial T}\frac{\partial G}{\partial J_\alpha}\cdot\frac{\partial J_\alpha}{\partial p}. \tag{2.34}$$

In a microscopic theory, which also concerns uniaxial pressure, the interaction of the magnetic system with the lattice has to be included, as shown in Refs. 77, 78 and outlined in the following. In real systems, the exchange constant between spins is determined from the exchange integral over the electronic wave functions. Thus, a change of the underlying lattice, i. e., a change of the inter-atomic distance u, induces a change of the coupling constants J_α in the Hamiltonian $\mathcal{H}$ of the spin system. Here, the *XXZ* model in a magnetic field is considered. In this system, besides the exchange constants J_{xy} and J_z, also the g factor can depend on u. As a function of the displacement u the energy density of the magnetic subsystem

$$E_m(u) = \frac{\langle \mathcal{H}(u) \rangle}{N\, V_S}, \tag{2.35}$$

where V_S is the volume per spin, may be reduced. However, displacing the ions by a distance u from their equilibrium position u_0 costs elastic energy $\mathcal{E}_e$ proportional to the Young's modulus E along the axis of distortion,

$$\mathcal{E}_e = \frac{E}{2}\left(\frac{u-u_0}{u_0}\right)^2. \tag{2.36}$$

Minimizing the sum of $\mathcal{E}_e$ and $\mathcal{E}_m$ yields a finite expansion of the lattice,

$$\frac{u-u_0}{u} = \frac{u_0}{E}\frac{dJ_\alpha}{du}\mathcal{S}_\alpha\,. \tag{2.37}$$

Here, the magnetoelastic coupling enters via the temperature- and field-dependent functions $\mathcal{S}_\alpha$. In case of the *XXZ* model in a transverse magnetic field these functions

---

[1] In condensed matter physics the Gibbs free energy may be well approximated by the free energy F which is usually calculated in theory, similar to the common approximation of $c_p \approx c_v$. Thus, in the following the free energy is considered instead of G.

can be identified with the derivatives of the free energy density $\mathcal{F}_{\mathrm{XXZ}}$, namely the spin-spin correlation functions and the magnetization,

$$\mathcal{S}_{xy} = \frac{\partial \mathcal{F}_{\mathrm{XXZ}}}{\partial J_{xy}} = \frac{1}{NV_S} \sum_i^N \langle S_i^x S_{i+1}^x + S_i^y S_{i+1}^y \rangle, \tag{2.38}$$

$$\mathcal{S}_{z} = \frac{\partial \mathcal{F}_{\mathrm{XXZ}}}{\partial J_{z}} = \frac{1}{NV_S} \sum_i^N \langle S_i^z S_{i+1}^z \rangle, \tag{2.39}$$

$$\mathcal{S}_{H} = \frac{\partial \mathcal{F}_{\mathrm{XXZ}}}{\partial g} = -\frac{\mu_0 \mu_{\mathrm{B}} H_b}{NV_S} \sum_i^N \langle S_i^x \rangle. \tag{2.40}$$

By further translating the derivatives of the coupling constants in Eqn. (2.37) to pressure derivatives, the relative length change of the axis i can be expressed as

$$\delta L_i(T,H) = \sum_\alpha \frac{\partial J_\alpha}{\partial p_i} \mathcal{S}_\alpha(T,H). \tag{2.41}$$

The experimentally observable relative length change $\frac{\Delta L_i}{L_i}$ as a function of temperature and of magnetic field, the thermal expansion coefficient α and the magnetostrictive coefficient λ can be related to $\delta L_i(T,H)$:

$$\frac{\Delta L_i(T)}{L_i} = \delta L_i(T, H = const)\,, \tag{2.42}$$

$$\frac{\Delta L_i(H)}{L_i} = \delta L_i(T = const, H) - \delta L_i(T = const, 0)\,, \tag{2.43}$$

$$\alpha(T) = \left.\frac{\partial\, \delta L_i(T,H)}{\partial T}\right|_H\,, \tag{2.44}$$

$$\lambda(H) = \left.\frac{\partial\, \delta L_i(T,H)}{\partial H}\right|_T\,. \tag{2.45}$$

From the numerical simulations the correlators $\mathcal{S}_\alpha$ can be obtained in two ways. Either the expectation values of the respective spin-spin correlations of Eqns. 2.38, 2.39 and 2.40 are calculated explicitly or the free-energy derivatives are performed numerically. Here, the latter method was used because it is applicable to arbitrary models and the free energy is easily obtained from all kind of calculations in the ALPS code. For a fixed set of model parameters J_{xy}, J_z and g the free energy is calculated as a function of temperature at a constant magnetic field. Then, the calculation is repeated with one parameter changed by a sufficiently small value ϵ and the respective derivative is obtained from the difference quotient

$$\frac{\partial \mathcal{F}}{\partial J_\alpha} \simeq \frac{1}{NV_S} \frac{F(J_\alpha + \epsilon) - F(J_\alpha)}{\epsilon}. \tag{2.46}$$

The resulting derivatives at fixed temperature and magnetic field are interpolated by multivariate splines of second order using MATHEMATICA [23]. The numerical error becomes negligible by choosing sufficiently small values both for the temperature and the magnetic-field steps as well as for ϵ. In Chapter 4.2.2 the correlators and the length change of Cs_2CoCl_4 as a function of temperature and magnetic field are compared to model calculations obtained in this way.

2.4 Quantum phase transitions

The quantum nature of matter plays a crucial role in the understanding of some all-day properties of materials that appear simple at first sight. For example the ferromagnetism of iron at room temperature and above is a purely quantum phenomenon. In the classical theories of phase transitions the change of a system's state is usually considered as a function of temperature. However, the ground state may also depend on other parameters like pressure, magnetic field or the electron density. Tuning one of these parameters to a critical value $g = g_c$ a transition of the system may arise, reflected in a change of the character of the wave function describing the ground state. The fact that the transition is driven not by temperature and by thermal fluctuations, but by another parameter g that introduces quantum fluctuations in the system, gives rise to the description as a “quantum phase transition”. Introductions into this wide field are given, e. g., in Refs. 79–82 and the basic concepts are outlined in the following. Both first- and second-order transitions as a function of g may arise, yet the continuous second-order case is more common. In this case, there is a characteristic energy Δ of the fluctuations, which for example may be the energy of the lowest excitations above the ground state,

$$\Delta \propto J \left| g - g_c \right|^{z\nu} , \tag{2.47}$$

that vanishes when approaching the critical point g_c, according to the exponent $z\nu$ that mostly is universal, i. e., it does not depend on microscopic details of the model.

Close to the transition, on a characteristic length scale ξ, the system resembles the properties of the critical point. Approaching g_c the length diverges with another exponent ν,

$$\xi \propto \left| g - g_c \right|^{-\nu} . \tag{2.48}$$

The ratio z of the exponents of Eqn. (2.47) and Eqn. (2.48) is called the dynamical critical exponent. It relates the energy scale Δ to the length scale ξ,

$$\Delta \propto \xi^{-z}. \tag{2.49}$$

A famous example for a quantum phase transition is the ferromagnetic one-dimensional Ising spin chain in a transverse magnetic field. Due to the ferromagnetic coupling a parallel alignment of spins is favored. At zero field there are two ground states with parallel spins between sites,

$$|\Uparrow\rangle = \prod_k |\uparrow\rangle_k , \quad \text{and} \quad |\Downarrow\rangle = \prod_k |\downarrow\rangle_k . \tag{2.50}$$

In real crystals one of them is selected as the true ground state, which breaks the spin-inversion symmetry and leads to a finite ferromagnetic moment that in a classical

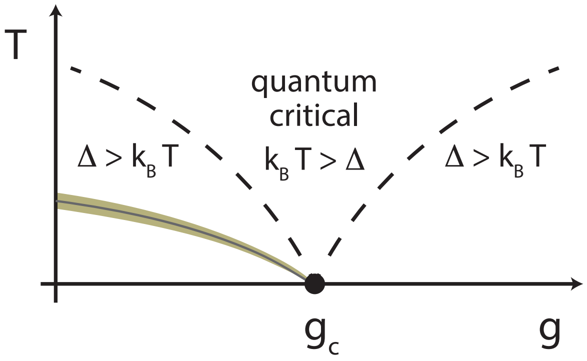

Figure 2.7: Quantum critical regime at finite temperature above a quantum critical point at $g = g_c$. The energy Δ is a characteristic of the ground state and $k_\mathrm{B}T$ is the size of thermal fluctuations. Depending on their ratio classical ($\Delta > k_\mathrm{B}T$) or quantum critical behavior arises. Dashed lines indicate crossover lines between these regimes. The shaded area and the thin line mark a possible classical phase transition line.

way is only destroyed by thermal fluctuations. Magnetic fields h_x perpendicular to the Ising axis, i. e., along the x axis, favor another state with the moments along the field direction. The ground state in the limit of $h_x \to \infty$,

$$|\Rightarrow\rangle = \prod_k |\rightarrow\rangle_k \quad \text{with} \quad |\rightarrow\rangle_k = \frac{|\uparrow\rangle_k + |\downarrow\rangle_k}{\sqrt{2}} \tag{2.51}$$

differs from the zero-field state in fulfilling the spin-inversion symmetry and in a vanishing ferromagnetic moment. In between these two extrema the ground state properties must change in a non-analytic way. The point where the ferromagnetic moment vanishes and the inversion symmetry is established defines the quantum critical point at $g = g_c$. This model was found applicable to the compounds $\mathrm{LiHoF_4}$ [1] and $\mathrm{CoNb_2O_6}$ [2]. Another model where quantum criticality arises as a function of the magnetic field in a similar way is the XY model [34]. The closely related XXZ model also shows a quantum phase transition in a transverse field, i. e., with the magnetic field in the XY plane and is compared to experimental data of $\mathrm{Cs_2CoCl_4}$ in Chapter 4.

Although the phase transition as a function of g is most prominent in the change of the ground-state wave function at zero temperature, the presence of the critical point g_c has consequences on the properties at finite temperature as well. In general the range of g where the critical point g_c influences a system's finite temperature properties is referred to as the quantum critical regime, depicted in Fig. 2.7.

Defining the quantum critical regime the dynamics of a system at finite temperature is considered. The thermal equilibration time τ_eq characterizes the time a system requires to recover its equilibrium state after perturbing it,

$$\tau_\mathrm{eq} = C\frac{\hbar}{k_\mathrm{B}T}. \tag{2.52}$$

This equation in fact represents the shortest time τ_eq that describes the equilibration due to quantum effects in the critical regime and only depends on the temperature and the universal constant C. In the classical regime, $\Delta > k_\mathrm{B}T$, long equilibration times

$$\tau_\mathrm{eq} \gg \frac{\hbar}{k_\mathrm{B}T} \tag{2.53}$$

are found. Here, thermal fluctuations are stronger than quantum fluctuations. Thus, the influence of quantum effects in this range is small and the system can be described classically.

In the quantum critical regime, on the contrary, quantum fluctuations characterized by Δ and thermal fluctuations of size $k_{\mathrm{B}}T$ are equally important, $k_{\mathrm{B}}T > \Delta$. In this range τ_{eq} becomes small,

$$\tau_{\mathrm{eq}} \approx \frac{\hbar}{k_{\mathrm{B}}T}, \tag{2.54}$$

and the dynamics of the system is understood only by including quantum effects. Within the quantum critical regime on short time scales and at small length scales the system looks similar to the ground state at the critical point g_c. At finite distance $|g - g_c|$ from the critical point this resemblance of the critical point is restricted to the typical length scale ξ. If thermal fluctuations arise before the system discovers its finite ξ, the properties are governed by the physics of the critical point g_c. With increasing temperature the thermal fluctuations become more relevant and thus the range of values g, where critical behavior is found, increases. This explains the rather counter-intuitive opening of the boundary between the classical and the critical regime in Fig. 2.7. The dashed lines in this sketch do not indicate phase transitions, but crossovers that follow a temperature dependence $T \propto |g - g_c|^{z\nu}$.

2.5 Magnetic order

Based on the Mermin-Wagner theorem, in systems where ordering would break a continuous symmetry there is no long-range order in one and two dimensions at any finite temperature [83]. Thus, the antiferromagnetic Heisenberg and XXZ models discussed in this thesis are not expected to show magnetic order at all. Yet, in real crystals with quasi one-dimensional magnetism often magnetic order is found when sufficiently lowering the temperature. This discrepancy is explained by deviations from the perfectly one-dimensional exchange assumed in the models. There are finite couplings of moments in all spatial directions. For example, in case of $\mathrm{Cs_2CoCl_4}$ (cf. Chapter 4) the ratio $J'/J \approx 0.05$ of magnetic exchange between to that within spin chains is small and the one-dimensional magnetism is hardly influenced by it. Nevertheless, J' induces magnetic order at a temperature of about $0.1\,J$. Even though J' is small in comparison to the dominant intrachain coupling, the energy gain from interchain couplings is obtained not only for a single pair of spins, but for finite segments of the spin chain. The length of these segments is characterized by the correlation length ξ. Assuming ξ is given in terms of a number of lattice sites, thus an energy $\xi \cdot J'$ is gained by aligning spins between chains. The temperature where magnetic order is induced depends on the size of J' and on how correlations decay. The temperature dependence of ξ typically is such that the correlation length becomes large at low temperature $T \ll J$ in a non-linear way, explaining the sudden onset of magnetic order and the rather small influence of the interchain couplings on the high-temperature properties.

As a function of an external parameter, like magnetic field or pressure, the formation of magnetic order may be influenced and eventually be fully suppressed at a critical value. In Fig. 2.7 the phase-transition line of magnetic order is sketched as a gray line and the temperature range where thermal fluctuations rule the phase transition is shaded in yellow. Here, the precise position of this line in the phase diagram, however, is chosen more or less arbitrarily. The critical point where the zero-temperature ground state changes and the classical phase boundary of magnetic order not necessarily have to merge at the same value g_c. Likewise, the dashed crossover line is not to be confused with the phase transition line of magnetic order. In the study of the magnetic order of Cs_2CoCl_4 in Chapter 4 in fact two different critical fields are found, similar to the obervations in other materials [84, 85].

3 Experimental

The influence of magnetic subsystems on the macroscopic properties of a crystal are usually most pronounced at temperatures of the same order as the associated magnetic exchanges. For the compounds studied in this work, the magnetic exchange constants range from about 1 K to more than 10 K. Thus, measurements of several thermodynamic properties were carried out close to liquid helium temperatures or even lower. In order to cool samples down to these temperatures different cooling methods were employed which are explained in Chapter 3.1. The thermodynamic properties analyzed in this thesis as well as the experimental techniques to measure them are introduced in the subsequent chapters.

3.1 Cryogenic setups

The HELIOX VL system is a versatile ^{3}He cryostat that allows custom sample holders to be operated in a high vacuum chamber and in a temperature range from 0.25 K to about 30 K. The cryostat allows one-shot cooling using ^{3}He in a closed system. As depicted in Fig. 3.1 the vapor pressure of ^{3}He in comparison to that of ^{4}He allows to cool to reasonably lower temperatures by pumping on the vapor of ^{3}He.

Via a sliding seal, the cryostat (Fig. 3.2) is slowly inserted into a conventional bath dewar. First, ^{4}He is evaporated by pumping through the ^{4}He pipe. The main cooling power is obtained at the λ-plate. Here, a typical temperature of about 1.8 K is reached. Gaseous ^{3}He stored in the reservoir then condenses and gathers in the pot at the lower cryostat's end. Subsequent pumping of ^{3}He is accomplished by the ^{3}He sorb that acts as a cryo pump. Cooling power is provided as long as the liquid ^{3}He is not fully evaporated. Thus, the base temperature of 250 mK can be maintained for a limited time of about 20 h, depending on the heat load during the measurement. Afterwards, the ^{3}He sorb has to be heated such that the adsorbed gas can liquify again, which is, however, accompanied by a rise of the sample holder's temperature to about 2 K. Subsequent cooling of the sorb by the λ-plate then allows to reach again a base temperature of

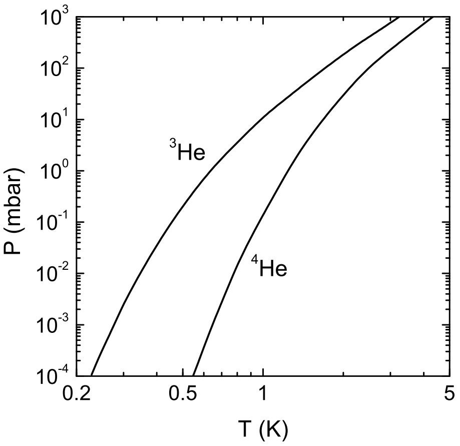

Figure 3.1: Vapor pressure of ^{3}He and ^{4}He, adopted from Ref. 86.

$\sim$ 250 mK. Higher temperatures up to about 30 K can be reached by either slightly heating the ^{3}He sorb, which changes the vapor pressure of the closed ^{3}He system, or at temperatures above about 2 K by directly heating the ^{3}He pot against the cooling power of the λ-plate. Due to the change of the heating mode and the anomalies of ^{4}He at low temperature and low pressure, the temperature stability of the system strongly varies. Close to 2 K the temperature stability does not suffice to carry out heat capacity measurements. Thus, the offset heating method described in Chapter 3.2.3 is imperative to obtain meaningful data in this temperature range.

^{3}He-^{4}He dilution refrigerators are the most common method to cool solid matter below 250 mK. They provide a continuous cooling down to temperatures as low as $\approx$ 5 mK. Due to high-frequency or heat radiation in typical measurement setups, however, the base temperature is raised by a few millikelvin. In a dilution fridge the remarkable physical properties of a mixture of the two helium isotopes ^{3}He and ^{4}He are utilized for cooling. A schematic drawing of a dilution fridge is given in Fig. 3.3. At temperatures below 0.87 K a mixture of at least 6.6 % ^{3}He in ^{4}He separates into two phases. Within the mixing chamber the ^{3}He-rich (concentrated) phase floats on top of the ^{4}He-rich phase (shown as dotted areas in Fig. 3.3). The lower (dilute) ^{4}He-phase has an almost temperature-independent solubility of ^{3}He of 6.6 %. Via an osmotic pressure ^{3}He is removed from this phase by pumping on the “still” which has a temperature of about 0.7 K. At that temperature the vapor pressure of ^{3}He is much larger than that of ^{4}He and in a range accessible with vacuum pumps. This allows to selectively extract ^{3}He from the dilute phase. The induced loss of ^{3}He from the dilute phase is compensated by a flow of ^{3}He from the concentrated phase across the phase boundary. As the specific heat of pure ^{3}He is larger than that of a dilution of it in ^{4}He, cooling is provided by the enthalpy difference of the two phases. To obtain a continuous cycle, the pumped gas is first precooled and condensed at a temperature of 1.5 K that is provided by conventional pumping of ^{4}He. The main impedance makes sure that the pressure is high enough for the incoming ^{3}He gas to condense and to enter the next stages as a liquid. The liquid ^{3}He is then cooled further by the still or via heat exchangers by the dilution traveling towards the still. Besides many other subtle construction details the design of the heat exchangers is crucial for the total performance of the refrigerator. Due to the increasing impact of thermal contact resistances at low temperatures, mechanical links, e. g., of the sample holder to the cryostat and the thermometers to the sample, have to be carefully

Figure 3.2: Individual components of the HELIOX VL cryostat used in a temperature range from 0.25 K to 30 K. A custom sample holder that spans the distance to the center of a magnetic field in a dewar (185 mm in the present case) can be attached to the lower end of the ^{3}He pot.

optimized. More details on the principle of dilution refrigerators and the fundamentals of cryogenic setups are given, e. g., in Ref. 86.

The measurements of thermodynamic quantities below 300 mK, discussed in this thesis, were acquired using a KELVINOX 300 by Oxford Instruments, which is a common instrument in the field of dilution fridges. Several optimizations of the existing setup were employed. A software based on LabVIEW [87] was developed to automatize the remote instrument control and monitoring. The 24-wire cabling of the mixing chamber's user port with a room temperature socket were renewed. Prior to this work it consisted of copper wire, which was replaced by low thermal-conductivity manganin wire (100 µm) to minimize heat conduction. The previous control of the temperature based on a resistance bridge (AVS-47B by Picowatt) and a separate temperature controller in some cases caused disturbing temperature jumps or even full breakdowns of the ^{3}He circulation caused by a change of the measurement range. Thus, these instruments were replaced by adapting a new AC resistance bridge (Lakeshore 370S) to the system. By careful shielding of heat radiation within the inner vacuum chamber the base temperature of the dilution fridge was approximately halved to 23 mK.

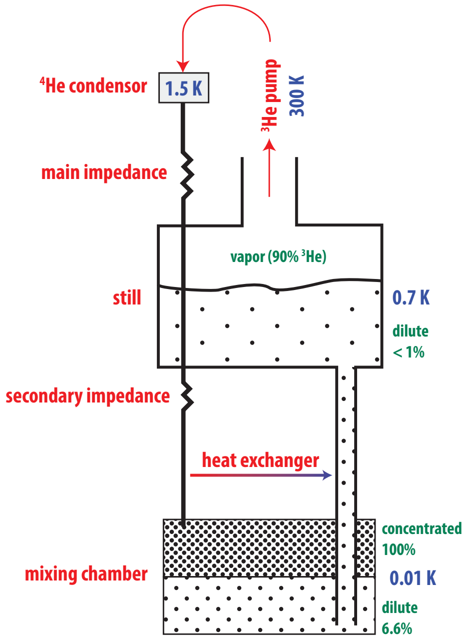

Figure 3.3: Schematic drawing of ^{3}He-^{4}He dilution refrigerator. Red labels specify the parts, blue labels indicate the temperature at different sites during operation, green labels give the respective phase name and percentage of ^{3}He concentration.

3.2 Specific heat

In statistical physics the specific heat at constant volume V, respectively at constant pressure P relates to the thermodynamic potentials,

- the internal energy $E = E(S, V)$,
- the free energy $F = F(T, V) = E - TS$,
- the enthalpy $W(S, P) = E + PV$,
- the Gibbs free energy $G = G(T, P) = E - TS + PV$

and to the entropy S via

$$\begin{array}{lllllll} S_{P,V} & = & -\frac{\partial F}{\partial T}\Big|_V & = & -\frac{\partial G}{\partial T}\Big|_P & , & \\ C_V & = & \frac{\partial E}{\partial T}\Big|_V & = & T\,\frac{\partial S}{\partial T}\Big|_V & = & -T\,\frac{\partial^2 F}{\partial T \partial T}\Big|_V , \\ C_P & = & \frac{\partial W}{\partial T}\Big|_P & = & T\,\frac{\partial S}{\partial T}\Big|_P & = & -T\,\frac{\partial^2 G}{\partial T \partial T}\Big|_P . \end{array} \tag{3.1}$$

While in solid-state experiments usually the pressure can be kept constant quite easily and thus C_p is measured, most theoretical considerations give the specific heat for constant volume C_V. The difference between both relates to the volume thermal expansion $\beta = \frac{1}{V}\frac{\partial V}{\partial T}$ and the compressibility $\kappa = -\frac{1}{V}\frac{\partial V}{\partial P}$ via

$$C_P - C_V = VT\frac{\beta^2}{\kappa}. \tag{3.2}$$

In this thesis several comparisons between experimental data and model calculations will be performed. Due to the small thermal expansion of solids the difference $C_P - C_V$ in these comparisons is safely negligible.

Being the temperature derivative of the thermodynamic potentials the heat capacity indicates the change of the energy of a system upon changing the temperature. Thus, from the temperature dependence of the heat capacity the energetic structure of excitations in a system can be probed. In principle all types of excitations, for instance lattice, electronic or magnetic excitations as well as phase transitions contribute and thus can be probed. At the same time the separation of these contributions often complicates the analysis. For example, the large lattice heat capacity of solids often overlaps with the other contributions.

The heat capacity C of a sample can be deduced by various experimental methods. Common to all of them is that heat is applied to the sample and that the temperature evolution as a function of time is monitored. Repeating this process at various base temperatures single $C(T)$ data points are obtained. Usually they are given normalized either to the mass of the sample or to the number of particles. In the following two methods which are common in low-temperature physics are discussed that are realized in the developed experimental setups presented afterwards.

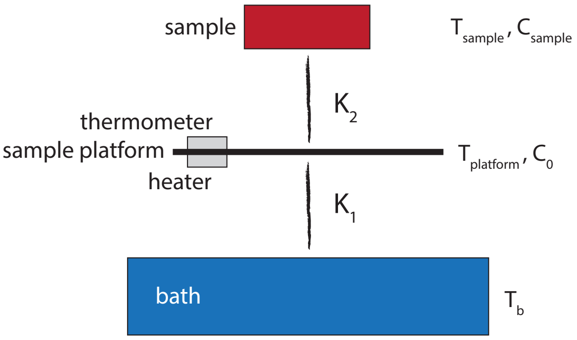

Figure 3.4: Schematic drawing of the experimental setup to measure the specific heat. Keeping the bath temperature T_b stable, a heating power is applied to the heater, which leads to a change of the sample platform's temperature T_{platform} as a function of time. The sample is attached to the platform via a finite thermal conductance K_2. The measured heat capacity $C = C_0 + C_{\text{sample}}$ consists of the empty sample holder's and the sample's contribution.

3.2.1 Quasi-adiabatic heat pulse method

The quasi-adiabatic heat pulse method represents a rather intuitive approach to the heat capacity. A certain amount of heat ΔQ is applied to a system. Under adiabatic conditions, the heat capacity C_p is directly obtained from the resulting temperature change ΔT,

$$C_p = \frac{\Delta Q}{\Delta T}.$$

In experiments true adiabatic conditions, however, cannot be realized, giving rise to the description of the method as quasi-adiabatic. The experimental setup is shown in a schematic view in Fig. 3.4. It consists of a sample platform on which a resistive thermometer and a heater are mounted. The thermal link between the sample platform, the thermometer and the heater is assumed to be ideal. The sample is attached to the platform usually by a small amount of grease which (in case of the low-temperature grease Apiezon N) solidifies upon cooling below room temperature. The respective thermal link K_2 of the sample to the platform in the ideal case is infinite. However, due to the increasing effect of thermal contact resistances at low temperature and the relatively small thermal conductivity of the grease a finite K_2 can manifest in the raw data as discussed below. In most setups the platform is held in place by nylon strings or sometimes by the leads of the thermometer and the heater itself. Thus the thermal conductance K_1 between the platform and the experimental environment is not zero as in a true adiabatic scenario. Actually, a finite $K_1 > 0$ is required to provide the cooling of the sample by the environment, respectively by the cryostat that provides the bath temperature T_b. Due to the finite K_1 and the radiation of heat, the lowest achieved platform temperature, however, lies above T_b.

Assuming ideal adiabatic conditions, the heat capacity is measured by applying heat, $\Delta Q = RI^2t$, to the system, where R is the resistance of the heater and t the time for which a current I is driven through the heater. The heat capacity is obtained by dividing ΔQ by the induced temperature rise ΔT. Due to the quasi-adiabatic conditions, the temperature as a function of time, however, differs from a simple step-like increase in several points. A schematic heat pulse is shown in Fig. 3.5. The heater is switched on at the time t_0 for a typical length of 2-3 s. Shorter times would reduce the error introduced by heat flowing to the sample environment during the heat pulse, yet the length of the current pulse then was increasingly important, which can become experimentally

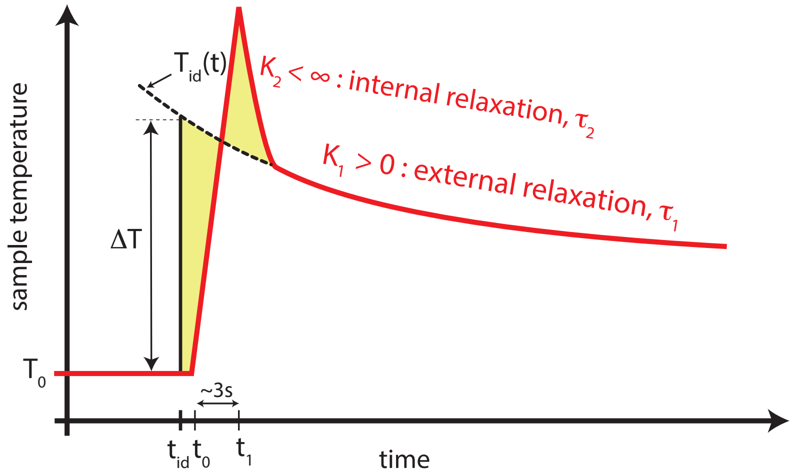

Figure 3.5: Schematic time dependence of the sample temperature in the quasi-adiabatic heat pulse method. Extrapolating the external relaxation to a virtual time t_{id} as defined by the equal-areas method the internal relaxation can be taken into account. From the temperature rise ΔT at t_{id} the heat capacity is calculated.

challenging due to the time constants of the electronics and the natural limit for the required increase of the current I. As the heater is attached to the platform, in first place the platform is heated. If the coupling of the sample K_2 is finite, during the heat pulse the platform temperature can exceed the sample temperature. In the $T(t)$-data this is reflected by an overshoot of the measured platform temperature and an equilibration of the platform and the sample by the so called internal relaxation after switching off the heater at t_1. This typically fast temperature relaxation, characterized by a time constant τ_2, is followed by another relaxation to the temperature of the bath, caused by the non-zero K_1. The temperature rise ΔT, thus, is not directly obtained from the measured temperature after switching off the heater, but by considering the heat flow equations of the system. The heat transfer Q_{off} from the platform to the bath can be calculated by integrating the measured temperature $T_{\mathrm{platform}}(t)$,

$$Q_{\mathrm{off}}(t) = K_1 \int_0^t \left(T_{\mathrm{platform}}(t') - T_0\right)\, dt'.$$

Here, T_0 is the equilibrium temperature before the application of the heat pulse. In the limit $t \to \infty$ the total area under the temperature curve $Q_{\mathrm{off}}(t \to \infty)$ equals the total applied heat ΔQ induced by the heater. This result is independent of the shape of $T(t)$ and holds true also for an idealized system without internal relaxation effects. For such an ideal system with equal heat capacities, with the same K_1, but with $K_2 \to \infty$, the time dependence of the temperature is given by

$$T_{\mathrm{id}}(t) - T_0 \propto e^{-t/\tau_1}.$$

Here, τ_1 is the time constant of the external relaxation. It relates to the sum of the platform's and the sample's heat capacity $C_0 + C_{\mathrm{sample}}$ via $\tau_1 = K_1(C_0 + C_{\mathrm{sample}})$.

However, in general K_1 is not known and τ_1 is rather obtained by fitting the measured temperature data by an exponential. Such, $T_{\mathrm{id}}(t)$ represents the extrapolation of the external relaxation data points to previous times. The temperature rise ΔT is now read off from T_{id} at a time t_{id}. In general t_{id} does not equal one of the true heater switching times, but is obtained from claiming that the total applied heat of the idealized system equals the experimental value,

$$Q_{\mathrm{off}}(t \to \infty) = \Delta Q = \int\limits_{t_{\mathrm{id}}}^{\infty} (T_{\mathrm{id}}(t) - T_0)\ dt.$$

This claim translates into the area below the experimental data and the $T_{\mathrm{id}}(t)$ curve being equal. In the sketch of Fig. 3.5 this is fulfilled if the yellow shaded areas are equal. From the temperature rise $\Delta T = T_{\mathrm{id}}(t_{\mathrm{id}}) - T_0$ the heat capacity is calculated bia

$$C_p = \frac{\Delta Q}{\Delta T} = \frac{RI^2 t}{T_{\mathrm{id}}(t_{\mathrm{id}}) - T_0}.$$

Using the equal areas method, internal relaxation effects can be corrected for. Besides the comparably simple analysis of the data, one drawback of the method, is the rather subtle dependence of the resulting ΔT and thus the heat capacity on the fit boundaries of $T_{\mathrm{id}}(t)$ to the data. In cases where τ_1 comes close to τ_2, separating the external from the internal relaxation can become difficult. In the application of the method to the low-temperature data of Cs_2CoCl_4 (Chapter 4.3.2) this uncertainty is reflected in a systematic error of the data of about 10%. Secondly, the demanded small thermal link K_1 lengthens the cooldown times in the experiment and renders the system quite vulnerable to mechanical vibrations and all kind of parasitic radiation.

3.2.2 Relaxation time method

The experimental setup for the relaxation time method differs from the heat pulse method in a reasonably larger coupling to the bath via $K_1 > 0$. Instead of a short heat pulse the exponential time dependence of the temperature after switching the heater is analyzed. A sketch of the typical time dependence during a heat pulse is shown in Fig. 3.6. Initially the system is in equilibrium with the temperature bath, respectively the cryostat that provides the cooling. In experiment, the sample temperature T_0, however, is not equal to the bath temperature T_b due to finite radiation of heat and high-frequency noise. These effects are considered by a finite offset power P_0 to the system. Actually, an intentional increase or even a control of the sample temperature between heat pulses yields a reasonably faster temperature control and can lower noise. For any finite value of P_0, realized via an offset current through the heater, the following analysis remains unaffected [88].

At time t_1 the heating power P is raised by ΔP by applying a current to the heater. Due to the increased power, the sample temperature rises with an exponential time dependence. At time t_2 the heater is switched off and again an exponential decay is observed. The time constant of both relaxation processes relates to the heat capacity

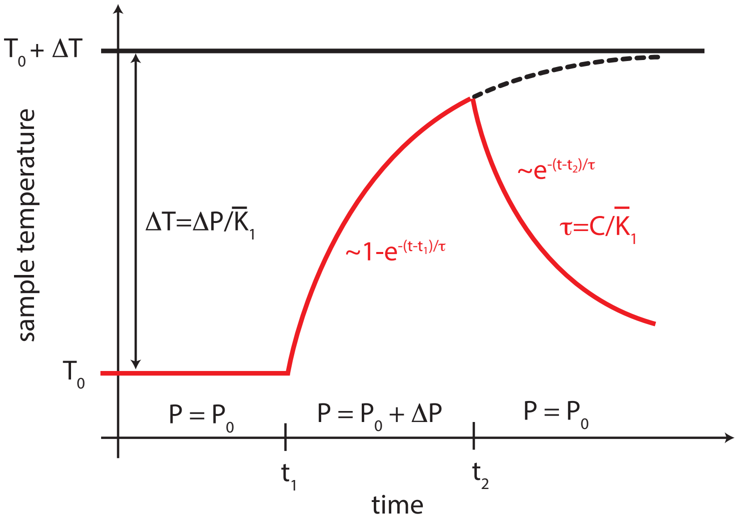

Figure 3.6: Schematic drawing of a heat pulse in the relaxation time method. At time t_1 the heating power is increased by ΔT. From the exponential rise of the temperature the thermal conductance K_1 is obtained. After switching off the heater at t_2 the sample temperature relaxes back to T_0 with a time constant $\tau = C/\bar{K}_1$.

as shown in the following. For simplicity an infinite $K_2 = \infty$ is assumed in the first place, which allows to describe the system by analytic expressions. Later the numerical analysis of data which are slightly modified by τ_2 effects will be discussed. If $K_2 = \infty$ only a single temperature $T = T_{\text{sample}} = T_{\text{platform}}$ and a single heat capacity $C = C_0 + C_{\text{sample}}$ has to be considered. Based on the first law of thermodynamics,

$$\Delta Q = C\, dT$$

the heat change of a system is reflected in a temperature change scaled by the heat capacity. Here, ΔQ consists of two contributions,

$$\Delta Q = \Delta Q_{\text{heat}} + \Delta Q_{K_1},$$

where $\Delta Q_{\text{heat}} = \int \Delta P\, dt > 0$ is the heat applied to the system via the heater and $\Delta Q_{K_1} < 0$ is the heat flow from the sample to the environment via the finite conductance K_1. In the experiment K_1 is realized for example by a platinum wire that is connected to the sample platform. During a heat pulse the platform temperature $T(t)$ changes as a function of time. Thus, the thermally conducting wire experiences different temperatures at its endpoints and the heat flow has to be calculated by integration. In lowest order the conductance can be approximated by an average value $\bar{K}_1$, which allows to describe the heat flow by a simple differential equation,

$$C\, dT = \Delta P\, dt - \bar{K}_1 (T - T_0)\, dt.$$

For the heating curve with $\Delta P > 0$ at times $t > t_1$ one obtains the solution

$$T_{\text{heat}}(t) = T_0 + \frac{\Delta P}{\bar{K}_1}\left(1 - e^{-(t-t_1)/\tau}\right), \quad \text{where } \tau = \frac{C}{\bar{K}_1}.$$

In analogy the relaxation of the sample temperature after switching off the heater at $t = t_2$ is given by

$$T_{\text{relax}}(t) = T_0 + \frac{\Delta P}{\bar{K}_1} e^{-(t-t_2)/\tau}.$$

From fitting of the experimental curves, thus, the thermal conductance $\bar{K}_1$ and the heat capacity C are obtained. The thermal conductance also follows from extrapolating the heating curve. The temperature rise ΔT induced by a constant heating power ΔP in the limit of $t \to \infty$ relates to the conductance via the steady-state equation $\Delta T = \Delta P/\bar{K}_1$. The curvature of the relaxation secondly determines τ, from which then $C = \tau \cdot \bar{K}_1$ is calculated. The statistics of C can be optimized by averaging over the time constant τ obtained from the heating curve and that from the cooling curve.

The advantage of the relaxation time method lies in the automatizeable analysis of the data in case of negligible τ_2 effects and the low achievable base temperature. The noise of the data can be lower than in case of the quasi-adiabatic heat pulse method, because more data points contribute to the final heat capacity C. The required measurement time for a single heating curve is approximately 2τ which suffices to extract τ by fitting. Thus, for a given heat capacity of the sample the thermal conductance $\bar{K}_1$ is to be chosen adequately. In case of strongly different samples, like large magnetic contributions on the one hand and purely phononic heat capacities on the other hand, a single setup cannot be used for both, but the conductance $\bar{K}_1$ has to be changed. In turn this can require lengthy calibrations of the systems after changing the conductance. Another drawback of the method is its inapplicability to measure sharp first order phase transitions with latent heat that occur within the temperature range of a single heat pulse. In the previous analysis the heat capacity C was assumed constant during a heat pulse, which is not fulfilled in case of the diverging heat capacity of systems with latent heat.

Besides the two methods presented above, a variety of other common methods exists to obtain the heat capacity of a sample. Among these are AC methods, differential scanning calorimetry (DSC), often in combination with thermogravimetrical analysis (TGA), and the continuous heating method, or others that rely on the numerical interpretation of the data, like the heat flow method (HFM) that was developed during this thesis for the application to the slow dynamics of spin ice compounds [89] (see e. g. Ref. 90 for a review of various methods).

A particular curve fitting method (CFM) to analyze the response of a system to applied heat is described in Ref. 91 for calorimeter setups like that sketched in Fig. 3.6. It can be applied both to quasi-adiabatic heat-pulse raw data and to the relaxation-time based data. Using this method the whole temperature response of the system, including τ_2 effects can be described. This allows a fully automated data analysis as performed by the heat-capacity option of the commercial PPMS setup by Quantum Design. Instead of analytic solutions of the heat flow equations, the authors show that a least squares fit of a sum of functions, numerically obtained from the raw data, yields all conductances as well as the time-dependent sample and platform temperature. The details of the analysis are, however, rather technical and are given in Ref. 91 in detail. A MATHEMATICA notebook [23] was developed in order to analyze the raw data based on this method. The heat capacity data of Cs_2CoCl_4 discussed in Chapter 4.2 were obtained from this analysis.

3.2.3 Experimental setup

Two different calorimeters were constructed and optimized during this thesis. Both follow the scheme shown in Fig. 3.4. They differ due to the different dimensions of the ^{3}He cryostat and the dilution refrigerator they are operated in and due to the varying requirements in the two temperature regimes. Both sample holders were manufactured from copper due to its non-magnetic properties and the high thermal conductivity at low temperature. Only reasonably below 0.1 K and in strong magnetic fields above 1 T the use of copper can become problematic due to a nuclear Schottky anomaly and the associated low thermal conductivity. These effects could be avoided by using components made of silver, at the cost of the mechanical stability. The sample platform in both cases consists of a thin ($\approx 100\,\mu$m) sapphire (Al_2O_3) plate. Sapphire stands out among many other insulating materials due to its high thermal conductivity at around liquid helium temperature that is essential for a fast thermal equilibration. Furthermore, it has a purely phononic heat capacity which reduces the empty holder's signal. Similarly, the heater, the thermometer and all other materials are chosen with respect to their properties at cryogenic temperatures. Comprehensive data of the specific heat and the thermal conductivity of various materials are given, e. g., in Refs. 92 and 86. In case of the quasi-adiabatic heat pulse method, materials with low thermal conductivity should be used for the wires and to fix the sample platform. For a versatile setup, the required larger thermal conductivity for the relaxation time based method can be realized using identical materials, but connecting the platform to the temperature bath with an additional wire of high thermal conductivity, for example with a platinum wire.

The first setup, shown in Fig. 3.7 (a), is constructed from different parts. The main part (1) consists of a solid copper tube that is screwed into the lower end of the cryostat's ^{3}He pot and that spans the distance to the field center. At the lower end a yoke serves as a pin plate for the thermal anchoring of the leads. Further, it allows to rotate the spherical frame (2) around an axis perpendicular to the magnetic field. The sample platform (3) is fixed with nylon strings (sketched as red lines) which are clamped using the ring (4). On top a thin plate (5) is mounted for the measurements. It acts as radiation shield and prevents the loss of the sample in case it detaches from the platform. From the back side four mounting screws and a sealing screw (6) are inserted. The mounting screws fit respective bores in the sapphire plate and are inserted during the attachment of the sample to stabilize the platform. The sealing screw covers a larger bore through which the backside of the platform is accessible. The leads for the thermometer and the heater are fed through another bore in the spherical frame. To avoid thermal links of the wires at that point the bore is additionally filled with a nylon spacer. From below the platform, four screws are inserted that can be risen to support the sample platform upon sample installation.

The low-temperature calorimeter, Fig. 3.7 (b), was designed aiming at an easier assembly and a more comfortable access to the internal wirings. Due to the smaller sample space a more sophisticated layout was chosen. The main frame (1) has a small rectangular plate on the front that is designed to hold eight connector pins to which the thermometer and heater wires are attached. Four brass cylinders (2) are inserted from

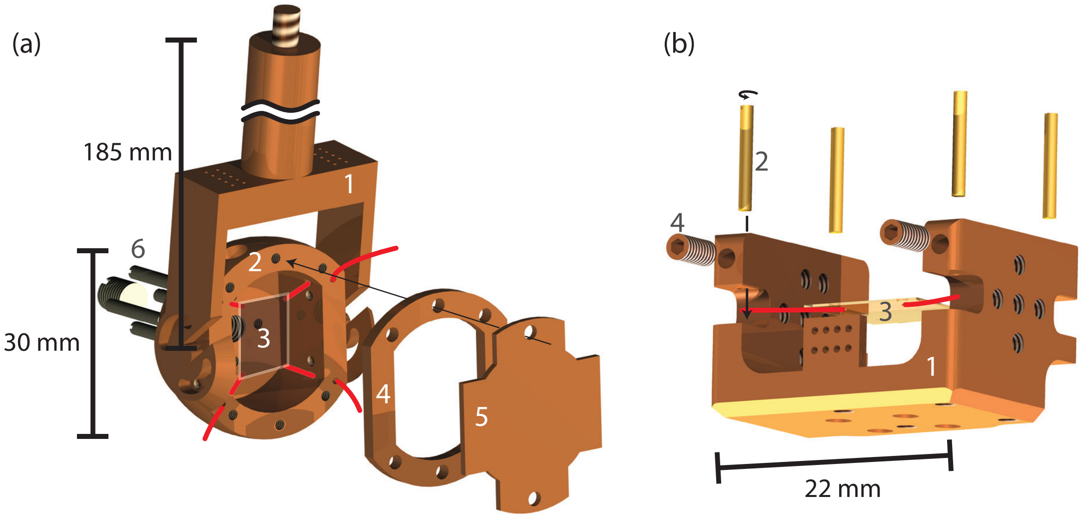

Figure 3.7: Drawing of the constructed calorimeter frames. The setup for the ^{3}He cryostat (a) consists of the primary connector to the cryostat (1) which fits the sliced spherical main frame (2). The sample platform (3) is held in place by strings (sketched in red) that are fixed with the clamping ring (4). The radiation shield (5) is fitted on top of the ring. From the other side four mounting screws and a larger sealing screw (6) can be inserted. The dilution refrigerator setup (b) consists of only a single frame (1). Four cylinders (2) can be inserted into the frame and the strings holding the platform (3) are tightened via turning the cylinders and fixing them with the lock screws (4).

top. Again, nylon wires are used to suspend the sample platform (3). The nylon strings are fixed to the cylinders and then tightened by turning the cylinders and locking them by the lock screws (4).

In Fig. 3.8 the assembled setups are shown before mounting a sample and connecting them to the cryostat. All copper parts were coated with gold in advance by electroplating, which explains the slightly yellow color of the components. While the ^{3}He setup (a) is designed to be attached to the cryostat directly, the low-temperature calorimeter is mounted to an existing universal sample holder with the various bores on all sides, as shown in Fig. 3.8 (b). After mounting the sample both calorimeters are covered by a customized radiation shield.

Heaters

In setup (a) a standard $27\,\mathrm{k\Omega}$ SMD chip heater is used. The temperature dependence of the chosen chip is tiny and it increases to only $28\,\mathrm{k\Omega}$ at a temperature of $250\,\mathrm{mK}$. A strongly temperature dependent resistance should be avoided, because then the applied heat could not be calculated by $R \cdot I^2 \cdot t$ any longer, but the voltage drop at the heater had to be measured as well. This would increase the required data transfer during heat pulses, which lead to a lower time resolution and complications for short heat pulses. Commonly, thin ($\lesssim 100\,\mathrm{\mu m}$) manganin or constantan wires are used for wiring the heater due to the low thermal conductivity, respectively the temperature-independent properties. The heater is connected in a pseudo 4-wire sensing: one of the voltage contacts is not attached directly to the heater chip but to the pin plate which serves

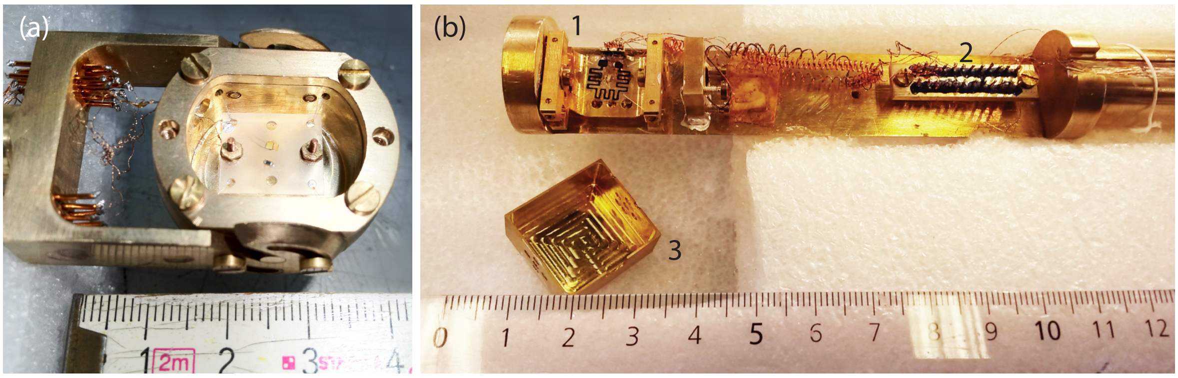

Figure 3.8: Photographs of the assembled heat capacity setups for the ^{3}He cryostat (a) and the ^{3}He-^{4}He dilution refrigerator setup (b). In the ^{3}He-^{4}He setup the calorimeter frame (1) is adapted to an existing sample holder and its pin plate (2). During the measurements the frame is covered by a radiation shield (3).

as a thermal bath. Such, the resistance of one of the current-carrying wires is assigned to the heating resistance. This partly compensates the effect that half of the resistive heat in both current leads flows to the bath and the other to the sample platform. A heater resistance much larger than that of the wires, thus, is advisable, because then Joule heating arises mainly in the heater and not in the wires and the latter effect is negligible.

In the low-temperature setup (b) instead of a chip heater a sapphire plate coated with a gold meander is used. Because of the lattice mismatch between sapphire and gold, chromium is deposited first as a buffer layer. The advantage of this heater lies in a low temperature dependence at $T < 1\,\mathrm{K}$, as only the residual resistance of gold contributes, and in a good thermal contact with the sample platform. On the other hand, the resistance of typical sputtered layers is rather low. The heater of the sapphire plate used here shows a residual resistance of $\approx 23\,\Omega$ below $1\,\mathrm{K}$. It is connected to the pin plate using $100\,\mu\mathrm{m}$ manganin wire of about $15\,\mathrm{mm}$ length with a resistance of about $1\,\Omega$ each.

Thermometers

In the high-temperature setup (a) a thin film resistance cryogenic temperature sensor is used (CX-1030-BC, Lakeshore). The bare chip version has a size of only $0.7{\times}1{\times}0.2\ \mathrm{mm}^3$. The thermometer was calibrated in magnetic fields up to $17\,\mathrm{T}$ previously [93]. Another type of temperature sensor is used in the low-temperature setup. The ruthenium oxide thick film sensor (RX-102A-B, Lakeshore) is specified for temperatures down to $\approx 50\,\mathrm{mK}$. As a drawback, the chip is considerably larger ($1.5{\times}1.3{\times}0.3\ \mathrm{mm}^3$) and above $\gtrsim 0.5\,\mathrm{K}$ the sensitivity is strongly decreased. A calibration of the sensor was performed before attaching it to the platform using a general purpose sample holder previously calibrated in another work [94]. The measured resistance versus the temperature is shown in Fig. 3.9. At low temperature $\lesssim 70\,\mathrm{mK}$ the slope of the curve deviates from the high-temperature trend. This behavior arises from a bad thermal coupling of the sensor to be calibrated. As the data at higher temperature can be well described by scaling a calibration generic for the type of sensor to the data, the scaled

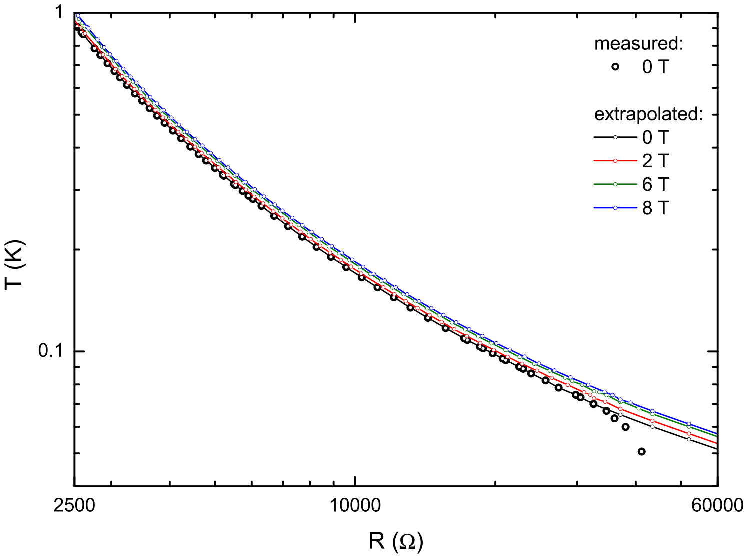

Figure 3.9: Temperature sensor calibration of the low-temperature calorimeter. Open symbols represent the resistance of the RuO_2 sensor (RX-102A-B, *RuO58*) as measured. Data points connected with solid lines contain extrapolated values at low temperature, see text.

generic calibration was used to extend the data to low temperature. As shown by solid lines the extrapolation yields a reasonable continuation of the slope. As measurements are performed at temperatures $T > 90\,\mathrm{mK}$, only, this extrapolation is not relevant for the data presented here, but allows for later measurements that might extend to lower temperature.

The calibration data are interpolated using Chebyshev polynomials, defined by

$$\log T = \sum_{k=0}^{N} A_k \cos\left(k \cdot \arccos\frac{(\log R - ZL) - (ZU - \log R)}{ZU - ZL}\right). \tag{3.3}$$

Here, ZU and ZL are chosen adequately to map the logarithmized data points to the interval $[0, 1]$. Care should be taken to obtain a smooth first derivative of $T(R)$ as otherwise artifacts in the final data can arise [93].

Addenda calibration

The total measured heat capacity C consists of three contributions, irrespective whether the relaxation time method or the heat pulse method is applied,

$$C = C_0 + C_{\mathrm{grease}} + C_{\mathrm{sample}}.$$

Here, C_0 is the heat capacity of the sample platform including the heater and the thermometer. C_{grease} stems from the grease which is used to attach the sample to the platform. From literature [95, 96] the temperature dependent specific heat c_{grease} of the commonly used Apiezon N grease is known, such that the absolute value of the greases' heat capacity can be calculated from the mass of the applied grease. The heat capacity of the sample C_{sample} is obtained by subtracting these two contributions from the measured total heat capacity. Typically, the molar heat capacity is given, which is

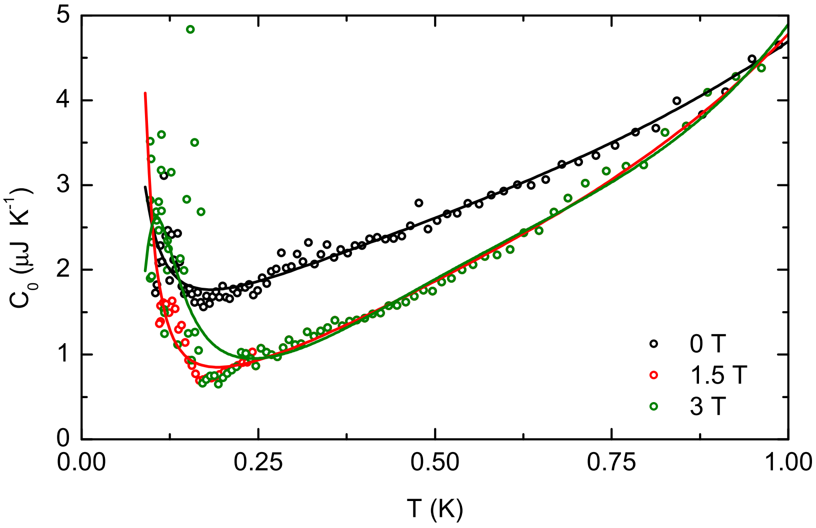

Figure 3.10: Addenda of the dilution fridge calorimeter. Solid lines are fits of the data (open symbols) using Chebyshev polynomials. Data for 1.5 T have been recorded only at lowest temperature.

calculated using the mass m of the sample, the molar mass m_{mol} of the sample and the mass m_{grease} of the grease,

$$c_p = (C - C_0 - m_{\text{grease}}\, c_{\text{grease}}) \cdot \frac{m_{mol}}{m}.$$

The heat capacity of the empty sample holder C_0, often referred to as addenda, is measured by two possible methods. In case of the quasi-adiabatic heat pulse method, the external relaxation without a sample on the platform might be too strong to apply the method. In this case, instead either the relaxation method can be employed or two pieces of the same reference material, but with different masses m_1 and m_2 are measured in two separate runs. From the obtained heat capacities $C_1 = C_0 + m_1 \cdot c_{\text{ref}}$ and $C_2 = C_0 + m_2 \cdot c_{\text{ref}}$, the specific heat of the reference c_{ref} and the addenda C_0 can be deduced. Accounting for the grease by C_0, one finds

$$C_0 = \frac{m_2 C_1 - m_1 C_2}{m_2 - m_1}, \quad c_{\text{ref}} = \frac{C_2 - C_1}{m_2 - m_1}.$$

In a setup based on the relaxation time method, the thermal conductance is usually chosen such that the relaxation time of the sample platform without a sample is in a range accessible with the used instruments. Standard AC resistance bridges (Lakeshore 370S, AVS-47B by Picowatt) give about 10 readings per second, such that a relaxation time of the order of a second can be resolved. Using other instrumentation also faster acquisition rates could be realized. However, the typical time constant of the internal relaxation and the response times of the commonly used ruthenium oxide temperature sensors lie in the range of a second as well. Thus, faster relaxations of the sample platform are not advisable for low-temperature setups. The analysis of heating and cooling curves during the addenda measurements is performed identical to that described in Chapter 3.2.2.

In Fig. 3.10 the addenda signal of the dilution fridge calorimeter (cf. Fig. 3.7 (b)) is shown. The data were obtained using the relaxation method and show a moderate scattering due to noise in the temperature acquisition that could be reduced in subsequent experiments. The overall size of the addenda lies in the typical range of a few μJ mol^{-1} K^{-1}. Below 0.1 K a strong increase is found that probably arises from nuclear Schottky anomalies of the manganin wires in the setup. It is shifted to a slightly higher temperature by increasing the magnetic field, while the overall heat capacity is suppressed up to a factor of about 2. As from 1.5 T to 3 T no significant change of $C(T)$ is found, the field dependence is sufficiently described by interpolation. The data are fitted by low-order Chebyshev polynomials, in analogy to Eqn. (3.3), are used. As shown by solid lines in Fig. 3.10, the polynomials give a reasonable description of the data. As the typical samples of Cs_2CoCl_4 investigated with this setup have heat capacities that are about three orders of magnitude larger than the addenda (see Chapter 4.3), the relevance of the addenda calibration is, however, very small.

Offset heating

In some temperature ranges especially the ^{3}He cryostat (Heliox VL, Oxford Instruments) shows strong temperature fluctuations. Close to the liquid helium temperature of 4.2 K the abrupt changes of the thermal conductance and the heat capacity leads to variations of the cryostat temperature as shown by the dashed line in Fig. 3.11 (a) for an exemplary heat pulse at about 4 K. The sample temperature (red symbols) follows these fluctuations, but with a smaller amplitude due to damping by the sample's heat capacity. The very heat pulse starting at $t = 60$ s is seen only vaguely. Instead cooling the cryostat to 0.7 K and heating the platform via an offset power P_0 to the target

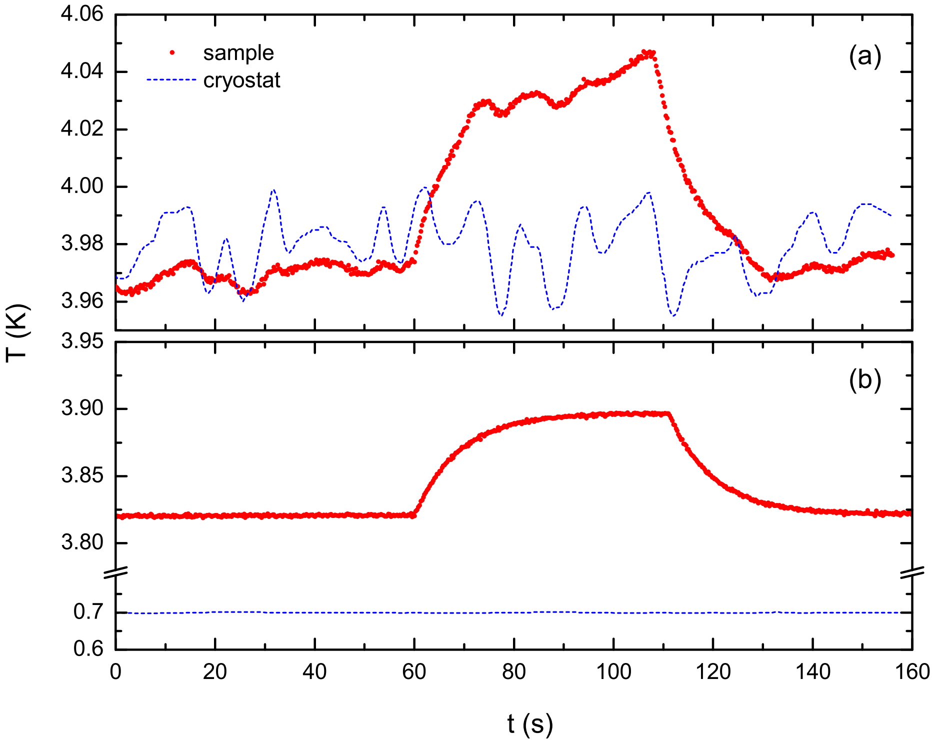

Figure 3.11: Heat pulse acquired without (a) or with (b) the application of the offset heating method. The dashed line indicates the temperature of the cryostat. Symbols are the sample temperature acquired synchronously.

temperature results in a far lower data noise, see Fig. 3.11 (b). Fluctuations of the cryostat temperature the less influence the sample temperature the larger the temperature difference is. Secondly, inherent cryostat issues can be avoided by choosing the cryostat temperature at will. As pointed out in Refs. 88 and 91, the heat flow equations can be extended to include the offset power and the analysis of heat pulses is preserved. In most cases the temperature control using the offset heating method additionally is faster than changing the temperature of the more massive cryostat. Details on the instrumentation and the automated temperature control and data acquisition are given in Ref. 93.

3.3 Magnetocaloric effect

In this chapter, the thermodynamics of the magnetocaloric effect is introduced, followed by the description of an experimental technique that allows to directly measure the entropy change as a function of the magnetic field. The magnetocaloric effect was first discovered in an experiment with iron rods that changed temperature in a varying magnetic field [97]. Nowadays, the main interest in the magnetocaloric effect derives from its potential application for a sustainable room temperature refrigeration [98, 99]. In thermodynamics [100, 101], the change of a system's entropy with changing the magnetic field relates to the change of the magnetization as a function of temperature via the Maxwell relation,

$$\left.\frac{\partial S}{\partial H}\right|_T = \left.\frac{\partial M}{\partial T}\right|_H . \tag{3.4}$$

Combined with the differential dS of the entropy,

$$dS = \frac{C_H}{T} dT + \left.\frac{\partial M}{\partial T}\right|_H dH \, , \tag{3.5}$$

the temperature change ΔT_{ad} during an adiabatic ($dS = 0$) change of the magnetic field from H_0 to H_1 is given by

$$\Delta T_{ad} = -\int\limits_{H_0}^{H_1} \frac{T}{C_H} \left.\frac{\partial M}{\partial T}\right|_H dH. \tag{3.6}$$

Here, $C_H = T \left.\frac{\partial S}{\partial T}\right|_H$ is the heat capacity at constant field H in analogy to the heat capacity at constant pressure. In solid-state physics, $c_H \approx c_p \approx c_V$ can be assumed due to the typically small volume expansion of samples. The integration of Eqn. (3.6), however, is rather complex, as T changes during the field sweep due to the adiabatic conditions. In turn, C_H is not constant either. The temperature change ΔT_{exp} measured in experiments under adiabatic conditions is referred to as the adiabatic magnetocaloric effect (MCE). The relation of ΔT_{exp} to the integrands of Eqn. (3.6), however, is not trivial. In an isothermal process ($dT = 0$), the differential dS simplifies and instead the entropy change ΔS is obtained,

$$\Delta S = \int\limits_{H_0}^{H_1} \left.\frac{\partial M}{\partial T}\right|_H dH. \tag{3.7}$$

In simple magnetocaloric materials like ferromagnets the magnetization typically decreases with temperature, $\left.\frac{\partial M}{\partial T}\right|_H < 0$. Thus, with increasing field, the temperature change $\Delta T_{ad} > 0$ is positive and the entropy decreases, $\Delta S < 0$. If instead the magnetization increases with increasing temperature, $\left.\frac{\partial M}{\partial T}\right|_H > 0$, the signs are opposite, $\Delta T_{ad} < 0$ and $\Delta S > 0$.

Some materials show both signs, depending on the magnetic field strength. In the spin-chain compound copper pyrazine dinitrate, discussed in Chapter 6, the latter case is realized in magnetic fields of a few Tesla. Increasing the field, due to quantum effects, the sign of $\left.\frac{\partial M}{\partial T}\right|_H$ eventually changes to negative and leads to a maximum of ΔS close to the critical field H_c. This effect arises from a quantum critical point of the one-dimensional magnetism at $T = 0$ and $H = H_c$. Another interesting parameter in the context of quantum criticality is the Grüneisen ratio Γ that conventionally describes the proportionality of the thermal expansion and the specific heat [102],

$$\Gamma = \frac{\alpha}{c_p} = \frac{1}{V_m T} \frac{\left.\frac{\partial S}{\partial p}\right|_T}{\left.\frac{\partial S}{\partial T}\right|_p} \tag{3.8}$$

In case a system is described by a single energy scale E, the value of Γ does not depend on temperature, but only on the pressure dependence of E. At a quantum critical point induced by pressure Γ diverges. If the external control parameter is not given by pressure but by the magnetic field, a similar definition of the Grüneisen ratio can be given [103],

$$\Gamma_H = -\frac{\left.\frac{\partial M}{\partial T}\right|_H}{C_H} = -\frac{1}{T} \frac{\left.\frac{\partial S}{\partial H}\right|_T}{\left.\frac{\partial S}{\partial T}\right|_H} = \frac{1}{T} \left.\frac{\partial T}{\partial H}\right|_S . \tag{3.9}$$

According to this definition Γ_H is not normalized, but has units of J^{-1}. The magnetic Grüneisen parameter can be determined in expriment from the temperature derivative of the magnetization and the specific heat. A large number of temperature-dependent measurements of M at different magnetic fields are required to numerically approximate $\partial M/\partial T$ from this data. This lengthy process also involves a certain numerical error due to the derivation of the data. Alternatively, based on the last equality of Eqn. (3.9) the change of the sample temperature as a function of the magnetic field can be measured. However, the demanded adiabatic conditions require a thermal decoupling of the sample from the measurement environment. In consequence, during a field sweep the temperature T substantially changes if the sample shows a magnetocaloric effect. Technically, it is not possible to acquire Γ_H as a function of the magnetic field at a constant temperature using this setup, but instead arbitrary lines in the temperature versus field space are scanned during the field sweep.

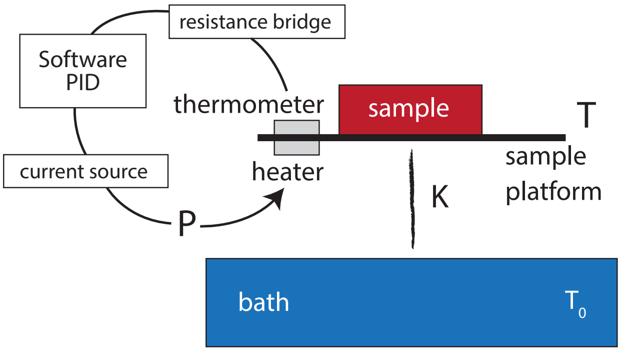

Figure 3.12: Schematic drawing of the setup to measure the magnetocaloric effect while continuously sweeping the magnetic field. The sample temperature T is kept constant via controlling the power P.

To avoid these experimental issues a new technique has been developed that is sketched in Fig. 3.12. It is based on a standard calorimeter used for measurements of the specific heat by the relaxation time method. The sample is mounted on a platform together with a thermometer and a heater. An external magnetic field is provided by a superconducting magnet and is varied with a constant rate as a function of time. During the magnetic field sweep the temperature T of the sample is kept constant via a PID controller. The thermometer is connected to a resistance bridge (Lakeshore 370S) which provides the input for a software PID controller operated on a computer running LabVIEW [87]. The PID output controls a current source that is connected to the heater. An extremely fast and accurate temperature control is required to realize isothermal conditions in the experiment. This requires a precise tuning of the control parameters P, I and D. These parameters depend on the heat capacity of the sample and on the finite thermal conductance K between the platform and the bath. However, changing the magnetic field, these quantities also change. Thus, choosing the control parameters a compromise between a fast control and a universal applicability of them has to be found. For the present measurements the temperature dependent parameters listed in Tab. 3.1 were used.

Simultaneously to the temperature control the voltage drop at the heater is measured to calculate the power $P = U \cdot I$ that is required to keep the temperature constant. The measurement is repeated both for increasing and decreasing the magnetic field. As shown below, the antisymmetric contribution to the field dependence of the power $P(H)$ relates to valuable physical quantities.

In the standard heat flow equations of a calorimeter the internal energy $E = E(S, V)$ is changed by the application of heat to the system. In its differential $dE = T\,dS = T\,\frac{\partial S}{\partial T}\big|_V\,dT = C_V\,dT$ the heat capacity is found. In general the entropy $S = S(T, H)$ depends on the temperature and on the magnetic field. Thus, the differential of the entropy,

$$dS = \left.\frac{\partial S}{\partial T}\right|_H dT + \left.\frac{\partial S}{\partial H}\right|_T dH, \tag{3.10}$$

contains two terms, where the latter usually vanishes because of the constant magnetic field during the experiment. However, in the present setup, the temperature is fixed and instead the magnetic field H is changed as a function of time. Thus, the differential of the internal energy $E(S, V, N)$ at constant volume takes the form,

$$dE = T\,dS = T\,\frac{\partial S}{\partial H}\bigg|_T dH. \tag{3.11}$$

In the experiment the sample temperature T is kept constant by adjusting the power P applied to the heater. This temperature in general is not equal to the bath temperature T_0, but exceeds it by $\Delta T > 0$. During the magnetic field sweep the power P is continuously adjusted to keep ΔT constant. The heat applied to the sample together with the heat flow to the temperature bath via the conductance K equals the change of the internal energy,

$$P(H)\,dt - K(H)\Delta T\,dt = dE. \tag{3.12}$$

Combining Eqns. (3.12) and (3.11), the heating power P can be related to the change of the entropy as a function of the magnetic field,

$$\frac{P(H) - K(H)\Delta T}{\gamma} = T\,\frac{\partial S}{\partial H}\bigg|_T , \tag{3.13}$$

with the sweep rate $\gamma = \frac{dH}{dt}$ of the magnetic field. The heating power $P(H)$ can be decomposed into a symmetric and an antisymmetric term with respect to the sweep direction by rewriting Eqn. (3.13) for increasing ($P_\uparrow$) and decreasing ($P_\downarrow$) the magnetic field,

$$P_{\uparrow,\downarrow}(H) = K(H)\Delta T \pm |\gamma|\,T\,\frac{\partial S}{\partial H}\bigg|_T . \tag{3.14}$$

The first term is the symmetric contribution to $P(H)$ and accounts for the heating of the sample platform to build up the constant temperature difference $\Delta T = T - T_0$. Ideally, this contribution does not depend on the magnetic field at all. However, the conductance $K(H)$ may have a finite field dependence. Yet, it does not depend on the sweep direction. Further effects that may be absorbed in the symmetric contribution of P are measurement artifacts like the inductive heating of the platform due to eddy currents, which also arises irrespective of the sweep direction. In contrast, the second term changes sign upon reversing the sweep direction, such that the quantity $\partial S/\partial H$ can

T (K)	P	I	D	$I_{\max}$ (A)
0.4	190	0.25	0.003	3×10^{-5}
0.7	140	0.2	0.004	3×10^{-5}
1	110	0.15	0.009	3×10^{-5}
2	90	0.1	0.01	3×10^{-5}
5	70	0.08	0.01	5×10^{-5}

Table 3.1: PID parameters of the magnetocaloric-effect setup. The first column indicates the maximum temperature T up to which the respective parameters are used. The PID control output ranges from 0 to 1 and is multiplied with the maximum current before sending to the current source.

be obtained from the difference of the experimental data for increasing and decreasing the field,

$$\left.\frac{\partial S}{\partial H}\right|_T = \frac{P_\uparrow - P_\downarrow}{2\,|\gamma|\,T}. \tag{3.15}$$

By integration the field dependence of the entropy can be deduced. To calculate the molar entropy S_m additionally the mass m and the molar mass m_mol of the sample have to be known,

$$S_m(H) - S_m(0) = \frac{m_\mathrm{mol}}{2m\,|\gamma|\,T} \int\limits_{H'=0}^{H} \left[P_\uparrow(H') - P_\downarrow(H')\right]\, dH'. \tag{3.16}$$

Assuming that only the entropy of the sample's magnetic subsystem changes as a function of the magnetic field, but not that of the sample holder or of other phonon systems, this result is independent of geometric details and does not require a previous calibration of the empty holder's signal. Especially, this process inherently separates phononic and magnetic contributions. Furthermore, using Eqn. (3.9) and approximating $c_H \approx c_p$ the Grüneisen parameter Γ_H is obtained in case the field dependence of the specific heat at the given temperature T is known,

$$\Gamma_H(H) = -\frac{\left.\frac{\partial S}{\partial H}\right|_T}{C_H} = -\frac{1}{2\,|\gamma|\,T}\,\frac{P_\uparrow(H) - P_\downarrow(H)}{c_p(H)\frac{m}{m_\mathrm{mol}}}. \tag{3.17}$$

Here, the factor of $\frac{m}{m_\mathrm{mol}}$ converts from the molar heat capacity to the extensive quantity C_H. If γ is given in units of T s^{-1}, Γ_H is obtained in units of T^{-1}. As the setup used for this measurements is identical to that of a specific heat calorimeter based on the relaxation method, the required $c_p(H)$ can be measured using the same setup. This minimizes possible errors due to a remounting of the sample in another setup or a mismatch of different thermometers.

3.4 Thermal expansion

The uniaxial thermal-expansion coefficient α_i of a solid can be obtained in experiment by measuring the length change ΔL_i of a crystal along the axis i. An established method to detect small relative length changes is the capacitance dilatometry. Various setups based on the original design of Ref. 104 have been developed previously for different applications and cryostats [105–107]. Commonly, they consist of a fixed frame and a movable part as shown in a schematic drawing in Fig. 3.13. Opposing capacitor plates with a radius r are mounted electrically insulated from the frames. The movable part is suspended via two copper beryllium (CuBe) springs. The sample is clamped via a fixing screw in between both frames in such a way that a length change of the sample is converted into a change Δd of the gap between the capacitor plates. Further effort in the construction of the capacitor is put into the minimization of stray fields, the coplanar alignment of the plates and the geometry of the suspension via the

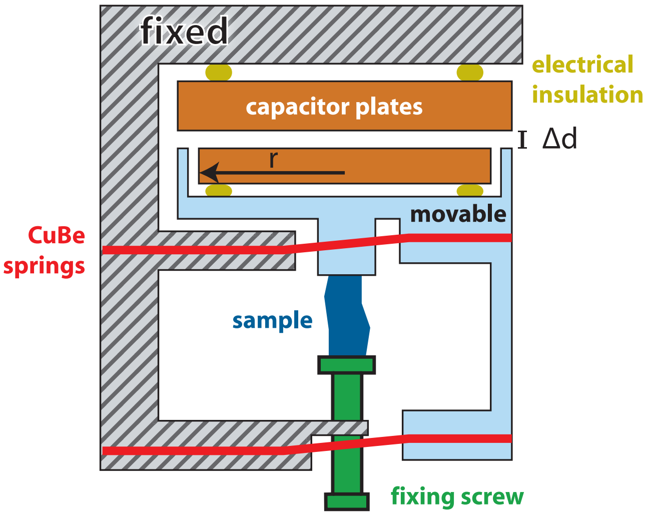

Figure 3.13: Schematic drawing of a capacitance dilatometer used to measure the thermal expansion of a sample. The sample (blue) is mounted in between two frames, where one is fixed (hatched area) and the other is movable (light blue). A length change of the sample translates into a change Δd of the spacing between the capacitor plates (orange areas).

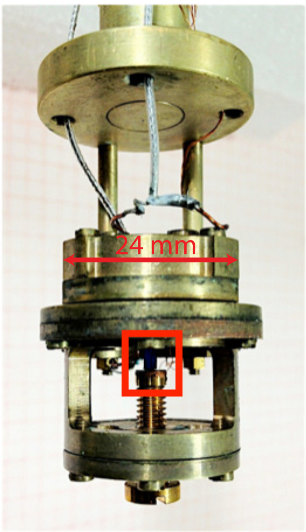

Figure 3.14: Low-temperature capacitance dilatometer made of copper. The sample (marked in red) is clamped between the fixed frame and the movable capacitor plate via fixing the screw from below.

springs. Details are given elsewhere [104, 105]. Apart from the design of the thermal-expansion cell, the measurement environment has to be optimized with respect to mechanical vibrations and the shielding of leads. Coaxial cables are used to measure the capacitance. It is obtained with high precision by using a commercial AC capacitance bridge (AH2550/AH2500 by Andeen Hagerling) that operates at a fixed frequency of 1 kHz. Two dilatometers constructed in the same way were used in this thesis. While one can be adapted to the ^{3}He cryostat, the other is mechanically designed for the dilution refrigerator. Each setup is equipped with a suitable resistive thermometer calibrated in magnetic fields. In Fig. 3.14 the dilution refrigerator setup is shown. The capacitor plates are contained in the center area. From above the coaxial cables (CC-SS series, Lakeshore) are fed through respective bores. A sample of Cs_2CoCl_4 is mounted in the area marked in red. The radius of the lower capacitor plate of 8.1 mm allows to exploit almost the full resolution of the capacitance bridges. From the measured capacitances C_1 and C_2 before and after the expansion of the sample the length change ΔL can be calculated,

$$\Delta L = \epsilon_0 \pi r^2 \left(\frac{1}{C_1} - \frac{1}{C_2} \right) . \tag{3.18}$$

Here, ϵ_0 is the vacuum permittivity and r is the radius of the smaller capacitor plate. Due to the strongly increasing capacitance for small distances between the plates and thanks to the high sensitivity of the capacitance bridges, depending on the geometry of the sample and on the plate radius r, length changes down to 10^{-10} m can be resolved.

From the measured length change ΔL the thermal expansion coefficient is obtained numerically,

$$\alpha_i = \frac{1}{L_{i,0}} \frac{\partial \Delta L_i(T)}{\partial T}. \tag{3.19}$$

In analogy, the magnetostrictive coefficient λ is obtained from the measured length change $\Delta L_i(H)$ as a function of the magnetic field H.

3.5 Thermal conductivity

In general the thermal conductivity $\underline{\underline{\kappa}}$ is a second-rank tensor which indicates the heat current $\mathbf{j}$ induced by a temperature gradient $\vec{\nabla}T$ in a material,

$$\mathbf{j} = -\underline{\underline{\kappa}}\vec{\nabla}T. \tag{3.20}$$

In the isotropic case, respectively by considering one-dimensional transport, $\underline{\underline{\kappa}}$ becomes a scalar κ and Eqn. (3.20) simplifies to

$$\frac{P}{A} = \kappa \frac{\Delta T}{\Delta x}. \tag{3.21}$$

To obtain a homogeneous heat current described by Eqn. (3.21), the ideally shaped sample for measurements should have one long and two shorter axes as shown in the schematic drawing of Fig. 3.15. It is attached with the lower end to a heat sink and a heater is mounted on top. Either SMD chips or wound manganin wires can be used for heating. The heating power P establishes a heat current perpendicular to the cross-sectional area A of the sample. In a steady state the temperature gradient is constant and can be probed by measuring the temperature difference ΔT between two points on the sample in a distance Δx. Two methods can be applied to measure ΔT. Depending on the temperature range either a thermocouple consisting of chromel and gold-iron alloys is used, or two individual suitable resistive thermometers are attached to the sample. Due to the reduced sensitivity of thermocouples below liquid helium temperature, depending on the temperature range both techniques were applied in this thesis.

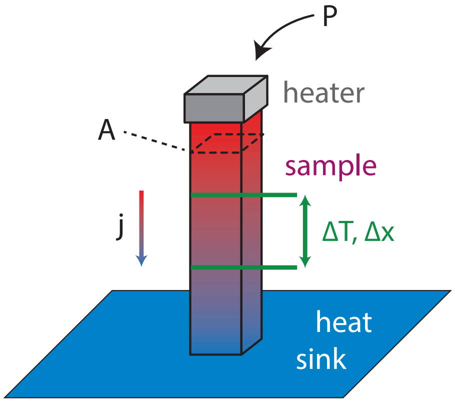

Figure 3.15: Schematic drawing of the setup to measure the thermal conductivity by the steady-state method. Applying a power P to the heater a heat current j to the sink is established, represented by a color gradient within the sample. The dashed line indicates the cross section A of the sample. The temperature gradient ΔT is measured at level positions in a distance Δx from each other.

During the acquisition of the field-dependent data discussed in Chapter 4.2.1 special emphasis was put on the sample temperature stability. In the experiment, the temperature gradient ΔT lifts the average sample temperature above that of the heat sink, respectively the cryostat. Depending on the thermal conductivity κ itself, this leads to a deviation of the target temperature. In a strongly temperature-dependent regime of κ reliable data were acquired only by iteratively adjusting the base temperature of the heat sink and the power P, such that ΔT and the average sample temperature remain constant. More details on the choice of wires, adhesives and on the further experimental procedure are given for example in Refs. 94 and 86.

4 The spin-1/2 *XXZ* chain Cs_2CoCl_4

The synthesis and crystal structure of the chlorine based salt Cs_2CoCl_4 (*Dicesium tetrachlorocobaltate*) was first reported by Porai-Koshits in 1956. High-quality single crystals of centimeter size can be grown by slow evaporation of the constituents [108]. Another study in the midst of the 20th century that involved Cs_2CoCl_4 aimed at some fundamental questions in crystal chemistry by comparing the crystal structures of a variety of salts [109]. By relating the cation element, its coordination and the anion/acido complex, Porai-Koshits strove for a methodology in the formation of such "complex compounds".

In 1964 Cs_2CoCl_4 was revisited for its anisotropic magnetic properties [4, 110]. While magnetic exchange was included in this analysis of susceptibility on a mean-field level, a quantitative comparison of the specific heat to a spin model in the temperature range where short-range correlations arise was carried out first by Algra *et al.* in 1976 [3]. Comparing their data to numerical results for antiferromagnetic spin chains of different anisotropies (obtained by Blöte in 1975 [111]), they found a good agreement with the XY-like model including an anisotropy parameter $\Delta = {}^1\!/\!_4$. However, all these studies restricted to zero magnetic field and mainly focused on temperatures $T > T_\mathrm{N}$. The magnetic order that arises at $T_\mathrm{N} \approx 0.2\,\mathrm{K}$ was discussed in few studies only [7, 8]. Especially, the magnetic ordering was discussed only in case of a magnetic field applied along a, but not for any other field direction. In this thesis, the thermodynamics of Cs_2CoCl_4 is investigated for magnetic fields applied along different crystallographic axes and for temperatures both above and below T_N.

After introducing the structure and the known magnetic properties of Cs_2CoCl_4 in Chapter 4.1, the experimental findings for temperatures above the magnetic ordering temperature $T_\mathrm{N} \simeq 0.22\,\mathrm{K}$ are presented in Chapter 4.2. By a combined analysis of specific heat and thermal expansion/magnetostriction and the inclusion of virtual excitations in the applied effective spin model, it is found that the compound is closer to the XY model than previously assumed in literature. Furthermore, the measured specific heat and thermal expansion of Cs_2CoCl_4 in magnetic fields up to 4 T reveal signatures of quantum criticality and will be compared to numerical calculations of the model. In Chapter 4.3 thermodynamic properties in the magnetically long-range ordered temperature regime are discussed. Upon applying magnetic fields in different directions, drastically different phases arise. Their relation to the one-dimensional magnetism as well as models for their microscopic origin are presented.

4.1 Introduction

4.1.1 Structure

Crystals up to centimeter-size of Cs_2CoCl_4 can be grown by slow evaporation from an aqueous solution with a stoichiometric ratio of 1:2 of the educts $CoCl_2 \cdot 6\,H_20$ and CsCl. They have a slightly transparent and dark blue appearance. A large single crystal grown during this thesis is shown in Fig. 4.1. As the crystals are water-soluble and rather brittle, they have to be treated with some caution. As part of my diploma thesis [93] initial test measurements of the specific heat of Cs_2CoCl_4 in magnetic fields were carried out using samples grown by R. Müller. In the course of the present thesis it turned out that these crystals exhibited a porous inner structure. Not only unknown enclosures within the hollows, but also differently oriented crystallites might be embodied in the crystals, leading to experimental uncertainties especially upon applying magnetic fields in different crystallographic directions. Interestingly, the crystals did not show any reflections upon various attempts of Laue diffraction. In Ref. 112 it is pointed out that the strong X-ray absorption properties of the crystal complicate the structure determination. The X-ray linear attenuation coefficient[1] of Cs_2CoCl_4

$$\mu_{\mathrm{Cs_2CoCl_4}} = 11\,\mathrm{mm}^{-1}$$

was determined using Mo-K_α radiation ($\lambda = 0.71\,\text{Å}$, $E \approx 17\,\mathrm{keV}$). This value probably originates from the absorption properties of the heaviest contained element cesium, which at this wavelength has a similar attenuation coefficient [113],

$$\mu_{\mathrm{Cs}} \approx 11.6\,\mathrm{mm}^{-1}.$$

Another possible reason might be given by the slight hygroscopic nature of Cs_2CoCl_4 which partly leads to a reconstruction of the crystal surfaces. Samples stored in air for some months show the tendency to accumulate microscopic crystallites at the surface

---

[1] The coefficient μ can be understood as a penetration depth and describes the attenuation of X-ray radiation with a primary intensity I_0 via the relation $I = I_0 e^{-\mu d}$. Here, I is the remaining intensity after the X-rays have passed the material of a thickness d.

Figure 4.1: Single crystal of Cs_2CoCl_4 (sample *3-2*). Crystal facets were identified using single crystal diffraction.

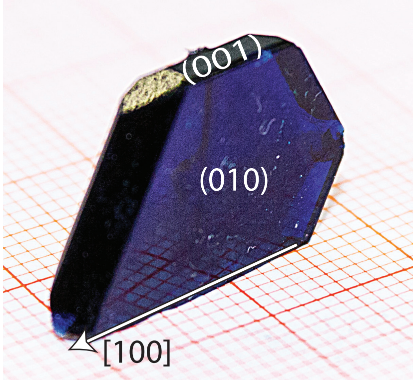

that lead to a brighter appearance of the sample surface. The same happens to crystals that are taken from solution and where excess solution was not sufficiently rinsed from the grown surfaces. This surface imperfectness might lead to the suppression of Laue reflections. However, the definite reason could not be clarified. At least, one can state that both Laue and single crystal diffraction are not influenced by the mentioned impurities embedded in the crystals, as the X-rays penetrate only few µm into the crystal. Instead of orientation via Laue images, some of the grown crystals were oriented based on the morphology. Others were successfully analyzed by using a single crystal diffractometer (Bruker APEX). Up to 1 cm size crystals were mounted on top of a 0.1 mm glass capillary and centered with an edge in the incident beam. In most cases reflections could be gathered and it was possible to identify the facets of the crystals, as indicated by the labels in Fig. 4.1. As reported in Ref. 93, the measured specific heat of the first batch of crystals scattered several percent from specimen to specimen, which might be due to the imperfect crystal quality. Therefore, these crystals were not used within this thesis.

The large high-quality single crystals used in this thesis were provided by Prof. L. Bohatý and Prof. P. Becker from the *Institute of crystallography, University of Cologne*. Their inner structure did not reveal any of the defects named above. All samples were prepared from the original crystal by sawing along the crystallographic axes. Typical sample sizes were about $2 \times 2 \times 3\,\mathrm{mm}^3$ with a weight of a few tens of mg.

The crystal structure of Cs_2CoCl_4 was first described by Porai-Koshits in 1956 with the orthorhombic space group *Pnma*. In some subsequent work [4–6] the structure was referred to as *Pnam*, which differs from *Pnma* simply by interchanging of b and c. In this work the description in terms of the original space group *Pnma* (D_{2h}^{16}, No. 62) is chosen, which translates to the following definition of the lattice parameters.

$$\begin{aligned} a &= 9.720(3)\,\text{Å} \\ b &= 7.313(3)\,\text{Å} \\ c &= 12.822(2)\,\text{Å}. \end{aligned}$$

Not only two choices of the space group are found in literature, but also two different origins are used. In the publications of Figgis *et al.* relative atomic coordinates for the Cs1, Cs2 and Co1 are 1/4. Algra *et al.* and Kenzelmann *et al.* decided to shift the unit cell by $(0, 0.5, 0.5)$, such that those positions are 3/4. Following the latter

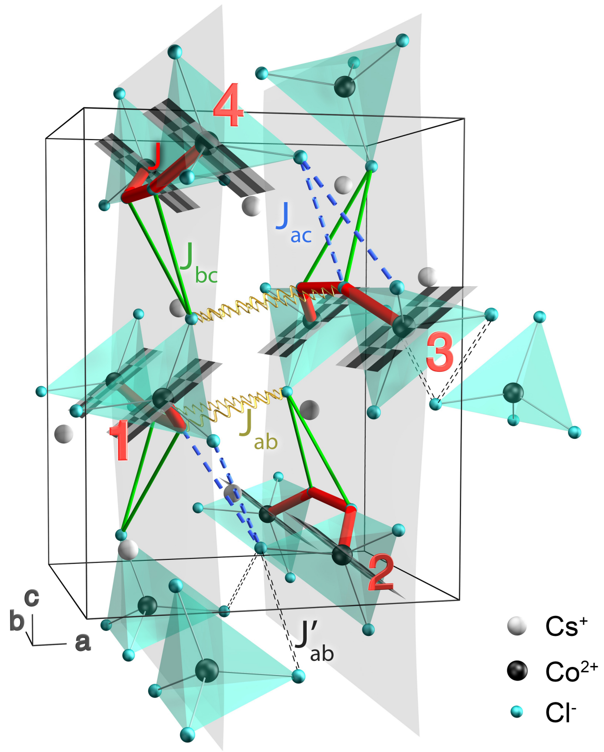

Figure 4.2: Schematic drawing of the unit cell of Cs$_2$CoCl$_4$ and of selected coordinated CoCl$_4$ tetrahedra based on structure data from Ref. 112, but with the unit cell shifted by $(0, 0.5, 0.5)$ in consistency with Refs. 3 and 8. Checker-board planes denote magnetic easy planes that appear in two orientations at sites (1 & 3) and (2 & 4). Dominant magnetic exchange paths are indicated by red bars. Gray shaded planes indicate bc planes on which chains of Co are coupled frustratedly via interchain couplings J_{bc} depicted in green. Non-frustrated interlayer couplings J_{ac} are dashed blue. Further frustrated couplings J_{ab} and J'_{ab} between every second bc layer are sketched in curled yellow lines and thin black dashed double lines.

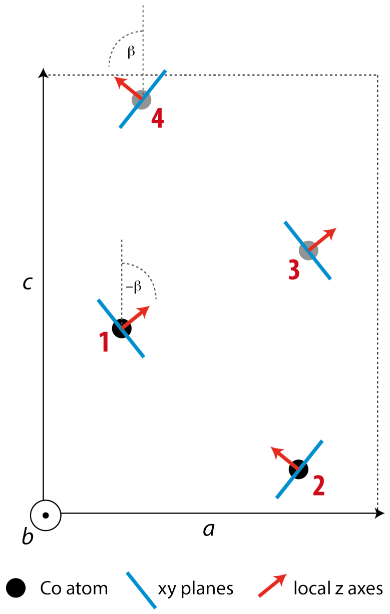

Figure 4.3: Simplified schematic representation of the structure of Cs$_2$CoCl$_4$ projected along the chain direction b. Black dots indicate the position of Co atoms with crystallographic positions $y/a = 1/4$, gray dots stand for Co atoms with $y/a = 3/4$.

publications the description with a shifted unit cell was chosen for this work. In Tab. 4.1, the relative atomic coordinates for both origins are given. A pictorial representation including selected atoms of neighboring unit cells is given in Fig. 4.2. The main building blocks are CoCl$_4$ tetrahedra that form one-dimensional chains along the b axis (sketched transparently green in Fig. 4.2). The cobalt ions are approximately located on bc planes (indicated by the slightly buckled gray sheets in Fig. 4.2). These sheets are separated by the non-magnetic Cs$^-$ ions. Their very position is of minor importance. Nevertheless, their occurrence mainly in between the sheets of Co^{2+} can be argued as a hint towards reduced dimensionality upon discussing the magnetism of the cobalt ions. Two cobalt atoms in the unit cell are located at $y/a = 0.25$ (sketched by black dots in Fig. 4.3) and two others occupy positions with $y/a = 0.75$ (gray dots in Fig. 4.3).

Atom	site	oxid.	origin chosen in Ref. 112			origin chosen here and in Refs. 3, 8 with the unit cell shifted by (0, 0.5, 0.5)		
			x	y	z	x	y	z
Cs1	4*c*	1	0.359 87(3)	0.25	0.100 74(3)	0.359 87(3)	0.75	0.600 74(3)
Cs2	4*c*	1	0.022 24(2)	0.25	−0.173 63(2)	0.022 24(2)	0.75	0.326 37(2)
Co1	4*c*	2	−0.235 14(5)	0.25	0.077 72(4)	−0.235 14(5)	0.75	0.577 72(4)
Cl1	4*c*	-1	−0.003 72(10)	0.25	0.099 93(9)	−0.003 72(10)	0.75	0.599 93(9)
Cl2	4*c*	-1	−0.312 34(1)	0.25	−0.088 80(7)	−0.312 34(1)	0.75	0.411 20(7)
Cl3	8*d*	-1	−0.325 97(9)	0.501 78(13)	0.152 83(8)	−0.325 97(9)	0.001 78(13)	0.652 83(8)

Table 4.1: Crystal structure of Cs_2CoCl_4. Relative atomic coordinates based on X-ray diffraction [112]. In analogy to Refs. 3 and 8 a shift of the unit cell is considered.

The magnetic properties of Co^{2+} are primarily affected by the tetrahedral coordination by Cl^- ions. However, the coordination does not reveal the fully tetrahedral symmetry, but is described by only one single mirror plane (cf. Fig. 4.8), which leads to a pronounced anisotropy of the easy-plane type that is discussed from the electronic point of view in Chapter 4.1.2. Due to the presence of 2-fold screw axes in the space group, all four tetrahedra within the unit cell are of equal type, but differ in their respective orientation around the cobalt atom. Their appearances are labelled by red numbers (1 to 4) in Fig. 4.2. The tetrahedral coordinations at positions 1 and 3 transform into each other by a rotation of 180° around b. The same applies to positions 2 and 4. However, transforming a tetrahedron with odd numbering to an even numbered involves an inflection. Thus, with respect to the macroscopic magnetic properties, sites 1 cannot be distinguished from sites 3. Again, the same applies to sites 2 and 4. This holds true as long as the magnetic anisotropy is treated as a single in-plane/out-of-plane type anisotropy ($\mathcal{D}$) only. An additional in-plane anisotropy was previously discussed, but could not be reliably extracted from the susceptibility data [4].

The direction of the anisotropy $\mathcal{D}$ defines a quantization axis for the spin (usually called z-axis). As $\mathcal{D}$ is given by the positions of the ligands local to each site, both z and the perpendicular x and y axes do not necessarily point along the crystallographic axes and can be in principle different at each site. In Cs_2CoCl_4, the relation of the local coordinate system x, y, z (often referred to as molecular) to the crystallographic axes is limited by symmetry. Possible orientations can be visualized as shown in Fig. 4.4 for a single tetrahedron, formed by the chlorine ions shown in green. In panel (a) only the mirror plane that intersects the cobalt site in each tetrahedron is sketched by a red area. At least one molecular axis is confined to the ac plane due to the mirror plane. This axis is chosen as z. The other two axes can either lie each out of the ac plane by an angle of 45° (panel (b) of Fig. 4.4) or one of the other axes lies within the mirror plane as well with the third perpendicular to the mirror-plane (panel (c) of Fig. 4.4). In the first case, the molecular g tensor necessarily is of tetragonal symmetry as indicated by the square checker-board plane in Fig. 4.4 (b) which can be identified with the magnetic easy plane of the tetrahedron. An additional in-plane anisotropy is excluded by symmetry in this configuration. In the second case, g_x may differ from g_y, opening the possibility of an in-plane anisotropy which is depicted by a non-square plane perpendicular to z in panels (c) and (d). The relation between x, y, z and a, b, c, however, is not fully determined by symmetry. The angle β between z and c is not restricted by one of the symmetry operations. Different values $|\beta| = 38.8°, 19.4°$ were

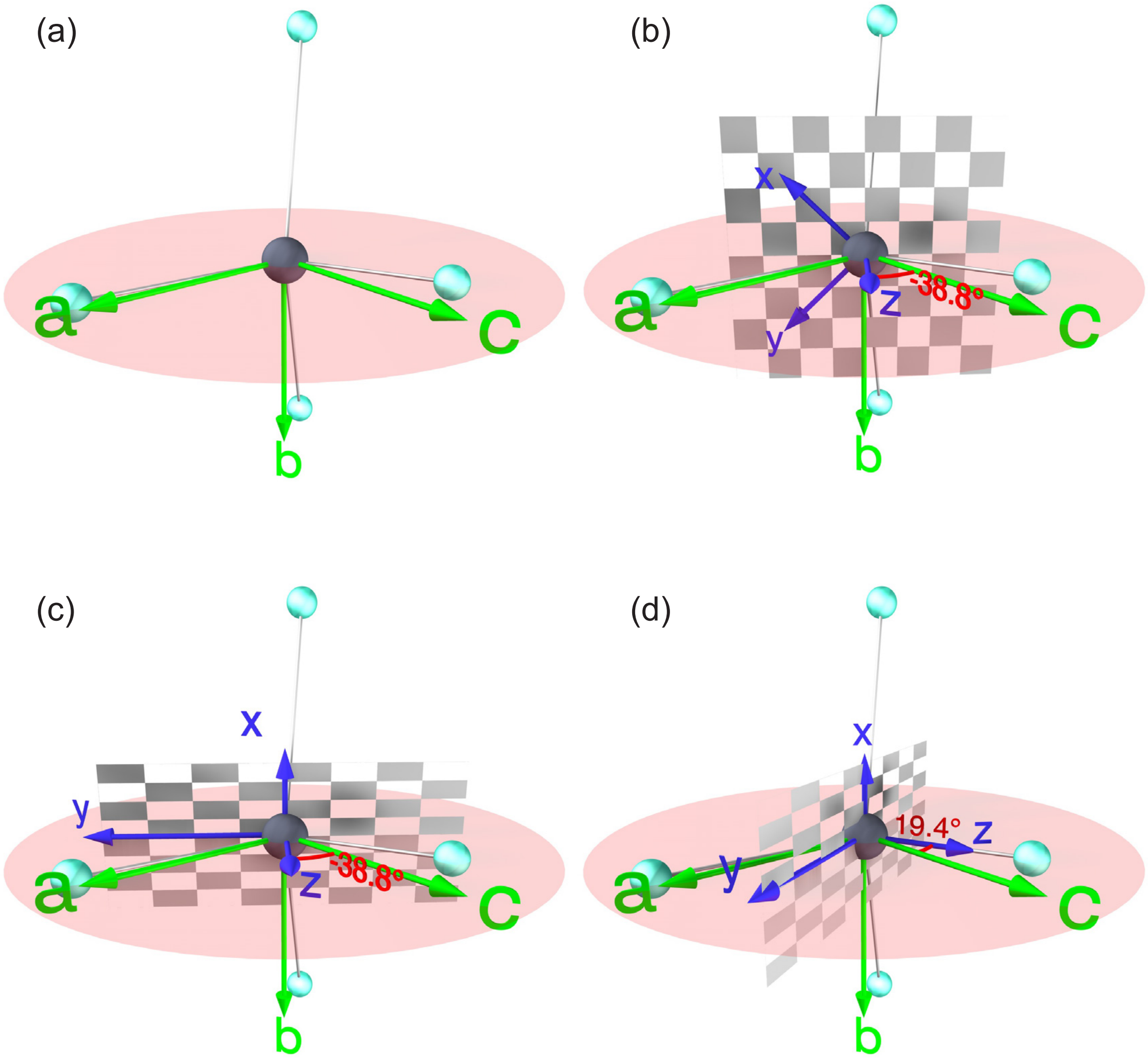

Figure 4.4: Sketch of the symmetry-allowed relations between the molecular (blue) and the crystallographic (green) coordinate system in one $CoCl_4$ tetrahedron. In (a) only the 4c site's mirror-plane (shaded red area) through the cobalt (black sphere) and the Cl-positions (green balls) are shown. In addition, in panels (b-d) the easy planes (checker-boards), spanned by the x and y axis, are shown. The angle β between the local z axis and the crystallographic c axis may be either $-38.8°$ (b,c) or $19.4°$ (d).

proposed in literature [4, 8, 110]. The case of $\beta = 38.8°$ corresponds to the situation in which z bisects the largest Cl-Co-Cl angle in the tetrahedron. This scenario is depicted in Fig. 4.4 (b) and (c) for the two possible rotations of the molecular axes x and y. The second proposed value of $\beta = 19.4°$ reflects the situation in which z is along the vector that connects the cobalt atom with the chlorine ion which shows the largest tilt away from one of the crystallographic axes, shown in Fig. 4.4 (d) for the orthorhombic choice of x and y.

Due to the low site symmetry and the consequently large number of crystal field parameters, it was not possible to determine β by crystal field theory (Chapter 4.1.2). For a discussion of the magnetic properties in the temperature range where no magnetic order arises, the value of this angle is not relevant. However, it might be of importance for long-range order as it affects the efficiency of interchain couplings.

More decisive is the sign of the anisotropy $\mathcal{D}$, because it determines whether easy-plane or easy-axis magnetism arises. In case of Cs_2CoCl_4 the value of the anisotropy $\mathcal{D}$ is positive, which leads to magnetic easy planes. In Fig. 4.2 they are sketched by checker-board planes and by blue lines in the schematic representation of the magnetic structure of Fig. 4.3. The easy planes are tilted away from the c axis by the angle β whose sign alternates between sites (1&3) and (2&4). Due to the rotational symmetries, these planes have the b axis in common. Thus, a magnetic field applied along this crystallographic axis is within all magnetic easy planes, i. e., perpendicular to all local quantization axes z at once. Upon the application of an effective spin model to the magnetic subsystem, magnetic fields H_x along this high-symmetry direction, thus, can be treated equivalently for all Co sites by introducing a magnetic field term $\propto g\mu_B\mu_0 H_x S_x^i$ in the Hamiltonian.

4.1.2 Magnetism

Magnetic exchange

In Cs_2CoCl_4 the magnetic Co^{2+} ions interact with each other via superexchange that involves two non-magnetic Cl^- ions. Due to the symmetry of the Co1 site, three different Co-Cl bond lengths are found per tetrahedron that each connect the central cobalt with a surrounding chlorine ligand. As their lengths $(2.261, 2.267, 2.258$ Å$)$ are very similar, the different magnitude of magnetic interactions via the possible superexchange paths is mainly determined by the chlorine-chlorine bond angles and the distances. As the overlap of orbitals is an exponential function of the distance, the interactions are, in a first approximation, ruled by the exchange paths with the shortest Cl-Cl distances up to a size of a few Å. In the unit cell, a shortest Cl-Cl distance of ~ 3.63 Å and three longer distances close to 4 Å are found. One further Cl-Cl distance of 4.4 Å

Cl sites	Connected Co^{2+} sites	l_{Cl-Cl} [Å]	d $[x/a, y/b, z/c]$	coupling constant	DM allowed
Cl3/Cl3	1-1, 2-2, 3-3, 4-4	3.63	$(0, 1, 0)$	J	✓
Cl1/Cl3	3-4, 2-1	4.05	$(.5, 0, -.34)$	J_{ac}	✓
Cl2/Cl3	2-3, 1-4	4.01	$(.03, -.5, .5)$	J_{bc}	✓
Cl2/Cl3	1-3, 2-4	4.04	$(.53, .5, .15)$	J_{ab}	
Cl1/Cl1	1-3, 2-4	4.46	$(-.47, .5, .15)$	J'_{ab}	

Table 4.2: Superexchange paths in Cs_2CoCl_4 along chlorine sites at distances l_{Cl-Cl} between Co^{2+} as labeled according to Fig. 4.2. The relative distance d between cobalt atoms that are connected via the respective exchange path accounts for the naming of the coupling constant. The possible contribution of Dzyaloshinskii-Moriya (DM) interactions is given by the non-existence of an inversion symmetry of the bond.

distance might be considered for the magnetism, although its impact on the magnetic properties is probably small. All paths considered here are listed in Tab. 4.2 and Fig. 4.5. The shortest Cl-Cl distance is found between the Cl3 sites of different tetrahedra. The respective distance d between two connected cobalt atoms is given for all bonds in Tab. 4.2 in units of the lattice constants. It indicates the spatial direction of the coupling. In case of the Cl3/Cl3 bond, d has a component along b only. In the other cases it always has one small component and two larger ones, which indicates that each of the bonds contributes to a magnetic coupling along one of the crystallographic axes or a diagonal between two of them. This will allow for the representation of the magnetic lattice in a more illustrative way later. The exchange integrals for the different paths are labeled as J_{ij} with i and j indicating the two largest components of d.

The exchange paths together with their bond lengths and angles are given in a schematic view in Fig. 4.5. Color codes and line styles are identical to the unit cell representation in Fig. 4.2. Most bonds are found not only in the orientation presented in Fig. 4.5, but also in configurations related by the rotational symmetries. The bond J (panel (a) of Fig. 4.5) stands out not only due to the small inter-chlorine distance, but also as it involves the largest bond angles and a mirror-plane perpendicular to b that intersects the Cl-Cl bond. From the thermodynamic properties presented in Chapter 4.1.3 it is known that this primary coupling is strongest and governs the magnetic properties

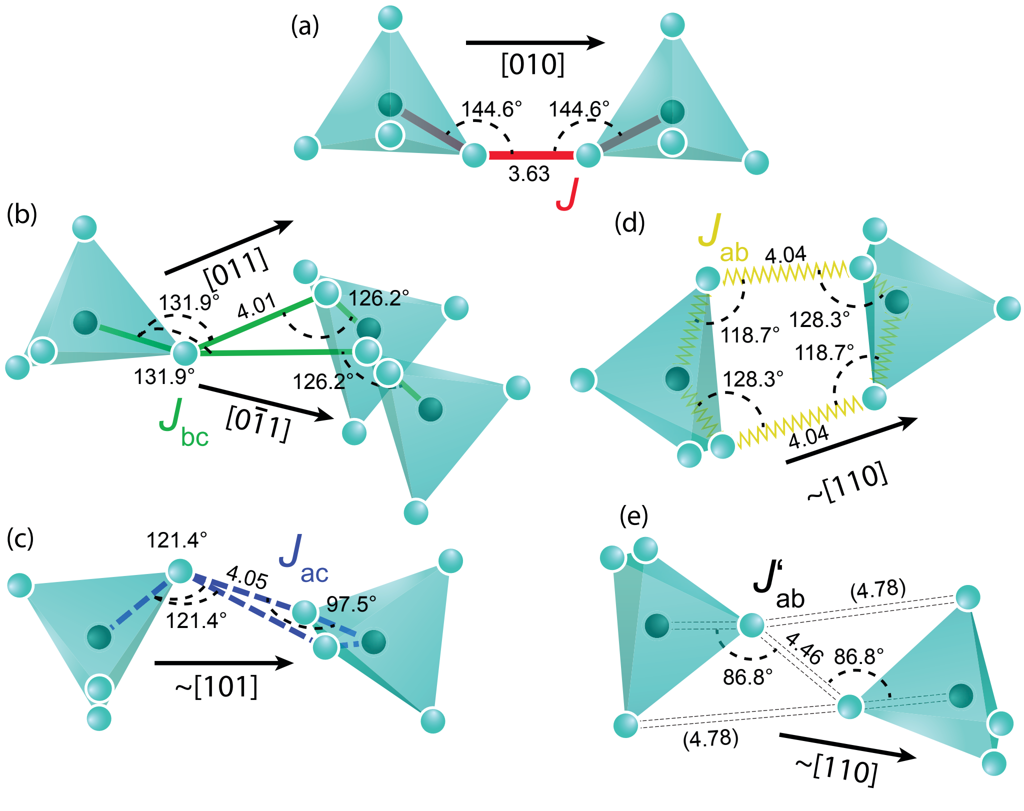

Figure 4.5: Sketch of the superexchange paths found in Cs_2CoCl_4. Spheres within the tetrahedra indicate Co^{2+} atoms. Magnetic exchange is via two chlorine ions (green spheres) in different directions as indicated by the black arrows for each pair of cobalt atoms. Cl-Cl distances are given in Å.

down to $\sim 220\,\mathrm{mK}$. All the other exchange paths might be considered as secondary, as their respective Cl-Cl distances are at least 0.4 Å longer and as they involve reasonably smaller Co-Cl-Cl angles that additionally differ from one tetrahedron to the other. The coupling J_{bc} differs from the other exchanges as it is found in the crystal structure to connect one cobalt atom to two others that differ in their b coordinate, see Fig. 4.5 (b). With the first path along [011], the second is along a respective $[0\bar{1}1]$ direction. In combination with an antiferromagnetic J this triangular configuration leads to magnetic frustration. In case of J_{ac}, depicted in Fig. 4.5 (c), two identical Cl-Cl distances lead to a "two-fold" exchange path that is asymmetric with respect to the angles in different tetrahedra. This exchange connects cobalt atoms along the approximate {101} directions, i. e., along $[101], [\bar{1}01], [10\bar{1}], [\bar{1}0\bar{1}]$. The next coupling J_{ab} is found between Co sites along the approximate [110] directions (Fig. 4.5 (d)). Here, in total four Cl^- ions are involved in the exchange between two sites. Within each tetrahedron two different angles are formed by the Co-Cl-Cl-Co paths. Furthermore, this coupling is found between one site and two neighboring sites that differ in their b component. Thus, this coupling is frustrated, too (not shown in Fig. 4.5 for simplicity). Additionally, this coupling is special as it is found only between sites 1 and 3 *within* the unit cell. The previously discussed couplings connect Co^{2+} within the unit cell as well as to those in neighboring unit cells. For example, J_{bc} connects sites 1 to site 4 within the unit cell as well as to site 4 in the unit cell neighboring along the $-c$ direction (see green bars in Fig. 4.2). In contrast, J_{ab} does for example not connect the cobalt atom at site 3 to the one at site 1 in the neighboring unit cell in the a direction, which is due to the particular orientation of tetrahedra. Nevertheless, there is yet another possible exchange path J'_{ab} forming this missing bond. It is sketched by thin dashed lines in Fig. 4.5 (e). However, it has Cl-Cl distances of ≥ 4.46 Å and almost orthogonal angles, which probably renders it at least another order of magnitude smaller than the other secondary couplings.

In compounds where spin-orbit coupling contributes to the magnetism, antisymmetric (Dzyaloshinskii-Moriya type) exchange might be considered for the explanation of non-collinear spin structures. The corresponding energy of two spins i and j

$$\mathcal{H}_{DM} = \mathbf{D} \cdot (\mathbf{S}_i \times \mathbf{S}_j) \tag{4.1}$$

depends on the size of the Moriya vector $\mathbf{D}$. In a simple superexchange path via an ion that is displaced by a vector $\mathbf{x}$ from the center of the spins i and j which are in a relative distance $\mathbf{r}$, the vector $\mathbf{D}$ is given as

$$\mathbf{D} \propto \mathbf{r} \times \mathbf{x}. \tag{4.2}$$

Even though the size of Dzyaloshinskii-Moriya (DM) interactions cannot be quantified *a priori*, the exchange paths can be analyzed if they allow for this type of exchange by symmetry. In general $\mathbf{D}$ vanishes only if the crystal fields of the associated spins are related to each other via an inversion. Necessarily, the inversion center must coincide with the center point of the two magnetic ions, because only then the very magnetic ions are transformed to each other. In the previous example a non-displaced ion, i. e., $\mathbf{x} = 0$ in Eqn. (4.2), leads to an inversion center in between spins and thus to a vanishing $\mathbf{D}$.

In Cs_2CoCl_4 the orientation of the tetrahedra involved in the couplings J, J_{bc}, J_{ac} are such that no inversion center exists between them. Thus, DM interactions are possible for these bonds. In contrast, both for J_{ab} and J'_{ab} there is an inversion center at half of the cobalt distance such that antisymmetric exchange is forbidden by symmetry for these couplings.

Magnetic Structure Model

The previously identified exchange paths are more illustratively represented by a simplified magnetic lattice. It is obtained from the original lattice by a continuous transformation of the lattice while preserving the coupling between sites. Slightly shifting the original Co1 position from $(-0.235, 0.75, 0.577)$ to the commensurate position $(-0.25, 0.75, 0.5)$ and translating every second bc plane by $c/2$ along c leads to cobalt positions confined to bc layers which are stacked along a as shown in Fig. 4.6 (a). In each layer two types of sites with different easy-plane orientations are present. The type of the site alternates along c and a, but not along the b direction. The coupling J acts within the layers between sites of equal type along b. As discussed later, this coupling defines the primary spin chains and is the dominant coupling. Within each layer the magnetic sites are shifted by half of a lattice constant along -b for increasing c.

The further couplings between sites in the following are classified as first- and higher order. Apart from the primary J the rank of the other couplings does not imply a statement about its ab initio unknown strength. The classification rather follows the steps by which the full lattice is constructed. Adding the "second-order" couplings between the chains leads to the magnetic lattice shown in Fig. 4.6 (b). Within the bc planes an anisotropic triangular lattice is formed by J and J_{bc}. Due to the triangular arrangement, the coupling J_{bc} is frustrated. In contrast to J, which couples sites of equal type, J_{bc} connects each site of one type to four sites of the other type. Additionally, layers are coupled non-frustratedly via J_{ac} along a. J_{ac} connects each site to two sites of different type.

In Fig. 4.6 (c) the "third-order" interchain couplings J_{ab} and J'_{ab} are indicated by zigzag and thin dashed lines, respectively. For the structural reasons discussed above, J_{ab} connects sites in every second bc layer only. This leads to an unconventional appearance of J_{ab} in the magnetic lattice and an enlargement of the magnetic unit cell. While the coupling is present between sites 1 and two sites 3 shifted along $+c$ in the next bc layer, the equivalent sites 3 shifted along $-c$ are not linked. Sites 2 are equivalently connected to sites 4 in the next layer, however only to sites 4 along $-c$. Last, the coupling J'_{ab} is discussed. Although it differs from the previously discussed couplings in a Cl-Cl distance that is yet another 0.4 Å larger, one may consider it for completeness. Namely, J'_{ab} arises in a similar fashion as J_{ab} and completes the inter-layer couplings missing from J_{ab}. In Fig. 4.6 (d) the projection of all couplings on an ac plane is shown. Essentially, the couplings J_{ab} and J'_{ab} add a frustrated inter-layer coupling between equal types of sites to the second-order couplings J_{bc} and J_{ac}. In contrast the second-order frustrated coupling J_{bc} and the second-order inter-layer coupling J_{ac} both exclusively couple sites with different easy plane orientations.

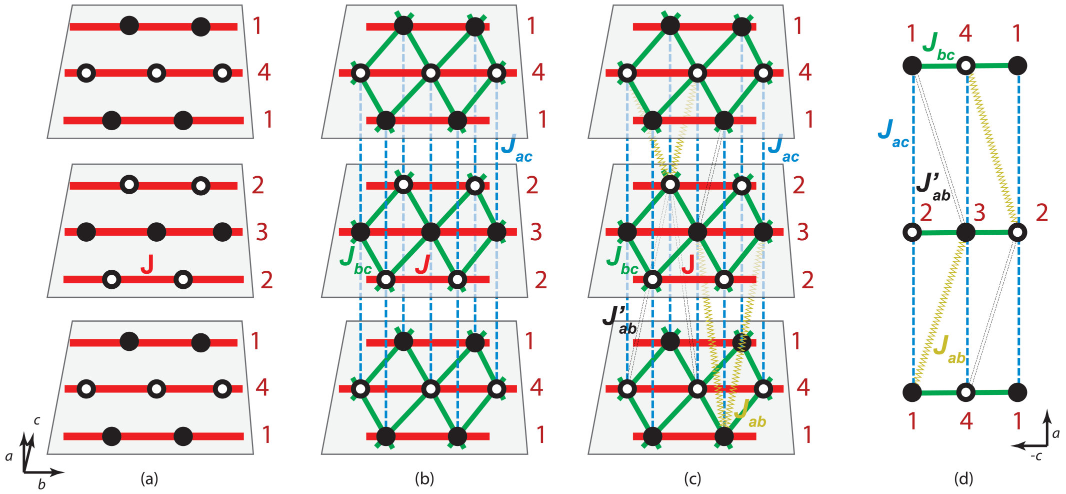

Figure 4.6: Magnetic lattice of Cs_2CoCl_4. Spin sites are approximately located on bc planes (shaded in gray). Different types of easy plane orientation are indicated by open and full symbols. The numbering of sites corresponds to the 4 unit cell sites in anology to Fig. 4.2. In (a) only the primary coupling J is displayed with red bars, in (b) further the frustrated in-plane interchain couplings J_{bc} (solid green lines) and the non-frustrated inter-plane couplings J_{ac} (dashed blue lines) are shown. In (c) next-order couplings are depicted as dashed yellow lines (J_{ab}) and as thin dashed black lines (J'_{ab}) that frustratedly couple bc planes. In (d) a projection of the full lattice along b is shown.

From the presented magnetic lattice potentially interesting magnetic phases may emerge. Depending on the ratio of the coupling constants one may expect very different properties like one-dimensional, two-dimensional, frustrated two-dimensional or even frustrated three-dimensional magnetism. Usually the individual coupling strengths may be obtained from a comparison of equilibrium properties to theory or a probing of the excited states which are exclusively sensitive to individual couplings. However, the magnetic lattice including first and second order couplings is already sufficiently complex to engage a large number of theoretical works about its ground state as a function of a magnetic field. The intensely studied compound Cs_2CuCl_4 is isostructural to Cs_2CoCl_4 and shows diverse magnetic phases at low temperatures [114–118]. The magnetic lattice including first-order interchain couplings of both compounds is identical and consists of anisotropic triangular layers within bc planes that are stacked along a. In Cs_2CuCl_4, the exchange constants J_{bc} and J within the triangular layers are of comparable magnitudes [119]. In contrast, the interchain interactions of Cs_2CoCl_4 are at least one order of magnitude smaller than the dominant intrachain interaction J [7, 120]. Thus, Cs_2CoCl_4 is close to the spin-chain limit and magnetic order is observed at lower temperatures than in Cs_2CuCl_4. Another important difference between both compounds arises from the different electronic configurations of copper and cobalt. In case of $Cu^{2+}(3d^9)$ the orbital momentum is quenched by the crystal electric field, which leads to an almost fully isotropic Heisenberg magnetism. In contrast, the orbital momentum of $Co^{2+}(3d^7)$ is finite and spin-orbit coupling causes strongly anisotropic magnetic properties of the easy-plane type in Cs_2CoCl_4. As the leading interchain couplings in Cs_2CoCl_4 are between sites of different easy-plane orientations, probably different mechanisms are relevant for the magnetic order than in Cs_2CuCl_4. On the one hand, the appearance of easy planes renders the model more complex. On the other hand, it partly reduces the degrees of freedom per site and, hence, might suppress the formation of non-collinear phases.

Another interesting consequence of the different magnetic anisotropies for different spin chains is that the significance of symmetric and antisymmetric interchain interactions depends on the relative angle between the anisotropy axes. This is easily seen for interchain couplings between two chains in case of a strong easy axis anisotropy. In case of a parallel alignment of the easy axes the symmetric part of the interchain coupling (denoted J') tends to align spins collinear to each other, which is easily fulfilled while obeying the easy axes. In contrast, the perpendicular spin alignment favored by DM-type interactions ($\propto \mathbf{D}$) has to overcome the anisotropy energy. However, in case of easy axes tilted by β the energy gain by symmetric exchange $J'\mathbf{S}_1 \cdot \mathbf{S}_2 \propto J' \cos\beta$ is even reduced to 0 in the limit of $\beta = \pi/2$, whereas DM interactions yield an energy proprtional to $-|\mathbf{D}|$ in that case. One might thus argue, that Heisenberg exchange is suppressed for spin chains with perpendicular easy axes while DM interactions gain in importance.

In Cs_2CoCl_4 the magnetic anisotropy, however, is of easy-plane type. For an easy-plane anisotropy the situation is more complex due to the additional degree of freedom. In case of parallel planes ($\beta \to 0$) symmetric exchange can benefit from collinear spins within the plane along any direction or from fluctuations as long as they are correlated. Similarly, for every given spin orientation in site 1 there is a configuration at site 2 which is perpendicular, such that an energy of the order $|\mathbf{D}|$ can be gained by antisymmetric exchange between chains. However, in case of planes tilted by an opposing angle $\pm\beta$, in terms of symmetric exchange now there remains a single state with an energy $-J'$ only, which is the collinear spin alignment along the rotation axis of the planes. This fact can be understood as an effective Ising anisotropy arising from the symmetric interchain couplings between spin chains which reveal a finite angle between their respective XY planes. The impact of an additional antisymmetric interchain interaction on this state now depends on the rotation β in a non-trivial way. In Cs_2CoCl_4, the actual ordering of magnetic moments might derive from symmetric and antisymmetric exchange combined with in- and out-of-plane anisotropies (see Chapter 4.3.1).

Effective spin model

Following the discussion in Chapter 2.3.1, the magnetism of Co^{2+} can effectively be characterized by a spin-$^1\!/_2$ model with anisotropic couplings due to the splitting of the four-fold orbital $S = 3/2$ state by the crystal field $\mathcal{D}$ as described by the single-ion Hamiltonian

$$\mathcal{H}_{si} = \mathcal{D}\left[S_z^2 - \frac{1}{3}S(S+1)\right] - h_x S_x. \tag{4.3}$$

An additional magnetic field h_x is considered perpendicular to the quantization axis z, which corresponds to the experimental situation for Cs_2CoCl_4 in case of magnetic fields applied along the crystallographic b axis. At zero magnetic field two doublets remain separated by $2\mathcal{D}$, leading to the application of the effective spin-$^1\!/_2$ model. In an applied magnetic field, the doublets are split as shown in Fig. 4.7 and the energies of the four non-degenerate states are

$$E_{1,2} = \frac{5\mathcal{D}}{4} \mp \frac{h_x}{2} - \sqrt{\mathcal{D}^2 + h_x^2 \pm \mathcal{D}h_x}, \tag{4.4}$$

$$E_{3,4} = \frac{5\mathcal{D}}{4} \mp \frac{h_x}{2} + \sqrt{\mathcal{D}^2 + h_x^2 \pm \mathcal{D}h_x}. \tag{4.5}$$

It depends on the sign of $\mathcal{D}$ which of the doublets is lower in energy. In Cs_2CoCl_4 the sign of $\mathcal{D}$ is positive [4, 110] such that the $|\pm 1/2\rangle$ states are lower. In the limit of low temperatures ($k_\mathrm{B}T \ll \mathcal{D}$) and small magnetic fields $h_x \ll \mathcal{D}$ (shown as shaded area in Fig. 4.7) the higher-lying $|\pm 3/2\rangle$ states are hardly populated such that they can be neglected and an effective spin-$1/2$ model can be applied to the states as marked in red in Fig. 4.7. An additional magnetic field not only enters the effective spin system, but also the parent spin-$3/2$ system. The splitting of the 4 single-ion spin-$3/2$ states as a function of the magnetic field h_x differs from a Zeeman-like splitting in two aspects. First, the splitting is non-linear. While the upper two states are almost independent on small magnetic fields, E_2 is initially enhanced such that in a simple picture the gap between the two doublet states is reduced. Second, in a magnetic field the 4 eigenstates are not pure $|S_z = \pm 3/2\rangle$, $|S_z = \pm 1/2\rangle$ states, but the magnetic field leads to an intermixing of them and establishes a new quantization axis x. The high-field states are, therefore, better characterized by quantum numbers $S_x = -3/2, .., +3/2$. The magnetic field h_x acting on S_x, thus, leads to a Zeeman-like linear splitting of the x-quantized spin states with slopes $\pm 1/2, \pm 3/2$ at high fields, shown as dashed lines in Fig. 4.7. These straight lines extrapolate to $E/\mathcal{D} = \pm 1/2$ at $h_x = 0$. In other words, they reveal a constant shift that is lower by $\mathcal{D}$ for the $S_x = \pm 3/2$ states. This is due to the finite expectation values $\langle S_x = \pm 1/2 | S_z^2 | S_x = \pm 1/2\rangle - \langle S_x = \pm 3/2 | S_z^2 | S_x = \pm 3/2\rangle = \mathcal{D}$, which can be understood as the residual fluctuation of the z component of the spin.

As the gap between the lower-lying states with the energies $E_{1,2}$ and the higher-lying states 3 and 4 remains finite in a magnetic field, an effective spin-$1/2$ system can be applied to the lower $|S_z = \pm 1/2\rangle$ states in analogy to the zero-field mapping of the exchange interactions outlined in Chapter 2.3.1. Yet, due to the intermixing of $|S_z = 3/2\rangle$ states by the magnetic field and by temperatures of the order of $\mathcal{D}$, the applicability of the effective spin-$1/2$ model is limited in both. Therefore, an agreement with the Hamiltonian derived from the parent spin-$3/2$ in the limit of large anisotropy,

$$\mathcal{H}_{XXZ} = \sum_i \left[J(S_x^i S_x^{i+1} + S_y^i S_y^{i+1} + \Delta S_z^i S_z^{i+1}) - g\mu_\mathrm{B}\mu_0 H_x S_x^i \right] \tag{4.6}$$

$$= \sum_i \left[J_{xy} \left(S_x^i S_x^{i+1} + S_y^i S_y^{i+1} \right) + J_z S_z^i S_z^{i+1} - g\mu_\mathrm{B}\mu_0 H_x S_x^i \right] \tag{4.7}$$

is only expected for a restricted field-/temperature range. As the limit of large anisotropy seems to be reasonably realized in Cs_2CoCl_4 at first sight, in literature a value of $1/4$ for the anisotropy parameter $\Delta = J_z/J_{xy}$ has been taken for granted [3–5, 7, 8]. However, in Chapter 4.2.2 it will be shown that due to the unique combination of the magnetic exchange and $\mathcal{D}$ in Cs_2CoCl_4 the excited $S_z = \pm 3/2$ states contribute in such a way that the system is effectively more XY-like, i. e., $\Delta < 1/4$.

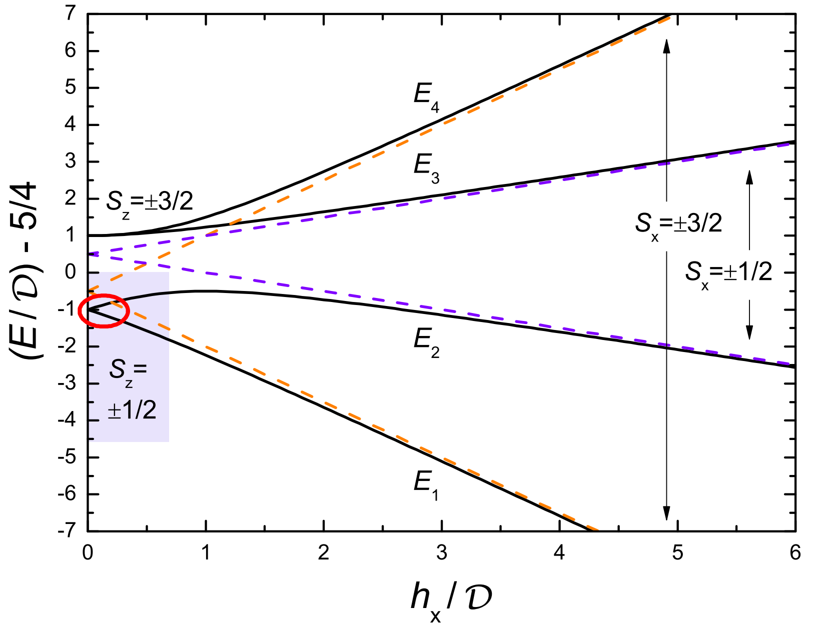

Figure 4.7: Splitting of the single-ion spin-3/2 states in a magnetic field $h_x = g_x\mu_B\mu_0H_x$ perpendicular to the quantization axis z. At $h_x = 0$ the low-lying states (marked in red) form an effective spin-1/2 system. Labels refer to $\mathcal{D} > 0$. Reversing the sign of $\mathcal{D}$ leads to the same dependences, but with an opposing order of the S_z states. Dashed straight lines have slopes 1/2 and 3/2 and intersect the y axis at $\pm0.5/\mathcal{D}$.

Easy-plane anisotropy

The magnetism of Co^{2+} with an electron configuration of $3d^7$ and a Hund's ground state of $S = 3/2$ and $L = 3$ is likely to show anisotropies due to spin-orbit coupling. In case of an environment of full tetrahedral symmetry T_d ($\bar{4}3m$) the orbital 3d levels split into the lower lying two-fold degenerate e levels and the three-fold degenerate t_2 levels, see Fig. 4.8 (a). Thus, a single energy scale (Δ_{CF}) suffices to describe the impact of the crystal field on the level splitting. Filling these levels with 7 electrons according to Hund's rule results in the e levels completely filled up by 4 electrons and the t_2 levels filled half by 3 electrons, i. e., $e^4t_2^3$. Thus, the orbital moment is quenched and in first order no anisotropy is expected.

As visualized in Fig. 4.8 (b), an additional tetragonal distortion of the tetrahedron along the (001)-direction, i. e., the direction of a line connecting the midpoints of two opposing edges of the tetrahedron, lifts the 3-fold symmetry axis [111]. The resulting tetragonal tetrahedron is described by the point group D_{2d} ($\bar{4}2m$). The t_2 and e levels are split further by the distortion depending on its sign. In case of a compression (elongation) those orbitals oriented within the xy-plane (d_{xy}, $d_{x^2-y^2}$) are lowered (raised) in energy, while those perpendicular to the xy-plane (d_{xz}, d_{yz},d_{z^2}) are raised (lowered). In a simplified electron picture this additional splitting enables a gain of angular momentum and thus in second order a gain of energy by intermixing of $e^3t_2^4$ states. The quantum mechanical origin of the resulting easy-plane or easy-axis anisotropy lies in the

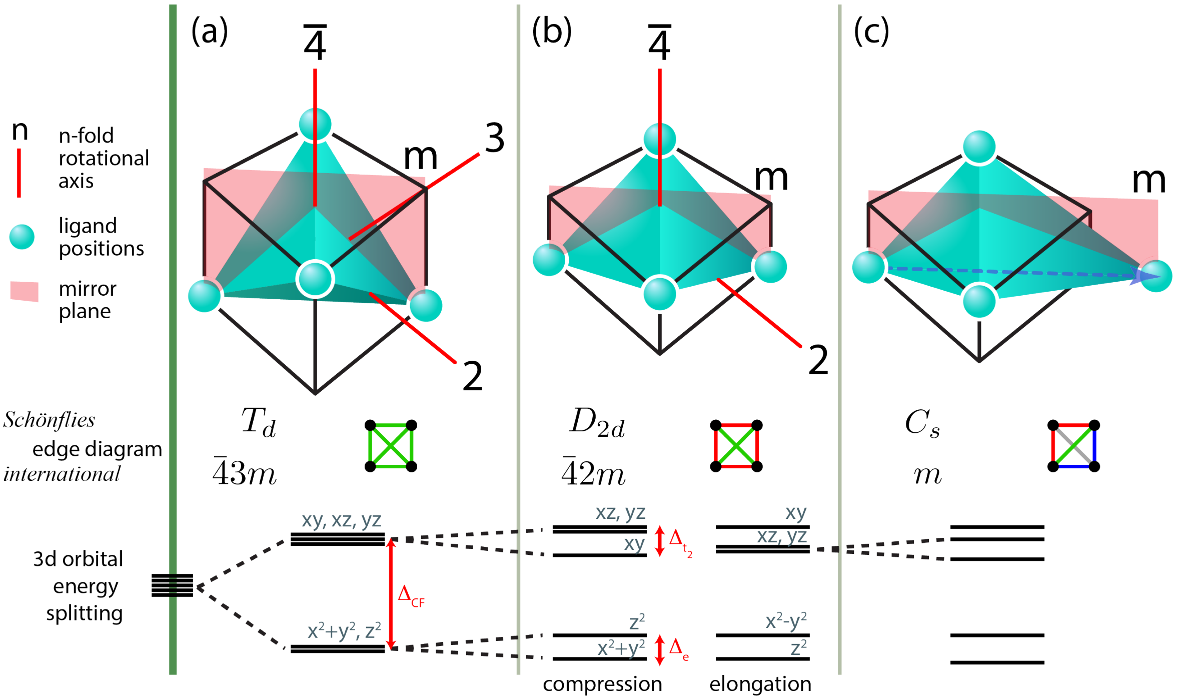

Figure 4.8: Illustrations of the tetrahedral symmetries T_d, D_{2d} and C_s and the splitting of the orbital 3d states by a crystal field of corresponding symmetry. Edge diagrams indicate tetrahedron edges of equal length by equal color. In Cs_2CoCl_4, the coordination of Co^{2+} is of C_s symmetry. The dashed blue arrow in (c) indicates the direction along which one of the ions is shifted.

off-diagonal matrix-elements of the spin-orbit coupling that enables transitions from the $e^4t_2^3$ ground state, described by Hund's rules, to these excited states [121].

In case of Cs_2CoCl_4, the local site-symmetry of the Co1 ($4c$) site in the space group $Pnma$ (see [122]) is C_s (m), which is even lower than the symmetry resulting from the tetragonal distortion described before. The actual Cl^- positions can be visualized best starting from the D_{2d} symmetry by shifting only one of the corners along the corresponding [110] direction. That way, the only symmetry left is a mirror plane spanned by this translation vector and the [001] direction, see Fig. 4.8 (c). The resulting crystal field is accordingly more anisotropic than in the D_{2d} case and also lifts the degeneracy within the t_2. Due to only one single remaining mirror-plane, the number of crystal field coefficients $a_{k,m}$ that are involved in a theoretical description in terms of crystal field theory is huge, compared to the famous case of d orbitals surrounded by ions sitting at the corners of an elongated or compressed octahedron. The coefficients calculated by solving the eigenpotential (cf. Chapter 2.1) of the corresponding point groups D_4h and C_s are listed in Tab. 4.3.

Whilst only three coefficients translating to the effective parameters $10Dq, \Delta_{e_g}$ and $\Delta_{t_{2g}}$ are needed in case of D_{4h}, the local site symmetry of the $4c$ site in Cs_2CoCl_4 is so low, that 13 independent crystal field coefficients have to be considered. Thus, an understanding of the electronic states and the origin of the magnetic anisotropy of Cs_2CoCl_4 is hardly obtained ab initio, but by considering the more illustrative higher

D_{4h} $4/mmm$ tetragonal distorted octahedron	C_s m Cs_2CoCl_4: Co^{2+} (4c site) coordination
	$a_{-1,1} = a_{1,1}, a_{1,0}$
$a_{2,0}$	$a_{2,-2} = a_{2,2}, a_{2,-1} = a_{2,1}, a_{2,0}$
	$a_{3,-3} = a_{3,3}, a_{3,-2} = a_{3,2}, a_{3,-1} = a_{3,1}, a_{3,0}$
$a_{4,0}, a_{4,4} = a_{4,-4}$	$a_{4,-4} = a_{4,4}, a_{4,-3} = a_{4,3}, a_{4,-2} = a_{4,2}, a_{4,0}$
3 independent	13 independent

Table 4.3: Crystal field coefficients $a_{k,m}$ for d orbitals in D_{4h} and C_s symmetries. The large number of parameters in case of Cs_2CoCl_4 complicates the application of crystal field theory.

symmetry group D_{2d} of a compressed tetrahedron, see Fig. 4.8 (b). In crystal field theory, instead of the tetrahedrally coordinated $3d^7$ system often the octahedrally coordinated $3d^3$ is considered, see [121, p. 470]. In the octahedral case, the energies of the e and t_2 levels are inverted. By switching from an electron picture to a hole picture, however, both systems can be analyzed equivalently. As the magnetic anisotropy can be understood in that context, the real coordination in Cs_2CoCl_4, described by an even lower symmetry, shall provide an even improved anisotropy effect. Most probably, the mechanism introducing the anisotropy is similar, although the true ground state might differ in details.

4.1.3 Literature results

Thermodynamics

After the first reports of the crystal growth of Cs_2CoCl_4 by Porai-Koshits in 1956, the anisotropic behavior of the magnetic susceptibility of the compound in a temperature range from 80 to 300 K was investigated by Figgis *et al.* [110]. The local directions K_1 to K_3 were defined, as shown in Fig. 4.9, and related the orientation of the molecular magnetic ellipsoid to the crystallographic axes. The direction K_3 was chosen such that it bisects the largest Cl-Co-Cl angle in the tetrahedron. This choice is not unique and it leads to an alternating rotation angle of magnetic easy planes $\beta = \pm 38°$ as discussed in Chapter 4.1.1. Due to differently rotated tetrahedra within the unit cell, the local anisotropies are reflected by the differences between the susceptibilities along the crystallographic axes. From a comparison to crystal field theory, several parameters (in addition to previous spectroscopic results [123, 124]) have been derived, e. g., the crystal field anisotropy $10Dq = -3200\,\mathrm{cm}^{-1}$ and the parameter $\Delta = -1000\,\mathrm{cm}^{-1}$ which gives the splitting of the free ion's ^4F ($3d^7$) ground term into the $^4T_2$ term and the lowest-lying $^4A_2$. This study, however, focuses on the spectroscopic point of view and only partially discusses magnetic exchange as a possible origin of the observed Weiss constant θ.

In the first study of the one-dimensional magnetism the specific heat as a function of temperature is investigated [3]. Four different contributions are seen in the data as shown in Fig. 4.10. At high temperatures the specific heat is dominated by phonons.

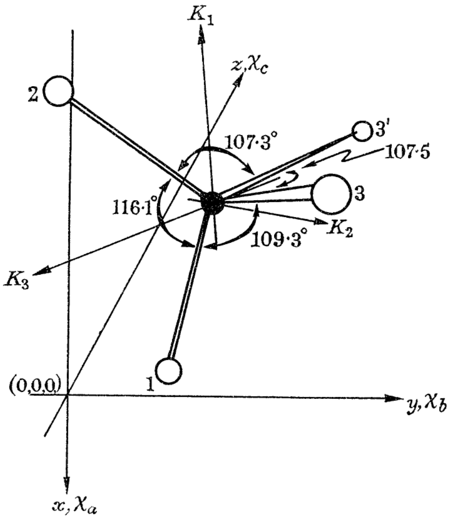

Figure 4.9: Relation of the local molecular coordinate system K_i to the crystallographic axes in a $CoCl_4$ tetrahedron of Cs_2CoCl_4. The choice of K_3 is free and only restricted by a mirror symmetry. (Taken from Ref. 110)

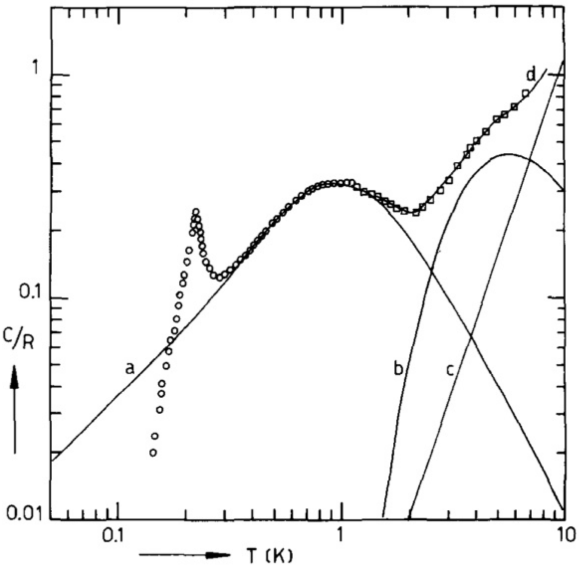

Figure 4.10: Heat capacity of Cs_2CoCl_4 as a function of temperature at zero field [3]. Different contributions to the total heat capacity (d) are seen: the magnetic specific heat of the one-dimensional spin chain (a), a Schottky-like contribution due to excited crystal field states (b) and an approximation of the phonon heat capacity by the Debye model (c).

They are treated by the low-temperature limit $c_p \propto T^3$ of the Debye model, even though the applicability of the T^3 approximation might be questionable in this temperature range. Around 5 K a hump is seen in the data. It is ascribed to a thermal population of the excited crystal states that evolve from the splitting of the S=3/2 states of Co^{2+} by the crystal field anisotropy $\mathcal{D}$. According to the Kramers theorem [30], two doublet states result that are split by an energy $\Delta E = 2\mathcal{D}$. By a comparison of the data around 5 K to the specific heat of a two level system with an energy gap ΔE,

$$c_{\text{Schottky}} = N_A k_\text{B} \, \frac{\Delta E^2}{k_\text{B} T^2} \frac{e^{\Delta E / k_\text{B} T}}{(1 + e^{\Delta E / k_\text{B} T})^2}, \tag{4.8}$$

generally referred to as Schottky contribution, similar values of ΔE are obtained in different studies (13.5 ± 1 K [3], 16.0 ± 0.4 K [4]). Algra *et al.* compare the maximum of the specific heat around 1 K to numerical data of the *XXZ* model as given by the Hamiltonian

$$\mathcal{H}_{XXZ} = -2 \sum_i J \left(S_x^i S_x^{i+1} + S_y^i S_y^{i+1} + \Delta S_z^i S_z^{i+1} \right). \tag{4.9}$$

They compare different anisotropies $\Delta = 0, 1/4, 1/2, 1$ and find the best agreement using a value of $\Delta = 1/4$. They work out a coupling constant $J/k_\text{B} = -1.4$ K. Using the convention of this thesis which differs by dropping the prefactor -2 in Eqn. (4.9), this value translates to $J/k_\text{B} = 2.8$ K. The impact of an additional perpendicular magnetic field on the splitting of the spin-3/2 states was calculated for a single ion in Ref. 5. In magnetic fields which are small in comparison to $\mathcal{D}$ the effective spin-$1/2$ model is argued to be applicable. However, this has not been verified by experiment in literature.

In Ref. 4 the magnetic susceptibility in a temperature range from 1.5 K to 20 K is analyzed. While at higher temperatures the susceptibility obeys a typical Curie-Weiss law with constants from ≃4 to 15 K [110], the measurements at temperatures below 20 K, see Fig. 4.11, reveal a deviation from the Curie Weiss behavior by an increasing anisotropy of the susceptibility on decreasing the temperature. The largest magnetization is found along the chain direction (i. e., the c axis in the convention used in Ref. 110), which can be understood from the fact that all easy-plane orientations in the unit cell have this axis in common. Thus, spins are most easily aligned along this direction in comparison to the other crystallographic axes for which at least the spins in one type of chain have to leave their easy plane. The data are compared to the spin-$3/2$ single-ion Hamiltonian

$$\mathcal{H} = \mathcal{D}(S_z^2 - 5/4) + \mathcal{E}(S_x^2 - S_y^2) + \mu_\mathrm{B}(g_x H_x S_x + g_y H_y S_y + g_z H_z S_z), \tag{4.10}$$

with in- ($\mathcal{E}$) and out-of-plane ($\mathcal{D}$) anisotropies. Due to the small effect of magnetic exchange in the paramagnetic region, i. e., $k_\mathrm{B}T \gg \mathcal{D} \gg J$, the analysis is extended to include magnetic exchange in a mean-field approximation. The single-ion principal axes x, y and z of Eqn. (4.10) relate to the crystallographic axes by a rotation which determines the mixing of the calculated molecular susceptibilities for the different crystallographic axes. In contrast to Ref. 110, the relation between molecular and crystallographic axes is not arbitrarily fixed in Ref. 4, but based on the cobalt ion's site symmetry (m) two possible orientations (see Chapter 4.1.1 for a discussion of them) of the molecular axes are tested. As the cobalt ion is located on a mirror plane one molecular axis has to lie within this plane. From the other two perpendicular axes either one may lie in the mirror plane as well, resulting in an orthorhombic g tensor, or they both lie rotated by 45° out of the mirror plane, rendering g_x and g_y equal.

However, both situations are reported not to describe the experimental data properly. The fit, shown in Fig. 4.11, was obtained allowing arbitrary rotations of the molecular axes and by using the parameters

$$\mathcal{D}/k_\mathrm{B} = 6.94\,\mathrm{K}, \quad \mathcal{E}/k_\mathrm{B} = 0.73\,\mathrm{K}, \quad J/k_\mathrm{B} = 2.7\,\mathrm{K}, \quad g_x = 2.65, g_y = 2.71, g_z = 2.51.$$

The molecular coordinate system was rotated by about 60° about z starting from the symmetry-proposed orthorhombic configuration shown in Fig. 4.4 (b). The resulting orientation is described as well by an angle $\beta = 38°$, but due to the arbitrary rotation the in-plane directions x and y are not symmetry-related, which is reflected by the different values of g_x and g_y. However, the authors state that a wide range of parameters and rotation angles are allowed for a similar description of the data, such that the anisotropies $\mathcal{D}$ and $\mathcal{E}$ are not well-fixed from the high-temperature data. Yet, the authors point out that a non-negligible value of the in-plane anisotropy $\mathcal{E}$ was found in all fits. They argue that the orientation of the molecular coordinate system different from the allowed positions might hint at further distortions of the $CoCl_4$ tetrahedra below room temperature similar to those observed in other compounds of the R_2CoX_4 series [125, 126]. The specific heat of Cs_2CoCl_4 is analyzed as well in Ref. 4. The data

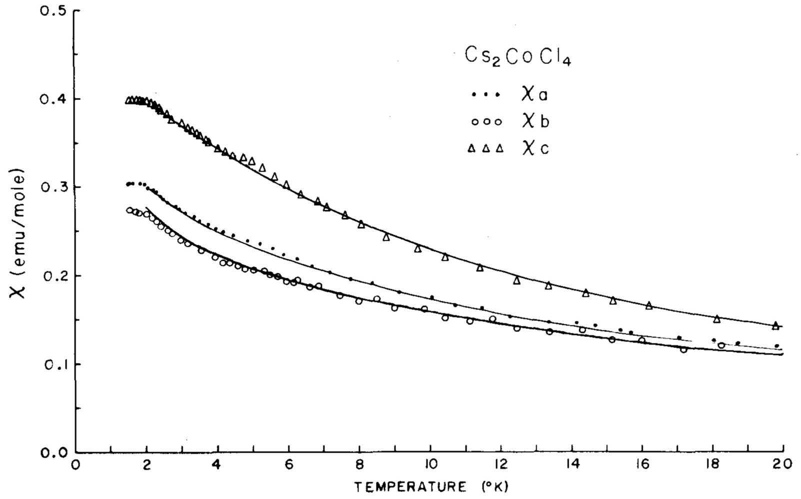

Figure 4.11: Magnetic susceptibility of Cs$_2$CoCl$_4$ as a function of temperature for all crystallographic axes. Solid lines are fits of a spin-$^3/_2$ model including in- and out-of-plane anisotropies, the exchange constant J and the principal g values g_x, g_y, g_z. Due to a different notation, the crystallographic axes b and c are interchanged in comparison to the convention used in this thesis and in other works. (Taken from Ref. 4)

are of rather poor quality and depending on the fit parameters approximate values of the coupling constant $J \approx 3.4\,\mathrm{K}$, similar to those of Ref. 3, are deduced.

From the high-temperature susceptibility, similar values of the isotropic spin-$^3/_2$ g factor $g_{3/2} = 2.4$ were derived [4, 5, 110]. The resultant expected saturation-magnetization of $g_{3/2}\,\mu_\mathrm{B}\,S = 2.4 \cdot {}^3/_2\,\mu_\mathrm{B} = 3.6\,\mu_\mathrm{B}$ was in fact observed in pulsed-field magnetization measurements [5]. The ordered moment that was found by neutron scattering at $T = 80\,\mathrm{mK}$, however, is $1.6\,\mu_\mathrm{B}$ only. This reduction is explained by strong quantum fluctuations in the ground state [8].

The susceptibility of Cs$_2$CoCl$_4$ in the low-temperature regime shows a maximum as a function of temperature around 1.5 K (cf. Fig. 4.12 [6, 7]). It indicates the presence of short range correlations and is a typical fingerprint of one-dimensional magnetism. In a large temperature range the susceptibility along the chain direction (i. e., the c axis in the convention of [7]) is largest just as in the previously discussed high-temperature data. An anomaly signals the onset of long-range order at about 0.3 K where the susceptibility along the chain direction drops below those of the other directions. This is understood by an antiferromagnetic order with spins mainly oriented along this axis as observed by neutron scattering (see Chapter 4.1.3). The first theoretical work, motivated by the experimental data of Ref. 6, concerns the transverse susceptibility as calculated via exact diagonalization of finite systems [6]. Due to finite size effects this comparison is limited to relatively high temperatures. Chatterjee tries to fit the data by calculations of the XY model based on the TMRG technique, i. e., DMRG at finite temperature [127]. In contrast to exact diagonalization, TMRG gives resilient data in a broader temperature range and for very long system sizes. As shown in Fig. 4.12, a moderate agreement within about 15% is achieved between the calculated transverse

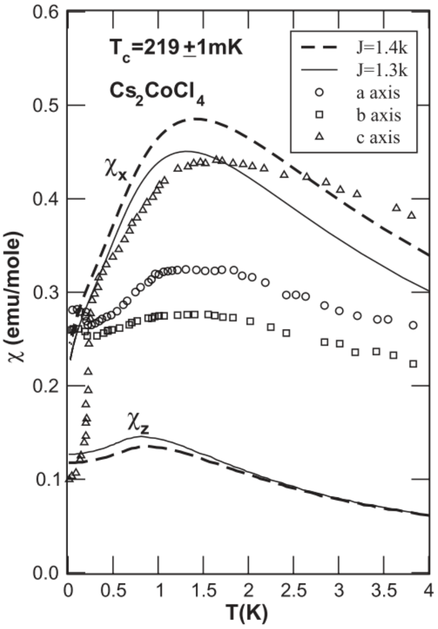

Figure 4.12: Susceptibility of Cs_2CoCl_4 from $\simeq$ 0.05 K to 4 K in comparison to TMRG results for the XY model. The crystallographic axes b and c are interchanged in comparison to the convention in this thesis. (Taken from Ref. 7)

susceptibility, i. e., for magnetic fields within the XY planes, and the data for the chain direction c at temperatures larger than $\simeq 0.3$ K by using a coupling constant J between 2.6 K and 2.8 K. At low temperature close to T_N, calculations and data even approach each other, whereas the description around the maximum is rather poor. This might be related to the fact that Cs_2CoCl_4 does not feature the full XY anisotropy that was assumed in the calculations. In fact, a reduced anisotropy would be reflected in a convergence of transverse (χ_x) and longitudinal (χ_z) susceptibilities, which in consequence would lead to a lower and more broadened χ_x. The order parameter as a function of temperature, as measured by the spontaneous magnetization [8], is compared to an analytic expression derived for the spontaneous magnetization I in the two-dimensional Ising model [128, 129]

$$I = \left(1 - \left[\frac{2x}{(1-x^2)}\right]^4\right)^{\frac{1}{8}}, \quad x = e^{-2J'/k_BT}. \tag{4.11}$$

In the context of magnetic order the Ising model is justified as the relative tilt of the magnetic easy planes and the presence of interchain couplings renders the system Ising like. From a fit of Eqn. (4.11) to the data, the interchain coupling $J' \simeq 0.095$ K is estimated.

In another theoretical work, the XXZ Hamiltonian with an anisotropy parameter $\Delta = 1/4$ is concerned in the full transverse magnetic field range using the Lanczos-method [66]. However, the results are not quantitatively compared to experimental data. By an inclusion of interactions between chains the experimental field versus temperature phase diagram is reproduced and the ratio of interchain couplings $J' \simeq 0.00458 \cdot J \simeq 0.01$ K is deduced.

From a comparison of the incommensurability of quasi-elastic neutron scattering to a model of coupled spin chains in Ref.120 the ratio between interchain (J') and intrachain

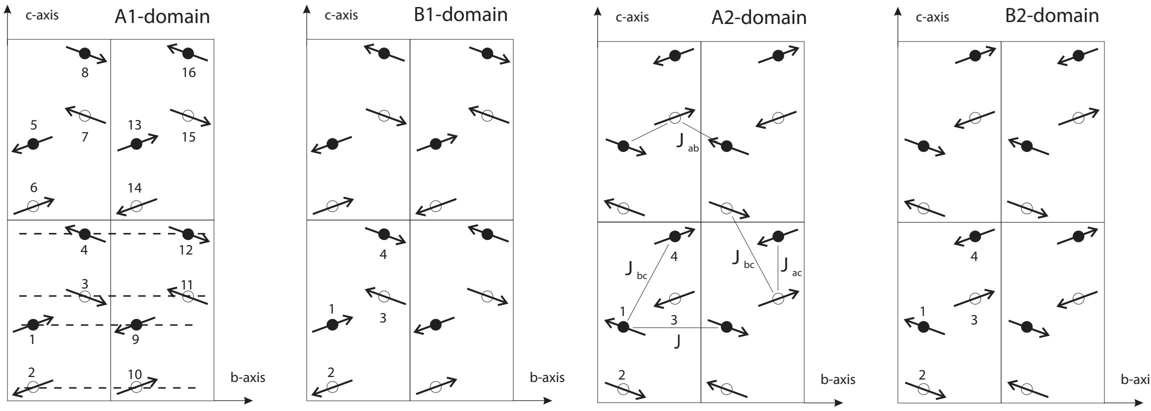

Figure 4.13: Magnetic order domains of Cs_2CoCl_4 at zero magnetic field. Solid and open circles represent Co^{2+} at approximate a-positions 0.25 and 0.75. Dashed lines indicate the chain direction. Couplings are depicted as lines. Sites k in unit cells $n = 1, .., 4$ are numbered as $k + n$ with k defined in analogy to Chapter 4.1.1. (Taken from Ref. 8)

(J) interactions was determined to $J' = (0.0471 \pm 0.016) \cdot J \approx 0.14\,\mathrm{K}$. The spin-wave excitations at $T = 0.3\,\mathrm{K}$ were measured via inelastic neutron scattering and an antiferromagnetic coupling constant $J_{\mathrm{SW}}/k_{\mathrm{B}} = 3.5 \pm 0.5\,\mathrm{K}$ was obtained assuming the 1D XY model.

Summing up, there is consensus in literature on the one-dimensionality of the magnetism of Cs_2CoCl_4 and on the primary coupling constant which in average is given as $J = 3 \pm 0.4\,\mathrm{K}$. Concerning the strength of interchain interactions J'/J, different values are published. They range from 0.01 to 0.14. Due to the different applied models and approaches, an evaluation of the results is difficult. Nevertheless, they indicate that interchain interactions are at least one order of magnititude smaller than the primary coupling J.

Magnetic order

The magnetic order at $T < T_{\mathrm{N}}$ is analyzed by Kenzelmann *et al.* [8]. Cooling below 217 mK at zero magnetic field, magnetic reflections are observed at the commensurate reciprocal positions $(0, n + 0.5, m + 0.5)$, which indicates long-range magnetic order. From group theory and a comparison of different models to the integrated intensities the ordered moments are found to be confined to the bc plane forming four possible domains with an enlarged unit cell as shown in Fig. 4.13. The structure can be understood as antiferromagnetic ordered chains along b with different relative orientations of neighboring spin chains. The different domains are transformed to each other by either flipping the sign of the b or the c components of the spins or by changing the phase between chains 1 and 3 and between 2 and 4 by π. A small tilt of moments away from the b axis by ≈ 15° and an equal population of A and B domains is found.

An increase of the antiferromagnetic intensities by small magnetic fields applied along a precedes a steep decrease of the intensity close to $H_c = 2.10\,\mathrm{T}$. From the identical field dependence of different magnetic intensities, it is concluded that the magnetic structure remains unchanged in small magnetic fields $H < H_c$ and that the moments cant into the field direction a as seen from an increasing ferromagnetic moment, i. e., the magnetization that was derived from the intensities of magnetic reflections at different temperatures $T < T_{\mathrm{N}}$ (Fig. 4.14). It shows an increasing slope for small magnetic fields, that can be understood by the canting of spins but also resembles the magnetization of the one-dimensional XXZ model (cf. Chapter 2.3.3). At the critical field H_c, where magnetic order disappears, the slope is maximal, but saturates at the reasonably larger crossover-field H_m. Because of the transversal components of the magnetic field the higher-lying $|S_z = \pm {}^3\!/_2\rangle$ states are intermixed and lead to a superimposed linear increase of the magnetization. From the absence of reflections in the bc plane for magnetic fields $H = 3\,\mathrm{T} > H_c$ and the saturation of the magnetization at a magnetic field $H_m \simeq 2.5\,\mathrm{T} > H_c$, a disordered spin-liquid state is suggested for magnetic field $H_c < H < H_m$. The authors summarize their findings in the phase diagram shown in Fig. 4.15.

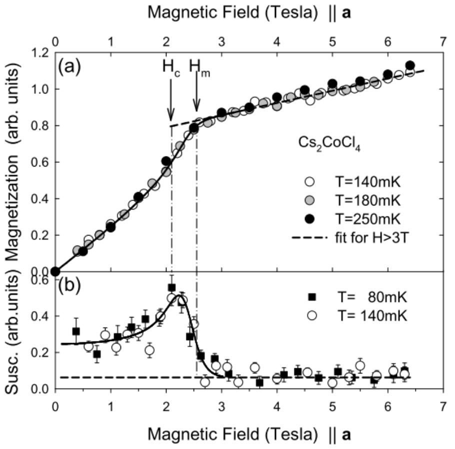

Figure 4.14: Magnetization of Cs_2CoCl_4 at different temperatures $T < T_{\mathrm{N}}$ for magnetic fields applied along a. (Taken from Ref. 8)

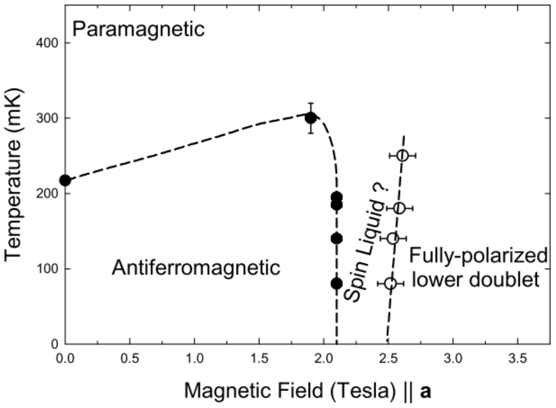

Figure 4.15: Magnetic field versus temperature phase diagram of Cs_2CoCl_4 as proposed in Ref. 8. Closed symbols indicate the onset of antiferromagnetic Bragg peaks in neutron scattering. Open symbols are the saturation field extracted from the magnetization.

4.2 One-dimensional magnetism

In this chapter the one-dimensional magnetism of Cs_2CoCl_4 is analyzed by a comparison of thermal expansion and specific heat data to calculations of the spin-$^1/_2$ XXZ model. As this model treats isolated spin chains, (complex) magnetic order phenomena cannot be understood from it. Thus, a comparison is valid only in a restricted temperature range. In Fig. 4.16 the different regimes of Cs_2CoCl_4 as known from literature [3, 4, 8], are sketched. At temperatures below $T_\mathrm{N} = 0.22\,\mathrm{K}$ magnetic long-range (3D) order is found. The physical quantities determining this phase transition are the interchain coupling J' and the correlation length ξ of the spin chain. At higher temperatures in the "1D" phase the interaction between spins of the order J leads to short-ranged correlations. Due to a non-population of higher spin states in this phase an effective spin-$^1/_2$ is formed. Beginning with temperatures $T \approx 2\,\mathrm{K}$ the spin-$^3/_2$ states start to contribute and a diminishing correlation length leads to a crossover to an uncorrelated "paramagnetic" regime at temperatures of the order of the anisotropy $\mathcal{D}$.

Two different experimental setups were employed to measure the thermodynamic properties of Cs_2CoCl_4. The ^{3}He cryostat (Heliox VL, Oxford Instruments) provides temperatures down to $\approx 250\,\mathrm{mK}$ with comparably small effort. Due to the coincidence that $T_\mathrm{N} = 0.22\,\mathrm{K}$ lies only slightly below the base temperature of the ^{3}He cryostat (see Fig. 4.16), this cryostat was merely used for the investigation of the magnetically non-ordered Cs_2CoCl_4 as presented in this chapter. The results from the measurements at lower temperatures, obtained using a dilution refrigerator (Kelvinox 300, Oxford Instruments), will be discussed in Chapter 4.3. In the following, selected data are shown for all thermodynamic quantities. The fits of the theoretical models, the phase diagrams and the further analysis, however, is based on the full data sets shown in Appendix B.

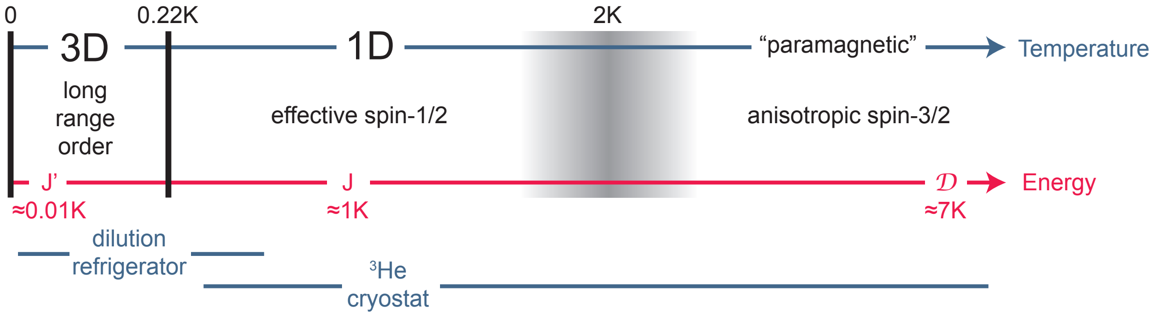

Figure 4.16: Temperature regimes and energy scales of Cs_2CoCl_4 in comparison to the experimental temperature ranges of the used setups. The shaded region around 2 K indicates a smooth crossover from a low-temperature regime dominated by the lowest Kramers doublet to a free-ion like regime where correlations can be neglected. By no means there is a thermodynamic phase transition at 2 K.

4.2.1 Experimental results

Specific heat

The specific heat of Cs_2CoCl_4 (sample *212a*) was measured using the relaxation time method and the home-built setup described in Chapter 3.2.3. The measurements were performed using a SMD platform heater (27 kΩ) wired with 50 µm manganin and a sample thermometer connected by 33 µm manganin wire. The sample platform was suspended to fishing line. The heat capacity of the addenda was measured in a separate run in zero field and in an applied magnetic field of 10 T. No significant field dependence of the addenda down to 250 mK was found. Therefore, it was assumed to be independent of the magnetic field. The sample with a mass of 8.21 mg and approximate dimensions of $1{\times}3{\times}1$ mm^3 was attached to the platform with a small amount of 0.44 mg Apiezon N grease. The grease was slightly heated by focusing a cold light-source on the sample platform. Such, the grease becomes less viscous and flows around the sample and out of the gap between sample and platform. In former measurements it turned out that the internal relaxation (τ_2) can be minimized with this technique. The sample holder was rotated such that the magnetic field aligns with the sample's b axis. All data presented in this chapter were acquired with the magnetic field $H \parallel b$.

In the whole temperature range from 250 mK to $\simeq 20$ K the relaxation method proofs very reliable. Exemplary raw data are shown in the lower panels of Fig. 4.17 for three different temperatures. In all curves the baseline was measured for 15 s before switching on the heater. The fact that the baseline does not show a sizable slope proves the temperature stability of the setup. In few of the curves acquired at temperatures well below 1 K a small τ_2 effect arises, which is reflected in a steep slope close to the switching times of the heater at 15 s and at about half of the time axis. Although the values of τ_2 obtained at different temperatures are comparable, the effect is seen clearest in the raw data at lowest temperature. Due to a dominating external relaxation and a decreasing data quality at elevated temperature, τ_2 effects are not directly identified in the raw data obtained above $\simeq 1$ K. The raw data were fit based on the numerical method described in Chapter 3.2.2. The resulting time constants and the calculated time dependence of the platform temperature is shown as red lines. The measured total heat capacity exceeds the signal of the addenda by at least two orders of magnitude at the lowest temperature. The contribution of the grease to the heat capacity is lower by another two orders of magnitude. Thus, the specific heat of the sample can be determined with high precision as small errors of the addenda heat capacity or of the mass of the grease are safely negligible.

The obtained specific heat of Cs_2CoCl_4 agrees with literature data within a few percent (see open symbols and green squares in Fig. 4.18). It shows the same four features already discussed in literature [3]:

- **Phonons** dominate at high temperatures $T \gtrsim 10$ K.
- A **hump around 5 K** is attributed to the thermal population of the second crystal-field Kramers doublet. In comparison to Ref. 3, the present data contain

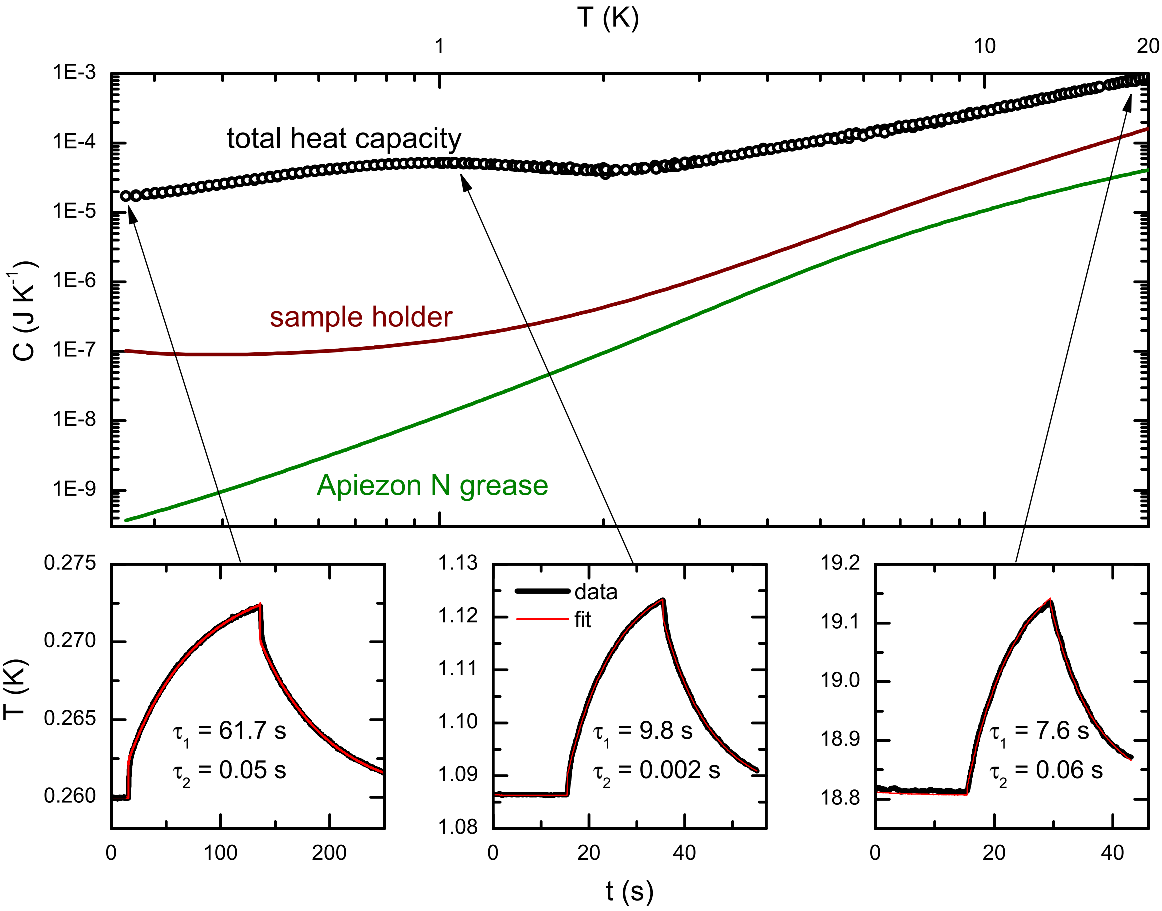

Figure 4.17: Contributions to the measured total heat capacity of Cs_2CoCl_4 in the one-dimensional regime. The sample holder was previously measured in a separate run. The heat capacity of the grease was calculated from the measured weight using literature data [96]. Exemplary raw data (black lines) at three different temperatures are shown in the lower panels together with fits of the temperature dependence, shown as red lines. The fit yields the external relaxation time τ_1 and the internal relaxation time τ_2 that is reflected in the steep flanks of $T(t)$ at the lowest temperatures.

more information on the phonon background and the Schottky anomaly around 5 K due to an increased density of points.

- The **maximum around 1 K** is found at an identical temperature, the maximum value however exceeds the results of Ref. 3 by about 7%. This difference may arise from the digitization of the literature data or from systematical differences in the experiments. Furthermore, a comparable spread for lower-quality samples was found previously [93].

- **Magnetic order** is indicated by a sharp peak at $T_{\mathrm{N}} = 228\,\mathrm{mK}$. The low-temperature data (gray triangles in Fig. 4.18) were obtained with a different setup in the dilution refrigerator. They confirm the absolute value of the high-temperature data and the magnetic order temperature found in Ref. 3. Beyond that, the peak shape in the present data is much sharper. The magnetic order transition will be discussed in Chapter 4.3.

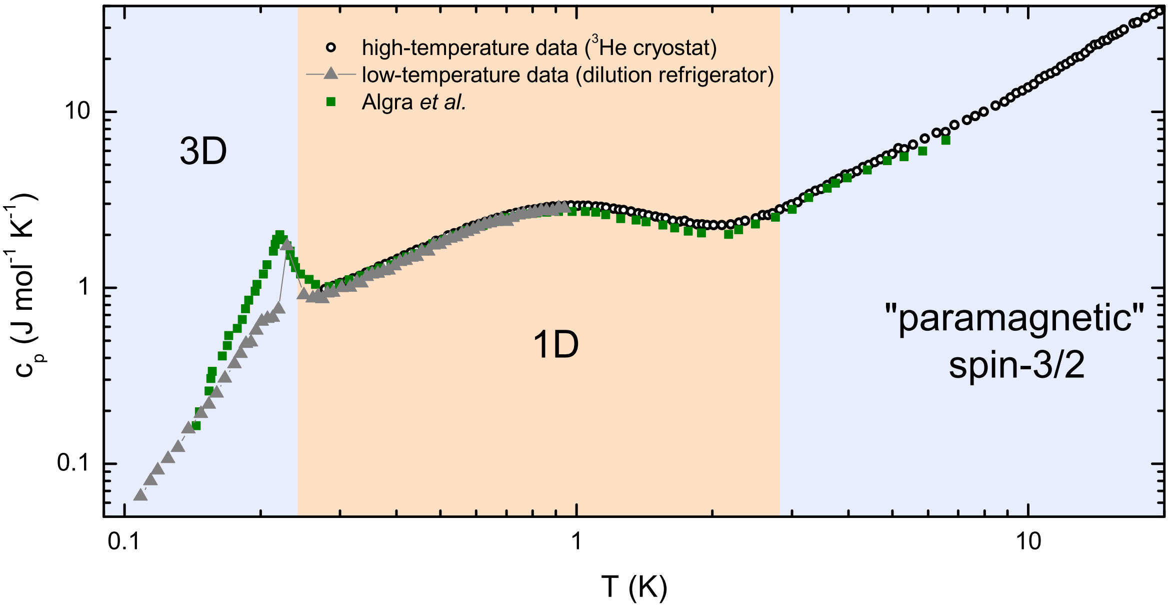

Figure 4.18: Heat capacity of Cs_2CoCl_4 measured using two different setups (^{3}He cryostat: open symbols, ^{3}He/^{4}He dilution refrigerator: gray triangles) in comparison to literature data of Ref. 3 (green squares). The shaded areas mark the approximate temperature regimes of the magnetic order (3D), the one-dimensional magnetism (1D) and of the "paramagnetic" range where correlations are negligible.

As shown in Fig. 4.19, in applied magnetic fields the broad maximum around 1 K is strongly influenced. In a magnetic field of 1 T it is broadened and shifted to lower temperature. A peak close to 0.3 K arises due to a positive field dependence of T_{N} in magnetic fields of 1 and 2 T. This effect is not of interest here, but will be discussed in the context of the magnetic order in Chapter 4.3. Increasing the magnetic field further suppresses the heat capacity, until the temperature dependence fundamentally changes at 3 T as is best seen by plotting c_p/T versus T (inset of Fig. 4.19). Despite the magnetic order anomalies at 1 and 2 T, a residual γ value is found for small fields. This indicates a linear temperature dependence of the specific heat as expected from one-dimensional spin chains at low temperature [130]. In large magnetic fields, $\gamma = c_p/T(T \to 0, H \geq 3\,\mathrm{T})$ seems to approach zero, which can be understood from the exponential temperature dependence of c_p in a gapped state.

In contrast, the specific heat at higher temperatures $\gtrsim 4$ K hardly depends on the magnetic field. In Fig. 4.19 the shaded area marks the approximate temperature range where the specific heat is dominated by phonons. Up to about 2 T the measured heat capacity in this temperature range matches the zero-field data. Only by further increasing the magnetic field, small deviations occur. Although magnetostriction can lead to field-dependent phonon branches, this effect is probably small in comparison to the field-induced shift of entropy to higher temperature. Comparing the data for 3 T and 4 T the tendency of a shift of the heat capacity to higher temperatures is seen. Thus, the rise of c_p in the phonon range probably is due to an increased magnetic heat capacity at high temperatures in large magnetic fields.

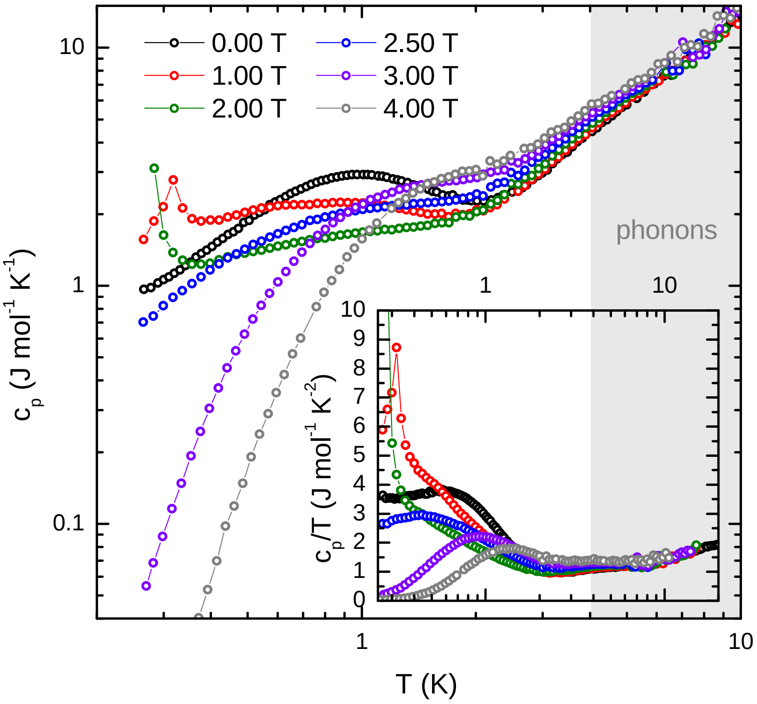

Figure 4.19: Specific heat of Cs_2CoCl_4 in the 1D-regime at different magnetic fields applied along b. In the inset c_p/T is shown on a linear scale versus temperature. The shaded gray area marks the approximate temperature range where phonons dominate.

Thermal expansion and magnetostriction

The thermal expansion and the magnetostriction of Cs_2CoCl_4 was measured using the home-built capacitance dilatometer described in Chapter 3.4. The sample (*Boh-2-2-2*, $m = 58.14\,\mathrm{mg}$) of dimensions $3.35{\times}2.8{\times}2.1\ \mathrm{mm}^3$ was mounted in a longitudinal configuration, i. e., such that the length change ΔL is measured parallel to the applied magnetic field $H \parallel b$. All temperature-dependent data were collected in a field-cooled mode with the magnetic field applied at approximately 2 K before cooling to 250 mK and subsequently measuring with increasing temperature followed by the measurement with decreasing temperature. Below 2 K the temperature was changed with a slow sweep rate of $10\,\mathrm{mK\,min^{-1}}$, data above 2 K were obtained with a sweep rate of $0.1\,\mathrm{K\,min^{-1}}$. Tiny hysteresis effects were observed below 1 K (see Fig. B.2 for all acquired data) that, however, might be of experimental origin. In comparison to the main signal these effects are very small and, thus, in Fig. 4.20 (a) only data with increasing temperature are shown. All measured length changes $\Delta L/L_0$ were shifted such that they match the magnetostriction measured at 2 K. The relative length change features a broad maximum around 3 K that is first shifted to lower temperatures by magnetic fields of up to $\simeq 2\,\mathrm{T}$. Close to this magnetic field $\Delta L/L_0$ is almost constant as a function of temperature. By further increasing the magnetic field, the low-temperature slope changes to a negative sign. At higher temperature $T \gtrsim 4\,\mathrm{K}$, the length is almost independent of the magnetic field. The field dependence is more directly seen from the thermal-expansion coefficient, shown in panel (b) of Fig. 4.20. It was obtained from the measurements by numerical derivation ($\alpha_i = \frac{1}{L_0}\frac{\partial \Delta L_i}{\partial T}$). At zero magnetic field a maximum arises around 1 K, similar to that seen in the specific heat, which is plotted for comparison with gray open symbols in Fig. 4.20 (b). The alikeness of the thermal expansion and the specific heat around 1 K can be understood from the Grüneisen scaling (see Chapter 4.2.2). At higher temperatures the thermal expansion coefficient

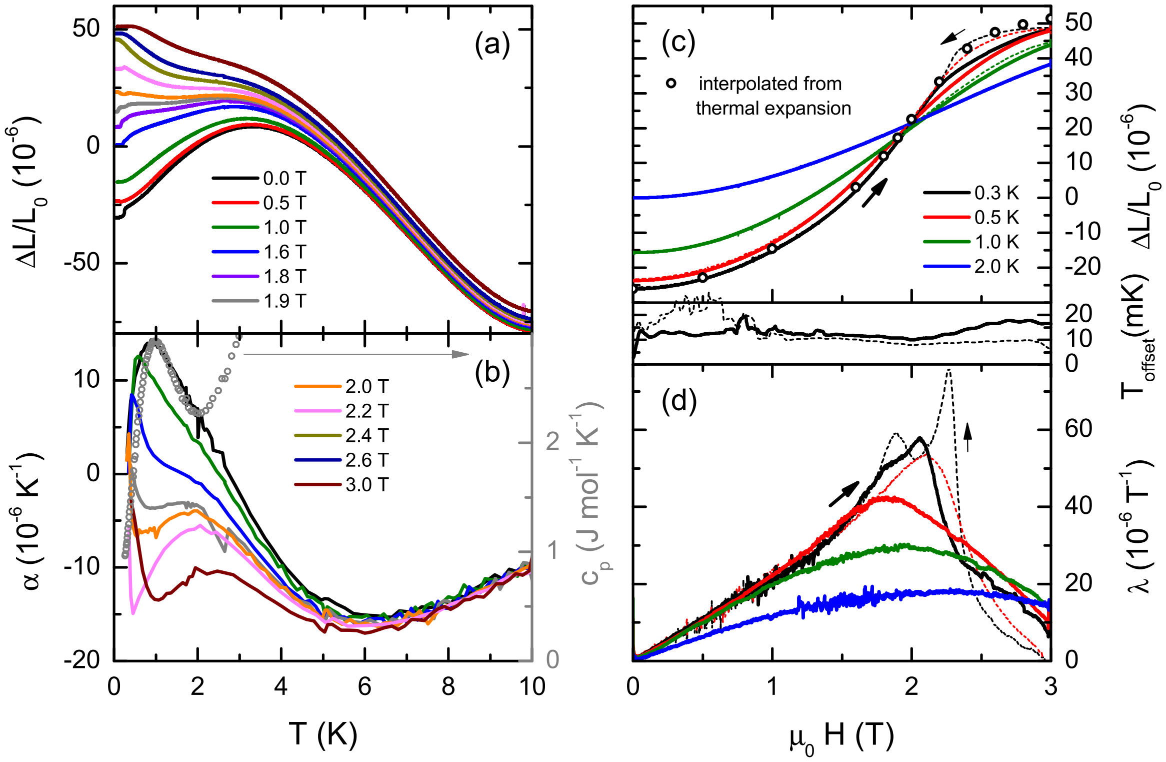

Figure 4.20: Thermal expansion and magnetostriction of Cs_2CoCl_4 of the b axis for different magnetic fields $H \parallel b$. Solid (dashed) lines are measurements with increasing (decreasing) temperature/field. The data in (a) and (c) were shifted with respect to the magnetostriction measured at 2 K. Open symbols in (c) are interpolated from the thermal expansion. The inset between panels (c) and (d) shows the difference between the sample holder temperature and the cryostat's temperature.

becomes negative and shows a minimum around 6 K. This minimum is associated with the thermal population of the second crystal-field doublet in analogy to the Schottky anomaly of the specific heat at that temperature. Similarly, in an applied magnetic field this feature is hardly influenced, whereas the zero-field maximum is shifted to lower temperature. At about 1.9 T the sign of α changes to negative in the whole measurement range. Also the low-temperature tail of α switches its sign from positive to negative below about 0.5 K at a magnetic field of $\simeq 2$ T. By further increasing the magnetic field a new maximum evolves around 2 K that is shifted to a slightly higher temperature $\simeq 2.5$ K in a magnetic field of 3 T.

The magnetostriction, shown in panel (c) and (d) of Fig. 4.20, was measured after cooling in zero magnetic field with a field sweep rate of 0.1 T min^{-1}. Due to experimental issues with flux jumps of the superconducting magnet, at low magnetic field $\lesssim 2$ T the length change ΔL reveals several spikes reflected as noise in the numerically derived magnetostriction coefficient. The curves obtained at 0.3 K and 0.5 K with increasing and decreasing magnetic field coincide at small fields, but deviate with increasing the magnetic field above 1.5 T. In this range the length gradually saturates as indicated by an inflection point in ΔL and a corresponding broad peak of λ at 2.06 T in the up measurements. Although hardly visible in ΔL, two anomalies are found in λ with decreasing field at 2.26 T and 1.88 T. At 0.5 K the measurements also show a small dependence on the sweep direction. However, here only one transition is signaled and the maximum of λ lies at slightly higher magnetic fields for sweeping the magnetic field downwards. The differences between the up and down measurements at both 0.3 K and 0.5 K, do not show a typical hysteretic behavior as expected, for example, in the vicinity of a first-order phase transition. This atypical behavior and the appearance of two anomalies in one of the curves might be of experimental origin. In the inset between panels (c) and (d) of Fig. 4.20 the temperature difference $T_{\mathrm{offset}} = T_{\mathrm{sample}} - T_{\mathrm{cryo}}$ between the sample and the cryostat in case of the measurement at 0.3 K is plotted as a function of the magnetic field. There is an overall finite difference between these temperatures due to the imperfect thermal coupling of the sample holder to the cryostat and due to eddy currents induced by sweeping the magnetic field which lead to a heating of the holder by about 10 mK at small magnetic fields. Several anomalies below ≈ 1.5 T are induced by the flux jumps of the cryomagnet as discussed above. They are typically present only at small magnetic fields of approximately 1 T and are not significant here. Interestingly, T_{offset} gradually increases up to about 20 mK at fields $\gtrsim 2$ T. This rise might stem from the magnetocaloric effect (MCE) of the sample. Indications for a magnetocaloric effect of $\mathrm{Cs_2CoCl_4}$ are also given by a strong sample temperature change while charging and discharging the magnetic field in between of heat capacity measurements. Although a temperature variation of 10 mK does not suffice to explain the sizable hysteresis effects, one has to keep in mind that the sample temperature is measured with a thermometer not attached to the sample itself, but to the copper dilatometer with a significantly larger mass than the sample, such that the actual sample temperature offset might be higher. Furthermore, the thermal conductivity of the sample drops in applied magnetic fields quite substantially such that the thermal equilibration is slowed down. Comparing the field dependence of the magnetostriction coefficient λ to the data acquired at lower temperature in the magnetic order regime (see Chapter 4.3 and Fig. 4.53) the two-peak structure strongly resembles the data acquired at $\lesssim 0.2$ K and the peak positions coincide surprisingly well with the two critical fields of a low-temperature magnetic order transition. This additionally supports the proposed strong MCE of $\mathrm{Cs_2CoCl_4}$ that leads to a sizable cooling of the sample upon decreasing the field.

The magnetostriction at 2 K does not show any hysteresis effects. Due to the elevated temperature, magnetocaloric effects are reasonably smaller. Thus, this curve was used to shift all temperature-dependent data with respect to it. Such, the magnetostriction can be extracted for discrete magnetic fields at arbitrary temperature also by interpolating the thermal expansion. The resulting interpolated magnetostriction is shown by open symbols in Fig. 4.20 (c). Concerning the presence of the two anomalies seen in λ at 0.3 K, no statement is possible due to the low point density. Yet, the interpolated data coincide with the field-dependent data at small fields, but deviate from the data for both sweep directions at fields $\gtrsim 2.2$ T while being closer to ΔL acquired with decreasing field. Therefore, the field-dependent data at lowest temperature and around 2 T should be treated with some caution.

The specific heat and the thermal-expansion coefficient, altogether show a similar structure. In a surface plot of all data, see Fig. 4.21, the typical thermodynamic signatures of low-dimensional spin chains are seen (cf. Chapter 2.3). While a valley arises in the specific heat around the critical field of about 2 T, the thermal expansion shows a sign change close to this field. At zero field c_p and α are related via the Grüneisen scaling and both show a similar maximum as a function of temperature. Above 1 K, the the thermal expansion coefficient α becomes negative, whereas c_p increases, which is explained by an opposite sign of the respective pressure dependence.

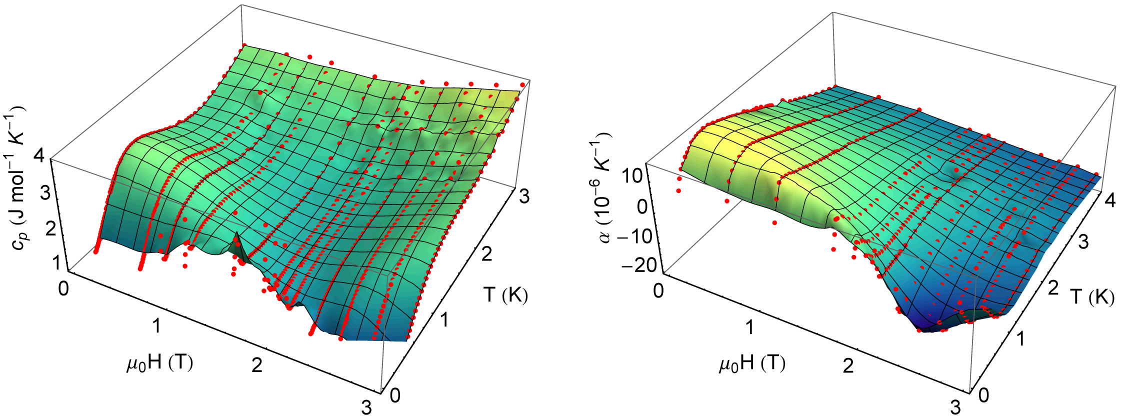

Figure 4.21: Specific heat and thermal-expansion coefficient of Cs_2CoCl_4 as a function of magnetic field and temperature. The surface is interpolated from the measured data points (red dots).

Thermal conductivity

The thermal conductivity of Cs_2CoCl_4 was measured using the steady-state method. For the temperature-dependent data above 30 K a thermocouple was used to measure the temperature gradient of the sample. The data at low temperature were acquired in a different setup by measuring the temperature gradient with two resistive thermometers calibrated in magnetic fields. The samples of typical dimension of 3×1×1 mm^3 were attached to the heat sink, i. e., the copper sample holder, with small amounts of silver glue. In some measurement runs the sample did not withstand the applied magnetic fields and scattered into pieces. Thus, various samples were used to obtain the full data set presented here. The quantitative agreement in the overlapping temperature range indicates the reliability of the data and the experimental procedure.

In Fig. 4.22 (a) the temperature dependence of the thermal conductivity is presented. Around 10 K it shows the typical phonon maximum. The absolute value of only few W m^{-1} K^{-1} indicates the generally rather low thermal conductivity of Cs_2CoCl_4. Below the phonon maximum at zero field, $\kappa(T)$ approximately follows a power-law dependence $\kappa \propto T^{\alpha}$. Depending on the considered temperature range, values of α range from 2.5 to 3, as found typically also for other compounds with phonon heat transport. Below 1 K, however, an unconventional upturn of the thermal conductivity arises in case the heat current is directed along the crystallographic b axis. The data $\kappa_a(T)$ obtained in the perpendicular configuration with $j \parallel a$, shown as gray lines in Fig. 4.22 (a), do not reveal a comparable anomaly at low temperature. This suggests a magnetic origin of the

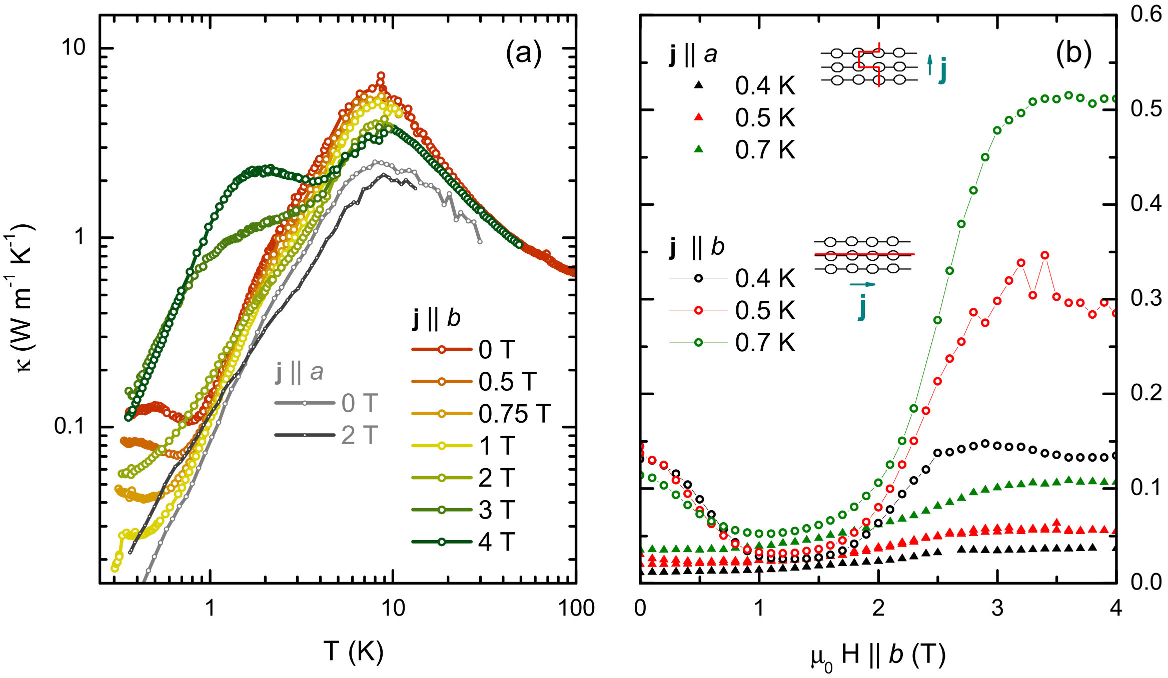

Figure 4.22: Thermal conductivity of Cs_2CoCl_4 as a function of temperature (a) and of magnetic fields (b) applied along the b axis. The heat current is directed along the spin chains, i. e., $\mathbf{j} \parallel b$ (open circles in both panels) and perpendicular to them along a, shown as lines in (a) and with closed triangles in (b).

increased low-temperature heat conductivity. In Cs_2CoCl_4 spin chains run along b, i. e., the direction along which the thermal conductivity is enhanced by a factor of about 10 in comparison to the perpendicular direction. In applied magnetic fields up to 1 T the low-temperature feature is gradually suppressed. The kink at about 320 mK in the data measured at 1 T probably stems from the onset of magnetic order due to the initial enhancement of T_N by small magnetic fields (see Chapter 4.3). The field dependence of κ with the heat current perpendicular to the spin chains is reasonably smaller and up to 2 T only small changes in the low-temperature range are found. Increasing the magnetic field further, besides a slight suppression of the phonon maximum around 10 K, in κ_b another low-temperature contribution arises starting at 2 T that evolves into an additional broad maximum around 1.5 K at 4 T.

The field dependence of κ, shown in Fig. 4.22 (b), consistently reflects the anisotropy of the thermal conductivity in a nearly field-independent κ_a and a more structured field dependence for heat currents $\mathbf{j} \parallel b$. At zero field a conductivity of about 0.1 W m^{-1} K^{-1} is found. Increasing the field, κ_b is continuously reduced and approaches the respective value for $\mathbf{j} \parallel a$ in magnetic fields of approximately 1 T. Up to 2 T the thermal conductivity is almost constant for both heat current directions and only by increasing the field further κ_b increases in form of a broadened step function. At about 3 T a saturation value is reached that increases in absolute value with increasing the temperature. A smaller rise is also seen in κ_a in this field range. In the context of a magnetic heat transport along the spin chains parallel to b, the small field-induced effects for $\mathbf{j} \parallel a$ can be explained either by a small misalignment of the sample, by a possible field dependence

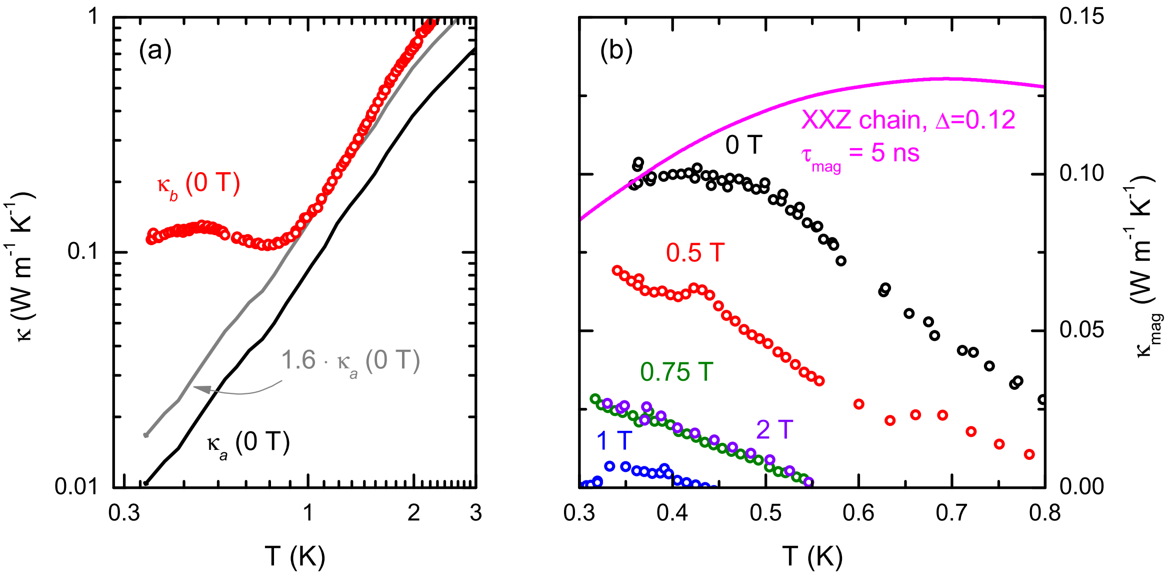

Figure 4.23: Low-temperature part of the thermal conductivity of Cs_2CoCl_4 that shows an additional contribution below 1 K for heat currents along b. By subtracting the scaled temperature dependence for $\mathbf{j} \parallel a$ (gray line), the magnetic heat conductivity $\kappa_{\text{mag}}(T)$ is obtained. The pink line in panel (b) represents the thermal conductivity of the *XXZ* chain using the parameters extracted in Chapter 4.2.2 and a constant scattering time $\tau_{\text{mag}} = 5\,\text{ns}$.

of the phonon-magnon scattering or by percolative processes in the perpendicular heat transport as sketched in Fig. 4.22 (b). The circles connected with lines indicate the spin chains along b, the red line denotes a sketch of a spinon hopping between spin chains with an intermediate propagation of it along the chain, which then could explain the appearance of signatures of κ_b in the data of κ_a.

The strongly anisotropic low-temperature heat transport, seen in both the temperature- and the field-dependent data, suggests a possible magnetic contribution κ_{mag} to the thermal conductivity. As electronic heat transport can be excluded in the insulating Cs_2CoCl_4, only phonons are to be considered as a background. For the temperature-dependent data, the phonon contribution is approximated from the measured κ_a. At temperatures above 1 K, where supposedly κ_{mag} is small, the data of κ_a and κ_b, however, do not agree quantitatively. This may be caused by anisotropic phonon branches and geometry errors. For compensation the data are scaled by a factor a defined by $a \cdot \kappa_a = \kappa_b$ in a temperature range of approximately $1\,\text{K} < T < 4\,\text{K}$. As shown in Fig. 4.23 (a), one obtains a reasonable extrapolation of the background to low temperature, which allows to extract κ_{mag} from the difference of the data. Repeating the process in applied magnetic fields yields an estimate of κ_{mag}, as shown in Fig. 4.23 (b). Due to the uncertainty induced by the extrapolation and the decreasing weight of the magnetic signal in applied magnetic fields, the data above 0.5 T and for $T > 0.7\,\text{K}$ are to be treated with some caution. In zero field a maximum is seen in $\kappa_{\text{mag}}(T)$ at about 0.4 K.

In theory, the thermal conductivity of *XXZ* spin chains is usually considered in terms of the Drude weight of the dynamics of magnetic excitations [131, 132]. Due to a finite zero-frequency weight, the intrinsic heat conductivity of integrable spin chains is expected to diverge [133–136]. In real systems, however, the thermal conductivity becomes finite due to extrinsic scattering. The experimental thermal conductivity κ_{mag} relates to the thermal Drude weight D_{th} via

$$\kappa_{\mathrm{mag}} = D_{\mathrm{th}} \cdot \tau_{\mathrm{mag}} \cdot N_S. \tag{4.12}$$

Here, the factor $N_S = \frac{4}{a \cdot c}$ with the lattice constants a and c takes into account that 4 spin chains running along b contribute per unit cell. The scattering time τ_{mag} relates to the mean free path l_{mag} and the velocity v of the quasiparticles via

$$l_{\mathrm{mag}} = v \cdot \tau_{\mathrm{mag}}. \tag{4.13}$$

At low temperature $T \ll J$ the Drude weight D_{th} approaches a linear temperature dependence [134, 135, 137, 138] and in theory usually is derived with k_{B} set to 1. Converting to the experimental experimental units of $\mathrm{W\,m\,K^{-1}\,s^{-1}}$, one obtains

$$D_{\mathrm{th}} = \frac{(\pi k_{\mathrm{B}})^2}{3\hbar} vT, \tag{4.14}$$

where v is the spinon velocity. In the present temperature range of $\kappa_{\mathrm{mag}}(T)$, however, the low-temperature limit is not fulfilled and the full temperature dependence of D_{th} has to be considered instead. In Refs. 134 and 137 the Drude weight $D_{\mathrm{th}}(T/J)$ is calculated for selected values of the anisotropy Δ. Using the established values of the primary coupling constant $J/k_{\mathrm{B}} \approx 3\,\mathrm{K}$ and of the anisotropy $\Delta \approx 0.12$ from literature [3, 139] and from Chapter 4.2.2, one obtains the expected temperature dependence of $\kappa_{\mathrm{mag}} \propto D_{\mathrm{th}}$. As described by Eqn. (4.12), the absolute value of the thermal conductivity additionally is proportional to the relaxation time τ_{mag}, which is not known a priori and depends on the contributing scattering mechanisms. First, a constant value $\tau_{\mathrm{mag}} = 5\,\mathrm{ns}$ is chosen such that the experimental zero-field data $\kappa_{\mathrm{mag}}^{\mathrm{exp}}$ at the lowest temperature of about 0.3 K are matched. The resulting thermal conductivity $\kappa_{\mathrm{mag}} = D_{\mathrm{th}}\,\tau_{\mathrm{mag}}\,N_S$ of the *XXZ* spin chain is shown as a solid line in Fig. 4.23 (b).

The clear disagreement of the peak position and the overall shape does not exclude the presence of magnetic heat transport, but suggests that it is strongly influenced by effects beyond the pure *XXZ* model. One explanation could be given by the influence of interchain interactions on the heat transport. Small perturbations like interactions between chains are known to significantly affect the heat conductivity in spin-$1/2$ Heisenberg models [140, 141]. However, no theory results for the present case of $T \lesssim J$ are available. Another interpretation of the deviations of the experimental κ_{mag} from the expectations can be given by considering external scattering mechanisms. The theory result solely concerns the intrinsic properties of the spin chain via the calculation of the finite-temperature Drude weights. Extrinsic scattering of magnons with phonons and/or with defects may become dominant with increasing temperature and explains the observed deviation from the intrinsic thermal conductivity of the spin chain. In analogy to the analysis of some cuprate spin-$1/2$ chains that show an extraordinarily large magnetic contribution to the heat transport [142–145], the temperature depen-

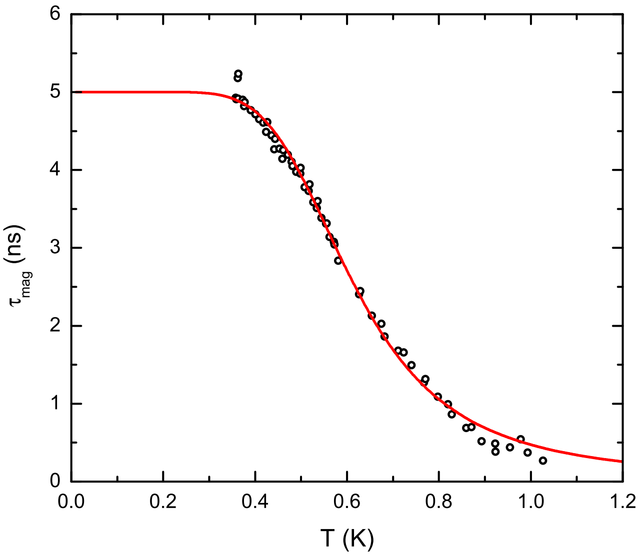

Figure 4.24: Relaxation time τ_{mag} extracted from the thermal conductivity of Cs_2CoCl_4 at zero field based on the Drude weight of the *XXZ* spin chain. The solid line represents a fit of Eqn. (4.16) to the data.

dence of the relaxation time τ_{mag} of the magnetic excitations can be derived from the experimental data $\kappa_{\text{mag}}^{\text{exp}}$ via

$$\tau_{\text{mag}} = \frac{\pi\,\kappa_{\text{mag}}^{\text{exp}}}{N_S\,D_{\text{th}}}. \tag{4.15}$$

In this context usually the mean free path is discussed, which relates to τ_{mag} via the spinon velocity v. However, v is a property of the linear low-temperature regime, which is left here. Thus, the scattering time τ_{mag} is analyzed instead of the mean free path in the following.

In Fig. 4.24 the resulting relaxation time is shown as extracted from the zero-field data of κ_{mag}. At low temperature ($T \lesssim 0.5\,\text{K}$) a relaxation time of few nanoseconds is found. While for low temperature the data show a slight tendency towards a saturation, τ_{mag} is strongly reduced by increasing the temperature and tends towards zero for $T \gtrsim 1\,\text{K}$. In other systems a similar dependence of the mean free path is found and a low-temperature saturation is explained by defect scattering, while the suppression with increasing temperature is attributed to umklapp scattering with phonons [142–147]. Considering these two effects, according to Matthiesen's rule τ_{mag} can be decomposed into a temperature independent defect scattering time τ_0 and a temperature dependent term describing the scattering with phonons [53, 148],

$$\tau_{\text{mag}}^{-1} = \tau_0^{-1} + \left(\frac{e^{T^*/T}}{AT}\right)^{-1}. \tag{4.16}$$

The solid line in Fig. 4.24 represents a fit of Eqn. (4.16) to the $\tau_{\text{mag}}(T)$ data. It yields a reasonable description using the parameters

$$\tau_0 = 5.0\,\text{ns}, \quad T^*/k_{\text{B}} = 2.9\,\text{K}, \quad A = 3.4 \times 10^{10}\,\text{K}^{-1}\,\text{s}^{-1}. \tag{4.17}$$

The low-temperature defect contribution τ_0 can be related to the mean free path of spinons at low temperature by using Eqn. (4.13) and the spinon velocity v. In the limit of $k_{\mathrm{B}}T \ll J$, which is fulfilled for the defect scattering, only spinons in a small region of the Brillouin zone contribute and the spinon velocity,

$$v = \frac{b}{\hbar}\frac{\pi}{2}J\,\frac{\sin\arccos\Delta}{\arccos\Delta}, \tag{4.18}$$

is a constant [138, 142, 147]. Here $b = 7.313\,\text{Å}$ is the lattice constant along the chain direction and Δ is the anisotropy of the spin chain. The obtained defect contribution to the mean free path,

$$l_0 = 1.5\,\mu\mathrm{m}, \tag{4.19}$$

is in a common range, yet about twice as large as observed in other spin chain systems with magnetic heat transport [145–147]. This suggests a rather low defect concentration in the samples. Dividing by the nearest neighbor distance, i. e., the lattice constant of the b axis, along which spin chains run, yields a scattering length of about 2000 unit cells.

The temperature T^* is the characteristic temperature of the phonon system, where umklapp scattering arises, and typically lies in the range of the Debye temperature Θ_{D}. In $\mathrm{Cs_2CoCl_4}$ a Debye temperature of about 70 K was found [3, 4, 93]. Yet, the fit results in a significantly smaller value of about 3 K. Even though the temperature-dependent suppression of the intrinsic thermal conductivity is explained by the model, one still may question the phononic origin of the scattering due to the mismatch of Θ_{D} and T^*. Another possible scattering mechanism is given by the excited crystal field states of $\mathrm{Cs_2CoCl_4}$. The crystal field anisotropy $\mathcal{D} \approx 7\,\mathrm{K}$ in fact is much closer to the characteristic temperature T^*. At present, however, no expression for the respective contribution to the mean free path is available to quantify the influence of the spin-$^3/_2$ states on the thermal conductivity. A calculation of the Drude weight of the spin-$^3/_2$ chain with an out-of-plane anisotropy could give further insight.

In applied magnetic fields, an overall suppression of κ_{mag} to lower absolute values, respectively a shift to lower temperature is observed, shown in Fig. 4.23 (b). As presently no calculations of the *XXZ* model's Drude weight in transverse magnetic fields are available, these data cannot be analyzed in analogy to the zero-field thermal conductivity. At 1 T, essentially no magnetic contribution is found on top of the phonon background. Increasing the field further, at 2 T a new signal arises that by coincidence lies close to the 0.75 T data. The high-field increase, yet, is better analyzed from the field-dependent data. Here, the magnetic heat transport is approximated simply from the difference of the thermal conductivities measured with different directions of the heat current, $\kappa_{\mathrm{mag}} = \kappa_b - \kappa_a$. As shown in Fig. 4.25 (a), the magnetic contribution closely resembles κ_b. The finite zero-field conductivity is suppressed by a field of about 1 T and the rise at 2 T, seen above in the temperature dependence becomes more pronounced with increasing temperature. In the inset the field dependence of the magnetic specific heat is shown for two exemplary temperatures of 0.4 K and 0.5 K. It is interpolated from the temperature-dependent data $c_p(T)$ presented above for various fields along b by

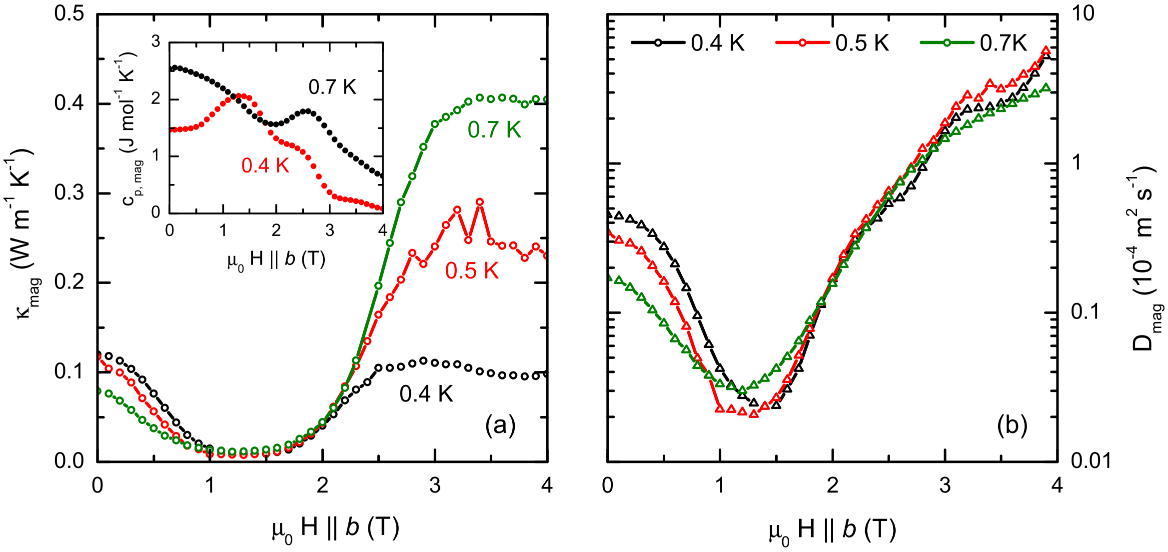

Figure 4.25: Field dependence of the magnetic contribution to the thermal conductivity $\kappa_{\mathrm{mag}}(H)$ of $\mathrm{Cs_2CoCl_4}$ at low temperature $T < 2\,\mathrm{K}$ (a) estimated from the anisotropy of κ. The diffusion constant $D = \kappa/c_p$, shown in (b), is calculated based on the field dependence of the specific heat, shown in the inset of (a), which is interpolated from the temperature-dependent data presented above.

subtracting the non-magnetic contributions (cf. Chapter 4.2.2). Although this process involves a certain error, it allows to estimate the magnetic diffusion coefficient D_{mag},

$$D_{\mathrm{mag}} = \frac{\kappa_{\mathrm{mag}}}{c_{\mathrm{mag}}}. \tag{4.20}$$

In the kinetic gas theory the diffusion coefficient D relates to the mean velocity v and the mean free path l of the heat-conducting particles via $D = v\,l$ and thus can be understood as the mobility of the particles. In Fig. 4.25 (b) the field dependence of D_{mag} is shown. While in the low-field regime the suppression of κ_{mag} is accompanied by an analogous reduction of D_{mag}, interestingly above 2 T the data for the different temperatures concurrently increase by about one order of magnitude. This indicates a strongly increasing mobility at high fields that in comparison to the low-field region only weakly depends on temperature.

Summarizing, the field- and temperature-dependent thermal conductivity can be interpreted as follows. At zero field extrinsic scattering mechanisms lead to a reduction of κ_{mag}. In addition to defect scattering, characterized by a mean free path $l_0 = 1.5\,\mu\mathrm{m}$, a second scattering mechanism with a characteristic energy scale of about 3 K contributes. Applying a magnetic field within the easy plane of spins leads to a suppression of κ_{mag}. This reduction can be understood as an intrinsic property of the spin chain arising from the opening of a gap in the magnon dispersion by the transverse magnetic field. At a field of about 1 T no indication for a magnetic contribution to κ is found. Further increasing the field, the gap in the magnon dispersion becomes again smaller and at the critical field of about 2 T excitations are gapless like in zero field. One may, thus, expect a maximum of κ_{mag} around the critical field and a reduction for larger fields due to the increasing spin gap. The experimental data show a rise of κ_b, but in contrast to the expectation not at the critical field, but for fields $H > 2\,\mathrm{T}$, i. e., larger than the critical field. A simple explanation of the high-field thermal conductivity in terms of an increased phonon contribution due to the suppression of magnon-phonon scattering can be ruled out from the anisotropy of κ also in this field range. Instead, the data suggest a magnetic origin of the field dependence. Due to the lack of theory results on the intrinsic properties of the *XXZ* spin chain in a transverse magnetic field, the true origin, however, cannot be clarified at present. From the indications for a low-energy scattering mechanism, maybe due to excited crystal field states, in the zero-field data, a field-induced contribution of the spin-$^3\!/_2$ states might consistently explain the rise of κ and of the diffusion coefficient D_{mag} above $2\,\mathrm{T}$. A quantification of this suggestion requires a calculation of the dynamical properties of a spin-$^3\!/_2$ chain in a transverse magnetic field.

4.2.2 Comparison to the 1D *XXZ* model

Fixed anisotropy $J_z/J_{xy} = {}^1\!/_4$

In previous studies the magnetic specific heat and the susceptibility of $\mathrm{Cs_2CoCl_4}$ was compared to the *XXZ* model assuming an anisotropy of the magnetic exchange $\Delta = J_z/J_{xy} = {}^1\!/_4$. In this chapter, it will be shown that fitting the whole magnetic field dependence of the specific heat and the thermal expansion, assuming this very same anisotropy, leads to inconsistencies that can be resolved only by extending the theoretical description to higher-order effects and relaxing the assumption of $\Delta = {}^1\!/_4$.

In analogy to the discussion in Ref.3, three main contributions to the total heat capacity can be identified in the data (Fig. 4.26). At temperatures above $\simeq 10\,\mathrm{K}$ the specific heat is dominated by phonons. The data can be described phenomenologically by a Debye model using a Debye temperature Θ_{D} and a scaling factor a_D,

$$c_v = a_D \cdot 9R\left(\frac{T}{\Theta_D}\right)^3 \int\limits_0^{\Theta_{\mathrm{D}}/T} \frac{x^4 e^x}{\left(e^x-1\right)^2}\,dx, \qquad R = N_{\mathrm{A}} k_{\mathrm{B}}. \tag{4.21}$$

Although in the analyzed temperature range up to $30\,\mathrm{K}$ optical phonons might contribute as well and, thus, the Debye model might be over-simplified to describe the data, the very choice of the phonon background affects only marginally the determination of the low-temperature (magnetic) contributions. Even in the simplest approximation of a T^3-dependence, as done in Ref. 3, the phonon heat capacity c_{ph} is lower than the other contributions by at least one order of magnitude or even fully negligible below $\simeq 2\,\mathrm{K}$. It rather provides a smooth background for the fitting of the second contribution: the higher-lying $|S_z = \pm{}^3\!/_2\rangle$ doublet state leads to a Schottky contribution around $5\,\mathrm{K}$ on top of the phonon heat capacity. The specific heat of a corresponding system with two equally degenerate energy levels separated by an energy gap $\Delta E = 2\mathcal{D}$, where $\mathcal{D}$ is the crystal field anisotropy, is given by

$$c_{\mathrm{Schottky}} = R\left(\frac{\Delta E}{k_{\mathrm{B}}T}\right)^2 \frac{e^{\Delta E/k_{\mathrm{B}}T}}{\left(1+e^{\Delta E/k_{\mathrm{B}}T}\right)^2}. \tag{4.22}$$

In the limit of low temperature ($T \ll \Delta E$) the specific heat c_{Schottky} is small due to the dominating exponential terms. At higher temperature ($T \gtrsim \Delta E$) it approaches a square dependence $c_{\mathrm{Schottky}} \propto T^{-2}$. In Fig. 4.26 the temperature dependence is shown as blue dashed-dotted line for $\Delta E = 13.9\,\mathrm{K}$ as extracted from the data in the further analysis below. Up to about 6 K, c_{Schottky} exceeds the phonon heat capacity and, due to the broad high-temperature tail, remains sizable up to $T \approx \Delta E$. The difference between the measured data c_p and the latter two contributions is attributed to the magnetic specific heat

$$c_{\mathrm{mag}} = c_p - (c_{\mathrm{ph}} + c_{\mathrm{Schottky}}). \tag{4.23}$$

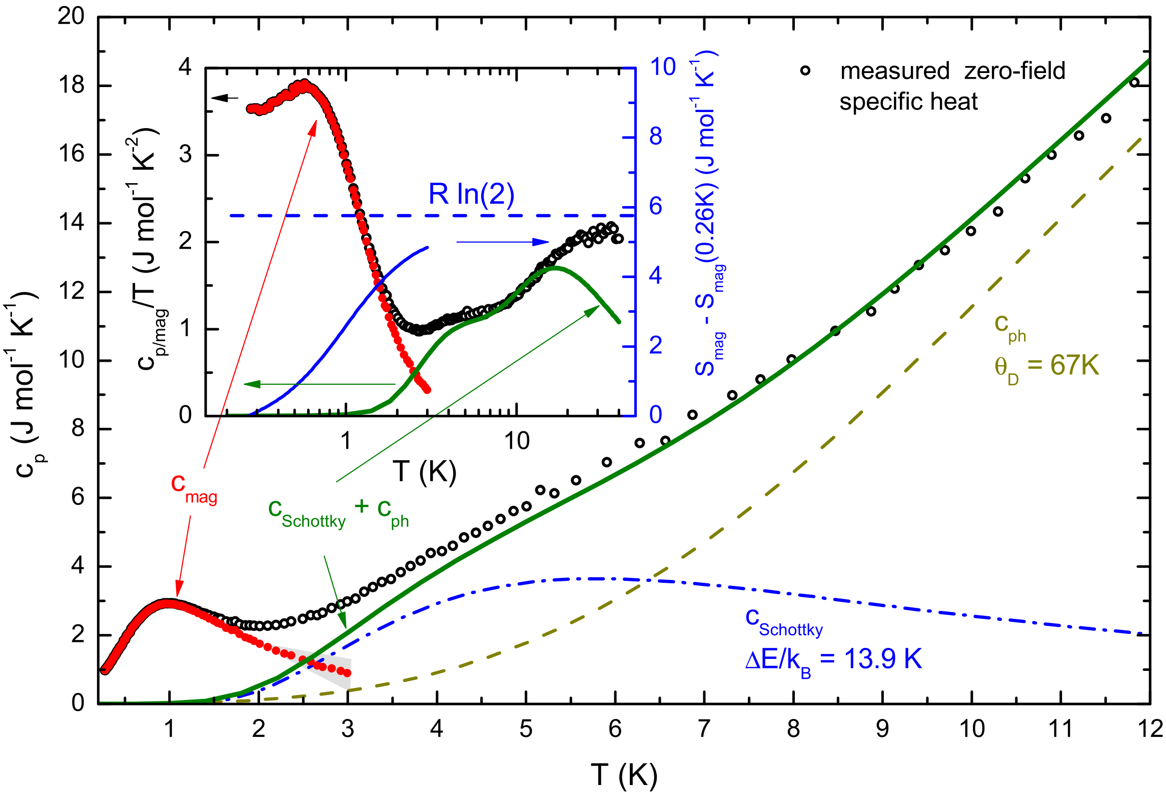

Figure 4.26: Contributions to the heat capacity of $\mathrm{Cs_2CoCl_4}$: (i) phonons (c_{ph}, yellow dashed line) dominating at $T \gtrsim 5\,\mathrm{K}$ as approximated by the Debye model; (ii) thermal population of the second Kramers doublet giving rise to a Schottky anomaly (c_{Schottky}, blue dashed-dotted line) around 5 K and (iii) the magnetic heat capacity c_{mag} (closed red symbols) as obtained by subtracting $c_{\mathrm{ph}} + c_{\mathrm{Schottky}}$ from the data. The shaded area marks the approximate error in the determination of c_{mag}. In the inset the measured data, the non-magnetic background and the extracted magnetic heat capacity is shown as c/T versus temperature together with the magnetic entropy $S_{\mathrm{mag}} = \int \frac{c_{\mathrm{mag}}}{T} dT$ (blue line, right scale).

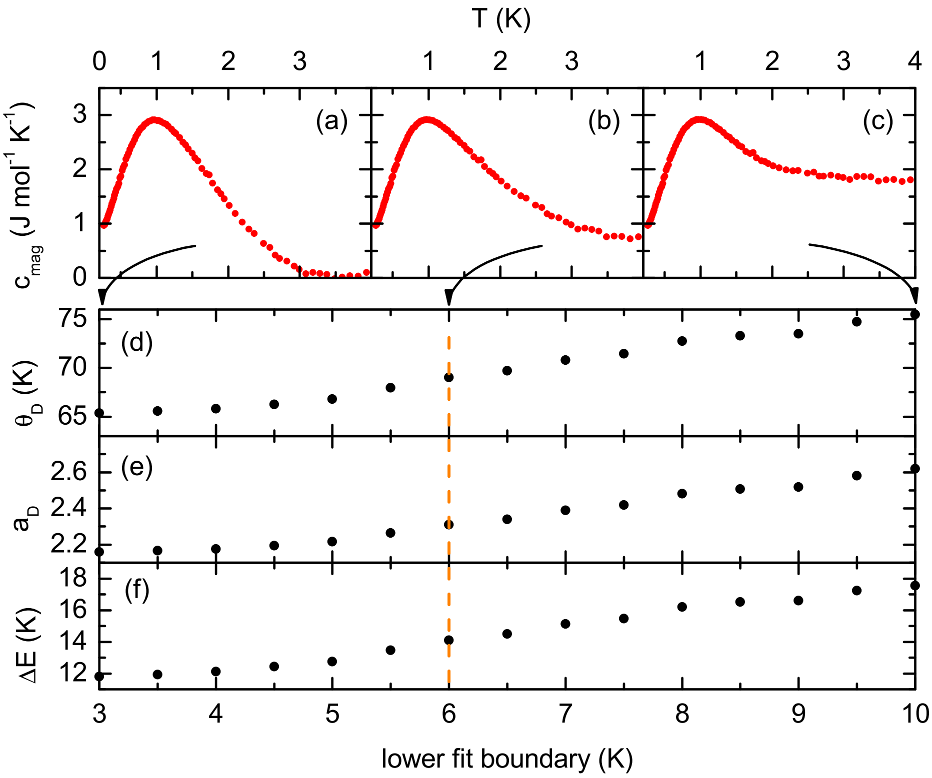

Figure 4.27: Three exemplary magnetic heat capacities c_{mag} (a-c) resulting from the parameters θ_D and a_D of the Debye model and from the energy gap ΔE. The parameters were obtained by fitting $c_\mathrm{ph} + c_\mathrm{Schottky}$ to the data as a function of the lower fit boundary (d-e). The upper fit boundary was fixed to 15 K. The dashed line marks the values used for the determination of c_mag as shown in Fig. 4.26.

Close to the maximum around 1 K it is nearly unaffected by the choice of the non-magnetic background. The "high-temperature" tail of the magnetic heat capacity above 2 K, however, is difficult to quantify due to the strongly increasing specific heat of the Schottky anomaly. Here, small changes of ΔE lead to a similar description of the non-magnetic heat capacity at $T \gg 2$ K, but to a more pronounced change of c_mag. In Fig. 4.27 the parameters $\theta_\mathrm{D}, a_\mathrm{D}, \Delta E$ and three selected calculated magnetic heat capacities c_mag are shown as obtained by fitting $c_\mathrm{ph} + c_\mathrm{Schottky}$ to the data in a restricted temperature range. The upper fit range was fixed to 15 K. This temperature was selected due to the decreasing data quality above this temperature and the increasing uncertainties introduced by applying the Debye model at temperatures where the simplifications of the model do not hold any more. The lower fit boundary varied from 3 K to 10 K. All fitted parameters significantly depend on the chosen fit boundary. In consequence, different magnetic heat capacities are obtained as shown for three different boundaries in Fig. 4.27 (a-c). Choosing a low fit boundary of 3 K leads to a substantial influence of the broad maximum around 1 K on the Schottky anomaly resulting in a rapid drop of c_mag above 2 K. In contrary a high fit boundary of 10 K (Fig. 4.27 (c)) neglects the largest part of the hump around 5 K and leads to an overestimate magnetic heat capacity that is almost constant above 2 K. Reasonable boundaries are to be found in between. A moderate temperature of 6 K as used in Fig. 4.27 (b) seems

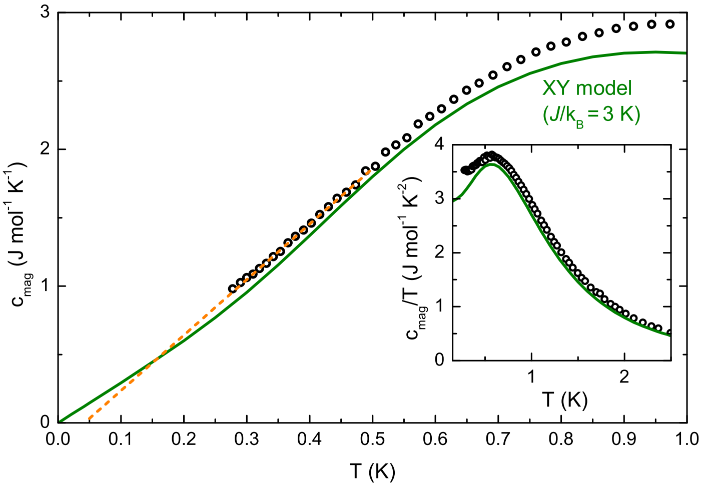

Figure 4.28: Low-temperature tail of the specific heat of Cs_2CoCl_4 above T_N (open symbols) in comparison to exact results for the *XY* model (solid line). The negative y-intercept of the extrapolation of the data (dashed line) and the kink in the calculation reveals that the asymptotic linear temperature dependence of c_p is not realized above T_N.

appropriate to include data points that inherit valuable information on ΔE, but not on the to-be-extracted magnetic heat capacity itself and leads to

$$\Delta E = 13.9\,\mathrm{K}, \quad a_D = 2.2, \quad \Theta_\mathrm{D} = 67\,\mathrm{K}. \tag{4.24}$$

The resulting magnetic heat capacity, as shown in Fig. 4.26, coincides with the measured data around 1 K. Above 3 K, the error by subtracting non-magnetic contributions (approximately indicated by the gray shaded area) becomes too large to extract meaningful values for c_mag. Plotting c_mag/T (inset of Fig. 4.26) a constant value seems to be approached at low temperature, $c_\mathrm{mag}/T \approx 3.5\,\mathrm{J\,mol^{-1}\,K^{-2}}$ for $T \to 0$. One might be tempted to infer a linear temperature dependence of the specific heat data below $\lesssim 0.5$ K as is in fact expected in the low-temperature limit ($T \ll J$) of the antiferromagnetic spin-chain models with an easy-plane anisotropy,

$$\frac{C}{R} = A\frac{k_\mathrm{B}T}{J}. \tag{4.25}$$

Here, the slope $A = \frac{2}{3}\frac{\arccos(\Delta)}{\sqrt{1-\Delta^2}}$ depends on the anisotropy $\Delta < 1$. The value of A ranges from $A_{xy} = \pi/3 \approx 1.05$ in case of the *XY* model ($\Delta = 0$) to $A_\mathrm{H} = 2/3$ for the Heisenberg model [130]. From the experimental slope, the coupling constant J could be derived. However, the easy-plane type models show peculiarities in thermodynamic properties even at very low temperature, e. g., due to significant low-temperature corrections in the Heisenberg model [42, 44, 45]. Thus, Eqn. (4.25) only applies to the data at very low temperature ($T/J < 0.1$), which is a prerequisite that might be questioned here. Exact solutions that extend to these temperatures are available only for the *XY* model [50] and for the Heisenberg model [46]. In Fig. 4.28 the data are plotted together with the specific heat of the *XY* model using an exchange constant $J = 3$ K as adopted from literature and close to the value derived below. Despite slight deviations from the data, probably due to the "wrong" anisotropy, the true low-temperature linearity of c_p sets in just below the experimental data. In the plot of c_{mag}/T (inset of Fig. 4.28) this is reflected in significantly suppressed values for the calculation below ≈ 0.5 K. Therefore, the limit of $T \ll J$ is not fulfilled for the experimental data $\gtrsim 0.3$ K and the coupling constant cannot be derived via Eqn. (4.25). Extrapolating the experimental data (dashed orange line) furthermore yields a negative y-intercept, which additionally argues against a true linear temperature dependence of c_p and shows that the low-temperature limit is not realized in the experiment.

Integrating c_{mag}/T gives the entropy gain of the magnetic system $S_{\mathrm{mag}}(T)-S_{\mathrm{mag}}(0.26\,\mathrm{K})$, (blue line, right axis in Fig. 4.26). The expected value of $R\ln 2$ of a spin-$1/2$ system is not obtained within the experimental range. Nevertheless, a further gain of the missing entropy can be expected first at lower temperature and second due to the fact that $S_{\mathrm{mag}}(T)$ is not saturated at 3 K. The deviation of $c_{\mathrm{Schottky}} + c_{\mathrm{ph}}$ (green line in Fig. 4.26) from the data above 20 K illustrates that the applied phonon model is purely phenomenological and that the obtained parameters should not be regarded as sample properties.

Summarizing, the non-magnetic contributions to the heat capacity could be well separated and despite some uncertainties above 2 K the magnetic heat capacity can be deduced quite reliably from $c_{\mathrm{mag}} = c_p - c_{\mathrm{Schottky}} - c_{\mathrm{ph}}$. In analogy to Ref. 3 the magnetic heat capacity is now compared to the XXZ model,

$$\mathcal{H}_{XXZ} = \sum_i \left[J_{xy} \left(S_x^i S_x^{i+1} + S_y^i S_y^{i+1} \right) + J_z S_z^i S_z^{i+1} - g\mu_{\mathrm{B}}\mu_0 H_b S_x^i \right] . \tag{4.26}$$

Exact diagonalization of $\mathcal{H}_{XXZ}$ was performed using the ALPS code [57]. For spin-$1/2$ systems with arbitrary on-site and interaction terms approximately 4 GB of memory suffice to solve a system consisting of 16 sites. Thus, the calculations can be performed using a standard desktop computer. Increasing the system size leads to an exponential growth of the memory consumption. Therefore, they cannot be analyzed using this code and require more sophisticated methods. At zero field the model reveals a rotational symmetry and S_z is preserved. Using this symmetry, the calculations can be extended to system size of up to $L = 18$ sites at zero field. In all calculations, periodic boundary conditions were used. First, the onset of finite-size effects at low temperature was analyzed by calculating the thermodynamic quantities for various system sizes (cf. Chapter 2.3). Finite size effects are negligible in the temperature range of interest here.

In Fig. 4.29 (a) the calculated zero-field heat capacity c_{XXZ} is shown as a function of the reduced temperature T/J for different values of the anisotropy $\Delta = J_z/J_{xy} = 0, 0.25, 0.5, 1.0$. With increasing Δ the curves shift to higher temperature and increase in their maximum value while essentially preserving their general shape. Finite size effects are negligible above $T/J \gtrsim 0.1$, which approximately corresponds to the magnetic order temperature $T_N/J \approx 0.3/3$, below which the model is not appropriate anyway. In Fig. 4.29 (b) the calculated specific heat is shown together with the extracted magnetic heat capacity c_{mag}. By adjusting the coupling constant J, the overall shape and the peak position of the experimental data around 1 K can be described using any of the anisotropies. The peak height, however, is determined by Δ and the best match is obtained for $\Delta = 1$, which would correspond to the special case of the Heisenberg model. This correspondence is misleading and $\Delta = 1$ can certainly be excluded. Because in the Heisenberg limit, no magnetic anisotropy would be present and, thus, the Co^{2+} spin $S = 3/2$ would not be split, which in turn would lead to a completely different

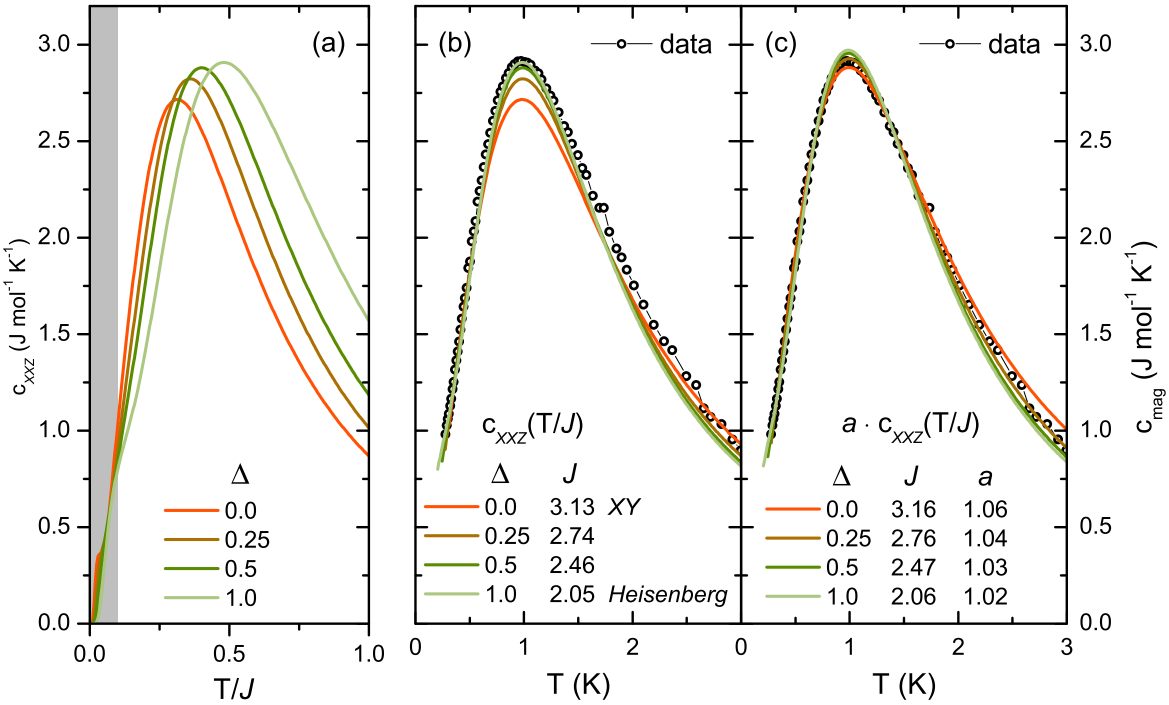

Figure 4.29: Exact diagonalization results (a) of the *XXZ* model, given by Eqn. (4.26), for finite rings of up to 18 spins assuming different values of the anisotropy $\Delta = J_z/J_{xy}$. The onset of finite size effects is indicated as a shaded gray area. In (b) the calculations are compared to the magnetic heat capacity (open symbols) by adjusting the coupling constant J. In (c) an additional scaling factor a is included.

scenario where the effective spin-$1/2$ system was not applicable at all. Instead, the resulting Δ rather depends severely on the measured absolute value of the heat-capacity peak. Therefore, an additional scaling factor was allowed to compensate for the experimental uncertainty which is typically in a range of a few percent. In Fig. 4.29 (c) the fit results and parameters are shown including a scaling factor a. For all anisotropies the data are reproduced in the whole temperature range. The strong resemblance of all fits shows that Δ cannot be unambiguously extracted from the magnetic heat capacity. An anisotropy $\Delta = 1/4$ is expected from theory in the limit of a strong crystal field anisotropy (see Chapter 4.1.2) and in literature this value was taken for granted. The present comparison to various anisotropies, however, shows that this assumption is not justified upon considering the specific heat, only. Nevertheless, assuming the anisotropy $\Delta = 1/4$ as in literature, the specific heat can indeed be described using the parameters

$$J_{xy}/k_\mathrm{B} = \Delta^{-1} J_z/k_\mathrm{B} = 2.76\,\mathrm{K}, \quad a = 1.03, \quad \Delta E = 13.9\,\mathrm{K}.$$

These values are close to those reported in literature [3, 4]. However, this simply shows that under the assumption of $\Delta = 1/4$ a description of c_{mag} is obtained that is consistent with literature. Using strongly different models and coupling constants, an almost identical description of the data is possible as well.

Thermal expansion

Next, the thermal expansion α_b (abbreviated as α in the following) along the b axis is considered. It relates to the free energy $\mathcal{F}$ of the system via $\alpha = \frac{1}{NV_S}\frac{\partial^2\mathcal{F}}{\partial p_b \partial T}$, where N is the number of sites in the calculation and V_S the volume per spin. Excluding interactions between the subsystems, the free energy can be approximated as a sum $\mathcal{F} = \mathcal{F}_{\mathrm{ph}}(\Theta_D) + \mathcal{F}_{\mathrm{Schottky}}(\Delta E) + \mathcal{F}_{XXZ}(J_{xy}, J_z)$ of independent potentials that depend on different energy scales Θ_D, ΔE and $J_{xy,z}$. Thus, the thermal expansion also linearly decomposes into $\alpha = \alpha_{\mathrm{ph}} + \alpha_{\mathrm{Schottky}} + \alpha_{XXZ}$. The phonon free energy $\mathcal{F}_{\mathrm{ph}}$ and the Schottky anomaly as described by $\mathcal{F}_{\mathrm{Schottky}}$ both depend only on a single energy scale and, thus, the Grüneisen relations

$$\begin{aligned} \alpha_{\mathrm{ph}}/c_{\mathrm{ph}} &= (1/V_m)\frac{\partial \ln \Theta_D}{\partial p_b}, && (4.27)\\ \alpha_{\mathrm{Schottky}}/c_{\mathrm{Schottky}} &= (1/V_m)\frac{\partial \ln \Delta E}{\partial p_b}, && (4.28) \end{aligned}$$

are obeyed with the molar volume $V_m = N_{\mathrm{A}} V_s$ and the volume $V_S = 235\,\mathrm{\AA}$ per spin, as obtained by dividing the unit cell volume by the number of spins per unit cell. As the *XXZ* model's free energy depends already at zero field on the two coupling constants J_{xy} and J_z, the Grüneisen scaling does not hold for the magnetic subsystem. Considering magnetoelastic interactions on a mean-field level the pressure dependence of the energy scales, on which the thermodynamic potential depends (i. e., the coupling constants J_{xy}, J_z and the electronic g factor), enter the theoretical description as shown in Chapter 2.3.3 and in Refs. 77, 78. Thus, the thermal expansion of the *XXZ* chain is given by the second derivatives of the free energy with respect to the temperature and to J_{xy}, J_z and g, scaled by the respective pressure dependences,

$$V_m \cdot \alpha_{XXZ} = \left(\frac{\partial^2 \mathcal{F}_{XXZ}}{\partial T \partial J_{xy}}\right)\frac{\partial J_{xy}}{\partial p_b} + \left(\frac{\partial^2 \mathcal{F}_{XXZ}}{\partial T \partial J_z}\right)\frac{\partial J_z}{\partial p_b} + \left(\frac{\partial^2 \mathcal{F}_{XXZ}}{\partial T \partial g}\right)\frac{\partial g}{\partial p_b}. \tag{4.29}$$

The parenthesized terms can be identified with the temperature derivatives of the spin-spin correlators

$$\begin{aligned} \frac{\partial^2 \mathcal{F}_{XXZ}}{\partial T \partial J_{xy}} &= \frac{1}{NV_S}\frac{\partial}{\partial T}\sum_i \langle S_x^i S_x^{i+1} + S_y^i S_y^{i+1}\rangle\,, && (4.30)\\ \frac{\partial^2 \mathcal{F}_{XXZ}}{\partial T \partial J_z} &= \frac{1}{NV_S}\frac{\partial}{\partial T}\sum_i \langle S_z^i S_z^{i+1}\rangle\,, && (4.31)\\ \frac{\partial^2 \mathcal{F}_{XXZ}}{\partial T \partial g} &= -\frac{\mu_0 \mu_{\mathrm{B}} H_b}{NV_S}\frac{\partial}{\partial T}\sum_i^N \langle S_x^i\rangle, && (4.32) \end{aligned}$$

and were obtained numerically by performing exact diagonalization of $\mathcal{H}_{XXZ}$ with $J = 1 = J_{xy} = \Delta^{-1} J_z$ using the ALPS code [57] and assuming the literature value of $\Delta = 1/4$. The last term (4.32) is proportional to the T-derivative of the magnetization along x times the magnetic field and, thus, only contributes for $H_b \neq 0$. Repeating the calculation for $J_{xy} \to J_{xy} + \epsilon$ and for $J_z \to J_z + \epsilon$, where ϵ is a sufficiently small number, the difference quotient can be calculated. The temperature derivative is then performed numerically from the interpolation of the temperature dependence which can be extracted with arbitrary precision from the diagonalization results.

The absolute value of the calculated bond correlator $\langle S_z^i S_z^{i+1} \rangle$ of the z component of the spin, shown in Fig. 4.30 (a), is smaller than that of the x and y components by about a factor of three which is due to the easy-plane anisotropy and the fact that two correlators contribute to $\langle S_x^i S_x^{i+1} + S_y^i S_y^{i+1} \rangle$. As expected, both correlators tend to zero at high temperature and increase in absolute value with decreasing temperature. The negative signs arise from the antiferromagnetic interaction. The data are shown down to $T/J = 0.1$, where finite-size effects set in. In case of long-range order a value of $-1/4$ would be expected for a single correlator, respectively $-1/2$ for the sum of two. These values are not achieved as the one-dimensional XXZ model does not show long-range order. The S_z correlator of spins in the ground state is known to be -0.101 for the XY model from the exact result by Katsura (indicated by a red line) [50]. The present correlation slightly exceeds this value, which is plausible due to the finite coupling of the S_z components of the spin in case of the assumed anisotropy $J_z/J_{xy} = 1/4$. In Fig. 4.30 (b) the temperature derivatives of the bond correlators are shown. Scaled by the respective pressure dependence of the coupling constant J_{xy}, respectively J_z, their sum forms the magnetic contribution α_{XXZ} to the thermal expansion. Although the derivative of the S_z correlator is smaller than that of the S_x and S_y correlator, the shape of both curves is very similar. They only differ in their high-temperature tail, opening the possibility to identify their individual contribution to α_{XXZ}.

In the fit of the data by α_{XXZ} the coupling constant was fixed to $J = 2.76\,\mathrm{K}$ and the Debye temperature to $\Theta_\mathrm{D} = 67\,\mathrm{K}$ as previously determined from the specific heat. Given that $\Delta = 1/4$, the peak position of c_p directly fixes J with a higher precision than the thermal expansion. The experimental zero-field data (obtained with increasing temperature) are fitted by

$$\begin{aligned}\alpha &= \alpha_\mathrm{ph} + \alpha_\mathrm{Schottky} + \alpha_{XXZ} \\ &= V_m^{-1}\left(c_\mathrm{ph}\frac{\partial \ln\Theta_D}{\partial p_b} + c_\mathrm{Schottky}\frac{\partial \ln \Delta E}{\partial p_b}\right) + \left(\frac{\partial^2 \mathcal{F}_{XXZ}}{\partial T \partial J_{xy}}\right)\frac{\partial J_{xy}}{\partial p_b} + \left(\frac{\partial^2 \mathcal{F}_{XXZ}}{\partial T \partial J_z}\right)\frac{\partial J_z}{\partial p_b},\end{aligned} \tag{4.33}$$

which leads to

$$\Delta E/k_\mathrm{B} = 15.7\,\mathrm{K}, \qquad \frac{\partial \Delta E}{\partial p_b} = -1.1\,\mathrm{K\,GPa^{-1}}, \qquad \frac{\partial \Theta_D}{\partial p_b} = 2.7\,\mathrm{K\,GPa^{-1}} \tag{4.34}$$

$$\frac{\partial J_{xy}}{\partial p_b} = 0.2\,\mathrm{K\,GPa^{-1}}, \qquad \frac{\partial J_z}{\partial p_b} = 1.2\,\mathrm{K\,GPa^{-1}}. \tag{4.35}$$

In Fig. 4.30 (c) the different contributions are shown separately. The phonon background (dashed yellow line) is much smaller than in the specific heat due to a small pressure dependence of the Debye temperature. The Schottky anomaly around 5 K, here, is of opposite sign than in the specific heat (dashed-dotted line) due to the negative pressure dependence of ΔE, which reduces by $\approx 1\,\mathrm{K}$ per applied pressure of 1 GPa.

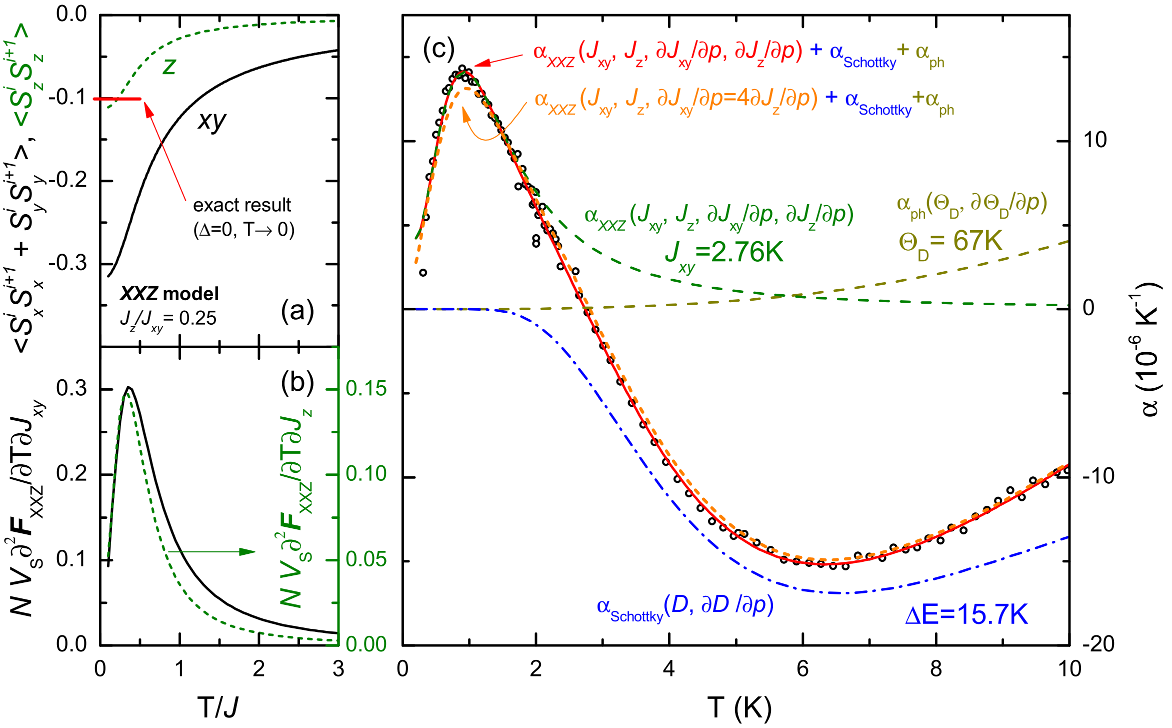

Figure 4.30: (a) Bond correlators of the different spin components for the XXZ model ($\Delta = 1/4$, $H_b = 0$) calculated by exact diagonalization for 16 sites using periodic boundary conditions. Panel (b) shows the temperature derivatives that - scaled by the respective pressure dependence of J_* - contribute to the thermal expansion of the one-dimensional model. (c) The thermal expansion coefficient measured with increasing temperature is fitted by a sum of the phonon contribution α_{ph} (yellow dashed line), the Schottky contribution α_{Schottky} (blue dashed-dotted line) and the magnetic contribution α_{XXZ} (dashed green line). The solid red line shows the sum of these contributions using the parameters given in (4.34). Fixing $\partial_{p_b} J_{xy} = 4\partial_{p_b} J_z$ causes some deviation from the maximum around 1 K (dashed orange line).

The thermal expansion of the one-dimensional magnetism around 1 K is treated using two different approaches. First, both pressure dependencies $\partial_{p_b} J_z$ and $\partial_{p_b} J_{xy}$ are fitted simultaneously and independently. From the anisotropy $\Delta = J_z/J_{xy} = 1/4$, however, the relative strength of $\partial_{p_b} J_z$ and $\partial_{p_b} J_{xy}$ is in principal already fixed and in a second fit the ratio of $1/4$ is kept constant. Fitting both $\partial_{p_b} J_z$ and $\partial_{p_b} J_{xy}$ independently one obtains the calculated thermal expansion α_{XXZ} shown as dashed green line in Fig. 4.30 (c). It peaks close to 1 K and the resulting overall sum of the contributions (red line) gives a good description of the data in the whole temperature range. Especially the data close to the maximum around 1 K are very well-described. The resulting pressure dependencies $\partial_{p_b} J_z = 1.2\,\text{K}\,\text{GPa}^{-1}$ and $\partial_{p_b} J_{xy} = 0.2\,\text{K}\,\text{GPa}^{-1}$ are, however, not in agreement with the anisotropy $\Delta = J_z/J_{xy} = 1/4$, from which one would expect $\partial_{p_b} J_{xy} = 4\,\partial_{p_b} J_z$.

Instead enforcing the ratio of $1/4$ by fixing $\partial_{p_b} J_{xy} = 4\partial_{p_b} J_z$ during the fit and keeping the non-magnetic parameters constant results in a slightly different pressure dependence of J_{xy},

$$\frac{\partial J_{xy}}{\partial p_b} = 0.7\,\text{K}\,\text{GPa}^{-1}. \tag{4.36}$$

The fit yields a very similar description of the high-temperature data (dashed orange line). Yet, the match with the data close to the maximum is poorer. Even though the difference between both fits is small, together with the big discrepancy of the ratio of the pressure dependencies from the expected $1/4$ these results suggest that the anisotropy Δ is different from $1/4$ as will be shown below. From the heat capacity analyzed in several previous studies this could not be detected due to the small dependence of c_p on Δ.

Extended description

Motivated by the inconsistencies encountered in the previous chapter and the indications for a deviation of Δ from the value of $1/4$ the derivation of the effective spin-$1/2$ system as outlined in Chapter 2.3.1 is reviewed in the following.

According to Hund's rules the orbital ground state of the magnetic Co^{2+} in Cs_2CoCl_4 has $S = 3/2$. Neglecting interchain interactions, the magnetism is thus primarily described in terms of a spin-$\frac{3}{2}$ system with magnetic exchange J_{H},

$$\mathcal{H}_{3/2} = \sum_i \left[J_{\mathrm{H}} \vec{\mathcal{S}}_i \vec{\mathcal{S}}_{i+1} + \mathcal{D}(\mathcal{S}_i^z)^2 - g_{3/2}\mu_{\mathrm{B}}\mu_0 H_b \mathcal{S}_i^x \right]. \tag{4.37}$$

Here, $\vec{\mathcal{S}}$ is a spin-$3/2$ operator, J_{H} is the Heisenberg exchange and H_b is an external magnetic field applied along b. The orbital ground state ($\mathcal{S} = 3/2$) is split by the crystal-field anisotropy $\mathcal{D}$ into Kramers doublets separated by an energy gap ΔE. At low temperature $k_{\mathrm{B}}T \ll \Delta E$, when the thermal population of the higher-energy doublet is exponentially small, a description of the low-energy $|\pm 1/2\rangle$-doublet in terms of an effective spin-$1/2$ XXZ chain arises,

$$\mathcal{H}_{XXZ} = \sum_i \left[J_{xy}(S_i^x S_{i+1}^x + S_i^y S_{i+1}^y) + J_z S_i^z S_{i+1}^z - g\mu_{\mathrm{B}}\mu_0 H_b S_i^x \right]. \tag{4.38}$$

Upon the projection of spin interactions on the low-energy doublet, the isotropic spin-$3/2$ magnetic exchange J_{H} is replaced by the anisotropic spin-$1/2$ couplings J_z and J_{xy}. The previously assumed ratio of $\Delta = J_z/J_{xy} = 1/4$ is derived in the limit of a large crystal-field anisotropy $J_{\mathrm{H}}/\mathcal{D} \ll 1$ by fully neglecting the $|\pm 3/2\rangle$ states. Instead performing a Schrieffer-Wolff transformation[1] on the Hamiltonian $\mathcal{H}_{3/2}$ up to first order in $1/\mathcal{D}$, one obtains, in the limit of small fields $g_{3/2}\mu_0\mu_{\mathrm{B}}H_b \ll \mathcal{D}$, the relations

$$J_{xy} = 4J_{\mathrm{H}},\ J_z = J_{\mathrm{H}}\left(1 - \frac{39}{8}\frac{J_{\mathrm{H}}}{\mathcal{D}}\right),\ g = 2g_{3/2}\left(1 - \frac{3}{2}\frac{J_{\mathrm{H}}}{\mathcal{D}}\right). \tag{4.39}$$

The technique known as Schrieffer-Wolf transformation dates back to a paper by J. Schrieffer and P. Wolff and subsequently was applied in many different fields of theoretical physics including quantum many-body systems [31, 32]. In the present case, besides the thermal activation of the higher-energy doublet $|\pm\frac{3}{2}\rangle$, which leads to the

---

[1] The Schrieffer-Wolff transformation on Eqn. (4.37) has been performed by M. Garst and E. Sela during the work on a common publication (Ref. 139).

Schottky anomaly around 5 K, the transformation takes also virtual excitations of these states into account that give rise to corrections of J_z and g. In the limit $J_{\mathrm{H}}/D \to 0$ these corrections are negligible and an anisotropy $J_z/J_{xy} = 1/4$ follows. Although the value of $J_{\mathrm{H}}/\mathcal{D}$ is assumed to be small, multiplied by the large numeric prefactor 39/8 the relative strength of the coupling J_z/J_{H} may be significantly reduced. A second consequence of the extended transformation concerns the Schottky anomaly and the crystal field anisotropy $\mathcal{D}$. In the previous chapter and in literature the Schottky anomaly was treated as a secondary, unfortunately overlapping effect and it was subtracted from the data to obtain the net magnetic contribution of the one-dimensional spin-$1/2$ system. However, both contributions actually derive from the same parent Hamiltonian $\mathcal{H}_{3/2}$ and are closely related. The anisotropy of the spin chain (Δ) and of the crystal field ($\mathcal{D}$) are not independent parameters, but by virtue of the introduced additional term $-\frac{39}{8}\frac{J_{\mathrm{H}}}{\mathcal{D}}$ in Eqn. (4.39) the size of $\mathcal{D}$ determines the anisotropy of the magnetic exchange in such a way that J_z/J_{xy} in general deviates from $1/4$.

The overall dependence of the longitudinal coupling J_z on $\mathcal{D}$ is sketched in Fig. 4.31. In the limit of infinitely large positive values of $\mathcal{D}$ the derivation outlined in Chapter 2.3.1 yields a longitudinal exchange that is $1/4$ of the parent spin-$3/2$ coupling J_{H}, respectively $9 \cdot J_{\mathrm{H}}$ in case of a negative sign of $\mathcal{D}$, shown as red dots and horizontal dashed lines in Fig. 4.31. For finite anisotropies $\mathcal{D} < \infty$, the coupling J_z is linearly reduced in first order as given by Eqn. (4.39) and sketched with the red line in Fig. 4.31. In principle J_z could become arbitrarily small for decreasing $\mathcal{D}$ such that the XY model is approached even further. Yet, the present mapping to the effective spin-$1/2$ model assumes the limit of $J_{\mathrm{H}}/\mathcal{D} \ll 1$, where the coupling of spins is minor to the splitting of the spin states by the anisotropy. Leaving this limit, the spin-$3/2$ physics is recovered gradually. One may, thus, expect an increase of J_z towards the isotropic case upon further decreasing $\mathcal{D}$. However, there is no general formula for $J_z(\mathcal{D})$ and the red line only indicates a guess for an approximate dependence in the effective spin-$1/2$ regime. Anyway, approaching $\mathcal{D} \to 0$ the initial assumptions for the application of an effective spin-$1/2$ model are no longer fulfilled as indicated by the shaded areas in Fig. 4.31.

The fact that, according to Eqn. (4.39), the system becomes more XY-like for initially decreasing the anisotropy $\mathcal{D} < \infty$ is rather surprising, because one might expect that the increasing contribution of all of the $|S_z = \pm 3/2\rangle$ states leads to a more isotropic system. The origin probably lies in the dependence of quantum fluctuations on the spin quantum number. Considering a single ion with an anisotropy $\mathcal{D}S_z^2$ the expectation value $\langle S_z \rangle$ is non-zero for $S = 1/2$ (leading to the residual value of $J_z/J_{\mathrm{H}} = 1/4$ in the limit of $\mathcal{D} \to \infty$) and decreases with increasing S. Thus, the decrease of J_z may be understood as an increased efficiency of the anisotropy in the virtually excited $|S_z = \pm 3/2\rangle$ states. In analogy to the resulting minimum of J_z for large positive $\mathcal{D}$ (sketched with the solid red line in Fig. 4.31) one may ask whether corrections also apply in the Ising limit of $\mathcal{D} \to -\infty$ and if they lead to a similar extremum of J_z/J_{H}. However, in this case, the corresponding virtual excitations contribute in an even higher third order of $J_{\mathrm{H}}/\mathcal{D}$ and are expected to reduce J_z/J_{H} below a value of 9, but not to increase the effective longitudinal coupling [149].

The specific heat and the thermal expansion are now again compared to model calculations of $\mathcal{H}_{XXZ}$ including the corrections to the longitudinal coupling. According to

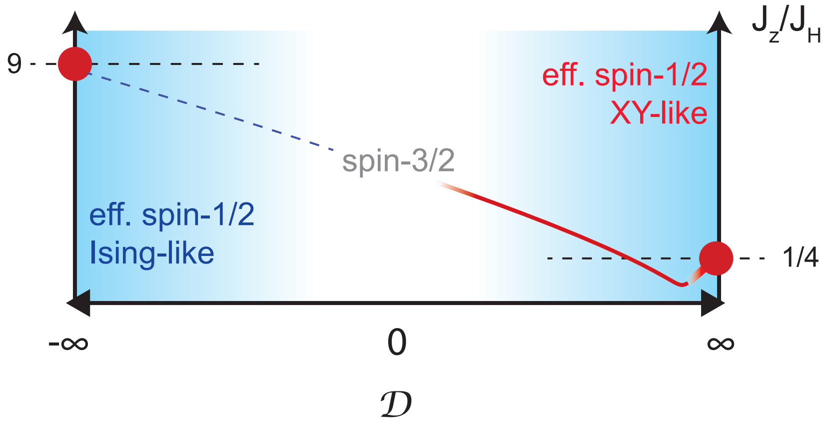

Figure 4.31: Sketch of the dependence of the effective spin-1/2 longitudinal coupling J_z/J_H on the crystal field anisotropy $\mathcal{D}$. For large positive (negative) anisotropy the XY (Ising) limit is approached (marked by red dots and horizontal dashed lines), for $\mathcal{D} \to 0$ the spin-3/2 physics is recovered (white shaded area). The solid red line represents the qualitative dependence of J_z for intermediate anisotropies $\mathcal{D} > 0$ based on Eqn. (4.39). The dashed blue line depicts the corresponding dependence in the Ising case.

Eqn. (4.39) the pressure dependence of J_{xy} directly relates to the one of the Heisenberg exchange J_H, whereas $\partial_{p_b} J_z$ additionally depends on the pressure dependence of $\mathcal{D}$,

$$\frac{\partial J_x y}{\partial p_b} = 4\,\frac{\partial J_\mathrm{H}}{\partial p_b}\,, \tag{4.40}$$

$$\frac{\partial J_z}{\partial p_b} = \left(1 - \frac{39}{4}\frac{J_\mathrm{H}}{D}\right)\frac{\partial J_\mathrm{H}}{\partial p_b} + \frac{39}{8}\left(\frac{J_\mathrm{H}}{D}\right)^2 \frac{\partial D}{\partial p_b}. \tag{4.41}$$

Thus, the thermal expansion at $H_b = 0$ is fully determined by the pressure dependencies of the Debye temperature Θ_D, of the single-ion anisotropy $\mathcal{D}$ and by that of the isotropic spin-3/2 Heisenberg exchange J_H. The individual pressure dependencies of the longitudinal and transverse couplings follow from Eqns. (4.40),(4.41) and by construction are consistent with the anisotropy

$$\Delta = \frac{1}{4} - \frac{39}{32}\frac{J_\mathrm{H}}{\mathcal{D}}. \tag{4.42}$$

Again, the maximum of the Schottky anomaly in temperature basically fixes $\mathcal{D}$. The pressure dependence $\partial_{p_b}\mathcal{D}$ is given by the strength of the anomaly around 5 K in α and the low-energy peak then essentially determines the last remaining parameter J_H and its pressure dependence $\partial_{p_b} J_\mathrm{H}$.

As the correlators and thermodynamic properties of the spin-chain are calculated via exact diagonalization for discrete values of J_H and $\mathcal{D}$, the fitting of the data cannot

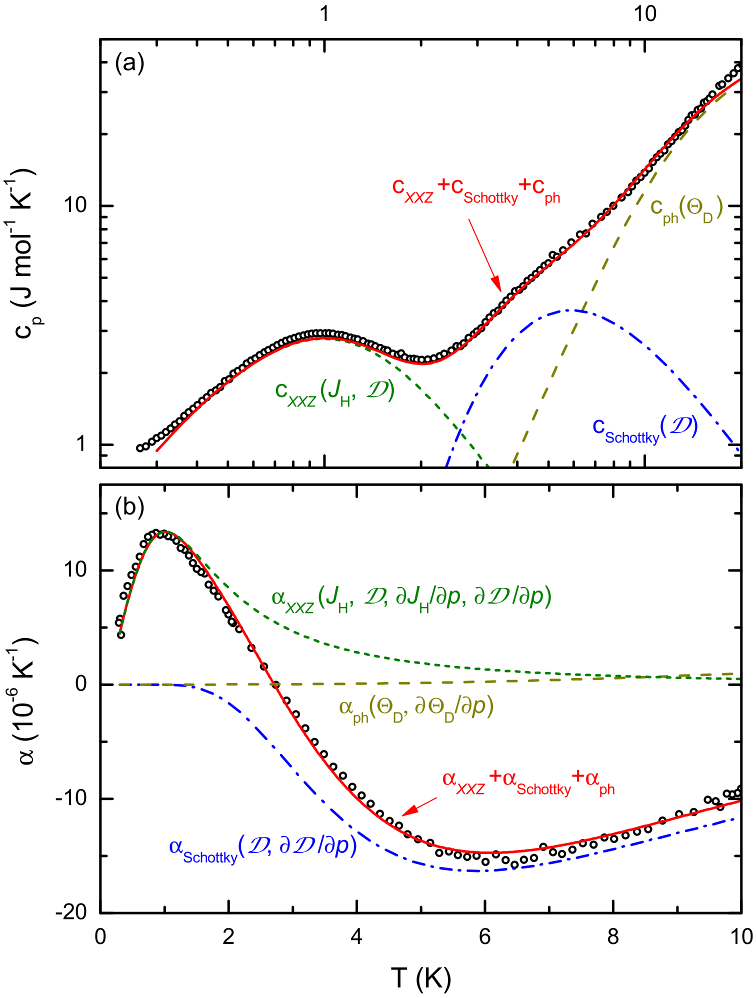

Figure 4.32: Fit of the specific heat (a) and the thermal expansion (b) by the spin-$1/2$ *XXZ* model extended to include virtual excitations of the $|S_z = \pm 3/2\rangle$ states. The yellow, blue and green lines represent the individual contributions of the phonons, the thermal population of the $S_z = \pm 3/2$ doublet and the magnetic contribution of the spin chain. The fit parameters (Eqn. (4.44)) are obtained by numerical minimization (see text).

be performed analytically. Instead, the exact diagonalization results are interpolated using multi-dimensional splines and the "cost function"

$$\begin{aligned} K[c^{calc}_{XXZ}, c_{\mathrm{Schottky}}, c_{\mathrm{ph}}] = & \sum_i \left[c^{calc}_{XXZ}(T_i, J_{\mathrm{H}}, \mathcal{D})\right. \\ & \left. + c_{\mathrm{Schottky}}(T_i, \mathcal{D}) + c_{\mathrm{ph}}(T_i, \theta_D) - c^{meas}_p(T_i)\right]^2 \\ & + \sum_j \left[\alpha^{calc}_{XXZ}(T_j, J_{\mathrm{H}}, \mathcal{D}, \partial p_b J_{\mathrm{H}}, \mathcal{D}, \partial p_b \mathcal{D})\right. \\ & + V_m^{-1}\left(\frac{\partial \ln \mathcal{D}}{\partial p_b} c_{\mathrm{Schottky}}(T_j, \mathcal{D}) + \frac{\partial \ln \theta_D}{\partial p_b} c_{\mathrm{ph}}(T_j, \theta_D)\right) \\ & \left. - \alpha^{meas}(T_j)\right]^2 \end{aligned} \tag{4.43}$$

is minimized by refining the parameters in a metropolis-like algorithm. In each step a random subset of all parameters is chosen and changed by a random real number $\in (-0.1, 0.1)$. Using adequate starting values, a convergence of the parameters is obtained within about 1000 steps. The phonon background is adopted from the previous analysis with a Debye temperature fixed to 67 K. As the numerical calculation of the spin correlators is rather time-consuming and has to be repeated for every exchange anisotropy (given by the values of J_H and $\mathcal{D}$), first $J_\mathrm{H}/k_\mathrm{B} \simeq 0.74\,\mathrm{K}$ and $\mathcal{D}/k_\mathrm{B} \simeq 6.9\,\mathrm{K}$ were approximated by minimizing K only for the zero-field specific heat data. Subsequently, all correlators were calculated and both the specific heat and the thermal expansion were fitted by refining $J_\mathrm{H}, \mathcal{D}, \partial_{p_b} J_\mathrm{H}, \partial_{p_b}\mathcal{D}$ and $\partial_{p_b}\Theta_D$. The resulting Heisenberg exchange $J_\mathrm{H}/k_\mathrm{B} = 0.743\,\mathrm{K}$ and the anisotropy $\mathcal{D}/k_\mathrm{B} \simeq 7.04\,\mathrm{K}$ remained essentially unchanged. The spin correlators were recalculated for these values and from the final simultaneous best fit to the measured specific heat and the thermal expansion one obtains

$$\begin{aligned} J_\mathrm{H}/k_\mathrm{B} &= 0.743\,\mathrm{K}, & \mathcal{D}/k_\mathrm{B} &= 7.04\,\mathrm{K}, \\ \frac{\partial \ln J_\mathrm{H}}{\partial p_b} &= 0.77\,\mathrm{GPa}^{-1}, & \frac{\partial \ln \mathcal{D}}{\partial p_b} &= -0.63\,\mathrm{GPa}^{-1}, \\ \frac{\partial \ln \Theta_\mathrm{D}}{\partial p_b} &= 0.01\,\mathrm{GPa}^{-1}. \end{aligned} \tag{4.44}$$

The sums of all contributions to the specific heat and to the thermal expansion (shown as red lines in Fig. 4.32) yield a good description of the data in the whole temperature range using these parameters. The phonons only add a small background α_ph (yellow dashed line) to the thermal expansion in the present temperature range, which is due to the comparably small relative pressure dependence of Θ_D of only $0.01\,\mathrm{GPa}^{-1}$. In other words, the measured thermal expansion is almost entirely of magnetic origin and the anisotropy $\mathcal{D}$ can be determined with a high precision from the Schottky anomaly. Due to the large negative pressure dependence $\partial_{p_b}\mathcal{D}$, the Schottky anomaly is seen as a minimum of the thermal expansion around 5 K. The negative sign of $\partial_{p_b}\mathcal{D}$ indicates that upon applying uniaxial pressure along the b axis, the lattice is distorted such that the anisotropy and, in consequence, the splitting of the doublet states is lowered. As previously discussed, a slight reduction of $\mathcal{D}$ leads to an increase of the XY anisotropy. This is in line with the obtained pressure dependence of the individual longitudinal and perpendicular couplings which relate to that of J_H via Eqns. (4.40),(4.41),

$$\frac{\partial J_{xy}}{\partial p_b} = 2.3\,\mathrm{K\,GPa}^{-1}, \qquad \frac{\partial \ln J_{xy}}{\partial p_b} = 0.8\,\mathrm{GPa}^{-1}, \tag{4.45}$$

$$\frac{\partial J_z}{\partial p_b} = -0.26\,\mathrm{K\,GPa}^{-1}, \qquad \frac{\partial \ln J_z}{\partial p_b} = -0.7\,\mathrm{GPa}^{-1}. \tag{4.46}$$

From the limit $J_\mathrm{H}/\mathcal{D} \ll 1$ one might expect that $\partial_{p_b} J_z$ is mainly determined by $\partial_{p_b} J_\mathrm{H}$ and that both bond correlators, Eqn. (4.30) and Eqn. (4.31), contribute with a similar weight to α_{XXZ}. However, the large value of $\partial_{p_b}\mathcal{D}$ compensates the small factor $(J_\mathrm{H}/\mathcal{D})^2 \approx 0.01$ and significantly reduces $\partial_{p_b} J_z \approx -0.1\,\partial_{p_b} J_{xy}$. Therefore the longitudinal bond correlator $\langle S^z S^z\rangle$ rarely contributes to α_{XXZ}.

From these results a magnetic anisotropy $\Delta = J_z/J_{xy} \approx 0.12$ follows, which is about half of the previously assumed value of $1/4$. Thus Cs_2CoCl_4 realizes the XY limit to a greater extent than thought before. This result is mainly based on the extension of the Schrieffer-Wolff transformation to the first order of $1/\mathcal{D}$ and the combined analysis of the specific heat and the thermal expansion. In previous studies only single thermodynamic quantities, like the specific heat in Ref. 3, were analyzed, which did not unveil the increased magnetic anisotropy. Translating to the notion of this thesis, a coupling constant $J_\mathrm{H}/k_\mathrm{B} = 0.68\,\mathrm{K}$ and an anisotropy $\mathcal{D}/k_\mathrm{B} = 6.8\,\mathrm{K}$ were derived under the assumption of $J_z/J_{xy} = 1/4$ in Ref. 3. Plugging these numbers into Eqn. (4.39), one obtains an anisotropy 0.13, which by itself is inconsistent with the assumed value of $1/4$ and close to the value obtained here.

Due to the negative pressure dependence of J_z under uniaxial pressure along the b axis, J_z/J_{xy} would decrease and Cs_2CoCl_4 would approach the XY limit even further. From the pressure dependence of the anisotropy Δ,

$$\frac{\partial \Delta}{\partial p_b} = \frac{\frac{\partial J_z}{\partial p_b}}{J_{xy}} - \frac{J_z}{(J_{xy})^2} \cdot \frac{\partial J_{xy}}{\partial p_b} \approx -0.18\,\mathrm{GPa}^{-1},$$

a pressure to realize $\Delta = 0$ of about 0.7 GPa can be estimated which lies in a range that is accessible in experiments. However, one has to keep in mind that in experiments typically hydrostatic pressure is applied, whereas the pressure dependencies derived here from the thermal expansion assume uniaxial pressure. The huge magnetic contribution to the heat capacity around 1 K, which is larger than the typical phonon contribution by several magnitudes, might open the possibility to investigate the critical properties of Cs_2CoCl_4 also by measurements of the specific heat or other thermodynamic quantities as a function of the applied pressure, respectively as a function of J_z. However, one has to keep in mind that the obtained pressure dependencies derive from a linear theory for small applied pressures and that the anisotropy $\mathcal{D}$ would be significantly lowered under pressure, leading to a gradual recovery of the spin-$3/2$ properties. At a pressure of 0.7 GPa required to fully suppress the longitudinal coupling the anisotropy $\mathcal{D}$ would be lowered to $\approx 4\,\mathrm{K}$. At the same time J_H would increase to $\approx 1.1\,\mathrm{K}$, such that the description of the system as an effective spin-chain degrades. As a function of pressure one might thus rather expect to observe a crossover from an anisotropic effective spin-$1/2$ chain to an isotropic spin-$3/2$ chain.

Summarizing, the simultaneous fit of the specific heat and the thermal expansion reveals that Cs_2CoCl_4 approaches the *XY* limit, as described by the anisotropy parameter $\Delta \approx 0.12$, to an even greater extent than previously assumed in literature. From the extended mapping of the interactions to the effective spin-$1/2$ system a consistent description of the thermodynamics is possible.

Magnetic field along *b*

As the zero-field data could be well described by the *XXZ* model, one may ask if the magnetic field dependence is explained by the model as well. The transverse magnetic field direction dictated by the crystal symmetry is of fundamental interest as it breaks the rotational symmetry of the model and induces a quantum phase transition at a critical field $g\mu_\mathrm{B}\mu_0 H_b^\mathrm{cr} = h_c$. The dependence of the critical field of the *XXZ* chain on the anisotropy Δ is known from different theoretical approaches [67, 150, 151] and in a mean-field approximation given by $h_c/J = \sqrt{2(1+\Delta)}$. In Fig. 4.33 both the mean-field and the DMRG results of Ref. 67 are shown. For small values of Δ they slightly differ. For the previously obtained anisotropy $\Delta \approx 0.1$ a critical field $h_c/J \approx 1.5$ can be read off from the black line, representing the DMRG result. Close to criticality peaks

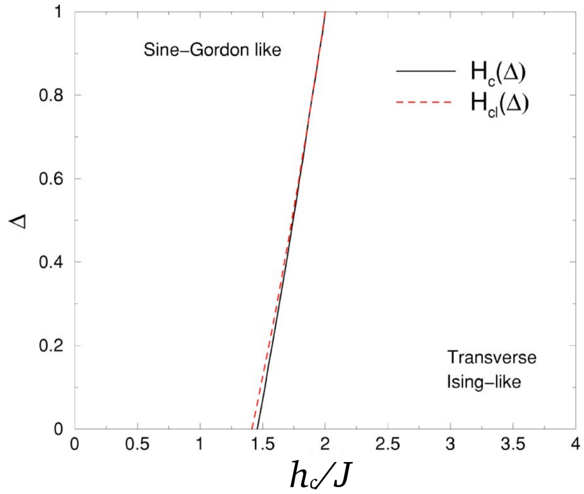

Figure 4.33: Critical transverse magnetic field of the XXZ chain as a function of the anisotropy Δ. The classical line $H_{cl}(\Delta) = \sqrt{2(1+\Delta)}$ is obtained from a mean-field Hamiltonian [151]. (Taken from Ref. 67)

are expected in the thermodynamic properties at finite temperature from very general considerations [103, 152, 153].

In Fig. 4.34 the measured specific heat and the thermal expansion are shown as $\frac{c_p}{T}$ and $\frac{\alpha}{T}$ versus T, respectively. In both quantities, a maximum, respectively a minimum, is seen which shifts as a function of the magnetic field. Below $\simeq 2.5\,\mathrm{T}$ the extrema are not resolved within the temperature range of the experiment. Plotting the peak position as a function of the magnetic field reveals a characteristic scaling $T \sim |H_b - H_b^{\mathrm{cr}}|^{\nu z}$, with $\nu z = 1$ (shown as dotted lines in Fig. 4.33 (c)) as expected for Ising criticality, that yields $H_b^{\mathrm{cr}} \approx 2\,\mathrm{T}$. From the experimentally observed critical field H_b^{cr} the g factor can be estimated as

$$1.5 \approx \frac{h_c}{J} = \frac{g\mu_{\mathrm{B}}\mu_0 H_b^{\mathrm{cr}}}{J} \quad \Rightarrow \quad g \approx 3.3.$$

As the extrapolation of the peak scaling is based on only few data points and as h_c/J is not exactly known but digitized from Fig. 4.33, the introduced error is relatively large. Another way to determine the g factor is given via comparison of the full specific heat data set in magnetic fields to the Hamiltonian $\mathcal{H}_{XXZ}$. In analogy to the zero-field case, exact diagonalization of $\mathcal{H}_{XXZ}$ has been performed for finite rings of 16 spins including the magnetic-field term $\propto g\mu_{\mathrm{B}}\mu_0 H_b S_x^i$. Concerning the specific heat, solely g enters in addition to the parameters already fixed by the zero-field data. Keeping the phonon background and the gap of the Schottky anomaly constant, the best fit is obtained using $g = 3.27$ (shown as solid lines in Fig. 4.35 (a)). This value confirms the previous result obtained by extrapolating the critical field H_b^{cr}. For the effective spin-$1/2$ model it agrees nicely with the estimated ordered magnetic moment $g\mu_{\mathrm{B}} \cdot \frac{1}{2} \approx 1.6\mu_{\mathrm{B}}$ that was inferred from neutron diffraction [8]. Via Eqn. (4.39) the obtained g factor also relates to that of the underlying spin-$3/2$ and one obtains $g_{3/2} = 1.9$. Similar to the observations in Ref. 8, this value is, however, significantly smaller than 2.4 as obtained from a Curie-Weiss fit of the high-temperature susceptibility [4, 5, 110]. In lowest order the isotropic $g_{3/2} = 2.4$ translates to the anisotropic spin-$1/2$ g-values g_{xy} and g_z via $g_{xy} = 2g_{3/2}, g_z = g_{3/2}$ [3]. Therefore a magnetic moment of $2.4\,\mu_{\mathrm{B}}$ would be expected

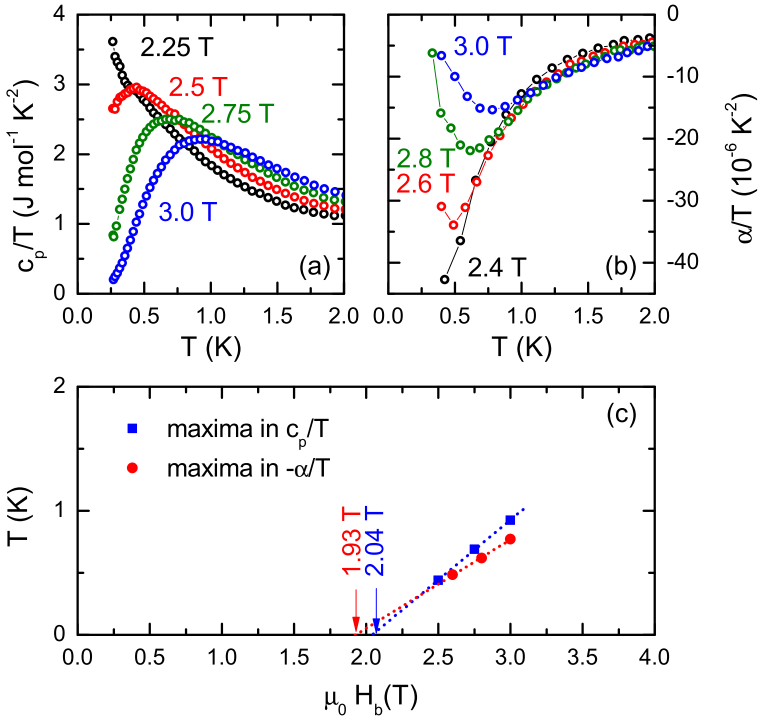

Figure 4.34: Extrema of $c_p(T)/T$ and $\alpha(T)/T$ scale linearly with the applied magnetic field. The extrapolation for $T \to 0$ yields a critical field $H_b^{\mathrm{cr}} \simeq 2\,\mathrm{T}$.

from the high-temperature susceptibility. The reduction of the ordered moment from this value is attributed to strong quantum fluctuations in the ground state [8].

So far only the specific heat in magnetic fields was discussed. Concerning the thermal expansion α_{XXZ} of the spin chain according to Eqn. (4.29) additionally the pressure dependence of the g factor contributes as scaling factor to $\partial_g \mathcal{F}_{XXZ}$. This term, however, appears to be negligible, as the fits to the thermal expansion data, shown by the solid lines in Fig. 4.35 (b), result in a vanishing $\partial_{p_b} g \approx 0$. From Eqn. (4.39) one can relate $\partial_{p_b} g$ to the zero-field pressure dependence of the parent spin-${}^3\!/_2$ g factor $g_{3/2}$,

$$\frac{\partial g}{\partial p_b} = \left(2 - \frac{3J_{\mathrm{H}}}{\mathcal{D}}\right) \frac{\partial g_{3/2}}{\partial p_b} - 3g_{3/2}\left(\frac{1}{\mathcal{D}}\frac{\partial J_{\mathrm{H}}}{\partial p_b} - \frac{J_{\mathrm{H}}}{\mathcal{D}^2}\frac{\partial \mathcal{D}}{\partial p_b}\right). \tag{4.47}$$

Solving Eqn. (4.47) one obtains $\partial \ln g_{\frac{3}{2}}/\partial p_b \approx 0.26/\mathrm{GPa}$. In contrast to the essentially pressure-independent g the value of $g_{3/2}$ in the spin-${}^3\!/_2$ framework increases as a function of pressure, which is mainly based on the large negative pressure dependence of $\mathcal{D}$. The reason for the different values of g obtained from the high-temperature data and from the correlations of the spin chain, might lie in the peculiar single-ion level splitting as described by Eqn. (4.3). The eigenvalues, plotted in Fig. 4.7 as a function of the magnetic field, show the typical Zeeman splitting in the limit of large fields, respectively small anisotropies $\mathcal{D}$. The splitting of the lower-lying $|S_z = \pm{}^1\!/_2\rangle$ states with energies E_1 and E_2 is characterized by a different slope g_{xy} in the limit of zero field,

$$E_1 - E_2 = 2h_x = 2g_{xy}h_x \cdot \frac{1}{2}, \tag{4.48}$$

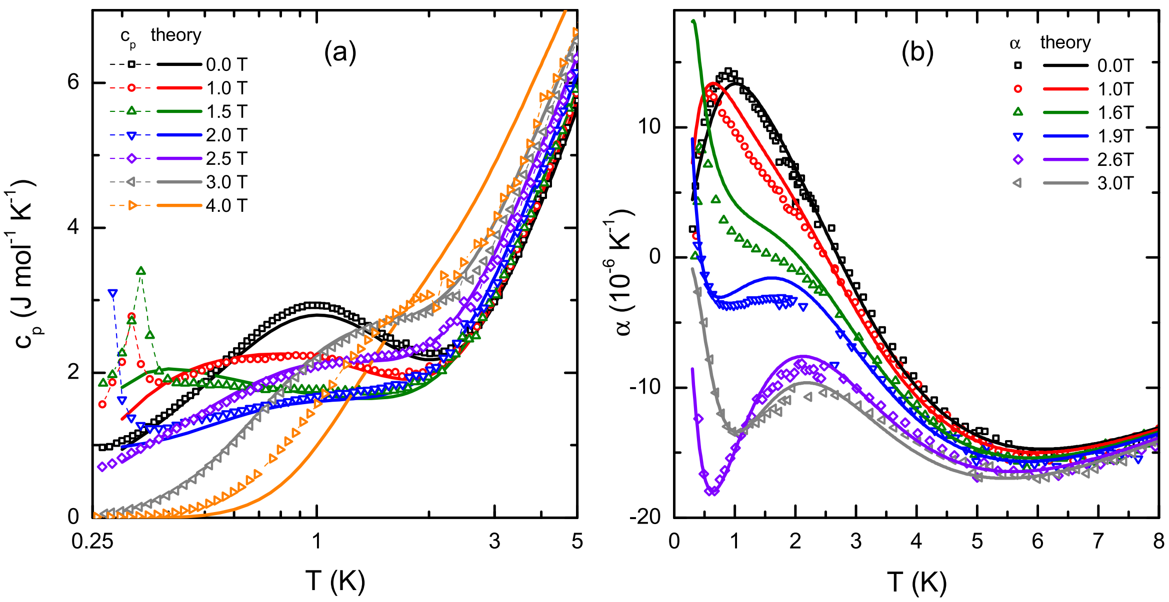

Figure 4.35: Specific heat $c_p(T)$ (a) and thermal expansion $\alpha(T)$ (b) of Cs_2CoCl_4 in magnetic fields applied along b in comparison to the *XXZ* model with an anisotropy $\Delta = 0.12$ (solid lines).

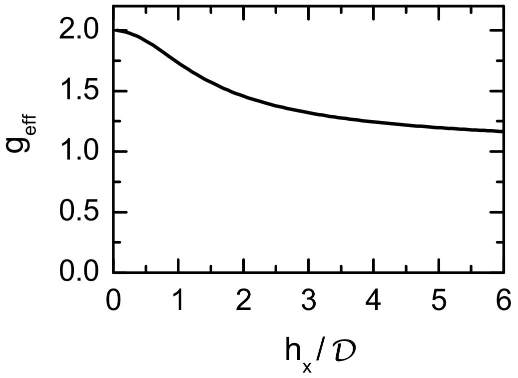

Figure 4.36: Field dependence of the gap between the two lowest single-ion states. Plotted is the effective g factor obtained by diagonalization of Eqn. (4.3) and expressing the splitting of the lowest Kramers doublet as a Zeeman-splitting of a spin-$1/2$.

where $g_{xy} = 2$ is also obtained via the application of the effective spin-$1/2$ model in lowest order. However, the single-ion energies E_1 and E_2 depend non-linearly on the magnetic field, such that the splitting $E_1 - E_2$ is non-trivial, but in a simple model can be rewritten by introducing an "effective" field-dependent g factor $g_{\text{eff}}(h_x)$, such that

$$[E_1 - E_2](h_x) = h_x - \sqrt{h_x^2 - h_x\mathcal{D} + \mathcal{D}^2} + \sqrt{h_x^2 + h_x\mathcal{D} + \mathcal{D}^2} = 2g_{\text{eff}}(h_x)h_x \cdot \frac{1}{2}. \quad (4.49)$$

While in the limit of zero field, $g_{\text{eff}}(B \to 0)$ the value of $g_{xy} = 2$ is recovered, at a finite field g_{eff} is reduced and approaches $0.5\,g_{xy}$ in the limit of large fields (see Fig. 4.36). Thus, necessarily the "real" zero-field g_{xy} factor is underestimated from a measure of the gap $E_1 - E_2$ at finite field. Finally, the apparent reduction of the g factor, however, is an artifact that originates from a finite entanglement of the spin states due to the transverse magnetic field, such that the eigenstates in finite field are no longer pure $|S_z = \pm 1/2, \pm 3/2\rangle$ states. In the limit of $h_x \to \infty$ the states are rather classified by the

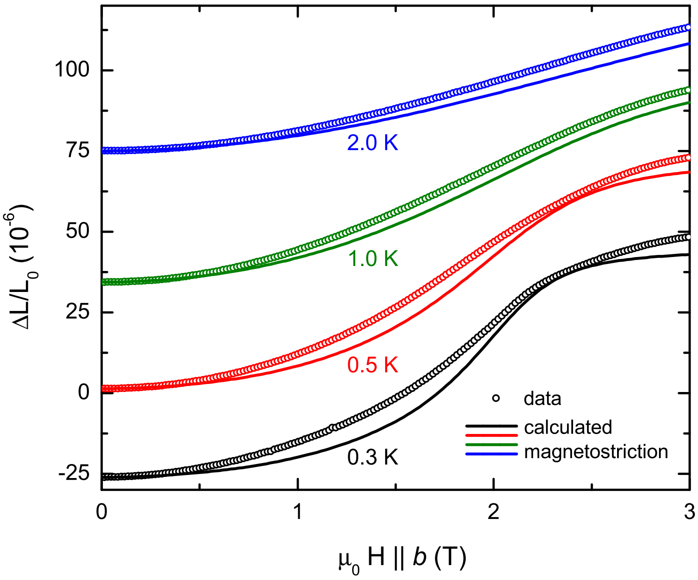

Figure 4.37: Magnetostriction of Cs_2CoCl_4 in comparison to exact diagonalization of the *XXZ* model with an anisotropy $\Delta = 0.12$. Symbols represent measurements with increasing field. Solid lines are calculations for different fixed temperatures using the parameters given in Tab. 4.4. Curves are offset by $25 \cdot 10^{-6}$ for each temperature.

quantum number $|S_x = \pm 1/2, \pm 3/2\rangle$. Therefore, the applied transverse magnetic field naturally borders the applicability range of the effective spin-$1/2$ system.

This is also reflected in the magnetostriction as compared to the exact diagonalization results in Fig. 4.37. The magnetostriction $\frac{\Delta L}{L_0}(H)$ of the *XXZ* spin chain is calculated based on the field dependence of the spin-spin correlators and the magnetization as described in Chapter 2.3.3. The respective pressure dependences were fixed to those obtained from the temperature dependence of the specific heat and the thermal expansion. The calculated length change was shifted such that it agrees with the data at zero field. A reasonable description of the overall shape is obtained, shown in Fig. 4.37 for selected temperatures. In general, the deviations between the calculation and the data seem to increase with increasing the magnetic field, which again shows the field-induced mixing of states. This is seen clearest at a temperature of 0.3 K, where the calculated length change saturates at high magnetic fields $H \gtrsim 2\,\mathrm{T}$, whereas the measurements, reveal a finite slope even at 3 T. This may arise from the intermixing of the crystal field states by the transverse field, in analogy to the finite slope of the magnetization in that field range (cf. Ref. 8). In addition to the specific heat that is well described by the theory up to 3 T, but not at 4 T, the magnetostriction indicates that the applicability range of the *XXZ* model is not limited by a sharp boundary, but that starting in between of 2 and 3 T the excited crystal field states start to contribute to the physics.

4.2.3 Conclusion

Measurements of the thermal expansion and the specific heat have been compared to numerical results of the *XXZ* model. A good description of the experimental data is obtained in a broad temperature and field range using the fit parameters given in Tab. 4.4. While the main coupling constant is close to that obtained previously in literature, the inclusion of virtual excitations of the spin-$3/2$ states shines a new light on the anisotropic magnetism of Cs_2CoCl_4 at low temperature. Based on the higher-order transformation of the coupling constants, the crystal field anisotropy $\mathcal{D}$, reflected by the Schottky anomaly around 5 K, is correlated to the one-dimensional magnetism. Together with the dominant coupling constant, the anisotropy $\mathcal{D}$ fixes the anisotropy of the spin chain. This relation has not been known previously and the anisotropy $\Delta = 1/4$ was assumed based on the limit $\mathcal{D} \to \infty$. As shown here, the anisotropy $\Delta \approx 0.12$ of the spin chain, however, is significantly smaller. This result is not specific for Cs_2CoCl_4, but may be of general importance for compounds where effective spin-1/2 models are applied. From Eqn. (4.39) one may expect significant corrections to the effective model in case that $\frac{39}{8}\frac{J_\mathrm{H}}{\mathcal{D}}$ is not negligible. Due to the large prefactor of $\frac{39}{8}$ this is the case even in system where the crystal field anisotropy is about one order of magnitude stronger than the correlations between magnetic moments.

The critical field of the spin chain $H_b^\mathrm{cr} \simeq 2\,\mathrm{T}$ not only manifests in the signatures in the thermodynamic quantities that scale linearly as a function of the magnetic field, but also in a sign change of the thermal expansion at lowest temperature close to 2 T, which is related to the accumulation of entropy near the critical field and is a characteristic signature of quantum phase transitions [152, 154, 155].

There are visible deviations between theory and experiment, especially for the thermal expansion at finite field. Yet, these differences are expected, because the description of Cs_2CoCl_4 in terms of a one-dimensional XXZ chain is restricted to a certain temperature and field range. At lowest temperature long-range order sets in. The transition temperature T_N is mainly determined by the strength of interchain couplings and by the correlation length of the spin chain. The purely one-dimensional XXZ model does not cover magnetic order, establishing a lower bound in temperature for its applicability of about 300 mK upon considering the field dependence of T_N. At high temperature $k_\mathrm{B}T/\mathcal{D} \gtrsim 2$ the second doublet states are populated and the system is rather described by a spin-3/2 system. Similarly, high magnetic fields lead to an entanglement of states

		pressure dependence / GPa^{-1}	
parameter	value	relative	absolute
J_H	0.743 K	0.77	0.6 K
$\mathcal{D}$	7.04 K	-0.63	−4.4 K
Θ_D	67 K	0.01	0.7 K
g	3.27	0	0
following from above:			
Δ	0.12	-0.7	-0.18
J_{xy}	2.97 K	0.8	2.3 K
J_z	0.36 K	-0.7	−0.26 K
$g_{3/2}$	1.9	0.26	0.5

Table 4.4: Parameters of the one-dimensional spin-1/2 XXZ chain as obtained by fitting the temperature dependence of the specific heat and thermal expansion in magnetic fields applied along the b axis. The pressure dependencies are given for uniaxial pressure along b.

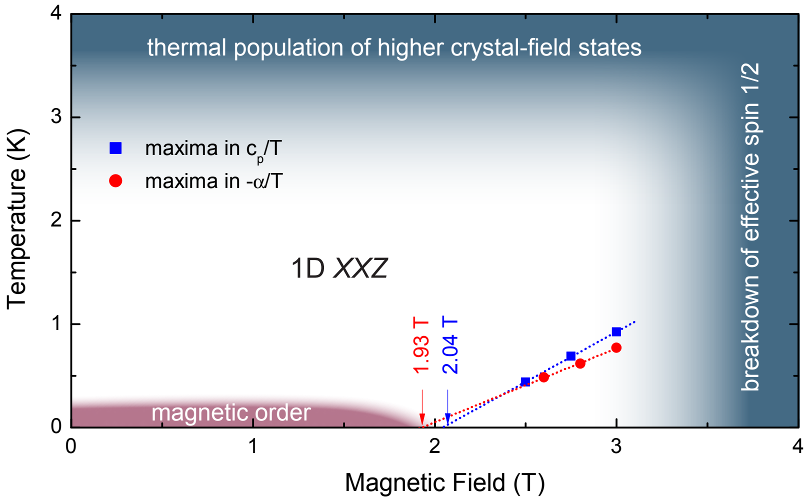

Figure 4.38: Phase diagram of Cs_2CoCl_4 showing the temperature- and magnetic field-range in which the one-dimensional spin-$1/2$ *XXZ* model is applicable (white area). In the blue shaded region an entanglement of higher-lying states results in a crossover to spin-$3/2$ physics. The extrema of specific heat and thermal expansion (closed symbols) extrapolate to the critical field of the spin chain $H_b^{\mathrm{cr}} \simeq 2\,\mathrm{T}$.

that are not part of the effective spin-$1/2$ model. As seen in Fig. 4.35 (a), the curve at 4 T fails to describe the experimental data, whereas at 3 T a reasonable match is obtained. A finite entanglement is also present at lower fields, as seen from the splitting of the ground-state doublet discussed above. Yet, the specific heat seems to be widely unaffected from an entanglement of states at small fields, whereas the deviations seen in the thermal expansion at small magnetic fields could be related to a more pronounced relative change of the individual correlators that contribute to α_{XXZ}.

From these considerations the applicability range of the one-dimensional effective spin-$1/2$ system can be sketched as shown in Fig. 4.38. The blue shaded region indicates the range where spin-$3/2$ states are intermixed. In the white area, the 1D *XXZ* model is well suitable to describe the thermodynamic properties of Cs_2CoCl_4. For a consistent picture the inclusion of virtual excitations of the higher-lying crystal field states is essential. In the specific heat and the thermal expansion maxima are seen that scale linearly as a function of the magnetic field, shown as symbols in Fig. 4.38. They extrapolate to the critical field of the spin chain close to 2 T and represent the typical manifestations of quantum critical behavior in the finite-temperature thermodynamic quantities. From these findings Cs_2CoCl_4 appears like an ideal model system representing a spin-$1/2$ chain with a nearly full *XY* anisotropy and the prospect of quantum criticality induced by magnetic fields applied along the *b* axis. In the following chapter the analysis of Cs_2CoCl_4 is extended to lower temperature, which involves approaching the possible quantum critical point at $\simeq 2\,\mathrm{T}$.

4.3 Magnetic order

In Chapter 4.2 the thermodynamic properties of Cs_2CoCl_4 were discussed considering a temperature range where the magnetism is governed by a dominant exchange coupling of the spins along the b axis. Due to finite couplings between spin chains magnetic order arises upon cooling at a temperature T_N of about 0.22 K as indicated by the specific heat [3]. From neutron scattering investigations the magnetic order is known to be antiferromagnetic with the magnetic moments lying in the bc planes (Fig. 4.39). In Ref. 8 the influence of a magnetic field, applied along the a axis, on the ground state properties has been investigated. Besides a slightly field-dependent antiferromagnetic phase boundary a spin-liquid state is proposed to arise close to 2 T. Magnetic field directions other than a are not discussed in literature. In this chapter, the analysis of Cs_2CoCl_4 will be extended to low temperatures of about 50 mK and the influence of magnetic fields applied along various directions will be discussed. In case of $H \parallel b$, a rich low-temperature phase diagram is found. Based on an analysis of the magnetic lattice and the respective exchange interactions, models for the magnetic order in the different phases are presented.

The orientation of the ordered moments of Cs_2CoCl_4 as reported in Ref. 8 reveals an intriguing detail whose far-reaching consequences are discussed at the beginning of this chapter, preceding the analysis of the thermodynamic data in the following chapters.

4.3.1 Zero-field magnetic order mechanism

From neutron scattering at zero field the magnetic moments are known to lie within bc planes in the ordered phase forming a small angle $\alpha \approx 15°$ with the b axis. One of the four antiferromagnetic domains is shown in Fig. 4.39 together with the magnetic exchange paths discussed in Chapter 4.1.2, shown as colored lines. Along the

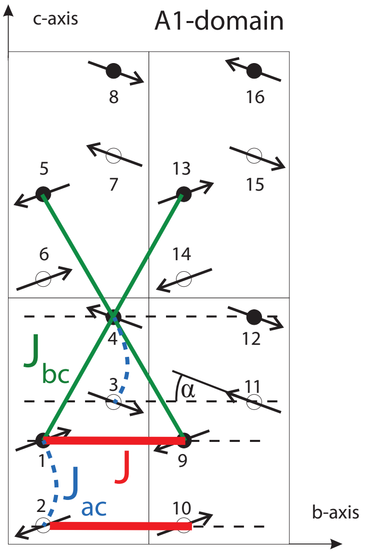

Figure 4.39: Ordered magnetic moments in the bc plane of the A1 domain of Cs_2CoCl_4 (adopted from Ref. 8). The dashed lines indicate the primary spin chains. Solid and open symbols depict the two different positions of spins along a in the unit cell at about 0.25 and 0.75, respectively. Spins are tilted away from the b axis by an angle $\alpha \approx 15°$. Colored lines indicate the intra- and interchain couplings.

spin chains, the moments are collinear. Neighboring spin chains coupled via the non-frustrated coupling J_{ac} reveal a phase shift of π, i. e., for example the moment at site 1 is anti-parallel to that at site 2. Spins belonging to different chains that are coupled in a frustrated way via J_{bc} are not collinear, but reveal a relative angle of $\pm 2\alpha$, with the sign depending on the considered domain. These relations hold for all four magnetic domains (see Fig. 4.13).

At first glance the tilt of spins away from the b axis by the angle α is surprising. For simplicity, consider a single pair of chains with a non-frustrated coupling J' between them and with easy-plane orientations that differ from chain to chain in a rotation around the b axis. An antiferromagnetic order with spins collinear to b would fulfill both the main coupling J, the interchain coupling J' and at the same time would not cost any anisotropy energy as the spins lie within the XY planes. The observed structure in contrast reveals a tilt of the moments within the bc planes away from the b axis. As spins are still collinear within the chains along b, the primary coupling J is fulfilled nevertheless. However, the finite angle between spins in neighboring chains is disfavored by the interchain coupling J_{bc}. Furthermore, the tilt requires all moments to leave their local easy planes, which costs an energy that is proportional to the anisotropy energy $\mathcal{D}$. To stabilize the observed state, another interaction must contribute which benefits from the tilt. One interaction that is often considered in case of non-collinear moments is the antisymmetric Dzyaloshinskii-Moriya (DM) interaction $\mathbf{D} \cdot (\mathbf{S}_i \times \mathbf{S}_j)$, which favors a perpendicular orientation of the spins. As spins within one chain are collinear, antisymmetric exchange within the chains can not be responsible for the tilt α. Thus, it must stem from DM interactions between chains. The responsible interaction can be identified from the observed magnetic order at zero magnetic field (Fig. 4.13). As the primary coupling J already was ruled out, only the further interchain couplings J_{ac}, J_{bc} and J_{ab} must be considered. J_{ab} can be ruled out as well because it does not allow for DM interactions by symmetry (cf. Chapter 4.1.2). In the actual magnetic structure J_{ac} is found only between spins that are collinear. Thus, DM interactions of J_{ac} can not account for the magnetic ground state. Finally, the frustrated coupling J_{bc} exclusively connects spins that have a finite angle to each other and it is allowed by symmetry. Thus, an energy gain by DM interactions on the J_{bc} bonds might explain the tilt of the moments away from the b axis within bc layers. The full magnetic structure could then be explained by the addition of the non-frustrated and symmetric inter-layer coupling J_{ac} which induces an antiferromagnetic order along a.

Dzyaloshinskii-Moriya interactions between chains

For a quantitative understanding how the magnetic order pattern is stabilized by an antisymmetric coupling along J_{bc} bonds, now a model system is considered that can explain the tilt of spins away from b. As J_{bc} (for simplicity $J_{bc} = J'$ in the following) is between sites of different easy-plane orientations only (see Chapter 4.1.2), the considered model is that of a pair of two spins at sites which belong to different chains. Here, sites 4 and 5 from the magnetic unit cell (Fig. 4.13) are chosen for a classical analysis of DM interactions as a perturbation of the antiferromagnetic ground state.

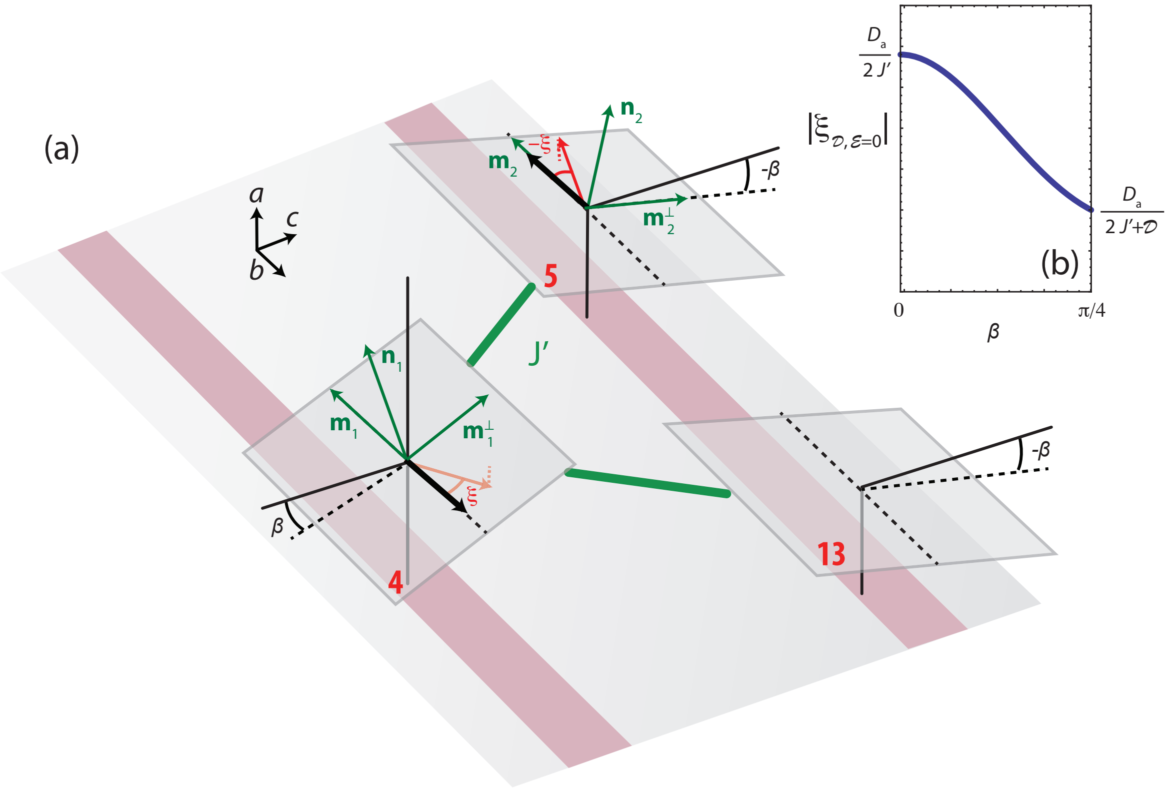

Figure 4.40: Sketch of a model system to explain the tilt of moments in the zero-field magnetic order of Cs_2CoCl_4 by Dzyaloshinskii-Moriya interactions. Chains are depicted by shaded red bars. The normal to the easy planes $\mathbf{n}_i$ and the in-plane directions $\mathbf{m}_i$ and $\mathbf{m}_i^\perp$ differ in the sign of a rotation $\pm\beta$ around b. Spins interact via the interchain coupling J_{bc} in the bc plane. Site numbers (shown in red) are given identical to Fig. 4.39. A small out-of-plane tilt angle ξ away from the b axis is considered as a perturbation of the antiferromagnetic state with spins along b (black arrows). Minimizing the energy yields $\xi_{\mathcal{D},\mathcal{E}}(\beta)$ as shown in (b) for $\mathcal{E} = 0$.

In Fig. 4.40 the easy planes of the sites 4 and 5 are shown as shaded planes. Site 5 and the neighboring site 13 belong to the same chain, depicted by red bars, and have the same easy plane orientation. In the following, however, only the energy between the two non-equivalent sites 4 and 5 is considered. Their easy planes differ by an opposing rotation

$$R_y^\alpha = \begin{bmatrix} \cos\alpha & 0 & \sin\alpha \\ 0 & 1 & 0 \\ -\sin\alpha & 0 & \cos\alpha \end{bmatrix} \tag{4.50}$$

of their local anisotropies by an angle $\alpha = \pm\beta$ around the y $(= b)$ axis. The normals to the planes

$$\mathbf{n}_1 = R_y^\beta \cdot \begin{pmatrix} 0 \\ 0 \\ 1 \end{pmatrix} = \begin{pmatrix} \cos\beta \\ 0 \\ -\sin\beta \end{pmatrix} \quad , \quad \mathbf{n}_2 = R_y^{-\beta} \cdot \begin{pmatrix} 0 \\ 0 \\ 1 \end{pmatrix} = \begin{pmatrix} \cos\beta \\ 0 \\ \sin\beta \end{pmatrix}$$

define the direction of the out-of-plane anisotropy. For completeness an additional in-plane anisotropy that favors one in-plane axis $\mathbf{m}_i$ over the perpendicular direction $\mathbf{m}_i^\perp$ is considered as well.

$$\mathbf{m}_1 = \mathbf{m}_2 = \begin{pmatrix} 0 \\ 1 \\ 0 \end{pmatrix} \quad , \quad \mathbf{m}_1^\perp = \begin{pmatrix} \sin\beta \\ 0 \\ \cos\beta \end{pmatrix} \quad , \quad \mathbf{m}_2^\perp = \begin{pmatrix} -\sin\beta \\ 0 \\ \cos\beta \end{pmatrix}$$

The antiferromagnetic state with all spins lying in their respective easy planes would correspond to

$$\mathbf{S}_4 = (0,1,0) \quad , \quad \mathbf{S}_5 = (0,-1,0)$$

and is represented by black arrows in Fig. 4.40. In Cs_2CoCl_4, this state is not the ground state at zero field, but it is perturbed by a small rotation $\pm\xi$ around the a axis, such that

$$\mathbf{S}_4 = (0, \cos\xi, \sin\xi) \quad , \quad \mathbf{S}_5 = (0, -\cos\xi, \sin\xi).$$

The opposing angle of the rotation yields a state with canted moments, which corresponds to the actual situation. The total energy E of two spins of neighboring chains can be calculated as the sum of the symmetric exchange J', the Dzyaloshinskii-Moriya interaction ($\propto \mathbf{D} = (D_a, D_b, D_c)$) and the anisotropy terms for the out-of-plane ($\mathcal{D} > 0$) and the in-plane ($\mathcal{E} > 0$) anisotropy.

$$\begin{aligned} E = \quad & J' && (\mathbf{S}_4 \cdot \mathbf{S}_5) \\ + \quad & \mathbf{D}\cdot && (\mathbf{S}_4 \times \mathbf{S}_5) \\ + \quad & \mathcal{D} && [(\mathbf{n}_1 \cdot \mathbf{S}_4)^2 + (\mathbf{n}_2 \cdot \mathbf{S}_5)^2] \\ + \quad & \mathcal{E} && \left[(\mathbf{m}_1 \cdot \mathbf{S}_4)^2 - (\mathbf{m}_1^\perp \cdot \mathbf{S}_4)^2 + (\mathbf{m}_2 \cdot \mathbf{S}_5)^2 - (\mathbf{m}_2^\perp \cdot \mathbf{S}_5)^2\right] \end{aligned} \tag{4.51}$$

For small values of ξ one finds the approximation

$$\begin{aligned} E = \quad & J' && [(2\xi^2 - 1) + \mathcal{O}(\xi^3)] \\ + \quad & 2D_a && [\xi + \mathcal{O}(\xi^3)] \\ + \quad & 2\mathcal{D} && \left[\xi^2 \sin^2\beta + \mathcal{O}(\xi^3)\right] \\ + \quad & 2\mathcal{E} && \left[\left(1 - \xi^2 \sin^2\beta\right) + \mathcal{O}(\xi^3)\right]. \end{aligned} \tag{4.52}$$

The symmetric coupling leads to a quadratic energy loss as a function of ξ, which is due to the cosine dependence of $\mathbf{S}_4 \cdot \mathbf{S}_5$ on the angle 2ξ between the spins. The linear term $\propto D_a$ derives from the sine dependence of the vector product of the spins on ξ. The quadratic anisotropy terms arise from the tilt with respect to the local anisotropy axes. Here, additionally the tilt β of the easy planes enters.

Due to the summation of linear and quadratic dependencies on ξ, a minimum at a finite canting results that depends on the easy plane rotation β. Minimizing Eqn. (4.52) in lowest order yields the canting angle

$$\xi_{\mathcal{D},\mathcal{E}} = \frac{-D_a}{2\,[J' + \mathcal{D} - 3\mathcal{E} - (\mathcal{D} + \mathcal{E})\cos 2\beta]}. \tag{4.53}$$

It linearly depends on the strength of Dzyaloshinskii-Moriya interactions D_a that favor a rotation of spins in the bc plane as observed by neutron scattering. The dependence of the tilt angle on the other model parameters is seen more easily in case of a vanishing in-plane anisotropy ($\mathcal{E} = 0$), where a simpler relation is obtained,

$$\xi_{\mathcal{D},\mathcal{E}=0} = \frac{-D_a}{2\left(J' + \mathcal{D}\sin^2\beta\right)}. \tag{4.54}$$

The tilt angle is reduced for increasing the anisotropy $\mathcal{D}$ and for increasing the angle β between the easy-plane anisotropies, because then the spins have to leave their easy planes upon tilting. The dependence of $\xi_{\mathcal{D},\mathcal{E}=0}$ on β is schematically shown in Fig. 4.40. The finite tilt angle for $\beta = 0$ is known as weak ferromagnetism in antiferromagnets [156]. Using Eqn. (4.53) and the observed tilt angle $\alpha = 15°$, the other parameters of the model can be deduced. The exchange constant J' may be estimated to $J'/k_\mathrm{B} \approx 0.1\cdot\frac{1}{6}\cdot 3\,\mathrm{K}$, with 0.1 being the approximate size of the interchain interactions (as given in Ref. 7) relative to the established primary exchange constant $J/k_\mathrm{B} \approx 3\,\mathrm{K}$, and using the factor $\frac{1}{6}$, as here only one of a total of 6 interchain couplings per site contributes. Using further values of $\mathcal{D}/k_\mathrm{B} \approx 7\,\mathrm{K}$ obtained above and $\beta = 38°$ the size of Dzyaloshinskii-Moriya interactions can be estimated in dependence of a possible in-plane anisotropy $\mathcal{E}$,

$$D_a/k_\mathrm{B} = -1.4\,\mathrm{K} + 0.8\cdot\mathcal{E}/k_\mathrm{B}. \tag{4.55}$$

Assuming that the in-plane anisotropy $\mathcal{E}$ is zero, as suggested from the XXZ magnetism in the one-dimensional regime, an antisymmetric exchange $D_a/k_\mathrm{B} = -1.4\,\mathrm{K}$ follows that is approximately one order of magnitude larger than the symmetric interchain coupling J'. As antisymmetric interactions typically arise as small corrections proportional to the parent symmetric coupling, this value seems unphysically large. However, smaller values of D_a could be realized for finite values of the in-plane anisotropy $\mathcal{E} > 0$. This might hint at the importance of an in-plane anisotropy for the magnetic ordering of $\mathrm{Cs_2CoCl_4}$. As introduced here, the in-plane anisotropy favors a state with spins not along b but along the local $\mathbf{m}_\mathbf{i}^\perp$ directions. In consequence, smaller DM interaction strengths suffice to explain the observed tilt angle $\alpha = 15°$. For a rough estimate of the in-plane anisotropy one may postulate that D_a is one order of magnitude smaller than the estimated interchain coupling, i. e., $D_a \approx J'/10 \approx -0.02\,\mathrm{K}$. This value of D_a then requires that

$$\mathcal{E}/k_\mathrm{B} \approx 1.8\,\mathrm{K}.$$

In comparison to the largest energy scale of the out-of-plane anisotropy $\mathcal{D} \approx 7\,\mathrm{K}$, this value seems reasonable, albeit too large to be fully neglected in favor of $\mathcal{D}$. In literature, an in-plane anisotropy was discussed previously in Ref. 4, but could not be reliably determined from high-temperature data. The fits typically resulted in $\mathcal{E} \lesssim 1\,\mathrm{K}$, which is significantly smaller than deduced here.

Summarizing, the tilt of moments out of the magnetic easy planes in $\mathrm{Cs_2CoCl_4}$ can be explained by Dzyaloshinskii-Moriya interactions between chains as shown here for one pair. Reasonable values of the interaction strength, however, require a sizable in-plane anisotropy. Comparing the derived value of $\mathcal{E} \approx 1.8\,\mathrm{K}$ to the established out-of-plane anisotropy $\mathcal{D} = 7\,\mathrm{K}$, an anisotropic magnetism would follow that is far from the easy-plane type. Yet, discussing this value, one should keep in mind that the present results are obtained in a purely classical description. More involved techniques (see

e. g. Ref. 157) might lead to corrections of D_a as well as of $\mathcal{E}$ and could give a full quantitative modeling of $\mathrm{Cs_2CoCl_4}$. Furthermore, as the angle 2β between easy-plane orientations enters in the absolute value of D_a, fixing $\mathcal{E}$, e. g., by ESR, might help to answer the question whether $\beta = -38.8°$ or $\beta = 19.4°$ (as proposed in Ref. 110) by a comparison to a thorough theory of the magnetic ground state. However, at present no theory is available that fully accounts for the complex magnetic lattice of $\mathrm{Cs_2CoCl_4}$.

In-plane anisotropy $\mathcal{E}$ in the one-dimensional spin chain

The comparatively large in-plane anisotropy $\mathcal{E}$ derived above is in contradiction to the established XY-like anisotropy of the one-dimensional spin chain magnetism of $\mathrm{Cs_2CoCl_4}$ at elevated temperature. Although corrections are expected from a more detailed theory, the large value might be justified by other means. In case the thermodynamic properties of the one-dimensional magnetism are hardly affected by a finite $\mathcal{E}$, it might be simply undiscovered from the high-temperature data and still drive the observed magnetic order. To model the impact of an in-plane anisotropy $\mathcal{E}$ on the one-dimensional magnetism the ALPS code was used [57]. The spin-$^3/_2$ Hamiltonian

$$\mathcal{H}^{3/2}_{\mathcal{D},\mathcal{E}} = \sum_i \left[J_\mathrm{H} \vec{\mathcal{S}}^i \cdot \vec{\mathcal{S}}^{i+1} + \mathcal{D}(\mathcal{S}^i_z)^2 + \mathcal{E}\left((\mathcal{S}^i_x)^2 - (\mathcal{S}^i_y)^2\right)\right] \tag{4.56}$$

gives the full description of the splitting of the spin-$^3/_2$ states by the the in-plane anisotropy $\mathcal{E}$ and the out-of-plane anisotropy $\mathcal{D}$. It has been implemented in the ALPS code as an individual spin model. The isotropic coupling of Heisenberg type $J_\mathrm{H} = 0.74\,\mathrm{K}$ and the anisotropy $\mathcal{D} = 7\,\mathrm{K}$ are fixed to the values derived in Chapter 4.2. Exact diagonalization of a chain lattice could be performed here only up to 8 sites, using periodic boundary conditions.

The calculated specific heat as a function of temperature for different values $\mathcal{E}$ is shown in Fig. 4.41 (a). The broad maxima at about 6 K arise from the splitting of the spin-$^3/_2$ states by the anisotropies $\mathcal{D}$ and $\mathcal{E}$. They represent the analogon to the Schottky contribution seen in $\mathrm{Cs_2CoCl_4}$ around 5 K, but with the inclusion of an additional in-plane anisotropy. Small values $\mathcal{E} \lesssim 1\,\mathrm{K}$ have very little influence on the Schottky contribution. The shift of the Schottky anomaly for increasing $\mathcal{E}$ can be understood as well by neglecting the interaction J_H and instead considering the splitting of the spin-$^3/_2$ states both by the in- and out-of-plane anisotropies as described by the single-ion Hamiltonian

$$\mathcal{H}^{\mathcal{D},\mathcal{E}}_{si} = \mathcal{D}\mathcal{S}_z^2 + \mathcal{E}(S_x^2 - S_y^2). \tag{4.57}$$

Diagonalization of $\mathcal{H}^{s,i}_{\mathcal{D},\mathcal{E}}$ yields the gap between the $S_z = \pm{}^3/_2$ and $S_z = \pm{}^1/_2$ states which linearly depends on $\mathcal{D}$ and $\mathcal{E}$:

$$\Delta E = 2\left|\mathcal{D} + \mathcal{E}\right|. \tag{4.58}$$

As shown in Fig. 4.41 (a) the Schottky anomaly around 5 K is thus simply shifted to slightly higher temperature by increasing $\mathcal{E}$. The decrease of the absolute value of the specific heat at the maximum is explained by the increasing separation of the low-temperature correlated regime from the Schottky anomaly by increasing $\mathcal{E}$. As the apparent gap ΔE of the Schottky anomaly only depends on the sum of $\mathcal{E}$ and $\mathcal{D}$, both quantities cannot be obtained simultaneously from the specific heat at high temperatures which remains a simple Schottky-like contribution. At temperatures comparable to the correlations more pronounced changes are expected due to the anisotropy of the exchange constants J_x, J_y and J_z which is induced by $\mathcal{E}$. Resilient data are obtained from $\mathcal{H}^{3/2}_{\mathcal{D},\mathcal{E}}$, however, only at temperatures $T \gg J_{\mathrm{H}}$, i. e., above $T \approx 2\,\mathrm{K}$. The numerical effort in exact diagonalization limits the system size to 8 sites such that at low temperature $T \lesssim 2\,\mathrm{K}$, where correlations dominate, the specific heat is strongly influenced by finite size effects (shown as shaded area in panel (a) of Fig. 4.41). For the inclusion of an in-plane anisotropy also in this temperature range, instead the effective spin-$1/2$ Hamiltonian is considered,

$$\mathcal{H}^{1/2}_{XYZ} = \sum_i \left(J_x(S^i_x S^{i+1}_x) + J_y(S^i_y S^{i+1}_y) + J_z(S^i_z S^{i+1}_z) \right). \tag{4.59}$$

Here S is a spin-$1/2$ operator and the in-plane anisotropy is reflected by the three individual couplings J_x, J_y and J_z. In comparison to the XXZ Hamiltonian derived in Chapter 2.3.1, also the couplings of the x and y components of the spin differ,

$$J_z = J_{z,0}, \quad J_y = J_{y,0} - \delta, \quad J_x = J_{x,0}. \tag{4.60}$$

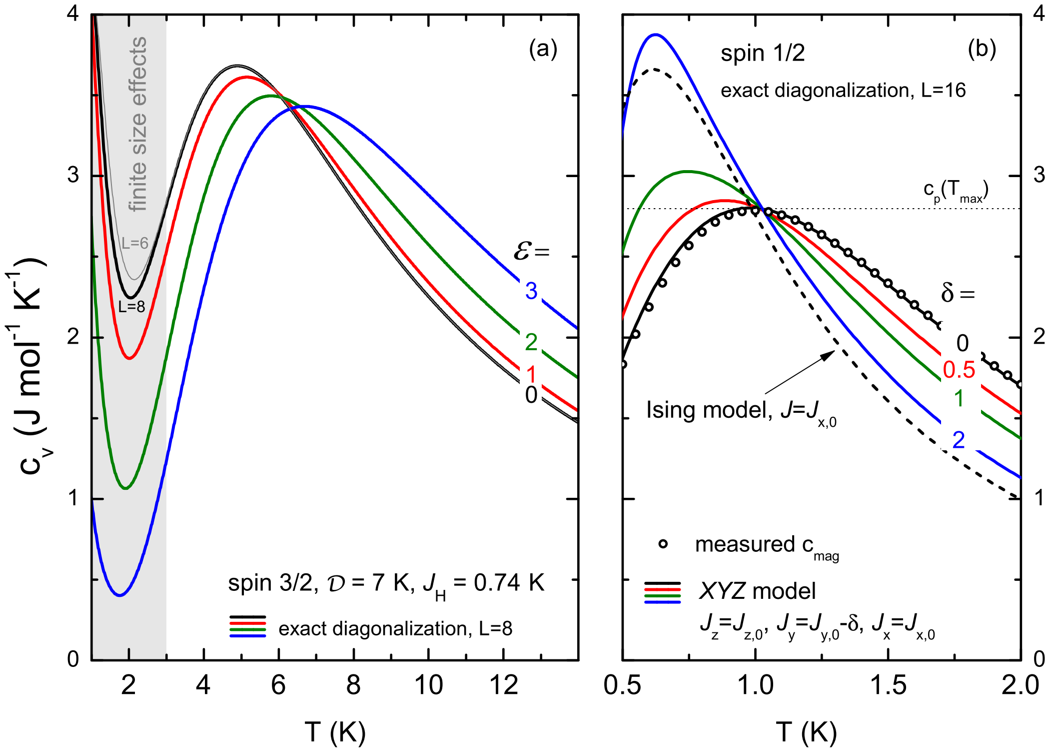

Figure 4.41: Specific heat of a spin-$3/2$ (a) and a spin-$1/2$ chain (b) with different in-plane anisotropies. Exact diagonalization of Eqns. (4.56) and (4.59) was performed for system sizes $L = 8$ and $L = 16$, respectively, using periodic boundary conditions. Open symbols indicate the magnetic contribution c_{mag} extracted from the measured specific heat (cf. Chapter 4.2.2).

The constants $J_{x,0} = J_{y,0} = 2.96\,\mathrm{K}$ and $J_{z,0} = 0.359\,\mathrm{K}$ were fixed to the values derived in Chapter 4.2.2. An in-plane anisotropy $\mathcal{E}$ is reflected in a reduction of J_y by δ. The calculated specific heat is shown in Fig. 4.41 (b) for different values δ. The translation from δ to the anisotropy energy $\mathcal{E}$ is not obvious and probably non-linear due to the breaking of a rotational symmetry by $\mathcal{E}$. By a comparison of the overlap of the calculated specific heat of both models one may, however, roughly estimate that a range of $\delta = 0 - 2$ corresponds to values $\mathcal{E} = 0 - 2\,\mathrm{K}$. With increasing δ the maximum position of the specific heat peak shifts to lower temperatures and the absolute value of the specific heat increases. As J_x becomes the sole dominant coupling for increasing δ, the Ising model (shown as dashed line) is approached. Due to the small, but finite value of J_z it will, however, not be fully realized even in the limit of $J_y \to 0$.

To answer the question if in-plane anisotropies can possibly be realized in the disordered phase of $\mathrm{Cs_2CoCl_4}$, the numerical results are compared to experimental data in the following. The Schottky-anomaly at temperatures $\sim 5\,\mathrm{K}$ provides only little information. It could incorporate both an in- and out-of-plane anisotropy as they enter the zero-field gap in the same way. Assuming that the gap of $7\,\mathrm{K}$, which was extracted in Chapter 4.2.2 actually consists of a sum $\mathcal{D}' + \mathcal{E} = 7\,\mathrm{K}$, an anisotropy $\mathcal{E} = 1.8\,\mathrm{K}$ requires a strongly renormalized primary anisotropy $\mathcal{D}' = 5.2\,\mathrm{K}$. In turn, the magnetism in the correlated temperature regime $T \approx J$ should be influenced significantly. The calculations for $\delta = 0$ (shown as solid lines in Fig. 4.41 (b)) coincide with the magnetic specific heat which is obtained from the measured c_p by subtracting the phononic and the Schottky contribution as modeled in Chapter 4.2.2. The specific heat, calculated for $\delta = 0.5$, could be roughly matched with the data as well by adjusting the coupling constants. The absolute value $c_p(T_{\max})$ of the specific heat peak at approximately $1\,\mathrm{K}$, indicated by a dotted line in Fig. 4.41 (b), however, is not changed by adjusting J, and is reproduced best for $\delta = 0$. Values $\delta > 0.5$ completely fail to describe $c_p(T_{\max})$. Finally, a sizable in-plane anisotropy in the one-dimensional regime of the order of $2\,\mathrm{K}$ can be ruled out by these calculations. A smaller anisotropy $\mathcal{E} \lesssim 1\,\mathrm{K}$ may possibly be hidden in an effective apparent gap at high temperature and a slight renormalization of the main coupling J. This result is in agreement with a study of the anisotropic susceptibility in the one-dimensional regime [4], which claims a small, but finite value of $\mathcal{E} \lesssim 1\,\mathrm{K}$ to describe the data. However, the authors confess that the analyzed data provides only little information on $\mathcal{E}$.

The fact that only small in-plane anisotropies $\mathcal{E} \lesssim 1\,\mathrm{K}$ might be possibly realized in $\mathrm{Cs_2CoCl_4}$ questions the previously derived phenomenological of the magnetic-order pattern, which asked for a comparably large $\mathcal{E} \approx 2\,\mathrm{K}$. Nevertheless, the model could be applicable if the magnetic order was accompanied by a structural distortion that induces or enlarges the demanded anisotropy within the magnetic easy planes.

Symmetry of Dzyaloshinskii-Moriya interactions

Although a tilt of moments away from the magnetic easy plane can be qualitatively explained by the model system discussed in Chapter 4.3.1, a further complication arises from the a priori unknown components of the Moriya vectors $\mathbf{D}_{ij}$ for different bonds. In principle $\mathbf{D}_{ij}$ can differ for every coupling between sites i and j. As $\mathbf{D}_{ij}$ has to fulfill

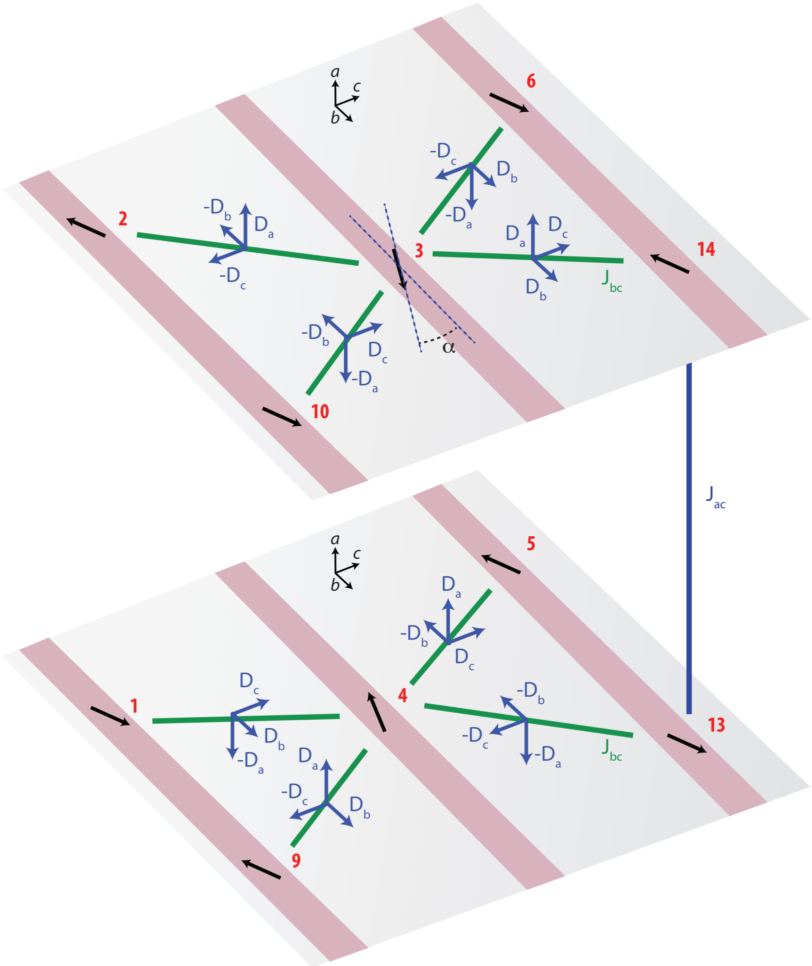

Figure 4.42: Magnetic order of spins (black arrows) in one (A1-domain) of the four domains of Cs_2CoCl_4. Besides the symmetric interchain couplings J_{bc} (green lines) and J_{ac} (solid blue line), the components of the Dzyaloshinskii-Moriya vectors are shown as small blue arrows in two neighboring bc layers. Sites are numbered equivalent to Fig. 4.13. (Based on the results of Refs. 8 and 116)

the space-group symmetry, one can, however, derive relations between $\mathbf{D}_{ij}$ for different sites i and j. Thus, for a given magnetic structure, the Dzyaloshinskii-Moriya energy

$$E_{\mathrm{DM}} = \sum_{i,j} \mathbf{D}_{ij} \cdot \mathbf{S}_i \times \mathbf{S}_j \tag{4.61}$$

might be simplified due to symmetry. For a well-defined relation one furthermore has to use a convention which spin comes first in the vector product $\mathbf{S}_i \times \mathbf{S}_j$. In analogy to Ref. 116, the convention used here is that the first spin in the product is the one with the smaller c component. In Fig. 4.42 the symmetry relations of $\mathbf{D}_{ij}$ are shown for the J_{bc} couplings as blue arrows. They were adopted from a symmetry analysis of the isostructural compound Cs_2CuCl_4 [116]. Along b and along c the components D_b, respectively D_c are preserved. Along a all components of $\mathbf{D}$ change the sign from one layer to another. To analyze whether the observed ordered state (shown as black arrows in Fig. 4.42) can benefit from DM interactions one can calculate the total energy E_{DM} by antisymmetric exchange for the given magnetic order using the named convention for the vector product. As spins coupled via J_{ac} are antiparallel from one layer n to the next and as the Moriya vectors $\mathbf{D}^n_{i,j}$ of layer n change sign from layer n to $n+1$ as well, the total energy can be deduced from that of a single layer:

$$\begin{aligned}
E_{\mathrm{DM}} &= \sum_n \sum_{i,j} \mathbf{D}^n_{i,j} \mathbf{S}^n_i \times \mathbf{S}^n_j = \sum_n \sum_{i,j} \left((-1)^n \mathbf{D}^1_{i,j}\right) \left((-1)^n \mathbf{S}^1_i\right) \times \left((-1)^n \mathbf{S}^1_j\right) \\
&= \sum_n (-1)^n E^1_{DM} \qquad (4.62) \\
&= 0.
\end{aligned}$$

Thus, no net energy gain results from any type of Dzyaloshinskii-Moriya interaction in the bc planes. This questions the applicability of the previously presented model. Although the model can explain the magnetic ordering of two isolated chains[1], it cannot account for the full magnetic order of Cs_2CoCl_4 due to the crystal symmetry.

As discussed in the context of the possibly finite in-plane anisotropy $\mathcal{E}$, another mechanism might resolve this issue. If the long-range magnetic order was accompanied by a lowering of crystal symmetry in such a way that D_a did not cancel for the whole lattice, the model could become reasonable again. In other words, Dzyaloshinskii-Moriya contributions to the frustrated coupling J_{bc} could then help to lift the frustration that one would experience for a pure triangular antiferromagnetic lattice. At the same time, this distortion could induce the in-plane anisotropy $\mathcal{E}$ that was discussed above, which enabled even small DM interactions to stabilize an order with moments not collinear to b. Such a structural distortion upon magnetic ordering and an accompanied lowering of symmetry is known from other frustrated systems like $BaCo_2V_2O_8$ [72], $CuFeO_2$ [158] or some pyrochlore antiferromagnets [159]. Also for several compounds of the R_2CoX_4 series [125, 126] structural transitions have been found, although they arise at higher temperatures between ∼200 K to 300 K and are independent of magnetic order. However, similar distortions of the $CoCl_4$ tetrahedra could influence the magnetism of Cs_2CoCl_4 at temperatures $T \lesssim T_{\mathrm{N}}$. However, the present data (cf. Chapter 4.3.2) do not give a microscopic evidence for such a distortion. In the thermal expansion at zero field a first-order transition is found accompanied by a sudden change of the lattice constants. Yet, this does not proof a change of the structure. The single study of the magnetic order by neutron scattering in Ref. 8 mainly focuses on the magnetic intensities and nuclear reflections have not been analyzed in detail. This question may be answered by other diffraction techniques at low temperature focusing on a possible structural change or by spectroscopy probing the crystal-field states above and below the magnetic order transition.

---

[1] Considering a single pair of chains only the component D_a, which alternates along b, cancels with the antiferromagnetically ordered spins within chains.

4.3.2 Experimental results

The magnetic order of Cs_2CoCl_4 was investigated by measurements of the thermal expansion and the specific heat. Magnetic fields were applied along different crystallographic and non-principal axes. In this chapter, first, experimental details are given before discussing the obtained thermodynamic data.

The heat capacity was measured using the home-built calorimeter introduced in Chapter 3.2.3. The samples with a typical weight of 10-30 mg were fixed to the sample platform by a small amount of Apiezon N grease. Although in most measurements the grease's contribution to the total heat capacity is negligible due to the large magnetic contribution of the sample it was weighed and subtracted based on an extrapolation of literature data available for higher temperature [95]. The addenda heat capacity was measured in a separate run and was subtracted as well. Its contribution is significantly larger than that of the grease, yet about two orders of magnitude smaller than the sample's signal (see Fig. 4.43 (a)).

In a first test run, the relaxation based method was employed. It was successfully applied at higher temperature and allows cooling to very low base temperatures due to the comparably strong thermal link. Selected raw data from a first test run using this method is shown in Fig. 4.43 (b). For this measurement two additional platinum wires (50 µm) were fixed to the sample holder and the sample platform as thermal links. For several reasons an analysis of the data is difficult. An increased internal relaxation time (τ_2) leads to a non-exponential time dependence, best seen by the flanks at $t = 30\,\mathrm{s}$ and $t \approx 160\,\mathrm{s}$ where the heater was switched on and off, respectively. As different sample shapes as well as different surface preparation did not significantly reduce the internal relaxation, the large τ_2 probably arises from a small thermal conductivity of Cs_2CoCl_4 at low temperatures. As the wanted sample's heat capacity is hidden in the small curvature related to the time constant τ_1, a significant error is introduced. Furthermore, the required long heating times induce further problems. As seen in Fig. 4.43 (b), the temperature does not relax back to the base line temperature, but to a higher value. Due to the strong thermal link and the troublesome heating dynamics via contact resistances, a part of the heat might flow to the sample holder leading to an elevated virtual bath temperature and nonphysically large heat capacities. These effects could be reduced by using shorter heating times and measuring smaller samples . However, then τ_1 and τ_2 would approach each other, rendering the extraction of the relevant τ_1 even more complex. Moreover, the rather strong coupling of the sample platform to the measurement environment adds noise to the data due to the limited temperature stability of the cryostat. In magnetic fields along a and b the magnetic order transition of Cs_2CoCl_4 turned out to be of first order with a substantial latent heat. Relaxation-time based methods are inappropriate to measure this kind of transitions, where the heat capacity strongly changes within a single heat pulse [91]. As the heat capacity, even of small samples of only few milligrams weight, is exceptionally large, the quasi-adiabatic heat-pulse method seems more appropriate instead. It allows a determination of c_p also in the vicinity of first-order transitions by a rather simple analysis with the drawback that the lowest reached temperature may be slightly higher due to the reduced thermal link. For the measurements by the quasi-adiabatic method the Pt-wire thermal links were completely removed and the sample platform was suspended using small diameter nylon fishing wire. Such, only the heater leads (100 µm manganin) and the thermometer leads (50 µm manganin) provide the cooling of the platform. Typical cooldown times from 1 K to ≈ 90 mK are in the range of six or more hours due to the long external relaxation. The thermal equilibration after applying a heat pulse of 2 s length to the sample is, thus, well described by a simple linear fit, shown as red lines in Fig. 4.43 (c) and (d). The internal relaxation time τ_2 nevertheless dominates the shape of the curve and leads to the temperature overshoot around the switching time of the heater at $t = 30\,\mathrm{s}$. The relative size of the overshoot reduces at higher temperature, as seen in Fig. 4.43 (c), while the slope of the external relaxation slightly increases.

In some of the raw data acquired close to a phase transition, an additional anomaly is observed, as shown exemplary in Fig. 4.43 (e) for a different sample in an applied magnetic field of 1.5 T. In comparison to the total temperature range of the data, the temperature rise ΔT is tiny, which indicates the strongly increased heat capacity at the

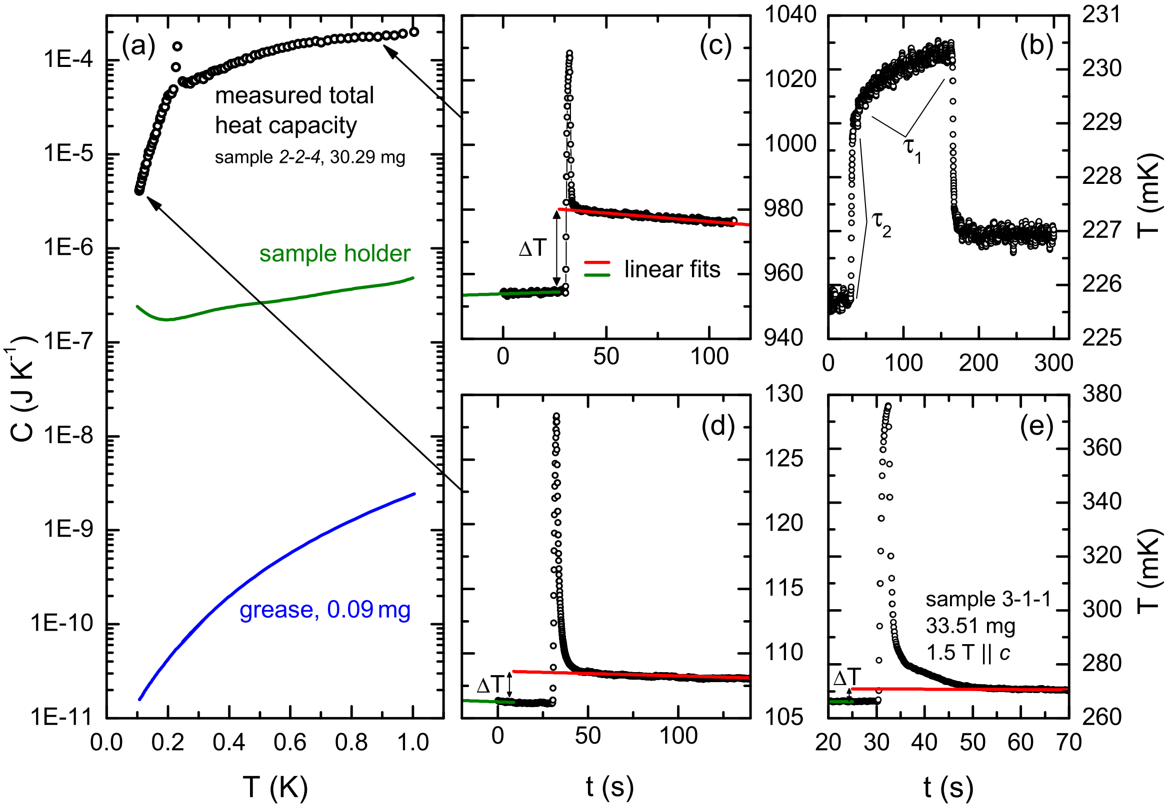

Figure 4.43: Exemplary raw data obtained in the magnetic order regime of Cs_2CoCl_4. Panel (a) shows the different contributions to the total measured heat capacity (open symbols). The sample holder contribution (green line) and the grease's heat capacity (blue line) are smaller by at least two orders of magnitude. Panel (b) and (c) show raw data acquired at ≈ 0.1 K and at ≈ 0.95 K using the quasi-adiabatic heat-pulse method. The green line is a linear fit to the baseline, the red line is a fit to the data range where the external relaxation dominates. A trial measurement using the relaxation method (d) is dominated by the internal relaxation τ_2. Some heat pulses in the vicinity of a phase transition (e) show an anomalous step-like relaxation.

phase boundary. Furthermore, at $t \gtrsim 35\,$s the temperature shows a modified relaxation which is not seen in other curves (e. g. Fig. 4.43 (c) and (d)). The thermal equilibration after switching off the heater is influenced by the small thermal conductivity of the sample and by the high contact resistances. After switching off the heater, the sample platform is reasonably warmer than the sample such that some parts of the sample may pick up more heat than others. In the vicinity of a phase transition, thus, a fraction of the sample volume might undergo the transition during heating as well as during the relaxation. These effects are reflected in the shape of the measured temperature of the sample platform by a large overshoot and by a non-trivial relaxation process. Moreover, possible temperature hystereses of c_p are suppressed by these dynamics due to the partial crossing of T_N during a single heat pulse even below T_N. The absolute values of c_p close to the transition temperature should, therefore, be treated with some caution. Due to the small width of the magnetic order peaks in the low-field range ($< 0.2\,$T), the transition temperature is fixed by only few data points and the peak shape is not fully resolvable. Yet, the appearance of latent heat indicates the first-order type of these transitions. In the analysis of the heat pulses, as described in Ref. 160 and Chapter 3.2.1, the internal relaxation and the non-homogeneous thermalization induce a systematic error of approximately 10 % to the absolute value of the heat capacity due to the dependence of the obtained ΔT on the fit boundaries (cf. Chapter 3.2.1). The following conclusions, however, rarely depend on the exact absolute values of the heat capacity. Especially the obtained phase diagrams are hardly influenced by the present τ_2 effect.

Thermal expansion and magnetostriction were measured using a home-built capacitance dilatometer [105]. The capacitance was measured with an AC capacitance bridge (AH2550A, Andeen Hagerling). At low temperatures of $\lesssim 0.1\,$K the thermalization of the sample holder and the sample itself have to be considered, as demonstrated by the odd relaxation phenomena in the specific heat raw data. First, thermal contact resistances and material properties are strongly influenced at low temperature, and secondly magnetocaloric effects can be more pronounced. To exclude these effects, very slow magnetic-field sweep rates down to $1\,\mathrm{mT\,min^{-1}}$ were used for the measurements. All data were acquired with the magnetic field applied parallel to the crystallographic axes along which the length change ΔL was measured. The uniaxial thermal-expansion coefficient α_i and the magnetostriction coefficient λ_i were obtained numerically, $(\alpha_i, \lambda_i) = \frac{1}{L_i}\frac{\partial \Delta L_i}{\partial (T, \mu_0 H)}$.

Zero-field specific heat

The specific heat of Cs_2CoCl_4 measured without an external magnetic field is shown in Fig. 4.44 in comparison to the digitized literature data of Ref. 3. Both data show an anomaly at $T_\mathrm{N} = 220 \pm 5\,$mK that indicates the transition from the high-temperature paramagnetic to the ordered antiferromagnetic phase. A similar transition temperature was found by neutron scattering [8]. Below the transition temperature, however deviations of the present data from the literature results are found. While the present measurement signals the magnetic order by an extremely sharp anomaly, the literature data of Algra *et al.* rather show a broad λ type anomaly that may be interpreted as

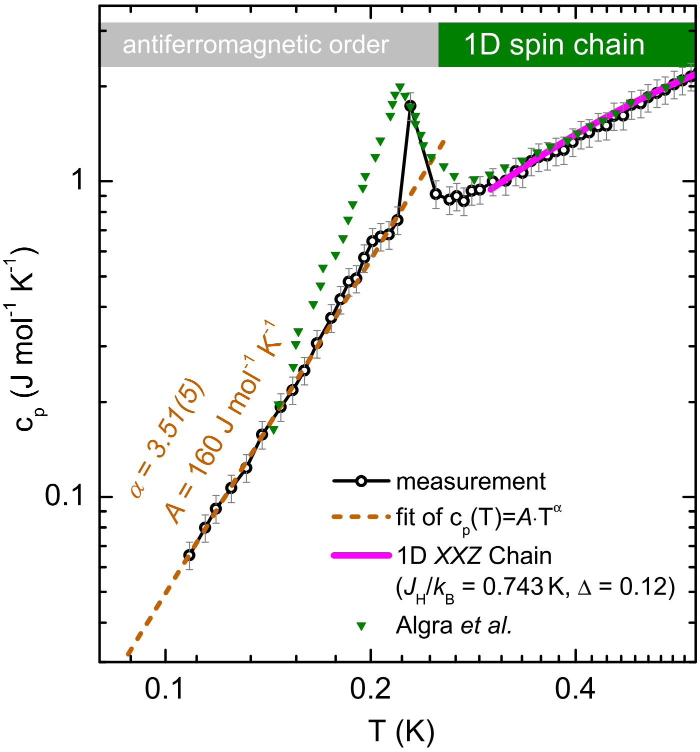

Figure 4.44: Specific heat c_p of Cs_2CoCl_4 below 0.5 K at zero field in comparison to the literature data of Ref. 3. The pink line is the calculated specific heat of the *XXZ* model as described in Chapter 4.2.2. The brown dashed line is a fit of a power-law $c(T) = A \cdot T^\alpha$ to the experimental data (open symbols).

an indication of a second order phase transition. From the present observation of a large latent heat in the raw data, as discussed above, and from the hystereses in the thermal-expansion data, shown below, the transition, however, is very likely to be of first order. The deviation of the data by Algra *et al.* probably arises from similar issues in the experiment that partially have been encountered here. In case of too large heat pulses that induce excessive heating of the sample up to or even above T_{N}, signatures of the phase transition can be induced in the data also below T_{N} which explains the enhanced specific heat below the transition. Above T_{N}, these issues are less severe and both data match each other. The temperature dependence of the molar specific heat for $T > T_{\mathrm{N}}$ is well described by the *XXZ* model as shown by the pink line which represents the zero-field exact diagonalization result discussed in Chapter 4.2.2.

Below T_{N} the temperature dependence of the present specific heat data resembles that of a power law $c_p \propto T^\alpha$ with $\alpha \simeq 3.5$, shown by a dashed line in Fig. 4.44. As the phonon heat capacity can be neglected in this temperature range, the power-law dependence must stem from the ordered magnetic subsystem. In the simplest case of an ordered antiferromagnet, one expects a temperature dependence of the specific heat $c_p \propto T^{d/n}$ from spin wave theory. Here, d is the dimension of the system and n the leading exponent of the magnon dispersion relation $\omega(\mathbf{k}) \propto k^n$. In case of an antiferromagnet ($d = 3$, $n = 1$) one expects a power-law $\propto T^3$ which differs from the experimental finding of $\alpha = 3.5$. This deviation might be explained by deviations of the magnon dispersion from the pure isotropic three-dimensional case. In an idealized three-dimensional system each spin interacts with z neighbors ($z = 6$ in case of a simple cubic lattice) in the same manner. In Cs_2CoCl_4, however, a strong interaction is found within chains along the b axis, whereas the interchain interactions are reasonably smaller by a factor γ. In addition, finite magnetic anisotropies may open a gap $\mathcal{D}_{\mathcal{A}}$ in

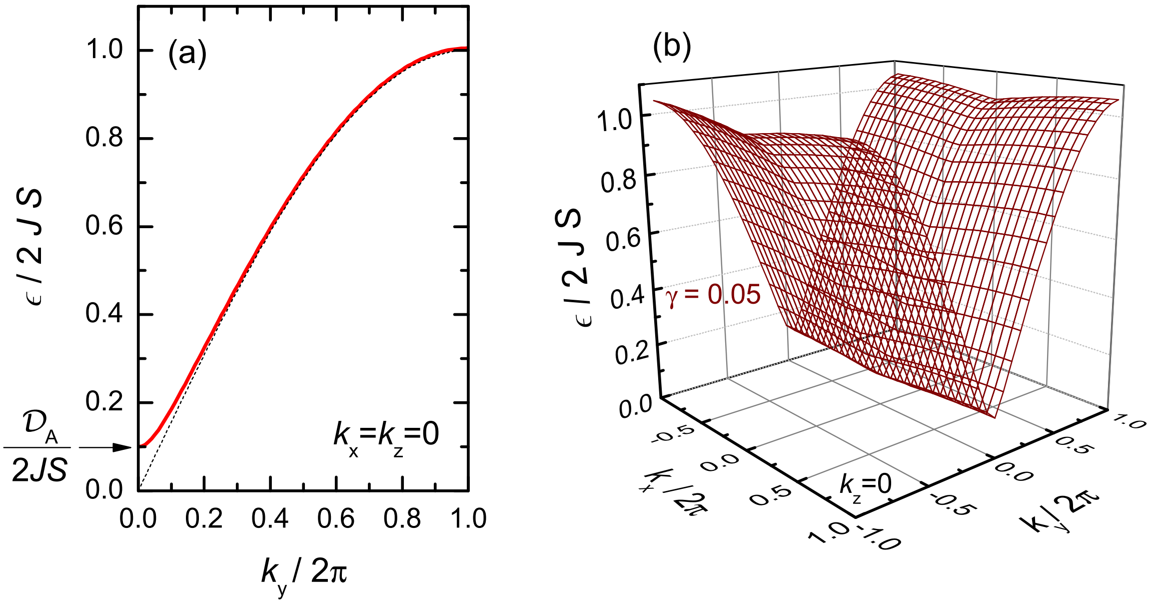

Figure 4.45: Dispersion $\epsilon(\mathbf{k})$ (cf. Eqn. (4.63)) plotted as a function of k_y (a) and as a function k_x and k_y (b). The assumed anisotropy gap $\mathcal{D}_\mathcal{A}/(2JS) = 0.1$ leads to a deviation of the dispersion from that of a pure antiferromagnet (dashed line) and at $\mathbf{k} \to 0$. In (b) the dispersion is plotted assuming $\gamma = 0.05$.

the spin wave dispersion at zero momentum. Identifying y with the chain direction, the classical magnon dispersion can, thus, be rewritten to account for these effects:

$$\epsilon(\mathbf{k}) = \sqrt{\left[2JS\left(\sin k_y + \gamma(\sin k_x + \sin k_z)\right)\right]^2 + \mathcal{D}_\mathcal{A}{}^2}. \tag{4.63}$$

As shown in Fig. 4.45 (a), the introduced anisotropy gap $\mathcal{D}_\mathcal{A}$ leads to a deviation of the magnon dispersion (red line) at small momenta from the pure case (dashed line) where excitations at $k \to 0$ are gapless. Along the reciprocal axes x and z the dispersion depends on γ. For a value of $\gamma = 0.05$ the dispersion along k_x is shallow as shown for fixed $k_z = 0$ in Fig. 4.45 (b).

Exploiting the symmetry of $\epsilon(\mathbf{k})$, the molar specific heat can be calculated from the internal energy for arbitrary dispersions by numerical integration

$$U = \sum_i \epsilon_i\, f(\epsilon_i) \longrightarrow U = \frac{8}{\pi^3} \iiint_0^{\pi/2} \epsilon(\mathbf{k}) f(\epsilon(\mathbf{k}))\, dk_x\, dk_y\, dk_z, \tag{4.64}$$

$$c_p \approx c_v = N_\mathrm{A} k_\mathrm{B} \iiint_0^{\pi/2} \epsilon(\mathbf{k}) \frac{d}{dT} f(\epsilon(\mathbf{k}))\, dk_x\, dk_y\, dk_z. \tag{4.65}$$

Here, f either stands for the Fermi- or for the Bose-Einstein distribution function,

$$f_\mathrm{Fermi}(E) = \frac{1}{1 + e^{E/k_\mathrm{B}T}}, \quad f_\mathrm{Bose}(E) = \frac{1}{e^{E/k_\mathrm{B}T} - 1}.$$

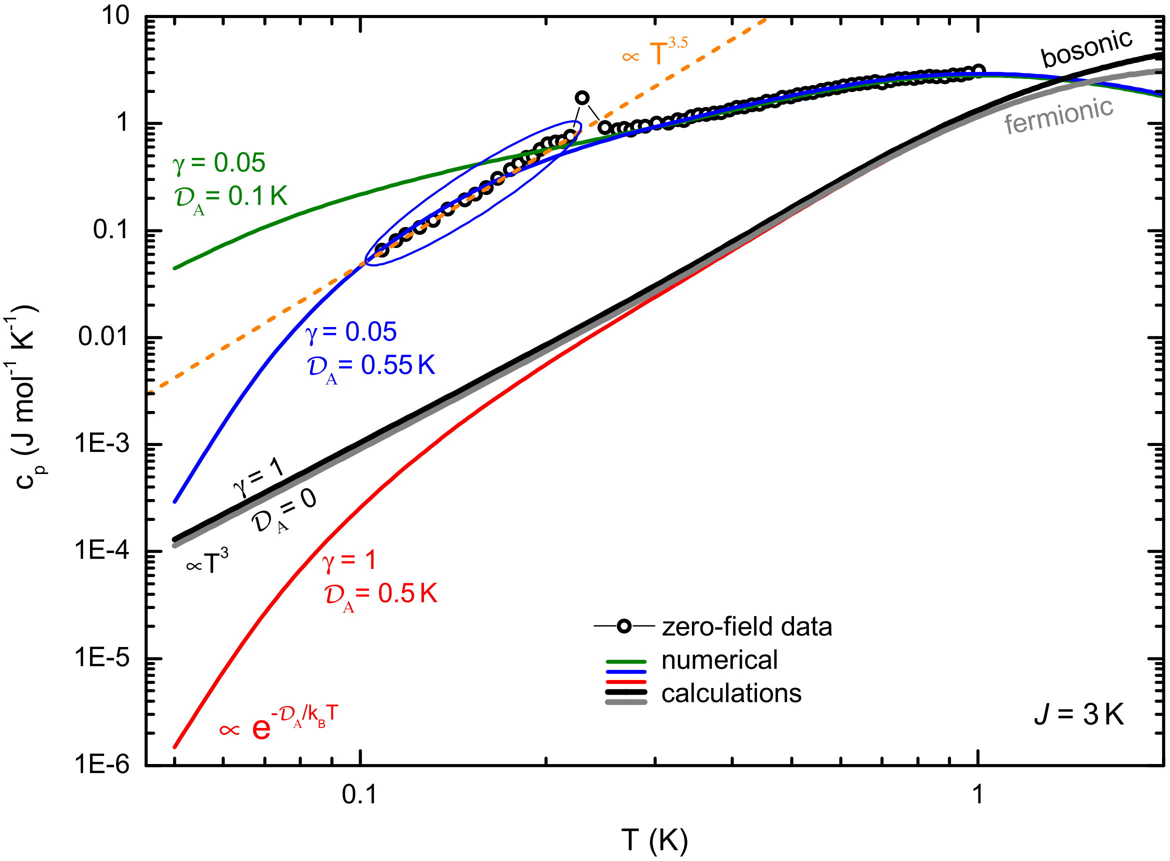

Figure 4.46: Molar heat capacity calculated for different dispersion relations $\epsilon(\mathbf{k})$ (Eqn. (4.63)) by varying the relative size γ of interchain couplings and the anisotropy gap $\mathcal{D}_\mathcal{A}$ (solid lines). In case of $\mathcal{D}_\mathcal{A} = 0$, both Bose- and Fermi statistics were applied (black, respectively gray line). All other lines were calculated using a fermionic distribution function. The coupling constant J was fixed to the spin-1/2 value derived at elevated temperature (cf. Chapter 4.2.2). The dashed orange line is a fit to the experimental data (open symbols) below $T_\mathrm{N} \approx 220\,\mathrm{mK}$. In the encircled data range the seeming power law is reproduced by the calculation for $\mathcal{D}_\mathcal{A} = 0.55\,\mathrm{K}$ and $\gamma = 0.05$.

Magnetic excitations in three dimensions (magnons) are bosons, while in antiferromagnetic spin chains excitations fractionalize into fermionic spinons. As shown in Fig. 4.46 for values of $\gamma = 1$ and $\mathcal{D}_\mathcal{A} = 0$ (black and gray line) the low-temperature heat capacity is essentially unaffected by the choice of the statistics and deviations only occur above 1 K which is not the temperature range of interest here. Due to the fermionic character of the excitations in one-dimensional spin chains, thus, the fermi distribution was used for the further calculations. In the isotropic case ($\mathcal{D}_\mathcal{A} = 0$, $\gamma = 1$) below $\approx 0.5\,\mathrm{K}$ the heat capacity follows the T^3 dependence expected for an antiferromagnet, which is reflected by $c_p(T)$ forming a straight line in the double-logarithmic plot of Fig. 4.46. Finite values of $\mathcal{D}_\mathcal{A}$ lead to an exponential suppression of the heat capacity at low temperature $T \lesssim \mathcal{D}_\mathcal{A}$ due to the introduced gap (plotted for a value $\mathcal{D}_\mathcal{A} = 0.5\,\mathrm{K}$ as a red line). Additionally changing the ratio γ between interchain couplings and the coupling along b leads to an increase of c_p at intermediate temperatures $T \approx \mathcal{D}_\mathcal{A}$ due to the increasing number of low-energy modes. The experimental data in the ordered phase (encircled open symbols) can be matched with the calculation using the parameters

$$J/k_{\mathrm{B}} = 3\,\mathrm{K} \quad , \quad \gamma = 0.05, \quad \mathcal{D}_{\mathcal{A}}/k_{\mathrm{B}} = 0.55\,\mathrm{K}. \tag{4.66}$$

Here, J was fixed to the high-temperature value obtained in Chapter 4.2.2 and the relative strength of the interchain coupling γ was inferred from neutron scattering data [120]. Within the restricted temperature range $T < T_{\mathrm{N}}$, where data points are available, the plotted blue line yields a reasonable description of the data. In this confined range the temperature dependence is well approximated by a power-law $c_p(T) \propto T^{3.5}$, shown as a dashed orange line. The experimentally observed power law, therefore, is not a universal scaling law, but originates from an anisotropic magnon dispersion which effectively generates an approximate power-law dependence in the restricted experimental temperature range. A similar description of the data is possible using slightly different values of γ and J, which in turn yields different but finite gaps $\mathcal{D}_{\mathcal{A}}$. Thus, for a quantitative analysis of $\mathcal{D}_{\mathcal{A}}$ microscopic studies, e. g., by electron spin resonance or inelastic neutron scattering are required.

The match of the experimental data by the model above T_{N} is striking, given that the fit of Eqn. (4.65) was performed to data points $c_p(T < T_{\mathrm{N}})$ only. However, this is partly by coincidence. In contrast to the assumed, gapped dispersion $\epsilon(\mathbf{k})$ the magnetic excitations of the *XXZ* model at zero field are gapless. Yet, the size of the gap $\mathcal{D}_{\mathcal{A}}$ is negligible above T_{N} as seen by comparing the specific heat for $\mathcal{D}_{\mathcal{A}} = 0.1\,\mathrm{K}$, shown as a green line in Fig. 4.46, which equals the blue curve for $T > T_{\mathrm{N}}$. Nevertheless, the assumptions, the classical spin wave theory is based on, are only partially fulfilled above T_{N}. In spin wave theory a static order is assumed and only small deviations from this state are considered. Above T_{N}, the *XXZ* spin chain, however, is ordered only on short ranges and quantum fluctuations are strong due to the small spin. Deviations from the "ordered" state are small only at low temperature $T \ll J$. In analogy to the discussion of the seemingly linear temperature dependence of $c_p(T \gtrsim T_{\mathrm{N}})$ in Chapter 4.2.2 the low-temperature limit $T \ll J$ is, however, not realized above T_{N}. Nevertheless, the good agreement of the calculated specific heat with the data above T_{N}, is explained by comparing the dispersion relation $\epsilon(\mathbf{k})$ of Eqn. (4.63) to that of the *XXZ* spin chain. In the limit of the exactly solvable *XY* model, the dispersion $\epsilon_{XY}(k)$ of magnetic excitation is known [130, 161],

$$\epsilon_{XY}(k) = 2J \cdot \cos k - h_z. \tag{4.67}$$

Here, a longitudinal magnetic field h_z leads to a linear shift of the dispersion and induces a transition at a critical field $h_c = 2J$. At zero field, ϵ_{XY} follows a simple cosine dependence. Expanding ϵ_{XY} at $k = \pi/2$ in lowest order gives a linear dispersion with a slope of $2J$, identical to the spin wave dispersion $\epsilon(k_y)$ in case of a vanishing anisotropy gap $\mathcal{D}_{\mathcal{A}} = 0$. At finite temperature $T > \mathcal{D}_{\mathcal{A}}$ the anisotropy gap is negligible and the specific heat is mainly determined by that slope. The match of the calculated specific heat also for $T > T_{\mathrm{N}}$, thus, is explained by the similar k dependence of the classical spin wave dispersion and the magnetic excitations of the one-dimensional *XY*-like spin chain.

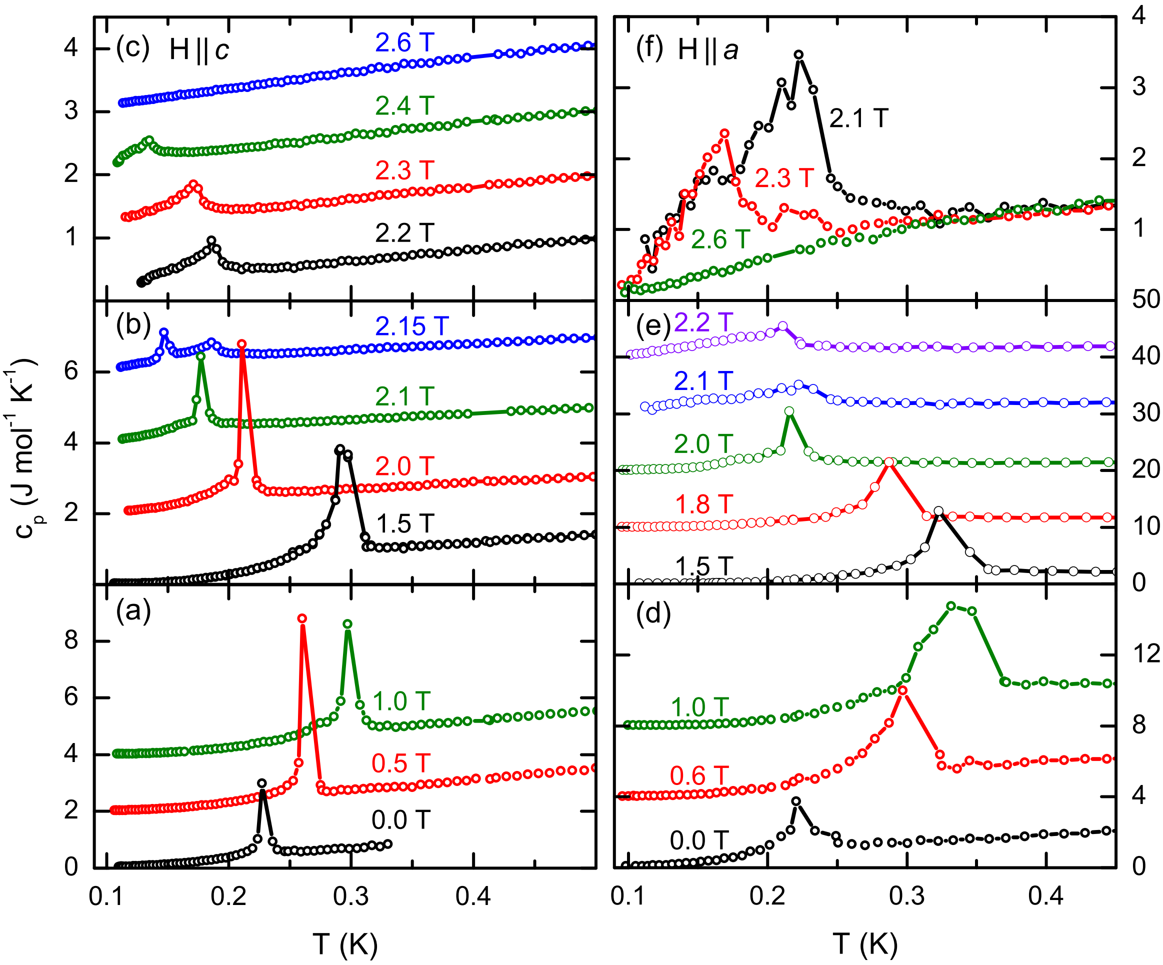

Figure 4.47: Specific heat of Cs_2CoCl_4 for magnetic fields applied along c (left) and a (right). Curves are offset with respect to each other by 2, 2, 1, 4, and 10 J mol^{-1} K^{-1} in panels (a) – (e), respectively.

Specific heat in magnetic fields along a and c

Figure 4.47 displays the specific heat of Cs_2CoCl_4 in magnetic fields applied along a or c. Up to 1.0 T, the temperature dependence of c_p in the ordered phase remains well described by the same power law $c_p \propto T^\alpha$ with $\alpha = 3.5$ as in zero field (see Fig. 4.48). Apart from this, the peak which indicates magnetic order shifts to higher temperatures with increasing field. This enhancement of T_N can be understood as a suppression of fluctuations by small magnetic fields and is also seen as an increase of the ordered moment as a function of the field [8]. For magnetic fields applied along a, a maximum transition temperature $T_\mathrm{N} \simeq 330$ mK is obtained at 1.0 T. The field dependence of T_N explains the appearance of peaks around 0.3 K in some of the high-temperature data presented in Chapter 4.2. Further increasing the magnetic field, T_N shifts back to lower temperatures and the power-law exponent gradually changes from $\alpha = 3.5$ to an even larger value of $\alpha \simeq 4.5$ at 2.0 T (green symbols in Fig. 4.48). As in zero field, the seeming power-law dependence in a restricted temperature range could derive from a dispersion which becomes increasingly gapped by magnetic fields. In a small adjacent

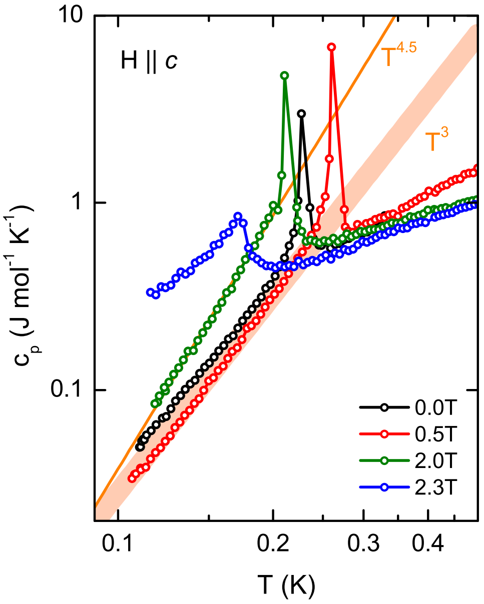

Figure 4.48: Specific heat of Cs_2CoCl_4 for selected magnetic fields applied along c. In this double-logarithmic plot straight lines represent a power-law temperature dependence $c_p \propto T^\alpha$. The shaded area represents $\alpha = 3$.

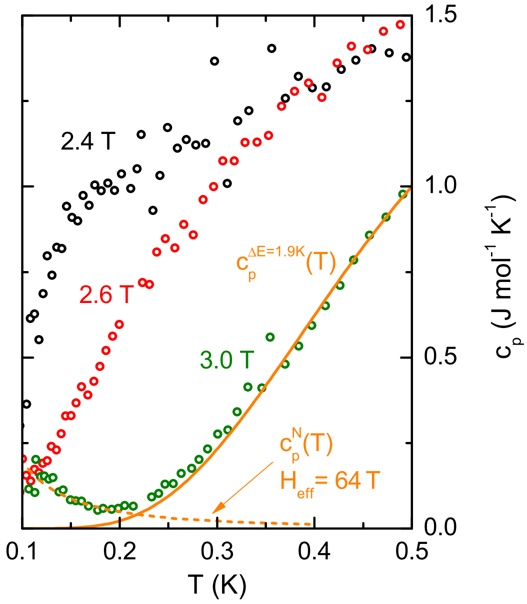

Figure 4.49: Specific heat of Cs_2CoCl_4 in magnetic fields applied along a. The experimental data (symbols) are fitted by the sum of a Schottky contribution (solid line) and a nuclear contribution (dashed line).

field range ($2.0\,\mathrm{T} < \mu_0 H \parallel a < 2.2\,\mathrm{T}$) the peak position hardly depends on the magnetic field, see Fig. 4.48 (e). In case of $2.1\,\mathrm{T} < \mu_0 H \parallel c < 2.3\,\mathrm{T}$ even a slight increase of the peak position is observed due to the higher data quality of these measurements. A fundamental change of the ground state properties is also signaled by a change of the temperature dependence of c_p in this field range from that at 2 T ($\alpha = 4.5$) as shown in Fig. 4.48 for the field applied along c. If a description by a power law is appropriate at all, due to the small temperature range, a value of α, however, is hardly obtained from the data. At a magnetic field $\mu_0 H \parallel c = 2.15\,\mathrm{T}$ instead of the previous single peak even a splitting into two distinct features is found. The lower-temperature peak resembles the previous single peaks at lower magnetic fields in shape and it follows an extrapolation of the peak position's field dependence. The additional upper peak is similar to those found at magnetic fields larger than 2.15 T. Further increasing the magnetic field, both transitions are suppressed to lower temperatures. Finally, above 2.5 T a gap-like behavior of the specific heat arises for both field directions.

Nuclear contribution to the specific heat at high fields

The data in the high-field range for $H \parallel a$ are shown in Fig. 4.49 in more detail. With increasing field the specific heat is suppressed, corresponding to the opening of a gap by the magnetic field. At 3 T the gap is large enough to neglect any dispersions and to phenomenologically describe the data by a simple two-level systems with an energy gap ΔE, yielding a Schottky contribution to the specific heat,

$$\frac{c_p^{\Delta E}(T)}{R} = \left(\frac{\Delta E}{k_{\mathrm{B}}T}\right)^2 \frac{e^{\Delta E/k_{\mathrm{B}}T}}{(1+e^{\Delta E/k_{\mathrm{B}}T})^2} \ . \tag{4.68}$$

A fit of $c_p^{\Delta E}(T)$ (solid line in Fig. 4.49) yields the field-induced gap $\Delta E/k_{\mathrm{B}} \simeq 1.9\,\mathrm{K}$. An additional low-temperature contribution arises at $T \lesssim 0.2\,\mathrm{K}$ which might stem from hyperfine interactions. The thermal population of the split nuclear spin states leads to another Schottky anomaly in the specific heat. Typically, in experiments only the high-temperature tail of this contribution is seen due to the small size of the splitting. In the high-temperature approximation of the heat capacity,

$$\frac{c_p^N(T)}{R} = \frac{I+1}{3I}\frac{(\mu_N \mu_0 H_{\mathrm{eff}})^2}{(k_{\mathrm{B}}T)^2} \ , \tag{4.69}$$

the effective field H_{eff} at the nucleus, the nuclear magneton $\mu_N = e\hbar/2m_p$ and the nuclear spin $I = 7/2$ (in case of cobalt) enter the temperature dependence. Fitting c_p^N to the low-temperature data yields an effective field $\mu_0 H_{\mathrm{eff}} \simeq 64\,\mathrm{T}$. This value lies in the typical range obtained for metals, but exceeds the value of about 20 T reported for pure cobalt [162, 163].

Thermal expansion and magnetostriction

Figure 4.50 shows the thermal expansion and the magnetostriction $\Delta L/L \parallel a$ as a function of temperature and magnetic field. In general, the field dependence of the order transitions resembles that extracted from the specific heat. Increasing the temperature at zero magnetic field a drop of approximately $2 \cdot 10^{-6}$ in $\Delta L/L$ signals the magnetic order. The obtained transition temperature of 240 mK is higher than the $T_{\mathrm{N}} = 220\,\mathrm{mK}$ found in the specific heat, marked by a dashed line in Fig. 4.50 (a). In addition, the transition shows a strong temperature hysteresis which is roughly centered around the transition temperature T_{N} obtained from the specific heat. The difference between both methods arises from the experimental issues during the acquisition of the specific heat data. A strong τ_2 effect, apparent in the specific heat raw data as discussed in Chapter 4.3.2, leads to a reduction of the hysteresis effects of c_p in comparison to the thermal expansion. In contrast to the step-wise acquisition of the specific heat, the thermal-expansion data are obtained while slowly, but continuously heating and cooling the sample. In addition, the average sweep rate is larger than in the specific-heat measurement which requires a lengthy temperature stabilization.

Before further discussing the data at finite magnetic field, the mechanism behind the hysteresis of the magnetic order transition at T_{N} is analyzed in more detail. The thermal expansion measurements with $\Delta L/L \parallel b$ were repeated at different sweep rates from 1 mK/min up to 50 mK/min (Fig. 4.51). Decreasing the sweep rate, the transition sharpens and at the smallest sweep rate a step-like anomaly arises, which is a typical indication for a first-order transition. The width of the hysteresis, however, does not

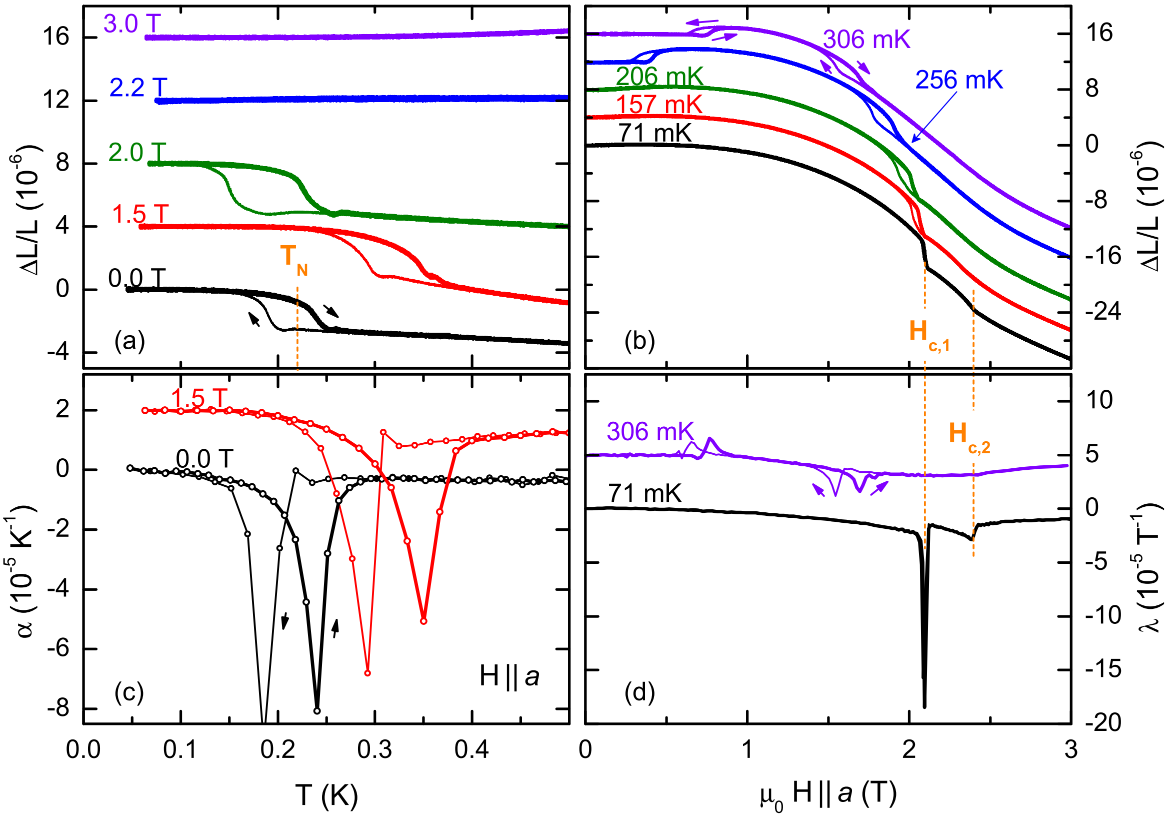

Figure 4.50: Thermal expansion (left) and magnetostriction (right) of Cs_2CoCl_4 in magnetic fields applied along a. The $\Delta L/L$ curves in panels (a) and (b) are offset with respect to each other by $4 \cdot 10^{-6}$. The values of α and λ in panels (c) and (d) are offset by $2 \cdot 10^{-6}$/K and $5 \cdot 10^{-5}$/T, respectively. Bold (thin) lines represent measurements with increasing (decreasing) temperature or field (indicated by arrows) acquired with rates of 3 mK/min or 5 mT/min, respectively.

remain finite in the limit of a vanishing sweep rate $\Gamma_s \to 0$. As plotted in the inset of Fig. 4.51, the dependence of the hysteresis width on Γ_s is rather fitted by a power-law with an exponent of 0.52. Due to the strong thermal coupling by clamping of the sample during the measurements, experimental origins for the narrowing of the hysteresis can be excluded. Instead, a simple model for the dynamics of domain walls at the phase transition can give an explanation for the observed square root dependence [164]. In this model the transition is assumed to be of first order and the motion of domain walls is supposed to be the driving mechanism of the transition rather than the nucleation of domains. At the Néel temperature T_N the ordered and the non-ordered phases in the system have the same energy. The difference of the free energy densities Δf between two phases is approximately linear in $T - T_N$ for a first-order transition and can be identified with a pressure on the domain wall. Moving a domain wall with an area A by a distance Δr leads to an energy gain

$$\Delta F = \Delta f \, A \, \Delta r. \tag{4.70}$$

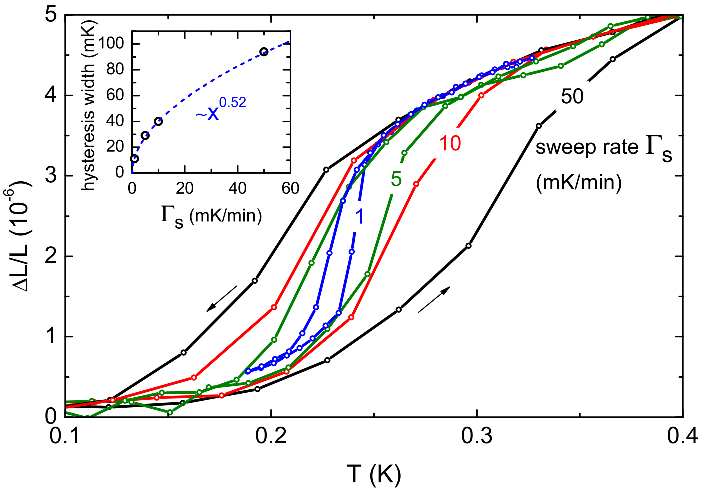

Figure 4.51: Temperature hysteresis of the Néel transition of Cs_2CoCl_4 in zero magnetic field. The thermal expansion $\Delta L(T) \parallel b$ was measured while continuously increasing or decreasing the temperature (indicated by arrows) with different sweep rates. Inset: The hysteresis width is a square root function of the sweep rate Γ_s.

Due to friction, the velocity v of a domain wall is proportional to the force, $v \propto \Delta f \cdot A \propto T - T_\mathrm{N}$. During the temperature sweep $T - T_\mathrm{N}$ changes with time as defined by the sweep rate Γ_s,

$$T - T_\mathrm{N} = \Gamma_s t. \tag{4.71}$$

The distance Δr that a domain wall has moved after time t therefore is given by

$$\Delta r = v \cdot t \propto \Gamma_s t^2. \tag{4.72}$$

Due to the increasing force as a function of time, Δr is a quadratic function of t. If after a time t_s a domain wall has traveled by a distance Δr_s which is of the order of the distance between nucleation centers of domains, the phase transition is completed. From Eqn. (4.72) one obtains the time $t_s \propto 1/\sqrt{\Gamma_s}$. The width of the hysteresis expressed in temperature, therefore, is given by

$$\Gamma_s t_s \propto \sqrt{\Gamma_s} \tag{4.73}$$

as observed in the experiment. Given that a latent heat was observed in the specific-heat raw data, the transition is inferred to be of first order and mainly driven by the motion of domain walls.

Upon the application of magnetic fields the hysteretic character of the transition is maintained and the transition temperature is shifted to higher temperature. A maximum transition temperature is reached at 1.5 T as indicated by peaks of the thermal expansion coefficient α centered around 320 mK (Fig. 4.50 (c)). Similar to the results for the specific heat, larger magnetic fields lead to a suppression of the critical temperature. However, no anomalies are present in the thermal expansion above 2.1 T, whereas clear peaks were observed in $c_p(T)$ at these fields. This contradiction is resolved by the fact that the thermal expansion α_i of the axis i is proportional to the uniaxial pressure dependence of the transition temperature, $\alpha_i \propto \frac{\partial T_c}{\partial p_i}$. In case of a second-order phase transition this derives from the Ehrenfest relation

$$\frac{dT_c}{dp_i} = T_c V_m \frac{\Delta \alpha_i}{\Delta c} \tag{4.74}$$

and in case of a first-order transition from the Clausius-Clapeyron relation

$$\frac{dT_c}{dp_i} = \frac{\Delta L_i/L}{\Delta S/V_m}. \tag{4.75}$$

The absence of anomalies in α does not exclude a phase transition, but only indicates that the transition temperature has a small pressure dependence. From Eqn. (4.75) one can, furthermore, deduce the pressure dependence of the critical temperatures by analyzing the sign of the anomalies of ΔL_i at the transition. Such, the evolution of phase diagrams as a function of pressure can be inferred as will be discussed in Chapter 4.3.3.

The magnetostriction in panels (b) and (d) of Fig. 4.50 at temperatures $T > 250\,\text{mK}$ shows two anomalies as a function of the magnetic field $H \parallel a$. Due to a maximum of $T_\text{N}(H)$ at about 1.5 T, the phase boundary between the paramagnetic and the ordered phase is crossed twice as a function of the field. These transitions are accompanied by a sizable hysteresis that narrows by decreasing the temperature. In case of the upper transition, the hysteresis even completely vanishes at the lowest temperature of 71 mK. The critical field is fixed by a sharp anomaly of λ at $H_{c,1} = 2.1\,\text{T}$. Additionally, a second transition appears at low temperature, which is seen as a kink in $\Delta L/L$ and as a small maximum in λ at a slightly larger magnetic field $H_{c,2} = 2.4\,\text{T}$ which is almost independent of the temperature up to 157 mK. No hysteresis is found at $H_{c,2}$ in any of the measurements which indicates that the transition at $H_{c,2}$ is of second order.

Magnetic field along *b*

A magnetic field along the b axis of Cs_2CoCl_4 is unique for the symmetry of the crystal, as it is the only field direction which lies within both types of magnetic easy planes (cf. Chapter 4.1.1). This fact gives rise to the description of the one-dimensional magnetism by the XXZ model in transverse fields, i. e., fields perpendicular to the local quantization axes of the spins. Concerning the magnetic order of Cs_2CoCl_4 this field direction is also special. As in the zero-field Néel-state the magnetic moments are oriented mainly along b, the application of magnetic fields collinear to the ordered spins might give rise to spin-flop transitions.

The specific heat for $H \parallel b$ (Fig. 4.52) indeed differs from those measured in magnetic fields applied along a and c. Instead of an enhancement of T_N by small fields, as in case of magnetic fields applied along a and c, here a suppression of the transition temperature by small magnetic fields is found. An additional small anomaly is seen around 130 mK in the 0.2 T-data, which indicates a more complex dependence of the ground state on the magnetic field. This anomaly is, however, only present at 0.2 T and not observed at 0.25 T, where again only a single peak is found. Starting above 0.4 T the single peak splits into two (marked by arrows in Fig. 4.52). The upper peak is shifted to higher temperatures in magnetic fields and reaches a maximum temperature of 0.35 K at a magnetic field of 1.5 T. The dependence of the lower peak on the magnetic field is more complex. First it is shifted to a minimum temperature of 117 mK at 0.75 T. Then it is shifted to higher temperature again and reaches a maximum of about 0.2 K at 1.5 T.

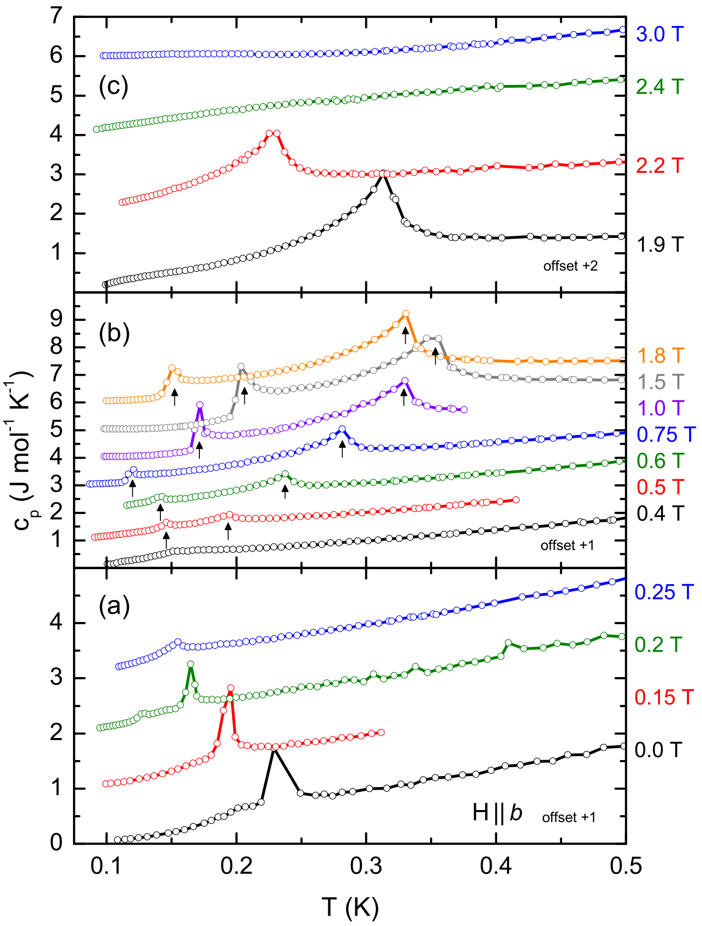

Figure 4.52: Specific heat of Cs_2CoCl_4 for different magnetic fields $H \parallel b$. Curves are offset with respect to each other. Two distinct phase transitions are present in a field range from 0.5 to 1.8 T (marked by arrows).

Increasing the magnetic field further, it is rapdily shifted to lower temperatures and cannot be observed any longer at 1.9 T. From 1.5 T to 1.9 T the upper transition has a comparably small dependence on the magnetic field before it is also shifted towards $T \to 0$ in magnetic fields larger than 2.2 T. At 3 T an overall suppression of c_p arises and the gap-like temperature dependence of the specific heat indicates the opening of a gap in the fully polarized phase.

Similarly, a rich magnetic-field dependence arises in the measurements of the thermal expansion and the magnetostriction (Fig. 4.53). The relative length change $\Delta L(T)/L$ at zero magnetic field shows a step-like anomaly close to T_{N} that is shifted to lower temperatures by increasing the magnetic field. As discussed above, the hysteresis of the transition depends on the temperature sweep rate. In contrast to the drop of $\Delta L/L$ upon increasing the temperature for $H \parallel a$, here, $\Delta L/L$ increases with increasing temperature, which indicates the contrary dependence of the transition temperature on pressures along b. Between 0.5 T and 1.3 T, the thermal expansion $\Delta L/L \parallel b$ is comparably featureless and does not show sharp anomalies as they are seen in the specific heat. Only above 1.5 T, at about 0.2 K a kink of $\Delta L/L$ reappears which shifts towards lower temperatures by increasing the magnetic field. Similar to the specific heat, two anomalies appear again at a field of 1.9 T which then are shifted to lower temperature by further increasing the field. Finally, both anomalies vanish at about 2.3 T. The magnetostriction data (Fig. 4.53 (c)) give further evidence for multiple phase transitions

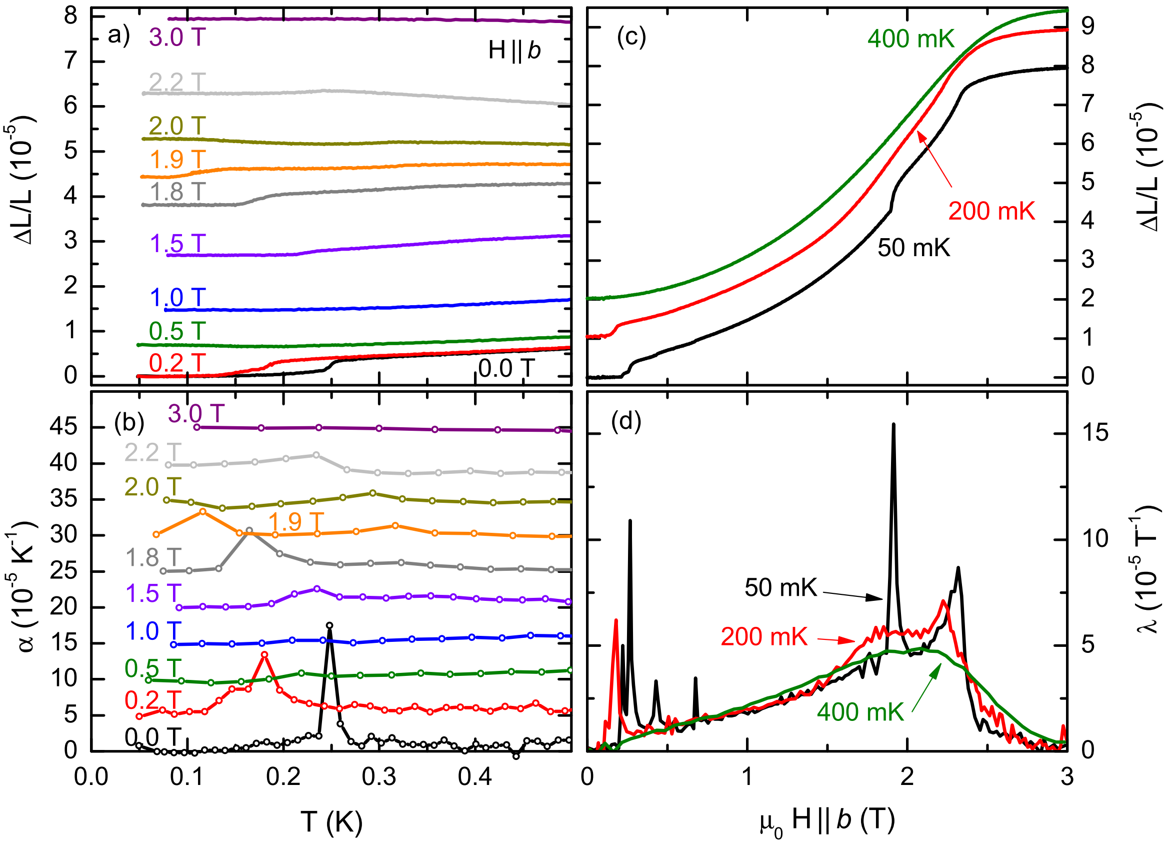

Figure 4.53: Thermal expansion (left) and magnetostriction (right) of Cs_2CoCl_4 in magnetic fields along *b*. In (a) the $\Delta L(T)/L$ curves for different magnetic fields are shifted according to the measured magnetostriction $\Delta L(H)/L$ at $T = 50\,\mathrm{mK}$ shown in (c). The other curves in (c) are offset by 10^{-5} and by $5 \cdot 10^{-5}/\mathrm{K}$ in (b). In all panels, only data obtained with increasing temperature or field are shown.

as a function of the magnetic field. A saturation of $\Delta L/L$ sets in at magnetic fields $\mu_0 H > 2.3\,\mathrm{T}$, similar to the magnetization, which for $H \parallel a$ is known to be saturated in this field range as well [8]. At the lowest temperature of 50 mK, three main features are found in the data. Two anomalies at 0.26 T and at 1.9 T are reflected as sharp peaks in λ, see Fig. 4.53 (d). Prior to the saturation an inflection point with an increased slope is found in ΔL which gives rise to a third peak of λ at about 2.3 T. Moreover, additional anomalies show up as small step-like increases of $\Delta L/L$ at 0.22, 0.43, and 0.67 T. However, they cannot be resolved when increasing the temperature to 200 mK. From the other dominant anomalies the upper two are broadened by increasing the temperature and can still be observed as maxima of λ at 200 mK. The lower transition remains sharp and is shifted to slightly smaller fields at that temperature. At 400 mK only a single, broad maximum of $\lambda(H)$ around 2 T remains, originating from the one-dimensional magnetism in the paramagnetic phase. In contrast to the magnetostriction data for fields along *a* no sizable field-induced hysteresis is found at any temperature in the data.

4.3.3 Phase diagrams

All phase transitions that were observed in the field- and temperature-dependent measurements of the thermal expansion and the specific heat are plotted in Fig. 4.54 as field versus temperature phase diagrams for the three principal magnetic field directions. In case of $H \parallel c$ only specific heat measurements were performed. For the other field directions the phase boundaries extracted from different techniques agree with each other within the bounds of hysteresis effects. As discussed above, the transition temperatures measured by the specific heat approximately bisect the hysteresis width seen in the thermal expansion. In general the phase diagrams for $H \parallel a$ and $H \parallel c$ closely resemble each other. The critical fields for $H \parallel a$ are slightly larger which can be explained by small anisotropies of the g tensor. The zero-field Néel temperature $T_\mathrm{N} \simeq 220\,\mathrm{mK}$ is initially enhanced by magnetic fields along a and c up to 1.5 T. Further increasing the field, the hysteresis is continuously narrowed and T_N is suppressed to zero temperature. From the combined observations by the different methods, an additional phase adjacent to the antiferromagnetic phase is revealed that is well defined by the specific heat data and also confirmed by the magnetostriction. The entry

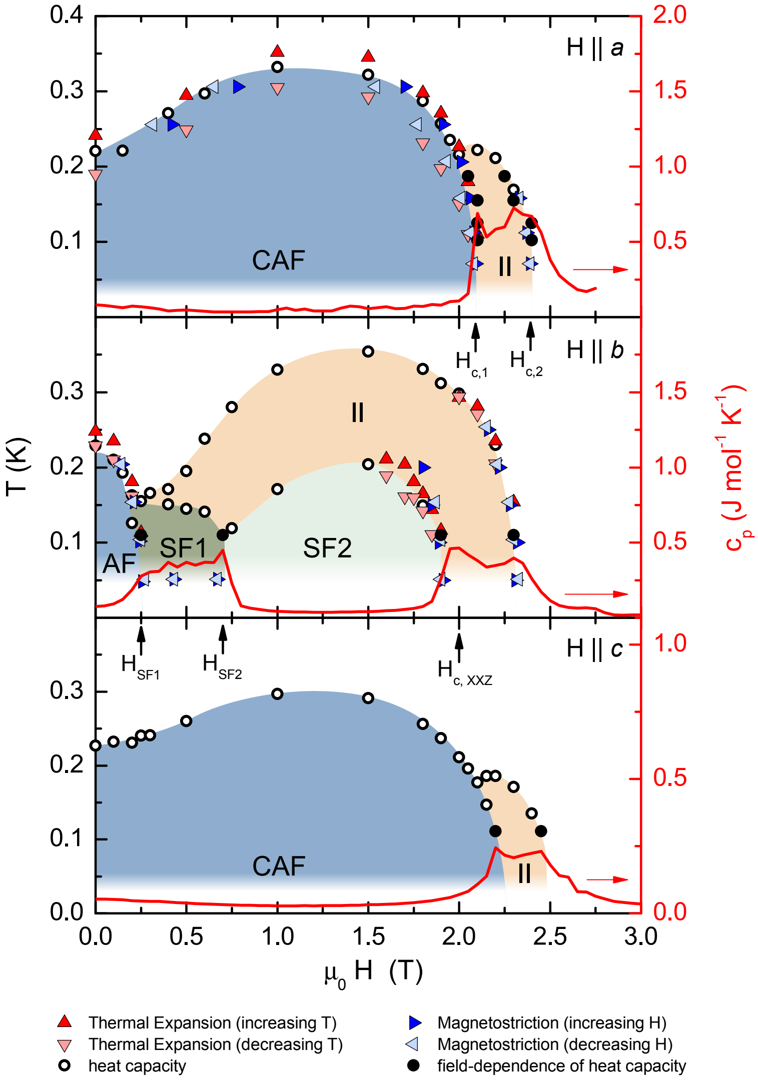

Figure 4.54: Phase diagrams of the low-temperature ordered phases of Cs_2CoCl_4 in the $H - T$ plane for magnetic fields along all three crystallographic axes. Symbols indicate anomalies in different thermodynamic properties. Shaded areas are guides to the eye. The field dependence of the specific heat (red lines, right scale) was measured at a constant temperature of 0.11 K. In case of $H \parallel b$ it indicates the presence of two spin-flop phases, SF1 and SF2. Within phase II $c_p(H)$ is strongly enhanced. $H_{C,XXZ}$ marks the critical field of the one-dimensional XXZ chain derived in Chapter 4.2.

of this phase, referred to as phase II in the following, is accompanied by a step-like increase of the specific heat (red line, right scale of Fig. 4.54) in-between the critical fields $\mu_0 H_{c,1} \simeq 2.1\,\mathrm{T}$ and $\mu_0 H_{c,2} \simeq 2.4\,\mathrm{T}$. In a study of the ordered phases of Cs_2CoCl_4 in fields along a, an identical critical field $H_{c,1}$ was found [8]. In magnetic fields larger than $H_{c,1}$ no signature of magnetic order were identified by Kenzelmann *et al.* and a spin-liquid state was proposed for magnetic fields $H_{c,1} < H < H_m$, where H_m is the saturation field of the magnetization. In addition to the neutron results of Kenzelmann *et al.*, both the specific heat and the magnetostriction, however, clearly indicate a phase transition at a second critical field $H_{c,2}$ and as a function of the temperature for fields $H_{c,1} < H < H_{c,2}$. This extension of the literature phase diagram gives good reason to doubt the conclusions of Kenzelmann *et al.* which are mainly based on a crossover line that was extracted from the magnetization.

The phase diagram for magnetic fields applied along b is more complex. Considering the similarities first, as a function of the magnetic field at lowest temperature a change of the ground state at magnetic fields $\gtrsim 2\,\mathrm{T}$ is indicated by the magnetostriction and by the heat capacity. The heat capacity in this field range is enhanced in the same way as for the entry of phase II for the other field directions. As, furthermore, the fitted power-law dependencies of $c_p(T)$ for $H_{c,1} < H < H_{c,2}$ are almost identical for all three magnetic field directions (see Fig. 4.55 and Tab. 4.5), the phase II is concluded to arise irrespective of the magnetic field direction. Yet, it is most favored by a magnetic field along b as demonstrated by the wide extension of the phase in the $H - T$ plane at finite temperature. From the specific heat data a maximum transition temperature around 1.5 T is found which represents an even larger enhancement of the zero-field T_N than for the other field directions. Moreover, phase II extends down to a small field of about 0.3 T where it merges with the antiferromagnetic phase and another low-temperature phase (SF1) in a triple point. The appearance of two peaks as a function of temperature in some of the specific heat data can be explained by additional low-temperature spin-flop phases. Differing from the other principal field directions, in case of $H \parallel b$ further low-temperature phases arise. According to Ref. 8 the magnetic order at zero field is characterized by moments mainly collinear to b, forming a small alternating angle of $\approx \pm 15°$ with the b axis. Neglecting this tilt the geometries with $H \parallel a$ and $H \parallel c$ are symmetry equivalent. In both cases an applied magnetic field is perpendicular to the ordered moments and leads to a canting of moments into the field direction. Due to the suppression of fluctuations by small fields,

		α		
Phase		$H\|\|a$	$H\|\|b$	$H\|\|c$
AF	(< 0.25 T)	3.5	3.5	3.5
SF1	(0.25-0.7 T)	-	3.02	-
SF2	(0.7-2 T)	-	complex	-
II	(≈2-2.4 T)	2.68(15)	2.63(4)	2.69(7)

Table 4.5: Exponents α of the power-law dependence of the specific heat $c_p \propto T^\alpha$ of Cs_2CoCl_4 for different magnetic field directions. The spin-flop phases SF1 and SF2 only arise in case of $H \parallel b$.

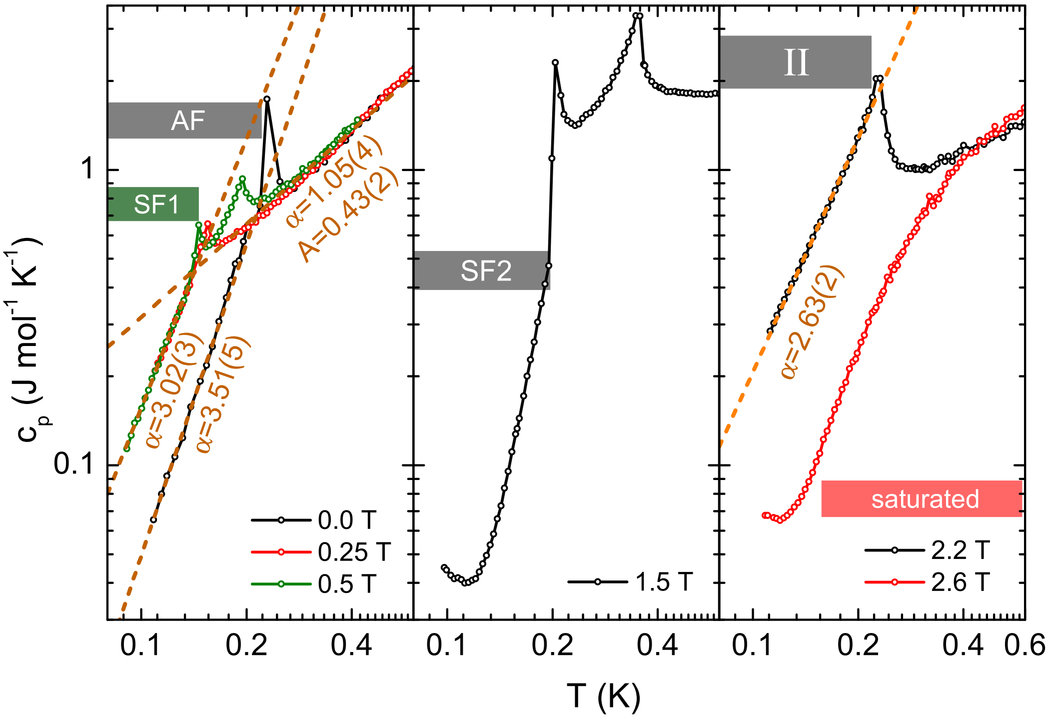

Figure 4.55: Selected temperature dependences of c_p in different low-temperature phases of Cs_2CoCl_4 in magnetic fields along b. Shaded labels indicate the respective low-temperature phase at the given magnetic field. Dashed lines are fits of $c_p(T)/R = A \cdot T^{\alpha}$.

in addition, the total ordered moment initially increases before the antiferromagnetic order reflections disappear at $H_{c,1}$. This gives rise to the denomination of this phase as a canted antiferromagnet (CAF). The case of $H \parallel b$, however, differs by the field having a large collinear component to the ordered moments. Such a configuration typically induces spin-flop transitions. The specific heat and the magnetostriction in fact indicate a transition at a small magnetic field $\mu_0 H_{SF1} \simeq 0.25\,\mathrm{T}$. While c_p strongly increases at H_{SF1}, the magnetostriction $\Delta L/L(H)$ shows a step-like anomaly, respectively the magnetostriction coefficient λ shows a sharp peak. The temperature dependence of c_p, that is described by a power-law with an exponent $\alpha = 3.5$ at zero field, also abruptly changes at H_{SF1} to a lower power of 3.0 (see Fig. 4.55), which clearly differs from the observation of a constant α in case of $H \parallel c < 0.5\,\mathrm{T}$ (Fig. 4.48). Up to $H_{SF2} \parallel b \simeq 0.7\,\mathrm{T}$ the exponent α remains constant. At H_{SF2} the magnetostriction coefficient shows another peak and the specific heat is strongly reduced again. At higher fields the temperature dependence of c_p is no more described by a simple power law. These findings are summarized in Tab. 4.5 and Fig. 4.55.

Further weak anomalies are seen at small magnetic fields in the magnetostriction data (Fig. 4.56), in both the data acquired with increasing and decreasing the magnetic field. At the lowest temperature of 50 mK, besides the two anomalies at H_{SF1} and H_{SF2}, that coincide with the rise of the heat capacity, small additional features occur which are marked by gray arrows in Fig. 4.56 and in case of the upper anomaly by symbols located within the phase SF1 in the phase diagram for $H \parallel b$ in Fig. 4.54. The upper anomaly close to 0.45 T, is hardly resolved at 100 mK and vanishes completely by

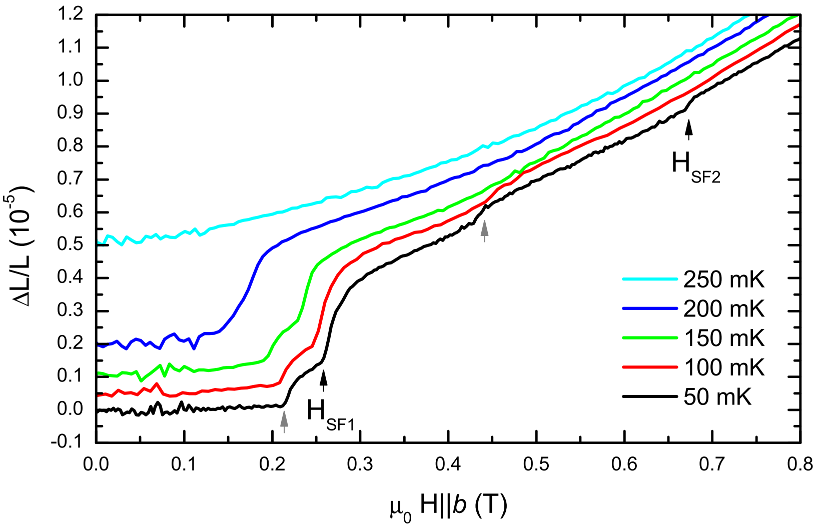

Figure 4.56: Low-temperature magnetostriction of Cs_2CoCl_4 in magnetic fields along b at selected constant temperatures. Labelled arrows mark the critical fields H_{SF1} and H_{SF2} that are in consensus with the sudden rise of the specific heat. Gray arrows indicate additional features in the data that might be related to domain effects. The data are offset by $5{\cdot}10^{-7}$.

increasing the temperature to 150 mK. The lower anomaly at about 0.21 T is present up to 150 mK and suggests a two-step character of the transition. At present the origin of these anomalies remains unsolved, although they might be related to domain effects.

Due to the mentioned geometry of the magnetic field being collinear to the ordered moments, an explanation of the transitions at H_{SF1} and H_{SF2} as a two-stage spin-flop transition arises. This kind of transition may develop from DM interactions between spins of neighboring chains. The symmetry of the Co-Cl-Cl-Co superexchange paths between spin chains in Cs_2CoCl_4 is indeed low enough to allow for DM interactions (see Chapter 4.1.2). As these interactions favor a perpendicular alignment of spins, they can stabilize a state where a spin-flop is performed only in every second neighboring chain. In an intermediate field range $H_{SF1} < H < H_{SF2}$ the energy gain by DM interactions overcomes the Zeeman energy of the non-flipped spin chain (see Fig. 4.57). Above H_{SF2}, finally, a fully spin-flopped state evolves. Such two-stage spin-flop transitions have previously been observed in other compounds with easy-plane magnetism, e. g., in $BaCu_2Si_2O_7$ [165].

In analogy to the textbook example of a spin-flop transition it can be shown from a classical calculation that by including DM interactions two phase transitions as a function of the magnetic field $\vec{h} = (0, h_y, 0)$ can emerge. In the geometry depicted in Fig. 4.57 the interaction terms can be explicitly calculated assuming classical spins parametrized by

$$\mathbf{S}_1 = \begin{pmatrix} \sin\alpha_1 \\ \cos\alpha_1 \\ 0 \end{pmatrix}, \quad \mathbf{S}_2 = \begin{pmatrix} \sin\alpha_2 \\ \cos\alpha_2 \\ 0 \end{pmatrix}. \tag{4.76}$$

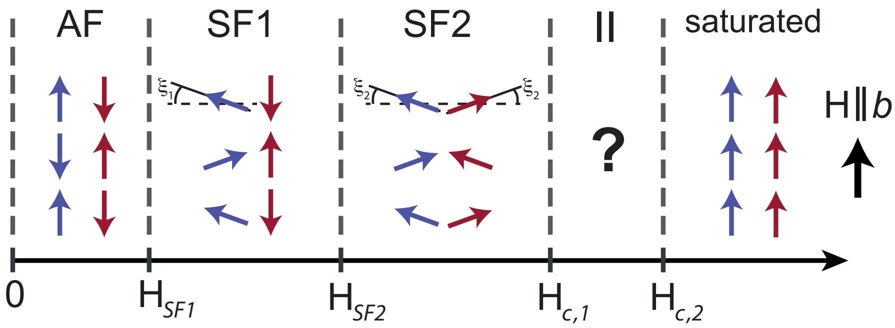

Figure 4.57: Schematic drawing of the magnetic ordered phases of Cs_2CoCl_4 as a function of the magnetic field $H \parallel b$. Arrows of different color represent spins of different chains with different easy-plane orientations. In the AF phase all spins are nearly antiparallel to each other and collinear to the field. In SF1 only half of the chains perform a spin-flop transition. SF1 is stabilized by Dzyaloshinskii-Moriya interactions between spins of different chains. In SF2, the DM energy is overcome by the field and a spin-flop is performed in all chains. Phase II could be an incommensurate or a nematic phase. In the saturated phase spins are aligned along the field direction.

The total energy of an arbitrary state with both spins in the x, y-plane, as defined by the angles α_1 and α_2, consist of five contributions:

$$\begin{aligned}
\text{intrachain:}\quad & E_J = -J\left(\sum \mathbf{S}_1^i \cdot \mathbf{S}_1^{i+1} + \mathbf{S}_2^i \cdot \mathbf{S}_2^{i+1}\right) \\
\text{DM:}\quad & E_{\mathrm{DM}} = -\mathbf{D} \cdot \mathbf{S}_1 \times \mathbf{S}_2 = -D_z \sin(\alpha_1 - \alpha_2) \\
\text{Zeeman:}\quad & E_Z = -\mathbf{h} \cdot (\mathbf{S}_1 + \mathbf{S}_2) = -h_y(\cos\alpha_1 + \cos\alpha_2) \\
\text{interchain:}\quad & E_{J'} = -zJ'\mathbf{S}_1 \cdot \mathbf{S}_2 = -zJ'\cos(\alpha_1 - \alpha_2) \\
\text{anisotropy:}\quad & E_A = -\mathcal{D}_{\mathcal{A}}\left[(\mathbf{S}_1 \cdot \mathbf{e}_y)^2 + (\mathbf{S}_2 \cdot \mathbf{e}_y)^2\right] = -\mathcal{D}_{\mathcal{A}}(\cos^2\alpha_1 + \cos^2\alpha_2).
\end{aligned}$$

In the term $E_{J'}$ describing the interchain interactions z stands for the number of neighboring chains to consider. The anisotropy $\mathcal{D}_{\mathcal{A}}$ defines the axis of the antiferromagnetic order at zero field and can be understood in analogy to the anisotropy gap in the magnon dispersion derived above. In the term E_{DM} the index i denotes the site along the chain 1, respectively 2. DM interactions are considered only within the x, y-plane, i. e., only the z-component D_z of the Moriya vector $\mathbf{D}$ contributes, weighted by the relative angle between the spins. Symmetric interactions J' between spins of different chains contribute by a cosine-dependence on the relative angle between them. Using the geometry sketched in Fig. 4.57 the energy of the spin configurations in the phases AF, SF1 and SF2 are given by

$$\begin{array}{lclllll}
E_{AF} & = & -2J & & & -zJ' & -2\mathcal{D}_{\mathcal{A}} \\
E_{SF1} & = & -J(1-\cos\xi_1) & -D_z\cos\xi_1 & -h_y\sin\xi_1 & & -\mathcal{D}_{\mathcal{A}}\left(\sin^2\xi_1 + 1\right) \\
E_{SF2} & = & -2J\cos\xi_2 & -D_z\sin 2\xi_2 & -2h_y\sin\xi_2 & -zJ'\cos 2\xi_2 & -2\mathcal{D}_{\mathcal{A}}\sin^2\xi_2
\end{array} \tag{4.77}$$

In the AF state all spins are collinear with the field. Thus, neither DM interactions nor the magnetic field term contribute. In the phase SF1 the intrachain exchange J is fully gained in one half of the chains and is lowered in the other with increasing the tilt angle ξ_1. In this state the interchain coupling J' cancels due to the alternating y-component of spins in chain 2. In phase SF2 the intrachain coupling is further reduced by the tilting of all spins into the field direction, whereas at the same time more Zeeman energy is gained by tilting. The tilt angles ξ_1 and ξ_2 are found by minimizing E_{SF1} and E_{SF2}. In second order of $\xi_{1,2}$ one finds that

$$\xi_1 = \frac{h_y}{J + D_z - 2\mathcal{D}_\mathcal{A}} \quad , \qquad \xi_2 = \frac{D_z + h_y}{J + 2zJ' - 2\mathcal{D}_\mathcal{A}}. \tag{4.78}$$

In turn, one obtains rather complex dependences of E_{SF1} and E_{SF2} on the magnetic field that in the present form only allow for numerical predictions. Neglecting the Dzyaloshinskii-Moriya term in phase SF2, simpler relations follow that agree well with the exact numerical results in the field range of interest. Phase SF2 is mainly determined by the large magnetic field and the influence of D_z is comparably small as it linearly enters Eqn. (4.77) scaled by $\sin\xi_2$, where ξ_2 is additionally assumed to be small. Therefore, DM interactions can be neglected in SF2, i. e., $D_z = 0$. Such, the energies of the spin-flop phases in second order of h_y are given by

$$E_{SF1} = -2J - \mathcal{D}_\mathcal{A} - D_z - \frac{h_y^2/2}{J + D_z - 2\mathcal{D}_\mathcal{A}}, \tag{4.79}$$

$$E_{SF2} = -2J - zJ' - \frac{h_y^2}{J + 2zJ' - 2\mathcal{D}_\mathcal{A}}. \tag{4.80}$$

Comparing the energies at zero field ($h_y = 0$) one finds that the AF phase is the ground state if $D_z < zJ' + \mathcal{D}_\mathcal{A}$, which means that DM interactions are small in comparison to the interchain coupling and the anisotropy which both favor a collinear order along b. If on the contrary $zJ' + \mathcal{D}_\mathcal{A} < D_z$ the phase SF1 becomes the ground state at zero field. Given that in the present definition $\mathcal{D}_\mathcal{A} > 0$ this translates into the condition that the antisymmetric part of the interchain interaction would have to be reasonably larger than the parent symmetric one, which then forced spins to align perpendicular to neighboring chains. As antisymmetric exchange mostly arises as a correction to the primary interaction this case is unlikely to happen in real systems. For any finite positive value of $\mathcal{D}_\mathcal{A}$ the phase SF2 cannot become the ground state at all. Thus, the present model correctly yields an antiferromagnetic ground state in zero field. Both phases SF1 and SF2, however, can be favored by a finite magnetic field. Depending on the ratios of the contributing interactions the half-spin-flop state SF1 eventually cuts the AF state at a smaller magnetic field than SF2 does. In second order of h_y the transition fields $h_{y,SF1}$ from the AF phase to SF1 and $h_{y,SF2}$ from the phase SF1 to SF2 are given by

$$h_{y,SF1} = \sqrt{2(D_z - 2\mathcal{D}_\mathcal{A} + J)(\mathcal{D}_\mathcal{A} - D_z + zJ')}, \tag{4.81}$$

$$h_{y,SF2} = \sqrt{2(\mathcal{D}_\mathcal{A} + D_z - zJ')/\left(2(J - 2\mathcal{D}_\mathcal{A} + 2zJ')^{-1} - (J + D_z - 2\mathcal{D}_\mathcal{A})^{-1}\right)}. \tag{4.82}$$

$$\tag{4.83}$$

Due to the complex analytical form of $h_{y,SF1}$ and $h_{y,SF2}$ the field dependence is analyzed easier by plotting the field dependence of E_{AF}, E_{SF1} and E_{SF2} for fixed values of the various constants. Fixing the anisotropy $\mathcal{D}_\mathcal{A} = 0.55\,\mathrm{K}$ to the value borrowed from the analysis of the power-law dependence of c_p above and assuming further constants

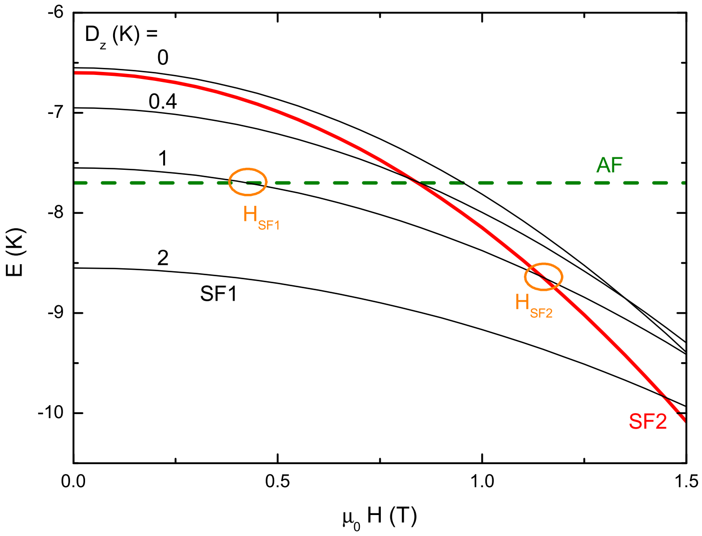

Figure 4.58: Energies of the phases AF (dashed green line), SF1 (red line) and SF2 (thin black lines) as a function of the magnetic field calculated from a classical model of interacting spin chains for different strengths of the DM interaction D_z using approximations of the further constants, see text. Orange circles mark the two-stage spin-flop transition fields that arise in case of an intermediate DM interaction strength.

from Chapter 4.2.2 like $J = 3\,\mathrm{K}$, $J' = \gamma J = 0.05J$ and $g = 3.27$, the dependence of the energies on the external field H is calculated which is related to h_y via $h_y = g\mu_\mathrm{B}\mu_0/k_\mathrm{B}H$. The interchain couplings are assumed to form a square lattice of chains ($z = 4$). Yet, the results hardly depend on the choice of z. As shown in Fig. 4.58 the energy of the antiferromagnetic state does not depend on the magnetic field at all and the field dependence of SF2 does not change for different values of the DM interaction D_z. For $D_z = 0$ the energy of state SF1 is larger than that of SF2 which yields the classical spin-flop transition at the crossing of E_{SF2} and E_{AF}. For very large values of D_z, the phase SF1 is strongly shifted downwards in energy and eventually can become the ground state at zero field. In Fig. 4.58 this scenario is represented by the line for a very large DM coupling $D_z = 2$. For intermediate values of D_z, an interesting case emerges. For an exemplary value of $D_z = 1\,\mathrm{K}$ two changes of the ground state as a function of the field arise. The critical fields are encircled in orange in Fig. 4.58 and given the simplicity of the model they agree reasonably well with the experimentally observed critical fields in $\mathrm{Cs_2CoCl_4}$ of 0.25 T and 0.7 T. The scenario of a two-stage spin-flop transition in $\mathrm{Cs_2CoCl_4}$ thus seems plausible and can be explained by a simple classical model. Nevertheless the value of $D_z = 1\,\mathrm{K}$ seems slightly too large as it exceeds that of the symmetric counterpart $J' = 0.15\,\mathrm{K}$. Further improvements of the model should account for the tilt of moments also in the AF ground state and include quantum effects. Further considering the different anisotropy planes in neighboring chains could help to extract physically meaningful properties like the coupling constants from a comparison to the phase diagrams and might even give hints at the nature of phase II that is preceded by SF2 in case of $H \parallel b$.

Pressure dependence of the phase diagrams

The anomalies of the thermal expansion at a phase transition according to the Clausius-Clapeyron relation in case of a first order transition, $dT_c/dp_i = T_c V_m \Delta\alpha_i/\Delta c$, and according to the Ehrenfest relation in case of a second order transition, $dT_c/dp_i = V_m \frac{\Delta L_i}{L}/\Delta S$, are proportional to the uniaxial pressure dependence of the transition temperature. For the pressure dependence of the critical field $H_c(p)$ the magnetic versions of these equations can be derived using the Maxwell relation $\frac{\partial S}{\partial p}\Big|_{T,H} = -\frac{\partial V}{\partial T}\Big|_{p,H}$ and $S = -\frac{\partial G}{\partial T}$ in case of a second order transition by equating the entropy of two phases:

$$S_1\left(H_c(p), p, T = const\right) = S_2\left(H_c(p), p, T = const\right) \tag{4.84}$$

$$\Rightarrow \frac{\partial S_1}{\partial H}\bigg|_p \cdot \frac{dH_c}{dp} + \frac{\partial S_1}{\partial p}\bigg|_H = \frac{\partial S_2}{\partial H}\bigg|_p \cdot \frac{dH_c}{dp} + \frac{\partial S_2}{\partial p}\bigg|_H \tag{4.85}$$

$$\Rightarrow -\frac{\partial^2 G_1}{\partial H \partial T}\bigg|_p \cdot \frac{dH_c}{dp} - \frac{\partial V_1}{\partial T}\bigg|_p = -\frac{\partial^2 G_2}{\partial H \partial T}\bigg|_p \cdot \frac{dH_c}{dp} - \frac{\partial V_2}{\partial T}\bigg|_p \tag{4.86}$$

$$\Rightarrow \frac{dH_c}{dp} = \frac{V\Delta\alpha}{\Delta(\partial M/\partial T)} \tag{4.87}$$

For uniaxial pressure p_i along the axis i one obtains

$$\frac{dH_c}{dp_i} = \frac{V\Delta\alpha_i}{\Delta(\partial M/\partial T)}. \tag{4.88}$$

In case of a first order transition one obtains another expression for the pressure dependence of the critical field from the equality of the Gibbs free energy at the critical field:

$$G_1\left(H_c(p), p, T = const\right) = G_2\left(H_c(p), p, T = const\right) \tag{4.89}$$

$$\Rightarrow \frac{\partial G_1}{\partial H}\bigg|_p \cdot \frac{dH_c}{dp} + \frac{\partial G_1}{\partial p}\bigg|_H = \frac{\partial G_2}{\partial H}\bigg|_p \cdot \frac{dH_c}{dp} + \frac{\partial G_2}{\partial p}\bigg|_H \tag{4.90}$$

$$\Rightarrow -m_1\frac{dH_c}{dp} + V_1 = -m_2\frac{dH_c}{dp} + V_2 \tag{4.91}$$

$$\Rightarrow \frac{dH_c}{dp} = \frac{\Delta V}{\Delta m} = \frac{\Delta V/V}{\Delta M} \tag{4.92}$$

Here, m_i is the extensive magnetic moment of the system which relates to the experimentally observed magnetization density M_i via $m_i = M_i V_i$. For uniaxial pressure one finds in analogy that

$$\frac{dH_c}{dp_i} = \frac{\Delta L_i/L}{\Delta M}. \tag{4.93}$$

The step-like increase of $\Delta L/L$ at zero field measured along b for heating above T_{N} for instance indicates a rising Néel temperature if pressure was applied along the b axis of the crystal. The pressure dependence of the critical field is more complex due to the contribution of the magnetization that is known in magnetic fields along a from Ref. 8, but only for a single fixed temperature. Thus, only the magnetic version of the Ehrenfest relation, Eqn. (4.93), can be applied to the phase boundary of the antiferromagnetic phase. Collecting the anomalies in all data measured along the a and the b axis the pressure dependence of the whole phase diagrams can be estimated. The approximate size of the respective anomalies at the various phase boundaries are sketched by arrows in Fig. 4.59. In case of $H \parallel a$, a consistent picture is obtained from

Figure 4.59: Modifications of the low-temperature phase boundaries of Cs_2CoCl_4 in magnetic fields and under pressure applied collinear to the field direction. Red arrows indicate the approximate size and sign of anomalies in the thermal expansion measurements, while blue arrows relate to the magnetostriction. The change of the phase boundaries under pressure is pictured qualitatively by the dashed green lines.

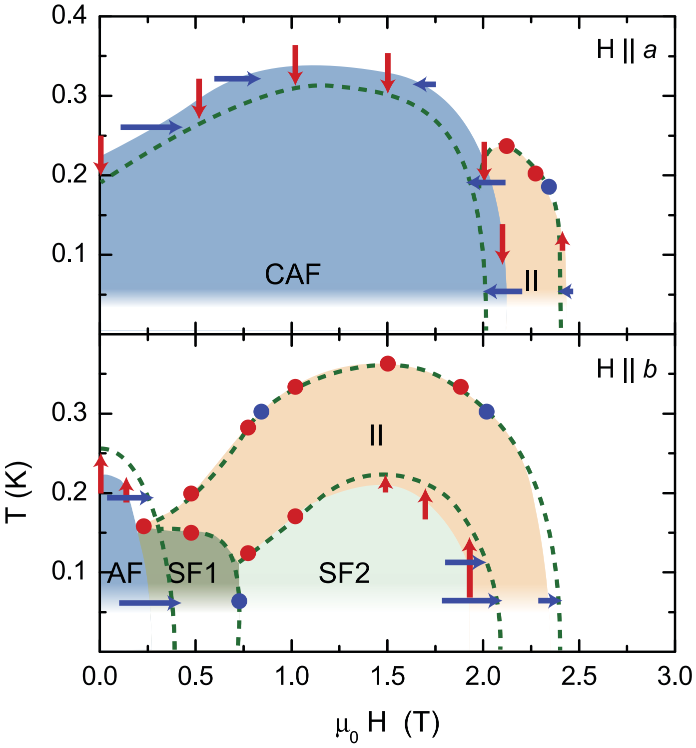

the thermal expansion and the magnetostriction data. The absence of features in case of magnetic fields $H \parallel b$ around 1.5 T indicates a constant phase boundary as a function of pressure (shown by the dots in the intermediate field range). At the critical field $H_{SF1} \parallel b$ of the antiferromagnetic phase of about 0.25 T the magnetostriction ΔL_b is increased step-like. In the scenario of a two-stage spin flop the magnetization should increase as well, which in turn, based on Eqn. (4.93), suggests an enhancement of the critical field by pressure. For both magnetic field directions $H \parallel a$ and $H \parallel b$ the antiferromagnetic phase is influenced most by applying pressure. The physical meaning of the transformed phase boundaries is hard to identify due to the interplay of the orbital-, lattice- and spin-degrees that all may contribute to the formation of magnetic phases and all may change differently under pressure. One possible interpretation of the opposing pressure dependence of the (C)AF phase could be that in case of pressure applied along the chain direction b, an increased intrachain coupling (as consistently observed in Chapter 4.2) leads to an enhancement of the critical temperature and the critical field. This explanation, however, is in opposition to the decrease of T_{N} for pressures applied along a for which one might speculate about an enhancement of the non-frustrated interlayer coupling, which in turn should increase T_{N} as well. Yet, the sheer size of interchain couplings typically plays only a minor role for the magnetic ordering temperature and other effects may overcome its increase. From the absence of clear anomalies at the spin-flop field H_{SF1}, a vanishing pressure dependence of H_{SF1} can be deduced. This might be understood from the fact that the transition at H_{SF1} into a state with perpendicular spins is mainly triggered by the antisymmetric couplings between chains and not by the intrachain coupling that one may expect to change most under pressure along b. Yet, the true origin of the overall pressure dependences of the phase diagrams might be hidden in more subtle properties of the electronic systems.

4.3.4 Non-principal field directions

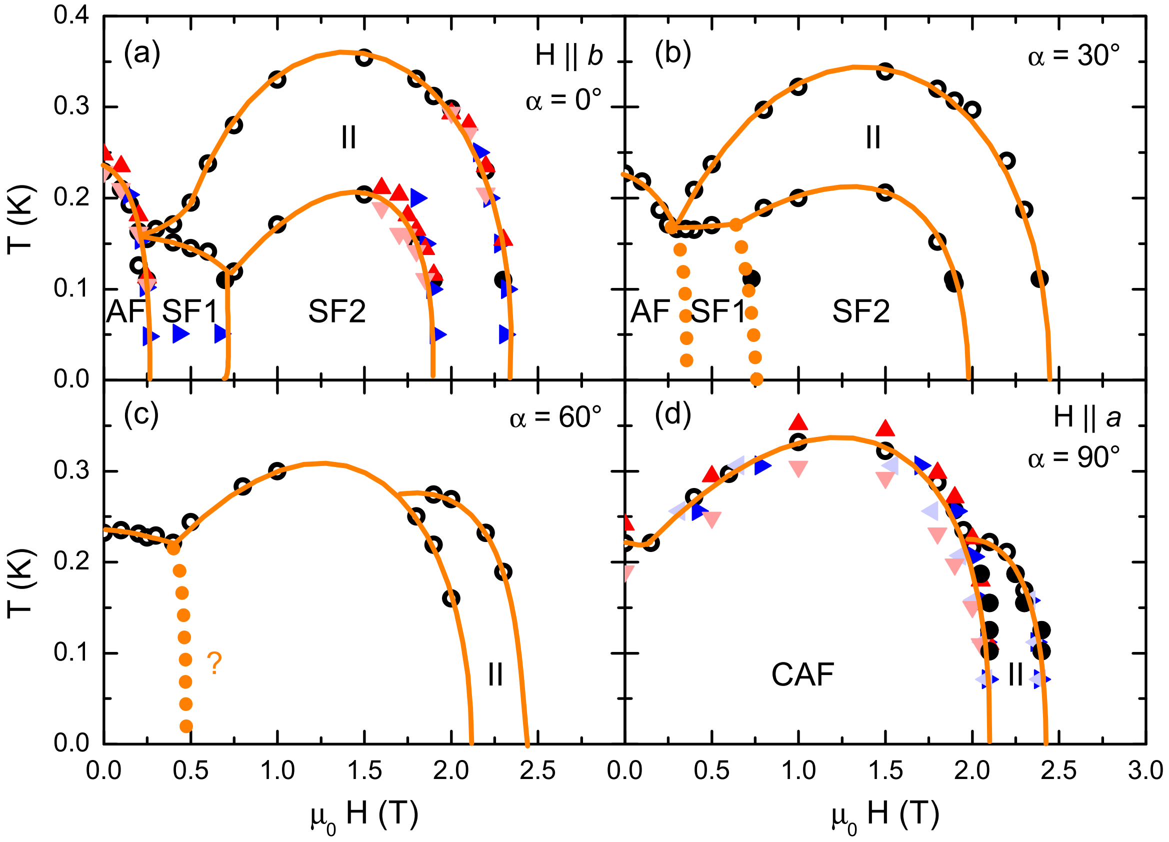

Figure 4.60: Low-temperature phase diagrams of Cs_2CoCl_4 for different magnetic-field directions $H \parallel (\sin\alpha\ \cos\alpha\ 0)$ as obtained from different thermodynamic quantities. Red triangles represent features of the thermal expansion, blue triangles stem from the magnetostriction, open (closed) symbols are extracted from the temperature- (field-)dependence of the specific heat. Solid orange lines are guides to the eye, dotted lines are approximate crossover lines.

From the identical power-law dependence of the specific heat and the similar values of the critical fields $H_{c,1}$ and $H_{c,2}$ for different magnetic field directions it was concluded that phase II arises by a similar mechanism for all field geometries. In case of $H \parallel b$, phase II, however, encloses a substantially larger $H-T$ phase space than for the other directions, such that one might question the similarity of these phases. In order to identify the different occurrences of phase II measurements of the low-temperature specific heat have been performed for non-principal field directions in between the crystallographic axes a and b. Magnetic fields were applied along $(\sin\alpha\ \cos\alpha\ 0)$ where $\alpha = 30°$ and $60°$. The phase diagrams were obtained from the anomalies of the specific heat data (see full data sets, shown in Appendix B). In Fig. 4.60 the results are compared to the phase diagrams for $\alpha = 0°$, i. e., $H \parallel (0\ 1\ 0)$, and for $\alpha = 90°$, i. e., $H \parallel (1\ 0\ 0)$. For $\alpha = 30°$ the main features of the phase diagram are identical to those for $H \parallel b$. The low-field spin-flop transitions are observed at similar critical fields as for $\alpha = 0°$. The boundaries of phase II are only slightly modified and a small shift towards larger fields is found, that can be explained by an increasing contribution of the larger g factor of the a axis. In the field dependence of the specific heat (Fig. 4.61), phase II is indicated

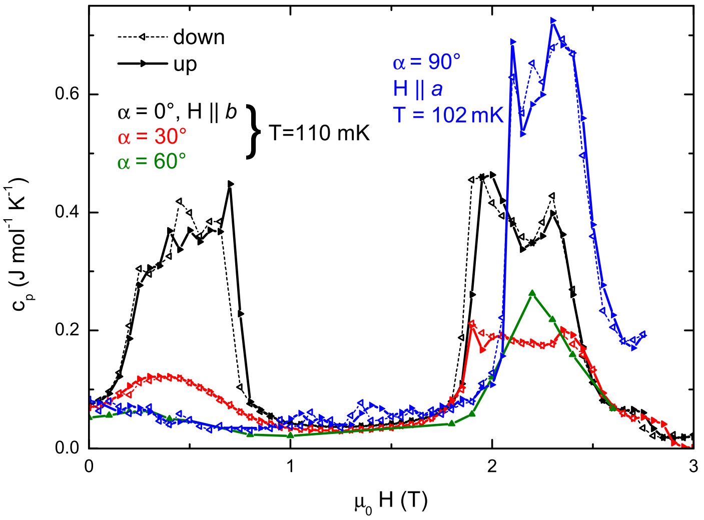

Figure 4.61: Specific heat $c_p(H)$ measured for different field directions $H \parallel (\sin\alpha \ \ \cos\alpha \ \ 0)$. Solid (dashed) lines represent data acquired with increasing (decreasing) the field. Data for $\alpha = 60°$ are interpolated from the temperature dependence $c_p(T)$ resulting in a lower data quality. Data for $\alpha = 90°$ were acquired at a constant temperature of 102 mK. Measurements for $\alpha < 90°$ were performed at 110 mK.

by the same plateau-like increase in between the two critical fields. The absolute value of the plateau is, however, decreased by about half in comparison to $\alpha = 0°$. The signatures of the spin-flop transitions at small fields are strongly broadened upon tilting. Thinking of the applied field as a superposition, the component along a at $\alpha = 30°$ already is half of the external field and may lead to an increasing collinear moment along a concurring with the spin-flop physics for fields along b. The spin-flop transitions thus may change their character to a continuous evolution of ordered moments that is rather described as a crossover. In Fig. 4.60 (b) the crossover fields as extracted from the maximum slope of $c_p(H)$ are indicated by dotted lines in the low-field region.

Increasing the tilt angle α to 60° leads to a further modified phase diagram, see Fig. 4.60 (c). Phase II no more merges with other phases at small fields in a tricritical point, but rather resembles the shape for $H \parallel a$. In the field dependence of c_p no signatures of spin-flop transitions are found at small fields. Yet, this may partly originate in the lower point density for this field direction. The initial field dependence of T_N shows a negative slope and a kink at $\simeq 0.5$ T similar to the spin-flop scenarios at smaller α and different from the phase boundary for $H \parallel a$. This suggests that a similar continuous change of the ground state is present for $\alpha = 60°$ than for $\alpha = 30°$ that is not resolved in the low-temperature specific heat. The suggested crossover region is indicated by a dotted line in Fig. 4.60 (c). The associated critical field is larger than for smaller α which could be understood from the small effective field along b that triggers the spin-flop transition and that is reduced by half for $\alpha = 60°$. However, the present data cannot proof this claim. Concerning the primary question on the identical nature of phase II for different α, the obtained phase diagrams do not give a uniform picture. Comparing $\alpha = 90°$ with $\alpha = 60°$ only a slight enhancement of phase II towards the shape at smaller α is seen. While the low-temperature spin-flop phases transform continuously, phase II, in contrast, seems to be rather stable upon variations of the tilt angle α away from the principal axes. On the plus side, this allows for extended microscopic studies of Cs_2CoCl_4 also by methods like neutron scattering where the accuracy of the magnetic field alignment might be lower than the ±2° in the present experiments.

4.3.5 Phase II

While the low-field phases AF, SF1 and SF2 could be successfully modeled by classical theories, the nature of phase II is still open. From the thermodynamic quantities it was found to arise in a restricted field range before saturation. The direction of the magnetic field seems to be important only at finite temperature. In the following, three possible scenarios are discussed: (i) a spin-liquid phase as proposed in Ref. 8, (ii) an incommensurate phase similar to that in Cs_2CuCl_4 [116, 117] and (iii) a nematic phase.

Due to the lack of antiferromagnetic reflections in the neutron scattering data for $H \parallel a$ within the bc plane and due to the non-saturation of the magnetization Kenzelmann *et al.* propose that phase II is a spin-liquid state. A spin-liquid state is characterized by the absence of magnetic order in the ground state. In quantum spin liquids the magnetic order is destroyed by quantum fluctuations and although a variety of compounds are discussed to be spin liquid candidates, amongst others, the prediction of a spin liquid state in the isotructural Cs_2CuCl_4 has recently been questioned [116]. The confusion about spin liquids partly arises from the lack of a universal theory and a definite experimental indication for it [166]. Although there are rare examples for finite temperature transitions into a spin liquid state [167], one would typically expect a continuous evolution of thermodynamic properties as a function of temperature with no indication of magnetic order transitions down to zero temperature. The clear presence of peaks in the present data, however, indicates a thermodynamic phase transition and suggests that in the magnetic field range of $H_{c,1} < H < H_{c,2}$ not a disordered spin-liquid state is realized, but rather that another type of so far unidentified order occurs in phase II of Cs_2CoCl_4.

Another possible scenario for phase II is an incommensurate magnetic state. For the isostructural Cs_2CuCl_4 it was shown that at high fields the consequence of frustration is magnetic order at incommensurate momentum [116]. The copper ions in Cs_2CuCl_4 show an almost complete isotropic Heisenberg magnetism, whereas the magnetism in Cs_2CoCl_4 is strongly anisotropic with magnetic easy planes alternating from chain to chain. Yet, both compounds are described by the same space group *Pnma* and share the same magnetic lattice of linearly coupled, frustrated triangular layers (Fig. 4.6). The symmetry-based arguments of Ref. 116, therefore, apply to Cs_2CoCl_4 as well. The consequence of the magnetic frustration is a shift of the minima of the gapped magnon excitations at high fields from the commensurate value of π to an incommensurate value. This can be understood from the fact that the frustrated coupling does not benefit from antiferromagnetic order, but from an incommensurate state. The tilt angle arises from the competition of the interaction within the chains, tending to align the spins collinear, with the frustrated coupling that linearly benefits from a state where neighboring spins along the chains tilt by a small angle from one site to the next. Reducing the field from the fully polarized state at reasonably low temperature the emerging incommensurate order can be thought of as a condensate of magnons at incommensurate momentum. This state could be further stabilized by DM interactions that also favor non-collinear spins. A further complication, however, arises from the magnetic easy planes in Cs_2CoCl_4 as noted in Ref. 8. At small magnetic fields, the presence of two easy-plane orientations establishes an effective Ising anisotropy along b due to interchain-couplings as this direction is the only common direction of easy planes. Depending on the angle 2β between the planes the formation of an incommensurate helical state, thus, becomes less effective and even is degenerate with the antiferromagnetic state if the planes are orthogonal ($2\beta = \pi/2$). In Cs_2CuCl_4 an incommensurate ordering wave vector along b was reported [117] and expected from theory [116]. In neutron scattering on Cs_2CoCl_4 [8], however, no signals of magnetic order were detected within the *bc* plane. Therefore, the ordering vector is either not within the *bc* plane due to additional non-discovered mechanisms or another phase comes into play.

The absence of magnetic order signals in phase II supports the explanation of the phase by a third scenario. In pnictide superconductors a nematic state arises from magnetic frustration depending on the electron doping [168]. As the magnetic lattice of Cs_2CoCl_4 also decomposes into two non-frustrated sublattices that are coupled in a frustrated way, similar arguments might hold. Denoting the magnetization of the non-frustrated pairs of chains (sites 1 and 2) by M_A and that of sites 3 and 4 by M_B, the free energy of the system does not contain a term $\propto M_A M_B$ linear in both magnetizations. Bond-terms between a site in the subsystem A and a second site in B cancel with its frustrated counterpart in case of antiferromagnetic correlations. A quadratic term $(M_A M_B)^2$, however, is allowed in the free energy. Although both systems can have zero magnetization, i.e., $\langle M_A \rangle = \langle M_B \rangle = 0$, in a nematic state the fluctuations of both systems are correlated, such that $\langle M_A M_B \rangle \neq 0$. Due to the free energy term $(M_A M_B)^2$ the frustration is lifted and a nematic state with correlated fluctuations may be stabilized. As discussed in Ref. 168, the resulting nematic state requires a large correlation length within the subsystems A and B, as realized, here, due to the increasing correlation length of the XY-type spin chains at low temperature [161, 169]. In this case the nematic phase should evolve as soon as the low-temperature transition is of second order. This agrees with the present experimental observations for Cs_2CoCl_4. The transition into the AF or CAF phase is of first order, whereas the transition into phase II always is of second order.

Although the scenario of a nematic phase is compatible with the experimental observations in this work and in literature, the present data cannot give evidence for its existence and a further analysis by microscopic methods is required.

4.3.6 Conclusion

From the combination of specific-heat and thermal-expansion data the magnetic field versus temperature diagrams of the ordered phases of Cs_2CoCl_4 were derived. In a small field range of about 0.3 T width a well-defined phase (II) bordering the antiferromagnetic phase is found. Two possible scenarios for its physics were proposed: (i) incommensurate magnetic order, (ii) a nematic phase characterized by correlated fluctuations. For magnetic fields applied along the crystallographic b axis, in addition, two further field-induced transitions arise. They can be understood as a two-stage spin flop transition arising from DM interactions between spin chains that stabilize an intermediate state with perpendicular moments. This kind of transition may be explained by a simplified microscopic model which yields an estimate of the order of the asymmetric exchange of about 1 K. An analysis of the symmetric and antisymmetric interactions between spin chains consistently yields an explanation of the tilt of moments in the zero-field ordered state. Similar sizes of DM interactions as those that trigger the two-stage spin flop transition, however, require an in-plane anisotropy of about 3 K. Yet, no signatures of a sizable in-plane anisotropy are seen in the thermodynamic data above the magnetic ordering temperature. Furthermore, due to symmetry, DM interactions should cancel for the whole lattice. Both issues may be resolved by a small structural distortion accompanying the magnetic order.

Given the complex magnetic ordering phenomena at low temperature, one may ask for the relation of these to the one-dimensional magnetism and whether signatures of the 3D order manifest also in the 1D regime and vice versa. In the study of the one-dimensional magnetism of Cs_2CoCl_4 in Chapter 4.2 a good agreement of the specific heat and the thermal expansion with the one-dimensional XXZ model in transverse magnetic fields was found. Due to the non-commuting magnetic field term, the rotational symmetry of the model is broken and a quantum phase transition emerges at a critical field which depends on the anisotropy of the chain. The critical behavior is indeed seen in the experiment as maxima of the thermodynamic quantities which scale linearly with the reduced field $|H - H_{C,XXZ}|$ (see Chapter 4.2.3). The compliance with the theory suggests a quantum phase transition in Cs_2CoCl_4 at a critical field $H_{C,XXZ} \simeq 2.0\,\mathrm{T}$. Due to finite interchain couplings, below a certain temperature magnetic order arises in real crystals. Applied magnetic fields H instead favor a fully polarized state and thus suppress the antiferromagnetic order, reflected in a field dependence of T_N. One might expect that the magnetic field where the antiferromagnetic order is suppressed to zero temperature coincides with $H_{C,XXZ}$ such as in other text-book examples for quantum criticality like $LiHoF_4$ [1], $CoNb_2O_6$ [2], $YbRh_2Si_2$ [170]. Cooling down at the critical field, the specific heat, in contrast, clearly indicates a finite-temperature transition into phase II. Furthermore, $H_{C,XXZ}$ does not match with any of the zero temperature critical fields $H_{c,1}$ or $H_{c,2}$, but rather lies within the phase II (see Fig. 4.54). The rather complex shape of the low-temperature phases of Cs_2CoCl_4 begs for the question how the magnetic order relates to the seeming quantum critical behavior at elevated temperature and whether the field dependence of the ordered states bears any resemblance with that of the one-dimensional chain.

In Ref. 8, the zero temperature phases of the XY model in a transverse field are discussed in prospect of a spin-liquid ground state proposed from neutron data. Quoting an early numerical study of the XY model [171], the authors build on the distinction between a field of $\sqrt{2}J$, where the ground state is said to be the classical Néel state, and a second field of $1.5J$ where the order breaks down and a quantum phase transition takes place. However, the conclusions of Ref. 171 are based on calculations for rather small systems of only 10 sites. In further theoretical analyses of the model, only a single critical field of the chain is discussed and obtained with high precision [67, 172]. The mean-field result in fact is $\sqrt{2}J$ for the XY model, respectively $\sqrt{2(1+\Delta)}$ for the XXZ model, while a slightly larger critical field of $\approx 1.5J$ is found by DMRG for the

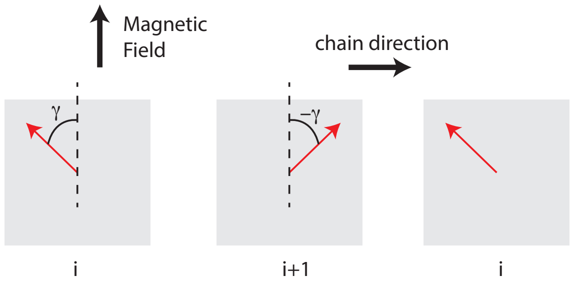

Figure 4.62: Sketch of the Néel type ground state of the *XXZ* model. At the critical field, the spins (red arrows) lie within their respective magnetic easy plane (shaded squares) and form an angle γ with the magnetic field direction.

XY model, which might explain the confusion about the two different critical fields in Ref. 8. The Néel-type ground state at the critical transverse field, however, should not be confused with the classical Néel state with collinear antiferromagnetic spins along the primary quantization axis z. It rather equals the strongly entangled high-field ground state in the famous transverse field Ising model. There, the magnetic field intermixes spin-up and spin-down states, such that at large fields the wave function is a product of the quantum mechanical superpositions of Ising-spin states $|{\rightarrow}\rangle_k = (|{\uparrow}\rangle_k + |{\downarrow}\rangle_k)/\sqrt{2}$ at each site k. In analogy, the transverse field in the *XXZ* models induces a spin-flop type state. At the critical field the ground state $|\Psi_{\text{Néel}}\rangle$ factorises into single-site states on two sub-lattices [172],

$$|\Psi_{\text{Néel}}\rangle = \prod_i |\psi_i\rangle\,, \tag{4.94}$$

$$|\psi_{2i+1}\rangle = a_1\,|{\uparrow_{2i+1}}\rangle + b_1\,|{\downarrow_{2i+1}}\rangle\,, \tag{4.95}$$

$$|\psi_{2i}\rangle = a_2\,|{\uparrow_{2i}}\rangle + b_2\,|{\downarrow_{2i}}\rangle\,, \tag{4.96}$$

where the coefficients a_1, a_2, b_1, b_2 can be identified with the spatial orientation of the vector $(\langle S_x^i\rangle\,, \langle S_y^i\rangle\,, \langle S_z^i\rangle)$ of the spin components expectation values at odd $(2i+1)$ and even $(2i)$ sites. At the critical field, the coefficients take such values that the spins lie within the easy planes and form a spin-flop type state with an angle 2γ between the two sublattices. This configuration is depicted in Fig. 4.62. According to Ref. 172, the angle γ relates to the anisotropy $\Delta = J_z/J_{xy}$ of the spin chain,

$$\cos\gamma = \sqrt{\frac{1+\Delta}{2}}. \tag{4.97}$$

In the *XY* limit ($\Delta = 0$), neighboring spins are orthogonal, i. e., $\gamma = 45°$. For finite anisotropies ($0 < \Delta < 1$ the angle reduces and becomes zero in case of the Heisenberg model ($\Delta = 1$). The resulting alternation of expectation values perpendicular to the field for $\Delta < 1$ resembles the Néel state. From the perspective of the one-dimensional system only a single critical field of about 2.0 T is indicated at which the ground state is of a "spin-flopped" Néel-type. In the context of the proposed two-stage spin-flop transition the spin configuration in the phase SF2 actually resembles this state. Thus, one may argue that the state SF2 is favored close to the critical field of the one-dimensional spin chain and an extension of SF2 across the critical field could be well explained. However, as clearly resolved within the experimental resolution, the upper critical field of SF2 is about 0.1 T smaller than the critical field of the spin chain. This might be explained by the various interchain couplings that favor phase II over SF2.

As shown in Ref. 172, the Néel-type ground state emerges in XXZ chains irrespective of the field direction at a critical field

$$h_c/J_{xy} = \sqrt{\frac{2(1+\Delta)^2}{2\cos^2\Theta + (1+\Delta)\sin^2\Theta}}. \tag{4.98}$$

Here, Θ is the angle of the external field $\parallel (\sin\Theta, 0, \cos\Theta)$ with respect to the local z axis. In a magnetic field applied to Cs_2CoCl_4 not along the crystallographic b axis, thus, a different critical field of the spin chain arises. Therefore, one may expect the occurrence of the 1D Néel type ground state in the low-temperature phases for $H \parallel a$ and $H \parallel c$ as well, but at a slightly different magnetic field, as described by Eqn. (4.98). For magnetic fields applied to Cs_2CoCl_4 not along the crystallographic axes, but along arbitrary directions, the two different types of easy plane orientations have to be considered and in principal two different critical fields can emerge. In case of $H \parallel c$, however, the critical field for both types of spin chains is identical due to symmetry. Assuming a rotation angle $\pi/2 - \Theta = \beta = 38°$ of the easy planes with respect to the c axis, the critical field upon application of the external field along c is given by

$$h_c^{|\beta|=38°}/J \approx 1.2 + 0.93\Delta. \tag{4.99}$$

The critical field is about 15% smaller than that in case of a transverse magnetic field, i. e., within the XY plane ($\Theta = 0$). Assuming the same g factor as for $H \parallel b$, one obtains a critical field $H_{c,XXZ} \parallel c \approx 1.7\,\mathrm{T}$ using the anisotropy $\Delta \approx 0.12$ derived for Cs_2CoCl_4. In the low-temperature data, however, no features are present at this field. Even more, the boundaries of the phase CAF, respectively of phase II, are rather shifted to larger magnetic fields. One explanation might be given by the fact that the antiferromagnetic ground state with spins mainly along b already represents the spin-flop state for fields applied along a and c. In that sense small magnetic fields just support the ordered state and the only other state favored upon increasing the field eventually is phase II.

The microscopic origin of phase II could not be fully clarified. Yet, the formation of an additional phase as a consequence of competing energy scales is a well established phenomenon that is also known from other fields of solid state physics. In different unconventional superconductors [173–178]., heavy fermion systems [179] and in organic materials [180], for example, a superconducting phase emerges close to magnetic order. In analogy to the strong magnetic fluctuations in some of these systems, in Cs_2CoCl_4 strong quantum fluctuations are induced by applied magnetic fields which have non-commuting components for all spatial directions due to the orientations of magnetic easy planes.

The magnetism of the isostructural Cs_2CuCl_4 has been subject of many experimental and theoretical studies (see exemplary Refs. 114–119, 181). As Cs_2CoCl_4 represents the easy-plane analogon to Cs_2CuCl_4 and shows a similarly complex and previously unknown low-temperature phase diagram for magnetic fields along b, it might be worth including Cs_2CoCl_4 in the discussions of various incommensurate and exotic phases in the future. From the fundamental side, the physics of phase II might go beyond a pure description of another low-temperature phase, but relate to more general phenomena like the emergence of superconductivity from a nematic phase in the pnictides [168].

5 Mixed systems $Cs_2CoCl_{4-x}Br_x$

The analysis of the thermodynamic properties of Cs_2CoCl_4 discussed in Chapter 4 reveals an easy-plane type magnetism and a rich low-temperature phase diagram of the compound. The differences to the isostructural Cs_2CuCl_4 mainly arise from the additional magnetic anisotropy of the Co^{2+} in a crystal field in contrast to the isotropic Cu^{2+}. In addition, the magnetism of Cs_2CuCl_4 is two-dimensional with frustrated in-plane couplings of the same order of magnitude [119, 182]. The coordination of copper by chlorine ions has a low symmetry (m). In Ref. 9 it is suggested that therefore an exchange of chlorine with the larger bromine is site-selective. Depending on the doping level x in the series $Cs_2CuCl_{4-x}Br_x$ thus distinct couplings are influenced and two critical concentrations are deduced, namely $x_{c1} = 1$ and $x_{c2} = 2$. At these concentrations the site-selective replacement of one type of chlorine sites is completed and another sets in. From the larger ionic radius of bromine, a change of the coupling constants and in consequence an increase of frustration for $x_{c2} = 2$ is suggested. In between the critical concentrations interestingly crystals of different symmetry can be grown [183]. From a solution kept at 50° C orthorhombic crystals are obtained for all x. At a solution temperature of 24° C crystals belonging to the tetragonal space group $I4/mmm$ grow. By heating or mechanical stress, e. g., due to milling, the tetragonal crystals transform to the more stable orthorhombic phase. Inspired by these findings, crystals of the cobalt-based series $Cs_2CoCl_{4-x}Br_x$ were synthesized. In literature no mixed crystals of this series are reported. Only few studies [184–186] concern the endmember Cs_2CoBr_4, but not in the context of a possible low-dimensional magnetism.

5.1 Sample preparation

Single crystals have been grown from an aqueous solution. A stoichiometric solution of the educts CsCl, $CoCl_2 \cdot 6H_2O$ and $CsBr_2$ was weighed in according to

$$2\ \mathrm{CsCl} + \frac{2-x}{2}\ \mathrm{CoCl_2} + \frac{x}{2}\ \mathrm{CoBr_2}\ \rightarrow\ \mathrm{Cs_2CoCl_{4-x}Br_x}.$$

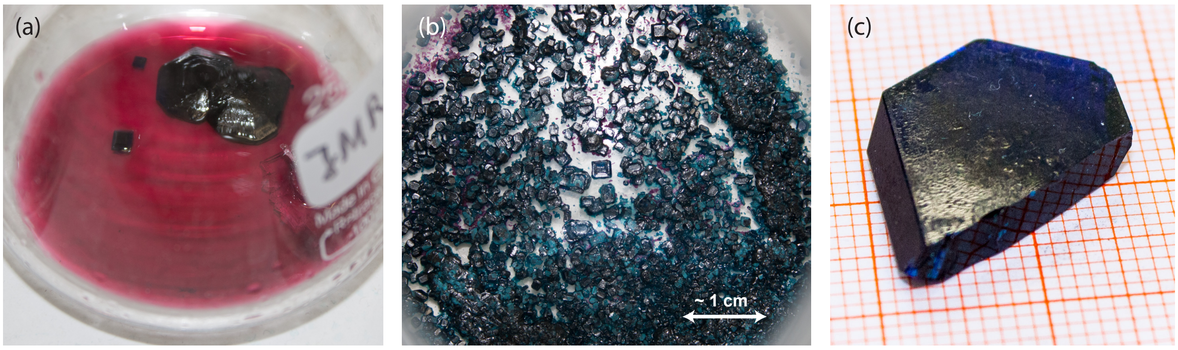

Figure 5.1: Crystal growth of $Cs_2CoCl_{4-x}Br_x$ by evaporation of the mother solution (purple liquid) in an Erlenmeyer flask (a). Many small crystallites form in case of too fast evaporation or wrong ambient conditions (b). In (c) a large single crystal of Cs_2CoCl_4 obtained under optimized growth conditions is shown.

Depending on the available materials, some solutions were prepared in analogy with CsBr and $CoCl_2$. A small excess (3-5%) of the bromide salt was used in analogy to the excess chloride usually taken for the synthesis of the undoped Cs_2CoCl_4. The solution was filled into an Erlenmeyer flask and covered by a lid. After initial heating of excess water, crystallites of approximately millimeter size formed from the saturated solution by slow evaporation at room temperature for about two weeks. Few crystals were selected by hand and allowed to grow in a separated part of the solution, others remained in the mother solution. In Fig. 5.1 (a) a flask containing the mother solution for $x = 3$ is shown. In this case, two small and two larger inter-grown crystals formed after about three months of slow evaporation. The growth results, however, strongly depend on the environmental conditions and on the evaporation rate. In Fig. 5.1 (b) a large number of small crystallites resulting from a less successful growth attempt are seen. Reducing the evaporation rate, in some cases crystals with well defined surfaces and of large size were obtained, as shown in Fig. 5.1 (c) for the undoped Cs_2CoCl_4.

At various points in time crystals of suitable size for experiments were extracted both from the mother solution as well as from the separated crystals to check for a possible change of the composition in the solution as a function of time. No indications for a change of stoichiometry among samples from the same solution were found in the diffraction data or in the specific heat data presented below. Solutions with substitution levels $x = 1, 1.5, 2, 2.5, 3, 4$ were prepared. For reference, an undoped ($x = 0$) solution was set up as well. Figure 5.2 displays selected grown crystals of the series. Up to $x = 2.5$ crystals of high optical quality and centimeter-size with well evolved facets were obtained. The largest one in case of $x = 2$ is about 2.5 cm long and weighs 7.8 g. For larger $x \geq 3$ the growth was more tempting. First, transparent crystallites formed in the solution. They probably consist of CsBr and intially grow due to the excess bromine. After further evaporation of the solution blueish crystallites formed. In comparison to lower doping levels they are, however, of lower optical quality (cf. Fig. 5.2). Still crystal facets are seen, but they show rough surfaces. Furthermore, the color of these crystals differs from the slightly transparent blue of the crystals for smaller x in a more turquoise color.

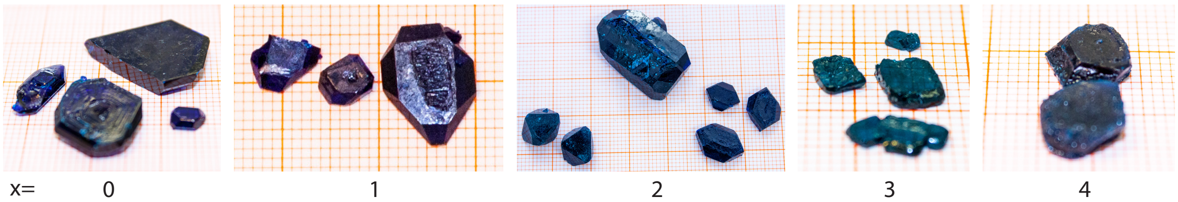

Figure 5.2: Grown single crystals of $Cs_2CoCl_{4-x}Br_x$ for values of $x = 0, 1, 2, 3, 4$ (left to right). For $x \leq 2$ only representative specimen, selected from a large number of single crystals, are shown. For larger x smaller crystals with rougher surfaces and slightly different color are obtained.

5.2 Structure determination

For all doping levels x one or two crystals were selected and ground for a structural investigation. Powder diffraction was performed with a Bruker D5000matic diffractometer in a Bragg-Brentano geometry using a copper anode ($\lambda(K_{\alpha_1})$=1.540 593 Å, $\lambda(K_{\alpha_2})$=1.544 427 Å). The powder was fixed to an object slide using diffelen oil and the data were acquired at room temperature from $2\theta = 12°$ to $122°$. Diffractograms of powder of the same x, but obtained from two different crystals extracted from the solution at a different time, strongly resemble each other. In Fig. 5.3, thus, only selected diffractograms are shown for each x. In the displayed range of small angles $2\theta < 35°$ the diffractograms (black solid lines) for $x = 0, 1, 1.5$ show about 20 peaks which shift to smaller angles upon increasing x. This shift is indicated by a dashed orange line in the upper three panels of Fig. 5.3. For $x \geq 2$ the number of observed reflections is approximately halved and no resemblance with the diffractograms for smaller x is seen. From $x = 2$ to $x = 4$ again a shift of peaks to smaller angles is found. The shift of peaks is expected due to the larger ionic radius of the bromine atoms introduced in the structure. They cause an increase of the lattice constants, respectively a decrease of the diffraction angle of the corresponding peak. The discontinuous change of the diffraction pattern at $x = 2$, however, is not expected from a symmetry-preserving doping series and suggests that the crystal structure of the parent Cs_2CoCl_4 is not stable upon exchanging half of the chlorine by bromine, but that a different structure is more stable under the given growth conditions. The results of Le Bail fits to the diffraction data (red lines in Fig. 5.3) using JANA2006 [187] confirm that crystals of different structure grew from the solution. Therefore, in the following x is referred to as *nominal*, meaning that it corresponds to the doping level in the series $Cs_2CoCl_{4-x}Br_x$ only for $x \leq 1.5$, but rather to the weighed in target stoichiometry for larger x. For $x = 0$ an excellent fit of the diffraction data is obtained by refining the lattice constants based on the structure data for Cs_2CoCl_4 of Refs. 108, 112. The difference between the observed and the calculated intensity, shown as blue line in Fig. 5.3, mainly represents the experimental noise. The resulting lattice constants and the unit cell volume are displayed in Fig. 5.4. For $x = 0$ they are very close to the literature data (orange stars) of Cs_2CoCl_4 from Ref. 108. The deviation of the lower-lying literature data of Ref. 112 might be related to the lower temperature of 140 K of that investigation. For finite doping levels $x < 2$ all diffractograms are successfully described by the orthorhombic structure of Cs_2CoCl_4 with refined the lattice constants. A slight increase of the

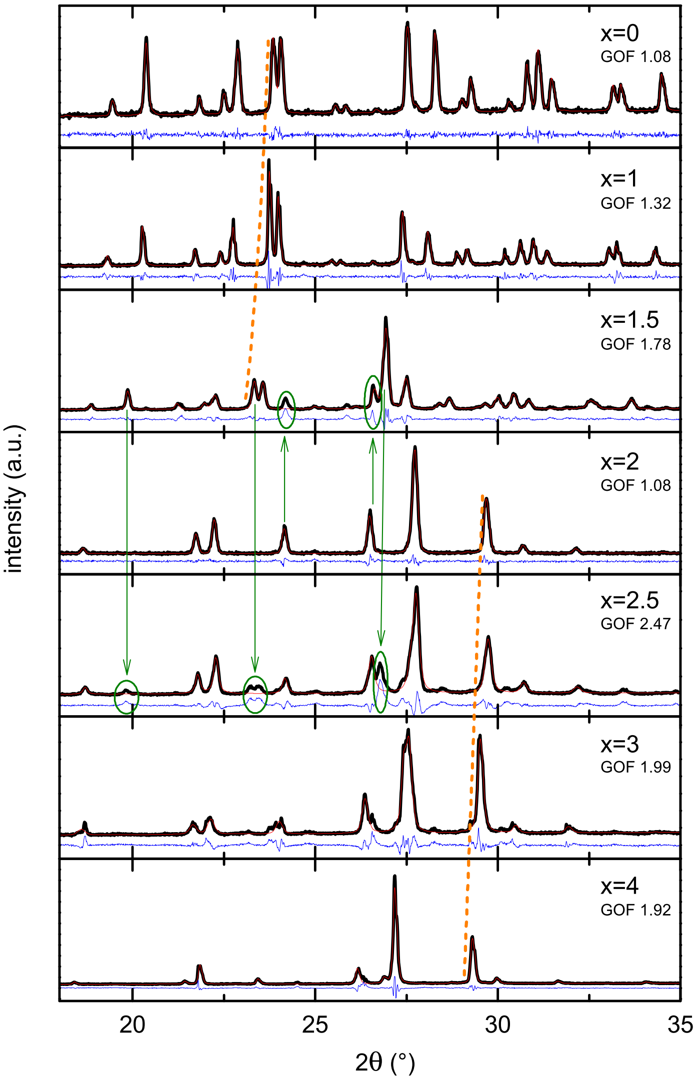

Figure 5.3: Powder diffraction data of $Cs_2CoCl_{4-x}Br_x$ at small angles 2θ for various nominal doping levels x. The data are normalized to the respective maximum intensity. Bold black lines are the acquired data. Thin red lines are obtained from the Le Bail method using an orthorhombic symmetry for $x \leq 1.5$ and a tetragonal structure for $x \geq 2$. Blue lines give the difference between observed and calculated intensity. Dashed orange lines indicate a shift of similar peak structures as a function of x. Green circled peaks probably stem from the intergrowth of small phases of different x as marked by arrows. The goodness of fit (GOF) is output by the employed crystallographic system JANA2006 [187] and equals the statistical "Chi squared".

goodness of fit as a function of x may be caused by imperfect grinding of the powder or by impurity phases in the crystals. A detailed comparison of the x dependence of the diffractograms reveals that signatures of other nominal x are contained in some diffractograms. As marked exemplarily for $x = 1.5$ and $x = 2.5$ by green circles and arrows in Fig. 5.3 a small fraction of the $x \geq 2$-patterns seems to be contained in the $x = 1.5$ pattern. Respective peaks at 24.2° and 26.6° for example may stem from a small phase of nominal $x = 2$. Vice versa, peaks of an $x = 1.5$ phase are recognizable in the diffractogram for $x = 2.5$. From a comparison of the relative intensities one may estimate the ratio of the impurity phase to a maximum of about 20 % for the extreme case of the nominal $x = 2.5$. In Ref. 184 the crystal growth of Cs_2CoBr_4 is reported and a large phase of about 45 % of Cs_3CoBr_5 is found. In fact, the present data for $x \geq 2$ are convincingly described based on the tetragonal symmetry of Cs_3CoBr_5 that belongs to the space group $I4/mcm$ and whose structure has previously been solved [188, 189]. An excellent agreement is achieved for the nominal $x = 2$ and for $x = 4$, while for intermediate values impurity phases seem to be more pronounced. The refined lattice constants for the nominal $x = 4$ are very close to the literature data (pink triangles in Fig. 5.4). An approximately linear dependence of the lattice constants upon decreasing

x from 4 to 2 is found. It roughly extrapolates to the lattice constants of the chlorine based Cs_3CoCl_5 expected at a nominal $x = 0$ [190, 191]. However, due to the initial growth of CsBr from the solution, the nominal x cannot be directly converted to a doping level $y \in [0, 5]$ in terms of the composition $Cs_3CoCl_{5-y}Br_y$. Nevertheless, bromine seems to be exchanged by chlorine also in the $Cs_3CoCl_{5-y}Br_y$ series as evidenced by the change of the lattice constants and the specific heat data presented below. From the optical quality of the crystals with nominal $x = 2$ the change of symmetry and crystal structure at this x is rather surprising since they grow in the same quality and size as the orthorhombic crystals for smaller nominal x.

Summarizing, two classes of doped crystals have grown from the different solutions. For nominal bromine contents $x = 0, 1, 1.5$ crystals of $Cs_2CoCl_{4-x}Br_x$ are obtained. For $x = 2, 2.5, 3, 4$ the tetragonal $Cs_3CoCl_yBr_{5-y}$ has grown from the solution, where y depends on x in a way that cannot be extracted from the present data. Yet, a comparison to the known lattice constants of Cs_3CoCl_5 [190, 191] suggests that y maps to x linearly. Due to the water solubility and the insulating behavior of the crystals a precise composition analysis by EDX was not successful. For a similar synthesis, the differences between the Br/Cl ratio in the solution and that of EDX estimates are reported to be negligible [183]. Thus, the nominal x probably provides a good estimate

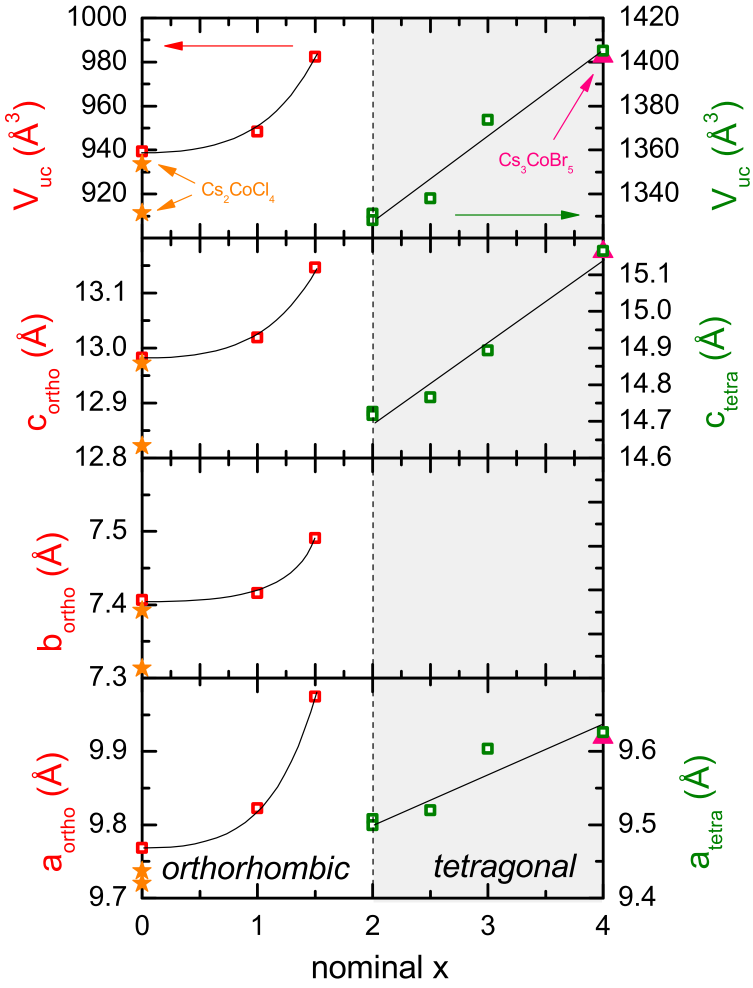

Figure 5.4: Lattice constants and the unit cell volume of the doping series $Cs_2CoCl_{4-x}Br_x$, where x is the nominal Br-content. Lines are guides to the eye. Below $x = 2$ the parameters are obtained from the diffraction data using the orthorhombic space group *Pnma*. For $x \geq 2$ the tetragonal space group *I*4/*mcm* was used. Literature values [108, 112] for $x = 0$ are shown as orange stars. Pink triangles indicate the lattice constants of Cs_3CoBr_5 as reported in Ref. 188. Crystals obtained for a nominal $x \geq 2$ (shaded area) belong to the $Cs_3CoCl_yBr_{5-y}$ series and have tetragonal symmetry.

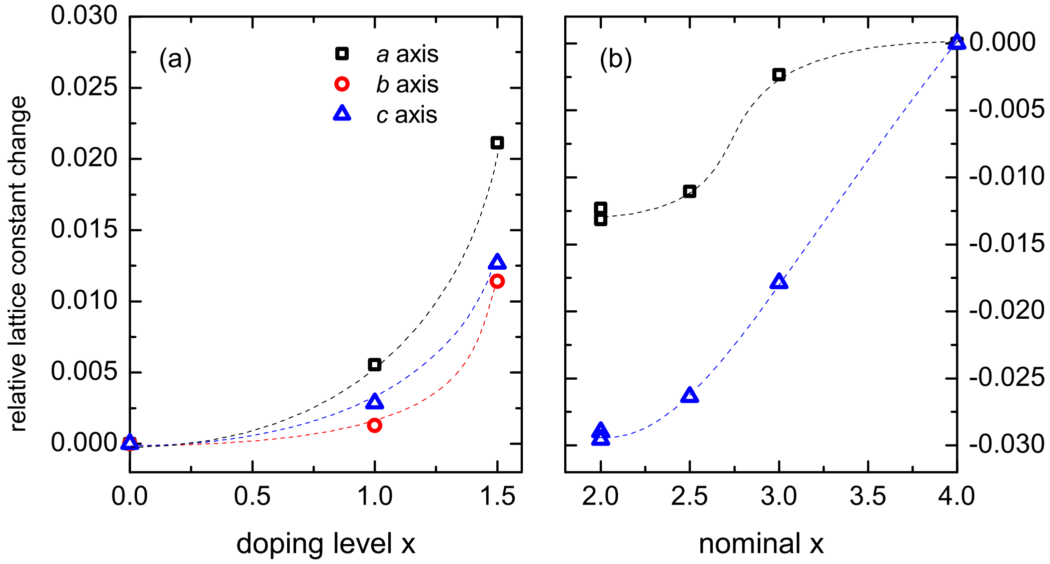

Figure 5.5: Relative change of the lattice constants $\frac{l_i - l_0}{l_0}$ in the doping series $Cs_2CoCl_{4-x}Br_x$ from the value for $x = 0$, respectively in the chlorine-doped Cs_3CoBr_5 with respect to the constants obtained for the nominal $x = 4$. Dashed lines are guides to the eye.

of the true composition for $x < 2$. Due to the lack of additional chemical data, it is used to identify crystals for larger x as well. Small intergrowth of the respective other structure are indicated by the diffraction data, especially for large x, and might explain the less distinct crystal facets. It could be possible to optimize the growth of the $Cs_2CoCl_{4-x}Br_x$ phase by varying the temperature of the solution in analogy to the results for the mixed systems $Cs_2CuCl_{4-x}Br_x$ based on copper [183].

The two systems grown here behave similar upon doping. In Fig. 5.5 (a) the normalized relative change $\frac{l_i - l_0}{l_0}$ of the lattice constants as a function of the nominal x is displayed. A non-linear and anisotropic change of the lattice constants arises. The influence of doping on the a axis is about twice as large as on the other axes, which could be interpreted in favor of a site-selective substitution, in analogy to the isotructural $Cs_2CuCl_{4-x}Br_x$ discussed in Ref. [183], There, the exchange of chlorine by bromine is not random among all chlorine position in the structure, but the Cl1 site is favored. This site, shown as red balls in Fig. 5.6, has the largest Co-Cl bond length in each tetrahedron. In analogy to the doping of Cs_2CuCl_4 it is predominantly occupied by bromine up to a critical concentration $x_{c1} = 1$. At this concentration statistically every Cl1 site is occupied by bromine. For entropic reasons the influence of doping on the Cl1 site occupation might extend slightly above x_{c1}. At reasonably larger x the other sites Cl2 and Cl3 are then occupied as well. As they also differ in symmetry, the doping in this regime may be site-selective as well. From the specific heat discussed below one may conclude that the Cl3 sites are occupied for $x > x_{c1}$. The Cl1 site contributes to the interlayer coupling J_{ac}, but not to the frustrated coupling J_{bc} between chains or to the primary coupling J, see Figs. 4.6, 5.6 and Tab. 4.2. From the larger ionic radius of bromine one may thus expect an increase of the coupling between layers for increasing x, respectively an enhanced ratio of J_{bc}/J, i. e., an increasingly two-dimensional mag-

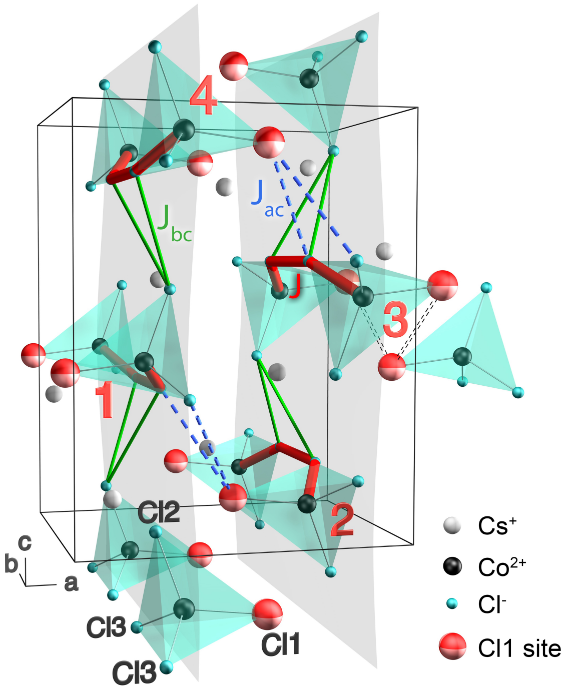

Figure 5.6: Crystal structure of Cs_2CoCl_4 with the highlighted position of the Cl1 sites (striped red balls) that are involved in a site-selective exchange of chlorine by bromine in the $Cs_2CoCl_{4-x}Br_x$ series for $x \leq 1$. Magnetic exchange paths within *bc* planes J_{bc} are sketched with green lines, those between layers (J_{ac}) are shown as dashed lines. The dominant exchange J along b is not influenced by an exchange of chlorine at the Cl1 site.

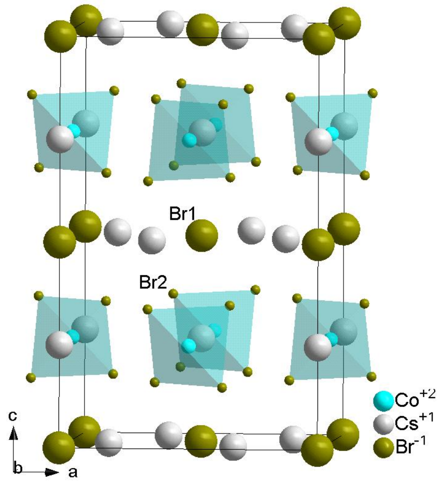

Figure 5.7: Unit cell of the tetragonal crystal Cs_3CoBr_5 of space group $I4/mcm$, based on the structure data of Ref. 189. Shaded tetrahedra indicate the coordination of the magnetic Co^{2+} by Br_4. Square lattices of $CoBr_4$ in the *ab* plane are separated along c by layers of cesium and bromine.

netism. A microscopic proof of a site-selective substitution could be given for example by identifying superstructure reflections via single-crystal diffraction of Cs_2CoCl_3Br.

The tetragonal crystals of the bromine-reach side also show a strong difference of the lattice constant's change as a function of the nominal x, see Fig. 5.5 (b). Here, the c axis is influenced strongly by replacing bromine with chlorine, whereas the a axis hardly changes from $x = 4$ to $x = 3$ and only then for even smaller x decreases similar to the c axis. In the structure of Cs_3CoBr_5 (shown in Fig. 5.7) also tetrahedra of $CoBr_4$ are found. In contrast to Cs_2CoCl_4, however, they are formed by a single site (Br2) and have full tetrahedral symmetry. The four Co-Br bond lengths within each tetrahedron are identical, such that no indication for a preferential substitution within the tetrahedra is given. Yet, there is a second non-equivalent Br site in Cs_3CoBr_5. One fifth of the total bromine occupies the Br1 site which is located in between the *ab* layers of $CoBr_4$ tetrahedra. The bonding character of these atoms to the cesium also contained in the layer probably differs from that of the $CoBr_4$ tetrahedra. Thus, one may speculate that the substitution of bromine and chlorine in the $Cs_3CoCl_yBr_{5-y}$ series is site-selective as well.

5.3 Thermodynamic properties

5.3.1 $Cs_2CoCl_{4-x}Br_x$

The specific heat of crystals with various nominal x has been measured using the relaxation time method in a temperature range of 0.25 K to 20 K. For the doping levels $x = 2, 3, 4$ each two crystals, extracted from the mother solution at different stages of the growth process, were measured to check for a possible degradation of the solution by non-stoichiometric growth. Very similar results were obtained for these crystals, which suggests that the crystals have grown with a constant stoichiometry. As shown in Fig. 5.8 (a) the specific heat of $Cs_2CoCl_3Br_1$ very closely resembles that of Cs_2CoCl_4. Close to 1 K the same broad maximum is observed. Its position coincides with that of the undoped compound. Yet, the Schottky anomaly around 5 K which is seen as a hump in the data of Cs_2CoCl_4 (magenta symbols) is reduced significantly. This may be the consequence of an increased crystal field anisotropy $\mathcal{D}$ induced by the introduced bromine. In turn, the Schottky anomaly is shifted to higher temperature and thus merges with the larger phonon background at higher temperature. This effect is even more pronounced in $Cs_2CoCl_{2.5}Br_{1.5}$, see Fig. 5.8 (b). If the anisotropy $\mathcal{D}$ increases one may expect that the magnetism of Co^{2+} in the doped systems at low temperature is still described as an effective spin-$^1/_2$. Nevertheless, small modifications of the low-temperature specific heat suggest that the magnetism is influenced in details. For $x = 1.5$ the broad maximum of magnetic origin is shifted to a slightly larger temperature of 1.18 K. This shift could be explained by an increased intrachain coupling in $Cs_2CoCl_{2.5}Br_{1.5}$. The proposed site-selective exchange of Cl1 atoms by bromine statistically is completed at $x = 1$ and for the given $x = 1.5$ further chlorine atoms in the tetrahedra are exchanged by bromine as well. Due to the stronger overlap of orbitals for the larger bromine the magnetic exchange along the b axis might be enhanced.

The change of the spin-chain magnetism and of the crystal field anisotropy can be modeled in analogy to Chapter 4.2.2 by fitting the sum of the specific heat of the XXZ model c_{XXZ}, a Schottky anomaly c_{Schottky} and a phonon background c_{ph} to the data. The phonon background is assumed identical to that of Cs_2CoCl_4 with a debye temperature $\theta_{\mathrm{D}} = 67\,\mathrm{K}$. The Schottky anomaly and the spin-$^1/_2$ chain are analyzed based on the extension of the Schrieffer-Wolff transformation to first order as introduced in Chapter 4.2.2. Fitting the data one obtains the spin-$^3/_2$ Heisenberg exchange J_{H} and the anisotropy $\mathcal{D}$. From these the anisotropy Δ and the effective spin-$^1/_2$ couplings follow. A reasonable fit of the data for $x = 1$ and $x = 1.5$ is obtained as shown by red lines in Fig. 5.8. In panel (c) the individual contributions to the total specific heat are displayed. In comparison to the undoped Cs_2CoCl_4, the Schottky anomaly is shifted to higher temperature and thus is the leading contribution only in a very restricted temperature range. In Tab. 5.1 the results for $x = 1$ and $x = 1.5$ are summarized and compared to those of the undoped Cs_2CoCl_4. For $Cs_2CoCl_3Br_1$ only a tiny change of J_{H} from the value of 0.74 K is found that lies within the experimental and the numerical errors during the fit. The anisotropy $\mathcal{D}$, however, is increased from 7.0 K to 8.1 K. Both dependencies are explained by a site-selective substitution that does not involve a cobalt ligand which mediates the dominant magnetic exchange along the b axis. Due

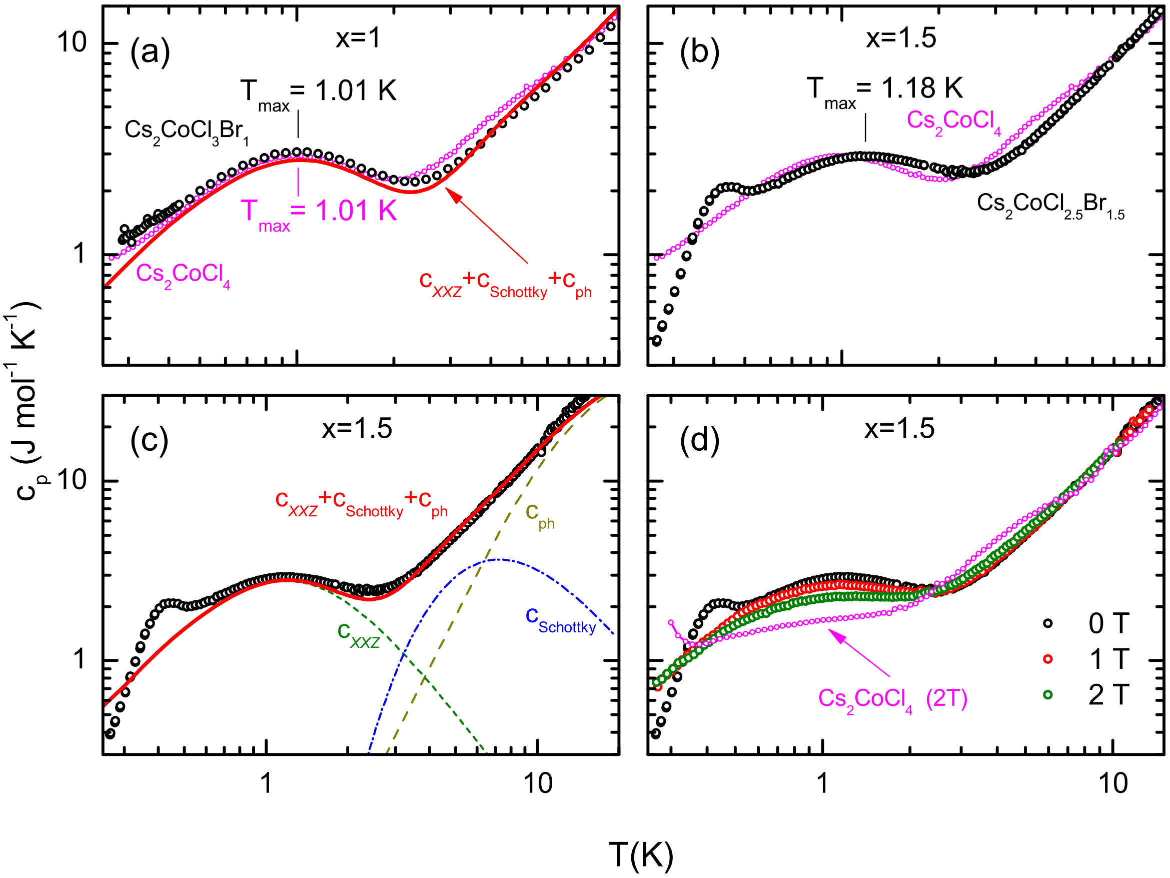

Figure 5.8: Specific heat of $Cs_2CoCl_{4-x}Br_x$ with $x = 1$ (a) and $x = 1.5$ (a-d). For comparison the specific heat of the undoped Cs_2CoCl_4 is shown by magenta symbols in panels (a-c). The maxima temperatures in (a) and (b) are obtained from a power-law fit. In (c) the individual contributions to the specific heat are shown as resulting from a fit of the *XXZ* model (dashed green line), a Schottky anomaly (dash-dotted blue line) and a phonon background (yellow dashed line) to the data. The sum of all contributions $c_{XXZ} + c_{\mathrm{Schottky}} + c_{\mathrm{ph}}$ is shown as a solid red line for $x = 1$ in (a) and for $x = 1.5$ in (c). In (d) the field dependence is compared to the data of Cs_2CoCl_4 for 2 T (pink symbols).

to the larger ionic radius of Br a change of the crystal field even for small x, however, is plausible. The increase of J_{H} to 0.88 K for $x = 1.5$ can be understood by a substitution of Cl atoms that contribute to superexchange paths along b for doping levels x larger than the critical concentration $x_{c1} = 1$. The anisotropy $\mathcal{D}$ increases approximately linear as a function of x. The anisotropy of the spin chain Δ only weakly changes, but remains well below the value of 0.25 previously assumed in literature and close to 0.12 as derived for Cs_2CoCl_4 in Chapter 4.2.

Besides the broad anomaly around 1 K, interestingly, an additional broad, yet smaller, feature arises at about 430 mK in $Cs_2CoCl_{2.5}Br_{1.5}$, but not in $Cs_2CoCl_3Br_1$. Two possible scenarios can be thought of to explain this anomaly: (i) a magnetic order transition, (ii) a more unconventional Berezinskii-Kosterlitz-Thouless (BKT) transition. In the first scenario, below 430 mK one may expect an antiferromagnetic order similar to that of the undoped compound. The size of T_{N} is mainly determined by the correlation

Compound	x	J_H/k_B (K)	$\mathcal{D}/k_B$ (K)	Δ	J_{xy}/k_B (K)	J_z/k_B (K)
Cs_2CoCl_4	0	0.74	7.0	0.12	2.96	0.36
$Cs_2CoCl_3Br_1$	1	0.76	8.1	0.14	3.04	0.41
$Cs_2CoCl_{2.5}Br_{1.5}$	1.5	0.88	8.7	0.13	3.52	0.44

Table 5.1: Magnetic exchange constants and the crystal field anisotropy of the doped compounds $Cs_2CoCl_{4-x}Br_x$ for $x = 0, 1, 1.5$.

length of the spin chain and by the interchain coupling. The increased value of T_N in comparison to Cs_2CoCl_4 may arise from a stronger coupling between the spin chains and from an increased correlation length due to the larger J_H. The broadening could be caused by disorder. On this basis, the fact that for $x = 1$ no comparable anomaly is found in the data, then indicates that the increase of the correlation length is the more efficient mechanism to raise T_N in comparison to the increase of the interlayer coupling. Namely, for $x = 1$ the interchain coupling J_H is not changed, but the coupling between chains is expected to be larger due to the introduced bromine in the same way J_H is increased from $x = 1$ to $x = 1.5$. The scenario (ii) of a BKT transition is based on the assumption that by doping the coupling between chains becomes so strong that $Cs_2CoCl_{2.5}Br_{1.5}$ approaches a two-dimensional system while preserving the XY anisotropy. In two-dimensional systems with a continuous rotational symmetry, e. g., the classical 2D XY model, a unique transition was identified by Berezinskii, Kosterlitz and Thouless [192, 193]. In the low-temperature phase correlations are long-ranged and decay with a power-law, whilst the high-temperature disordered phase is characterized by exponentially decaying correlations. A rather sharp peak of the specific heat is expected from Monte-Carlo simulations at the critical temperature $T_{BKT}^{S=\infty} \cdot k_B/J \approx 0.70$, where the decay of the correlation function changes [194]. For the quantum spin-$1/2$ XY model this transition also arises [195], but at a lower temperature $T_{BKT}^{S=1/2} \cdot k_B/J \approx 0.34$, where J is the exchange constant of spins on a square lattice. Models of the XXZ type as well show the transition, but with $T_{BKT}^{S=1/2}$ reduced further. Up to $\Delta = 0.5$, however, the additional suppression of $T_{BKT}^{S=1/2}$ is negligible [196]. Yet, the expected transition temperature $0.34 \cdot J_{xy}/k_B \approx 1.2\,\mathrm{K}$ is reasonably larger than the observed $\simeq 0.4\,\mathrm{K}$ and the present data show a strong broadening of the transition. As discussed in Ref. 197 bond disorder in the 2D XY model leads to a broadening and suppresses the transition to lower temperature. Nevertheless, the large anomaly around 1 K speaks against a purely two-dimensional magnetism in $Cs_2CoCl_{2.5}Br_{1.5}$. Crystals with higher doping levels $x > 1.5$ could be of interest to observe a possible reduction of the one-dimensional signatures around 1 K. An increase of weight of the anomaly around 0.4 K in these crystals could give evidence for a smooth transition to a 2D magnetism upon doping. From the present data, a dimensional crossover, however, cannot be stated.

Last, the field dependence of the specific heat of $Cs_2CoCl_{2.5}Br_{1.5}$, shown in Fig. 5.8 (d), is discussed. Due to experimental issues with the orientation of the crystals the crystallographic direction along which the field is applied cannot be given. The anomaly around 430 mK has vanished at the smallest field of 1 T. An overall suppression of the heat capacity by the magnetic field is seen, which is in analogy to the field dependence of Cs_2CoCl_4 discussed in Chapter 4.2. Even though, the influence of applied magnetic fields is comparably small. The difference to the 2 T-data of Cs_2CoCl_4, shown by magenta data points in Fig. 5.8 (d), can be explained by a change of the primary energy scale J_H in the system and by a possibly increased coupling between spin chains.

Crystals with doping levels $x > 1.5$ could be of large interest. In the present work, however, they could not be grown from the solutions at room temperature. The crystal growth of Cs_2CoBr_4 has been reported in literature [184, 185], but the magnetic properties were not investigated.

5.3.2 $Cs_3CoCl_{5-y}Br_y$

For nominal $x > 1.5$, crystals of different stoichiometry, but with similar structural motifs have grown from the solution. For completeness the specific heat of these crystals will be discussed in the following. The data are normalized using the molar masses under the assumption that the nominal doping $0 \leq x \leq 4$ maps linearly to $0 \leq y \leq 5$, i. e., $y = \frac{5x}{4}$.

Both endmembers Cs_3CoCl_5 and Cs_3CoBr_5 share the same tetragonal space group $I4/mcm$ (No. 140) [191, 198, 199]. The lattice constants of the bromine compound are larger by about 4%. In the crystal structure of both compounds (Fig. 5.7) the magnetic Co^{2+} are surrounded by tetrahedra, similar to the coordination in Cs_2CoCl_4, but here the tetrahedra are highly symmetric. The crystal field strength is similar to that of Cs_2CoCl_4 ($\mathcal{D}_{Cl_4} \approx 7.0\,\mathrm{K}$). For Cs_3CoCl_5 an anisotropy $\mathcal{D}_{Cl_5} \approx -6.2\,\mathrm{K}$ was found, respectively $\mathcal{D}_{Br_5} \approx -7.7\,\mathrm{K}$ for Cs_3CoBr_5 by ESR [188, 200]. The larger anisotropy for the bromine compound goes along with the observation of an increase of the anisotropy by doping Cs_2CoCl_4 with bromine. Yet, the sign of the anisotropy is opposite here. Thus, the Kramers doublets are inverted and instead of easy planes an easy axis is established in the compounds. Due to the high symmetry in comparison to Cs_2CoCl_4 only a single local easy axis follows, which is along the crystallographic c axis. Within the ab plane, the Cl_5/Br_5 tetrahedra form a square lattice. Along c the layers are separated by layers of CsBr. From susceptibility [201] and specific heat data [188] both compounds are known as Ising systems. While in Cs_3CoCl_5 the magnetic exchange seems to be three dimensional, for Cs_3CoBr_5 a dominantly two-dimensional magnetism was proposed. The mixed systems thus could be of high interest to investigate a possible transition from 2D to 3D magnetism. Magnetic order arises at $T_N(Cl_5) = 0.523\,\mathrm{K}$ for Cs_3CoCl_5 and at $T_N(Br_5) = 0.282\,\mathrm{K}$ for Cs_3CoBr_5. The difference of the transition temperatures is partly explained by the different dimensionality [56]. In case of the chlorine compound, G-type antiferromagnetic order along c was found [202].

Based on the literature data of the endmembers the present specific heat data (Fig. 5.9) for $x = 2, 2.5, 3, 4$, respectively $y = 2.5, 3.125, 3.75, 5$ can be understood as follows. For $y = 5$ the temperature dependence as expected equals that of Cs_3CoBr_5. In Fig. 5.9 (a) the specific heat of two individual samples (black and red symbols) are compared to the results on Cs_3CoBr_5 of Ref. 188 (green line). Only the high-temperature tail of the magnetic order transition at 282 mK is seen in the present data. Due to the extremely large heat capacity of even small samples at this temperature and the following long

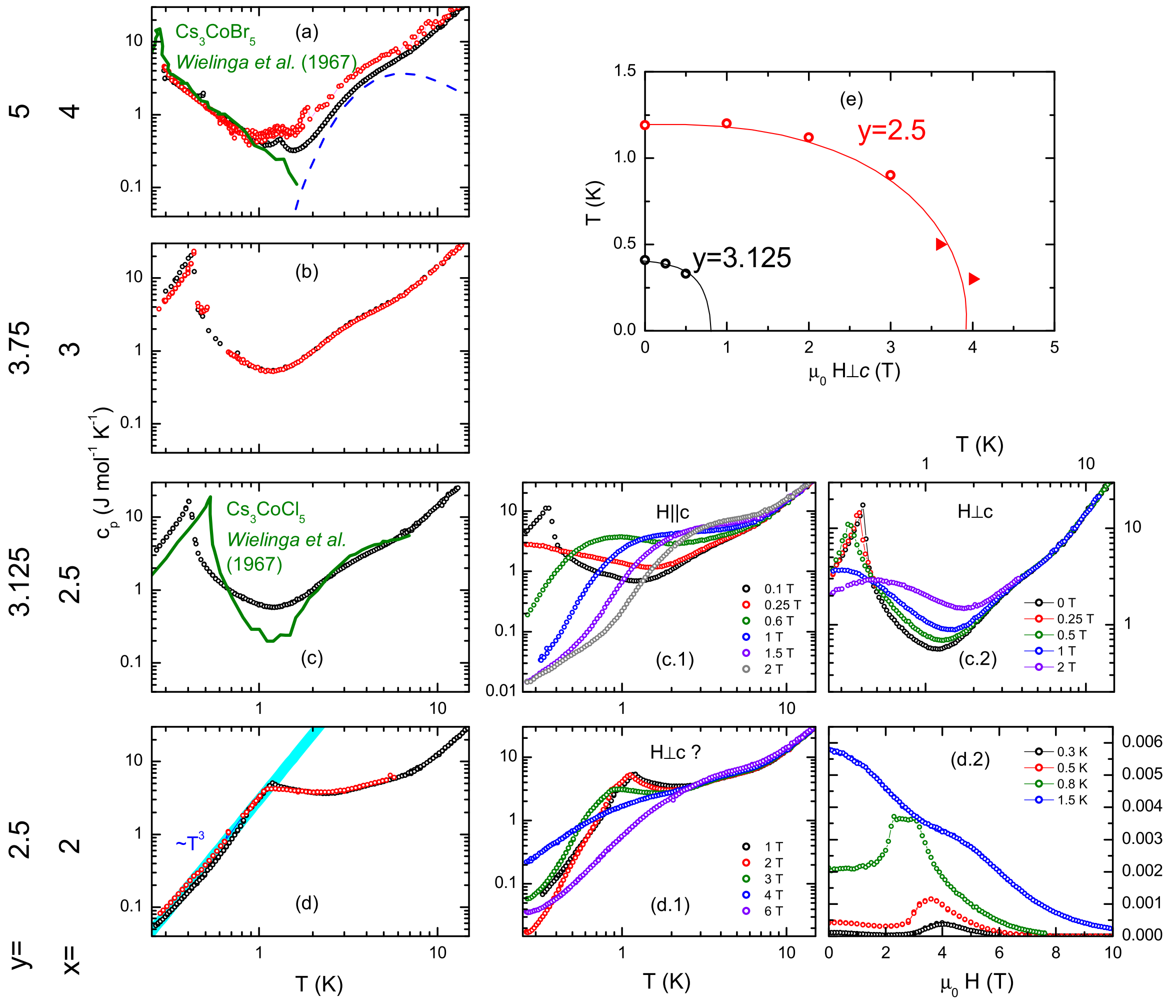

Figure 5.9: Specific heat of the $Cs_3CoCl_{5-y}Br_y$ series for doping levels $y = 5, 3.75, 3.125, 2.5$, calculated from the nominal doping $x = 4, 3, 2.5, 2$, see text. In (a-d) the respective zero-field specific heat is shown. Black and red symbols stem from samples of different batches. The green line in (a) and (c) display the specific heat of the compounds Cs_3CoBr_5 and Cs_4CoCl_5 digitized from Ref. 188. The dashed blue line in (a) represents a Schottky anomaly with an energy gap of 15.4 K. The specific heat of $Cs_3CoCl_{2.5}Br_{2.5}$ (d) shows a power-law dependence (shaded area) $c_p(T) \propto T^3$. The specific heat in magnetic fields applied parallel and perpendicular to the Ising axis are shown in panels (c.1) and (c.2) for $y = 3.125$ and in (d.1) for $y = 2.5$. Panel (d.2) shows the field dependence of c_p for $y = 2.5$. Circles in the phase diagram (e) for the perpendicular field direction are obtained from the temperature dependence of c_p, triangles from the field dependence. Lines are guides to the eye.

cool-down times the present measurements were started only at about 300 mK. The bump in the data around 5 K is described quantitatively by a Schottky anomaly assuming a gap of $2\,|\mathcal{D}_{Br_5}| \approx 15.4\,\mathrm{K}$ as probed by ESR [200]. Reducing y to 3.75 or 3.125 very similar specific heat curves are obtained (symbols in Fig. 5.9 (b) and (c)). They only differ from the latter by an increase of T_N to about 410 mK, similar for both doping levels. The fact that almost no change is observed from $y = 3.75$ to $y = 3.125$ may be explained again by a site-selective doping. The different changes of the lattice constants a and c for large y (Fig. 5.5 (b)) suggest that from $y = 5$ to $y = 3.75$ mainly one type of bromine is exchanged by chlorine and an isotropic evolution of the lattice constants arises for smaller y. This is in agreement with the strong increase of T_N starting from $y = 5$ and almost no dependence on y between $y = 3.75$ and $y = 3.125$. Thus, a large part of the transition from the 2D magnetism of the Br_5 compound to a three-dimensional system seems to arise in the range from $y = 5$ to $y = 3.75$ by an exchange of the bromine at the inter-layer site Br1 with chlorine, see Fig. 5.7. Nevertheless a further increase of T_N for $y < 3.125$ is expected from a comparison to the literature data of $\mathrm{Cs_3CoCl_5}$, shown as green line in Fig. 5.9 (c), which reveal a similar structure, but a shift of the low-temperature part by another 100 mK.

However, upon reducing y further, the expected evolution towards the data of $\mathrm{Cs_3CoCl_5}$ is not found. Instead, the data obtained for $y = 2.5$ stand out in that the magnetic order temperature with 1.2 K lies well above that of both endmembers of the series. The Schottky anomaly around 5 K is still seen, which indicates that the individual tetrahedral coordinations are preserved. Below 1.2 K the temperature dependence of $c_p(T)$ follows a power law with an exponent 3 as expected from an ordered antiferromagnet in three dimensions. Unfortunately, crystals of the tetragonal $\mathrm{Cs_3CoBr_5}$ structure with smaller y were not obtained from the solutions. Yet, they might be interesting to observe the further evolution of c_p for smaller y. Finally, at $y = 0$ the known properties of $\mathrm{Cs_3CoCl_5}$ (green line in Fig. 5.9 (c)) should be recovered. Based on the present data, the definite reason for the exceptional properties of the $y = 2.5$ crystals cannot be clarified. Interestingly, these crystals could be grown in size and quality inferior to those for larger nominal x. Similar to the mixed systems of $\mathrm{Cs_2CuCl_{4-x}Br_x}$, possibly different structures of varying thermal stability could coexist for distinct doping levels x, which maybe was not be revealed here and requires a further analysis of the $y = 2.5$-crystals e. g. by TDA/TGA. Another possibility is a more complex disorder effect induced by the random distribution of Br/Cl atoms within the tetrahedra in the ab layers.

In applied magnetic fields the strong Ising anisotropy of the system becomes evident. In Fig. 5.9 (c.1) the specific heat in case of $y = 3.125$ is shown for different magnetic fields applied collinear to the Ising axis c. In a small field of 0.1 T the magnetic order transition is still resolved. At 0.25 T it is suppressed below the temperature range of the experiment. Starting at 0.6 T, an increasing gap is signaled by the strong suppression of c_p at low temperature and an exponential temperature dependence in case of 0.6 T and 1 T. At higher fields the exponential behavior does not precisely hold and a kink is seen below 1 K. When the field is applied perpendicular to the Ising axis of the spins a much smaller field dependence is found, see Fig. 5.9 (c.2). Up to 0.5 T the magnetic order temperature remains almost unchanged. In comparison to $H \parallel c$, a reasonably smaller change of c_p is seen upon increasing the field further. While for the parallel direction the specific heat is reduced by about three orders of magnitude at 2 T, for the perpendicular direction the g factor seems to be reduced by a factor of about 8 as approximated from the coarse similarity of the curves for $H_\parallel = 0.25\,\mathrm{T}$ and $H_\perp = 2\,\mathrm{T}$. This emphasizes the Ising character of the system. In $\mathrm{Cs_3CoCl_{2.5}Br_{2.5}}$ the field dependence of c_p, shown in Fig. 5.9 (d.1) and (d.2), in general is comparable to the case of $H \perp c$ for smaller y, but it extends over a wider field range. The crystal orientation for $y = 2.5$ could not be unambiguously identified. Nevertheless, a field direction $H \perp c$ is suggested by the small field dependence of the magnetic order temperature. Up to 3 T the zero-field anomaly at 1.2 K is shifted to a slightly lower temperature of about 0.9 K. The field dependence $c_p(H)$ at the lowest temperature of 0.3 K indicates a transition at about 4 T. For an estimate of the relevant energy scales the data points of $T_{\mathrm{N}}(H \perp c)$ obtained for the compounds with $y = 2.5$ and $y = 3.125$ are plotted in the phase diagram of Fig. 5.9 (e) with open symbols. Data points extracted from the field dependence of $c_p(H)$ are shown as triangles. In the $y = 2.5$ system, the stability of magnetic order is larger by a factor of about three.

Model systems where a magnetic field can be applied perpendicular to the Ising axis of a spin system are of fundamental interest due to the possible emergence of quantum criticality, see e. g. Refs. 1, 2, 81, 82. From the experimental point of view $Cs_3CoCl_{2.5}Br_{2.5}$ is a promising candidate for further investigations as the transition temperatures lie in an easily accessible temperature range. However, the mechanism by which the crystals of this doping level separate from the others should be resolved by extensive structural investigations and the extension of the series to lower y.

5.4 Conclusion

Aqueous solutions have been set up to grow crystals of the $Cs_2CoCl_{4-x}Br_x$ series. As revealed consistently by structural investigations and measurements of the specific heat at low temperature, up to a nominal concentration $x = 1.5$ of bromine single crystals isostructural to the orthorhombic Cs_2CoCl_4 have been grown. No differences of the lattice constants or the specific heat data between samples of different batches have been detected. This indicates a stoichiometric growth of the crystals from the solution. The change of the lattice constants as a function of x is anisotropic. In analogy to the mixed systems $Cs_2CuCl_{4-x}Br_x$, this suggests a site-selective exchange of bromine and chlorine [9, 183], in good agreement with the x dependence of the coupling constant J_{H} and the crystal field anisotropy $\mathcal{D}$ extracted from the specific heat. While $\mathcal{D}$ is continuously enhanced by increasing x, the magnetic exchange remains unchanged from $x = 0$ to $x = 1$ and then increases by about 15% for $x = 1.5$. This dependence is explained by an exchange of chlorine by bromine predominantly at the Cl1 site up to $x = 1$ and a subsequent exchange of Cl^- ions at site Cl3 that contributes to the dominant magnetic exchange. The expected increasingly two-dimensional magnetism is not indicated by the specific heat data that only show a slight shift of the maximum around 1 K known from the undoped Cs_2CoCl_4. At $x = 1.5$ an increased magnetic order temperature is found that can be explained simplest by the larger primary coupling constant for this doping level. From the theory point of view, the appearance of a BKT transition, expected in two-dimensional XY-like systems, could be of large interest. Magnetic compounds showing a transition of the BKT type are rare, but the nature of the transition may be related to the physics of high-temperature superconductors that are based on two-dimensional magnetism as well [203, 204]. Increasing the present doping level $x > 1.5$ may open the possibility to alter the couplings between the chains further and eventually suppress the one-dimensional magnetism in favor of a 2D XY system.

From the solutions set up for various doping levels, $Cs_2CoCl_{4-x}Br_x$ crystals with $x > 1.5$ could not be grown. Altering the growth conditions, e. g., by a controlled evaporation at temperatures above room temperature, could help to extend the doping series to larger x. At present, however, crystals of a different structure were obtained for $x = 2, 2.5, 3$ and 4. From powder diffraction they could be identified as chlorine-doped variants of Cs_3CoBr_5, which also contain tetrahedra formed by $CoBr_4$, but the magnetism shows an Ising anisotropy, in contrast to the easy-plane magnetism in Cs_2CoCl_4. The Ising magnetism is reflected in the specific heat data acquired with magnetic fields parallel and perpendicular to the Ising axis. In Cs_3CoBr_5, the onset of magnetic order at about 280 mK is seen as a peak of the specific heat that is well described by the Ising model. As a function of the doping y in the series $Cs_3CoCl_{5-y}Br_y$ the peak shifts to higher temperature, consistent with the end value of 523 mK known for Cs_3CoCl_5 [188]. The change of the order temperature can be explained by a change of the coupling along c by an analogous site-selective doping in between the tetrahedra that are located on ab layers. At $y = 2.5$ interestingly, an exceptionally large magnetic order temperature is found. It may be explained either by a subtle disorder effect, or at $y = 2.5$, respectively $x = 2$, a structural variant grows from the solution that is similarly unstable as in case of $Cs_2CuCl_2Br_2$ [183]. Crystals extending the $Cs_3CoCl_{5-y}Br_y$ series to $y \leq 2.5$ may give further insight into the possibly interesting properties arising in between the two known endmembers.

6 The Heisenberg spin chain $Cu(C_4H_4N_2)(NO_3)_2$

Copper pyrazine dinitrate is a model system for the isotropic spin-$1/2$ Heisenberg chain. The magnetic Cu^{2+} ions form well separated spin chains along the a axis. In comparison to the intrachain coupling constant of about 10 K, the magnetic order temperature $T_N \approx 0.1\,K$ is extremely low. This allows to study the system in a wide temperature- and magnetic-field range and to compare it to the rich magnetism that arises from the one-dimensional Heisenberg model, which is a textbook example for a low-dimensional spin chain. In this chapter, measurements of the specific heat, the thermal expansion and the magnetization up to the critical field of the spin chain are compared to high-precision calculations of the Heisenberg model.

6.1 Introduction

In the field of low-dimensional spin systems the Heisenberg model stands out due to both its simplicity on the one hand and its intriguing diversity of theoretical aspects on the other hand. Up to date, a wide field of research concerns the physics emerging from different model hamiltonians. A large number of theoretical techniques were employed to investigate the physical properties for different lattices and coupling scenarios. For example, the correlations of quantum spins on a two-dimensional lattice are considered as a key aspect for the understanding of cuprate-based high-temperature superconductors. In this context, quantum critical phenomena, i. e., the emergence of different ground states as a function of a non-thermal control parameter, play an important role. One of the plainest models, where quantum criticality can be observed, is the one-dimensional antiferromagnetic Heisenberg spin-$^1/_2$ chain,

$$\mathcal{H} = J \sum_i \mathbf{S}_i \cdot \mathbf{S}_{i+1} + h\, S_z^i. \tag{6.1}$$

Here, a quantum phase transition arises as a function of the field h. At zero magnetic field the ground state at $T = 0$ is given by the Bethe-Ansatz and the magnetic excitations form a gapless two-spinon continuum [40]. Applying a magnetic field the spatial isotropy is broken and a finite magnetization arises. Finally, the ground state character changes at the critical field $h_c = 2J$. Signatures of this transition can be observed in macroscopic properties also at finite temperature. However, model crystals of this type are quite rare. Not only an isotropic magnetism is asked for, but as well a unique crystal structure is required that supports a magnetic exchange of a one-dimensional character.

One compound with a high degree of one-dimensionality and no magnetic order down to a very low temperature $T_\mathrm{N} = 107\,\mathrm{mK}$ is the antiferromagnetic spin-$^1/_2$ chain compound copper pyrazine dinitrate (CuPzN, short for $Cu(C_4H_4N_2)(NO_3)_2$). In this compound, the coupling of the magnetic Cu^{2+} ions reveals a strong spatial anisotropy. Although the copper ions are separated by a comparably large distance of 6.7 Å along the a axis, the superexchange by the intermediate $C_4H_4N_2$ rings along that axis is relatively large as characterized by the coupling constant $J/k_\mathrm{B} \simeq 10\,\mathrm{K}$, derived consistently from different methods [13, 205–207]. Interchain couplings were estimated to be three orders of magnitude smaller [11], which renders the compound an ideal model system for the analysis of field-induced quantum criticality in a one-dimensional magnet. The Heisenberg model was successfully applied to describe the specific heat [13], the magnetization [17] and the thermal conductivity [208] of CuPzN. However, most of these studies do not cover the regime of quantum criticality at low temperatures close to the quantum critical field $g\mu_\mathrm{B}\mu_0 H_c = 2J$ (i. e., $T < 1\,\mathrm{K}$, $H \approx 14\,\mathrm{T}$). In this chapter, measurements of the thermal expansion, the magnetostriction, the specific heat and the magnetization in the full magnetic field range, where quantum critical behavior is expected, are compared to the Heisenberg model.

6.1.1 Structure

Crystals of the cupric nitrate-pyrazine complex $Cu(C_4H_4N_2)(NO_3)_2$ were first grown by slow evaporation in 1970 and the orthorhombic crystal structure of space group *Pmna*, shown in Fig. 6.1, was solved via X-ray analysis [209]. The lattice parameters and the atomic coordinates are summarized in Tab. 6.1. The magnetic Cu^{2+} ions are linked along the crystallographic a axis via aromatic rings of $C_4N_2H_4$ (pyrazine), shown in Fig. 6.1 (b). Each copper ion is surrounded by two nitrate groups, that lie in planes perpendicular to the chain axis a. Due to the electronic configuration of Cu^{2+} ($3d^9$), which implies a quenching of the orbital momentum in the local environment of *2/m* symmetry, one expects only weak magnetic anisotropies. A large spacing of Cu ions in

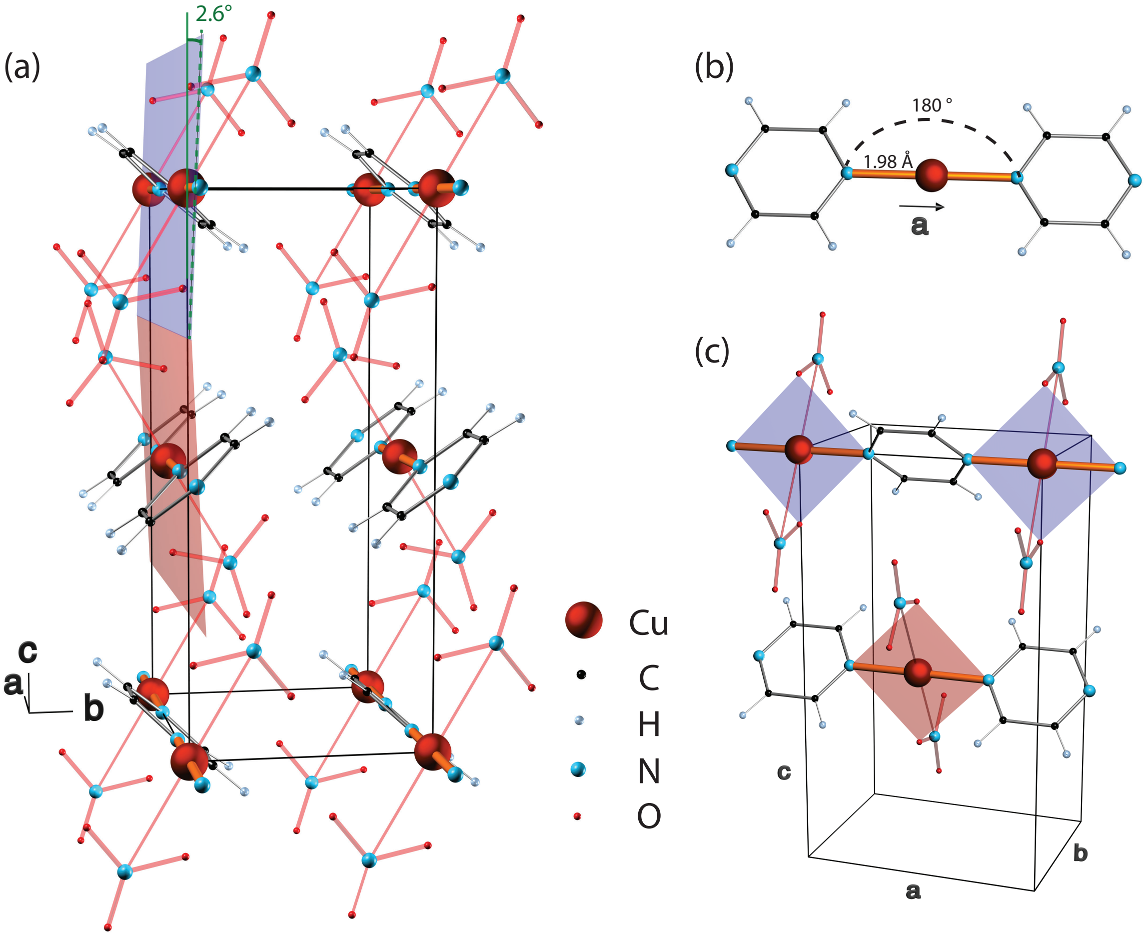

Figure 6.1: Sketch of the crystal structure of $Cu(C_4H_4N_2)(NO_3)_2$ (CuPzN), based on structure data of Ref. 209. In (a) the unit cell is shown together with shaded planes that indicate the two non-equivalent Cu sites that differ by a rotation $\pm 2.6\,^\circ$ around the a axis from one chain to the neighboring along c. In (b) a single copper ion together with the neighboring pyrazine ring that mediates the dominant exchange along a is shown. In (c) the planar coordination of Cu in two selected chains is depicted by the blue and red shaded planes.

the b and c direction combined with a short copper to pyrazine-nitrogen distance of 1.98 Å in the a direction gives rise to one-dimensional magnetism via superexchange paths Cu-pyrazine-Cu along a.

A close analysis of the structure reveals that the copper sites are not fully symmetry-equivalent. The planar coordination of copper is given by two pyrazine nitrogens and two nitrate oxygens which are closest to the center copper. This coordination is described by the site symmetry $2/m$ and arises in two orientations in the crystal structure that differ in a rotation by an opposing angle of $\pm 2.6\,^\circ$ around the a axis away from the ac plane [207]. The two types of coordination are depicted as blue and red shaded planes in Fig. 6.1 (a) and (c). The rotation of the planes, shown as a dashed green line in Fig. 6.1 (a) alternates along the c direction, but not along the chain direction a. As a consequence, the g factors along the crystallographic axes ($g_a = 2.2053$, $g_b = 2.265$ and $g_c = 2.063$, measured in Ref. 16 by ESR) are a superposition of the individual molecular

$Cu(C_4H_4N_2)(NO_3)_2$, space group *Pmna* (No. 53)
a=6.712(1) Å, b=5.142(1) Å c=11.732(2) Å

			atomic coordinates		
Atom	site	symmetry	x/a	y/b	z/c
Cu1	$2a$	2/m..	0	0	0
C1	$8i$	1	0.396 66(56)	0.166 49(83)	−0.064 76(35)
H1	$8i$	1	0.324(12)	0.288(14)	−0.1064(57)
N1	$4e$	2..	0.295 66(55)	0	0
N2	$4h$	m..	0	0.262 58(102)	0.193 56(42)
O1	$4h$	m..	0	0.017 67(87)	0.171 11(31)
O2	$4h$	m..	0	0.413 83(100)	0.110 29(42)
O3	$4h$	m..	0	0.333 53(106)	0.292 26(40)

Table 6.1: Positions and atomic coordinates of $Cu(C_4H_4N_2)(NO_3)_2$ in the space group *Pmna* obtained from X-ray diffraction [209].

g factors. The deviation of the g factor from the value of 2, expected for the spin-only magnetism of Cu^{2+} ($3d^9$), is explained by finite crystal anisotropies and higher-order effects that recover part of the angular momentum quenched by the crystal field. Due to the fact that the molecular and the crystallographic coordinate systems only differ in a rotation around the chain direction a, applied magnetic fields do not induce staggered fields within a single spin chain. Above the magnetic order temperature, where spin chains can be treated as well isolated from each other, thus, a single spin chain in a magnetic field is sufficiently described by a magnetic field term $\propto h\, S_z^i$ as given in Eqn. (6.1).

6.1.2 Literature

In one of the first studies of the magnetism of $Cu(C_4H_4N_2)(NO_3)_2$, the one-dimensional magnetism of the compound due to superexchange has been identified [205]. Using powder samples the susceptibility down to 2.9 K is compared to the Ising model. From a slight mismatch to the data, it is assumed that the Heisenberg model may be more appropriate. In another study of the susceptibility [206], single crystals are investigated by measurements of the susceptibility parallel and perpendicular to the chain direction a. From a Curie-Weiss fit of the high-temperature data from 20 to 60 K the g factors $g_\parallel = 2.04$ and $g_\perp = 2.11$ and a Weiss constant of about 5 K is found. A comparison of the low-temperature susceptibility data, shown in Fig. 6.2, to the one-dimensional Heisenberg model (solid lines) yields an exchange constant $J/k_\mathrm{B} = 10.6\,\mathrm{K}$ and similar g factors. The Ising model, assumed in Ref. 205, is shown not to describe the data.

In a zero-field study of the specific heat in Ref. 10 below 10 K a broad maximum on top of the phonon background and a linear low-temperature dependence is found, shown in Fig. 6.3. Using a coupling constant $J/k_\mathrm{B} = 10.4\,\mathrm{K}$ an excellent agreement with the Heisenberg model is obtained. Close to 10 K small deviations are found that are accounted either to a Schottky contribution of pyrazine impurities in the sample or to a phonon background c_ph that is not described by a simple power law $c_\mathrm{ph} \propto T^3$.

The g factors along the crystallographic axes show a small anisotropy due to a finite angular momentum and have been evaluated by ESR [207, 210],

$$g_a = 2.05, \quad g_b = 2.27, \quad g_c = 2.07. \tag{6.2}$$

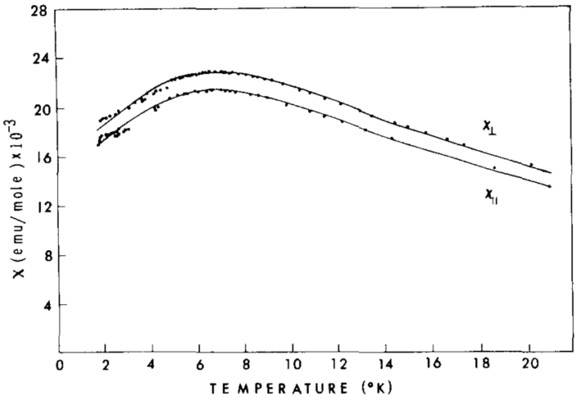

Figure 6.2: Susceptibility of CuPzN, measured parallel to the chain axis a and perpendicular to it, fitted by the 1D Heisenberg model with $J/k_\mathrm{B} = 10.6\,\mathrm{K}$, $g_{||} = 2.03$, $g_\perp = 2.10$. (Taken from Ref. 206)

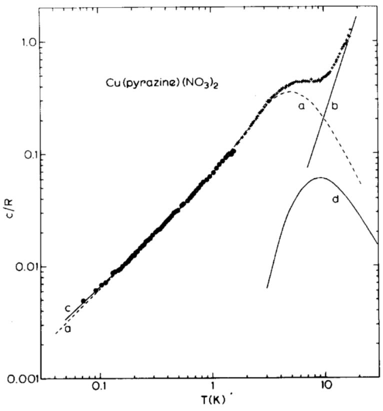

Figure 6.3: Zero-field specific heat of CuPzN, measured using powder and microcrystalline samples in comparison to the 1D Heisenberg model with $J/k_\mathrm{B} = 10.4\,\mathrm{K}$. (Taken from Ref. 10)

In these early studies, the influence of magnetic fields on the system has not been studied. The quantum phase transition of the Heisenberg chain at $g\mu_\mathrm{B}\mu_0 H_c = 2J$ is not discussed in any of the analyses of the thermodynamic properties in literature. In the thermal transport a magnetic contribution arises and in the quantum critical regime signatures of the quantum critical field of about 15 T are seen [208]. In a zero-field muon-spin relaxation experiment a very low magnetic order temperature $T_\mathrm{N} = 107\,\mathrm{mK}$ has been found [11]. Comparing this temperature to Monte Carlo results on the ordering temperature T_N of the Heisenberg model on a square lattice [211], the ratio $J'/J = 4.4 \times 10^{-3}$ between inter- and intrachain couplings is derived.

The low-temperature magnetization of CuPzN, shown in Fig. 6.4, has been analyzed up to the critical field of the spin chain [17, 212]. Based on the exact solution by the Bethe ansatz for $T = 0$ a coupling constant $J/k_\mathrm{B} = 10.8\,\mathrm{K}$ and a g factor of 2.3 is derived. Although the temperature of 80 mK is below $T_\mathrm{N} = 107\,\mathrm{mK}$, no indication for magnetic order is found. From the derivative $\partial M/\partial H$ a critical field of 13.97 T is derived. At the critical field, a power law of the magnetization $M \propto 1/\sqrt{T}$ is found.

The magnetic excitations of the Heisenberg chain form a two-spinon continuum, which has been resolved in detail in CuPzN by inelastic neutron scattering [13, 15]. Excitations extending the creation of two spinons are investigated with great success in the related compound $\mathrm{CuSO_4{\cdot}5D_2O}$ [12]. The advantage of that compound lies in the availability of large single crystals and the smaller saturation field of about 5 T. The energy scale that determines the saturation field is the primary coupling constant and in both systems it is reasonably smaller than in most other realizations of the Heisenberg model. In many copper compounds the exchange constants are in the range of 1000 K [213, 214]. In these systems, magnetic fields accessible in laboratory equipment, do not suffice to severely influence the spin chain.

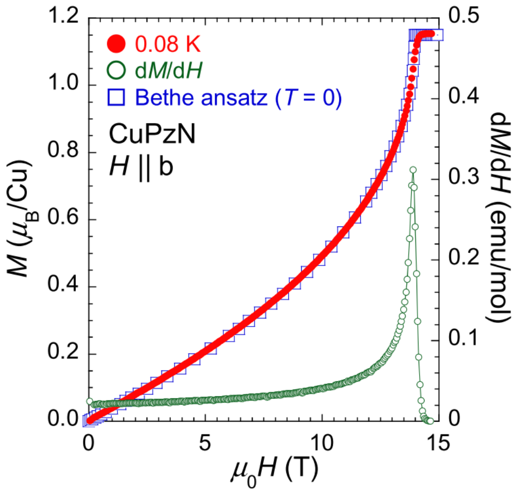

Figure 6.4: Magnetization of CuPzN, measured as a function of the magnetic field applied along b at 80 mK (red dots) in comparison to zero-temperature results using the Bethe ansatz (open squares). (Taken from Ref. 17)

In CuPzN the saturation field of about 14 T lies in a range that is accessible in experiments. The thermodynamic properties of the compound, however, have been investigated only at reasonably smaller magnetic fields. In Ref. 13 the specific heat is analyzed, but only up to 9 T. Apart from a small change in the low-temperature slope of $c_p(T)$, that is related to a renormalization of the spinon velocity, true quantum critical signatures are not discussed.

6.2 Experimental results

Large single crystals of copper pyrazine dinitrate have been provided by Mark M. Turnbull (Carlson School of Chemistry and Biochemistry, Clark University, USA). They grow in a typically needle-shaped geometry with the crystallographic c axis as the longest axis and with b as the shortest axis. The crystals are rather brittle and may cleave if not treated carefully. They have a slightly transparent, blue color. The as-grown crystals have rather rough surfaces. Thus, from the available crystals a single suitable sample of adequate geometry was selected and used for the measurements of all thermodynamic quantities presented in the following.

The specific heat, the magnetization and the magnetocaloric effect were measured using a sample of CuPzN of about 7 mg weight with the approximate dimensions of $5{\times}2{\times}0.5\,\mathrm{mm}^3$. The specific heat was measured using the home-built ^{3}He calorimeter described in Chapter 3.2.3 by the relaxation-time method. Down to the base temperature of the cryostat of 250 mK no internal relaxation effects were observed. In the whole temperature range the external relaxation time was of the order of a few seconds, which allowed to robustly determine the specific heat by the relaxation method. The addenda heat capacity was measured in a separate run including a small dependence on applied magnetic fields up to 15 T. The influence of the addenda's heat capacity on the obtained specific heat, however, is small as the sample's signal exceeds the addenda's contribution by about one order of magnitude at low temperature $T < 10\,\mathrm{K}$. The magnetocaloric effect was measured in the same run using the experimental technique described in Chapter 3.3. For comparison the specific heat was also measured using the heat capacity option of the commercial PPMS setup (Physical Properties Measurement System, Quantum Design).

For the magnetization measurements an existing capacitance magnetometer was used, described in more detail in Refs. 106, 215. A new sample holder was adapted to the magnetometer which allows to mount the sample with the b axis along the magnetic field. In contrast to the conventional method, where the magnetometer is placed in a magnetic field gradient by positioning it 5 cm off from the magnetic field center of the superconducting magnet, here, it was placed in a distance of only 2 cm. Such, the magnetic field at the sample position is maximized to a field of 15.4 T in an external field of 17 T, sufficiently high to reach the saturation field of the system. As the magnetic moment of the available CuPzN sample at small fields is comparable to that of the empty sample holder, in advance a calibration of the sample holder was performed for both distances of 5 cm and 2 cm from the magnetic field center.

The thermal expansion and the magnetostriction of the a axis have been measured by J. Rohrkamp. Here, the data taken from Ref. 216 are compared to precise results of the Heisenberg spin chain. The data were acquired using a home-built capacitance dilatometer in a temperature range from 250 mK to 20 K. The dilatometer was mounted in a perpendicular configuration, i. e., with the magnetic field of up to 17 T applied along the b axis, while the relative length change $\Delta L_a/L_0$ was measured along a. The thermal expansion coefficient α_a and the magnetostrictive coefficient λ_a were obtained by numerical derivation, $(\alpha_a, \lambda_a) = \frac{1}{L_0}\frac{\partial \Delta L_a}{\partial (T,H)}$. For simplicity, the subscript a is dropped in the following for all three quantities.

The slightly larger value of g_b in comparison to the other axes was utilized in all experiments to maximize the magnetic field range accessible in the experiment. All data shown below were acquired with the magnetic field H applied along b. In most cases selected data is shown, see Appendix B for the full data sets of thermodynamic quantities.

6.2.1 Thermal expansion and magnetostriction

The length change of CuPzN was measured along the chain direction a in magnetic fields applied along b. The crystallographic a axis was chosen for the measurements because the largest contribution of the spin chain magnetism to the length change has been found for this axis [217]. In Fig. 6.5 the relative length change as a function of temperature and magnetic field together with its respective derivatives is shown. The data of $\Delta L/L_0$ were shifted according to the magnetostriction acquired at 0.25 K and to the thermal expansion measured at zero field. All temperature-dependent data show a common behavior for temperatures $T > 15$ K, where the lattice contribution dominates. Below 10 K an additional contribution arises that is best analyzed from the thermal expansion coefficient α, shown in Fig. 6.5 (b). Around 5 K it reveals a broad maximum that shifts to lower temperature with increasing the magnetic field. At 13 T a strong divergence-like increase of the low-temperature tail arises that changes its sign by increasing the field to 14 T. For even larger magnetic fields a new minimum of $\alpha(T)$ arises at about 1 K. The change of the sign of α is a typical fingerprint of a

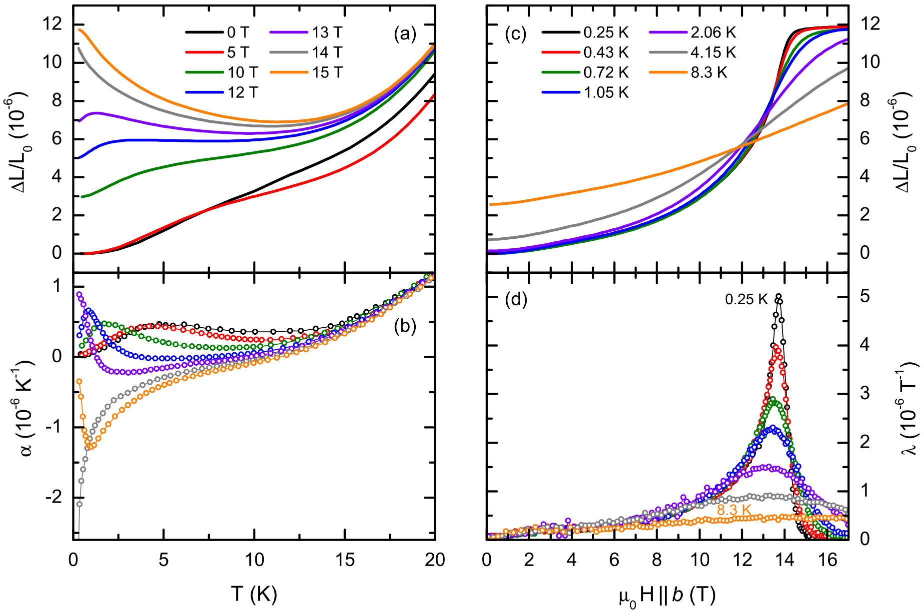

Figure 6.5: Thermal expansion and magnetostriction of CuPzN measured along the *a* direction with magnetic fields applied along the *b* axis.

quantum phase transition at the critical field of the spin chain [152, 154, 155]. The critical field is also reflected in the magnetostriction, plotted in Fig. 6.5 (c) and (d). At low temperature $T \lesssim 1\,\mathrm{K}$ the length change $\Delta L(H)$ saturates at about 14 T, also reflected in a peak of λ. With increasing the temperature, the features broaden and above 4 K a rather featureless field dependence arises. The overall size of the thermal expansion and the magnetostriction of about 10^{-5} is rather small in comparison to Cs_2CoCl_4 (cf. Chapter 4.2) or to other low-dimensional spin compounds [77]. The origin of the small lattice expansion lies in a small magnetoelastic coupling of the system and to some degree is consistent with the fact that CuPzN does not form a non-magnetic ground state via a Spin-Peierls transition [218], which is the alternative to magnetic ordering commonly discussed in the field of one-dimensional systems for spin-$^1\!/_2$ chains [219]. Systems with a large thermal expansion like $CuGeO_3$ [220–222] and several other spin-$^1\!/_2$ chain compounds [223–225] show a Spin-Peierls transition. However, in $Cu(C_4H_4N_2)(NO_3)_2$ the magnetoelastic coupling is so small that instead magnetic order is stabilized. The size of interchain interactions in addition is very small, which explains the low Néel temperature.

6.2.2 Specific heat

In Fig. 6.6 selected data of the specific heat c_p are shown. At zero field the temperature dependence above 10 K is dominated by phonons. The specific heat measured with the home-built setup and with the commercial setup lie on top of each other, see inset of Fig. 6.6 (a). As expected from the Debye model, at low temperature $T \lesssim 30\,\mathrm{K}$ the specific heat approximately follows a power law $c_p \propto T^3$, shown by an orange line in Fig. 6.6 (a). Although there are deviations above 20 K, the extrapolation of the phonon specific heat to low temperature reveals an additional magnetic contribution to c_p in form of a maximum around 5 K which exceeds the phonon signal by at least one order of magnitude. Below about 1 K a linear temperature dependence arises as expected

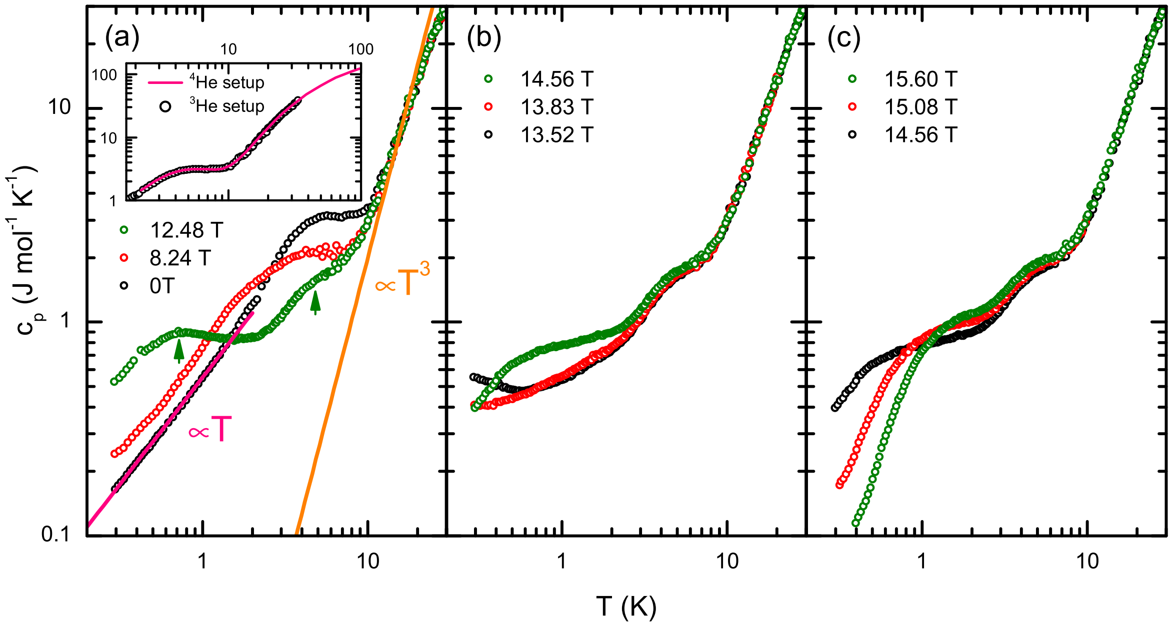

Figure 6.6: Specific heat of CuPzN as a function of temperature at different constant magnetic fields applied along b. In (a) straight lines indicate power laws $c_p \propto T$ (pink) and $c_p \propto T^3$ (orange). In the inset the data obtained with two different setups are compared.

for various one-dimensional spin chains [130]. In magnetic fields applied along b the low-temperature specific heat changes, while the phonon background above about 10 K remains essentially unchanged. Up to about 13 T the zero-field maximum reduces in absolute value and shifts to lower temperature. At 12.48 T two main features can be identified in the data, marked by green arrows in Fig. 6.6 (a). The broad maximum around 0.8 K continuously evolves from the zero-field maximum. The additional upper maximum lies close to the temperature of the zero-field maximum at about 5 K, but is reduced in absolute value. It is found as well in all data acquired at larger magnetic field. From 13.52 T to 14.56 T, shown in panel (b) of Fig. 6.6, the temperature dependence of c_p below 1 K fundamentally changes and for even larger magnetic fields an increasing spin gap is indicated by the strong suppression and a redistribution of the specific heat to higher temperature.

The strong dispersion of the low-temperature specific heat is more clearly seen in the field dependent data $c_p(H)$, plotted in Fig. 6.7 for different constant temperatures from 0.3 to 2.5 K. All data show a well-defined minimum at about 14 T that slightly shifts to larger fields with decreasing the temperature. Below 1 K a double-peak structure of $c_p(H)$ is resolved. At elevated temperature only the low-field maximum is resolved within the experimental field range. This universal field dependence arises from the increasing entropy close to quantum critical points [152].

6.2.3 Magnetocaloric effect

The magnetocaloric effect was analyzed by keeping the sample temperature fixed while sweeping the magnetic field. The required large magnetic fields of more than 14 T

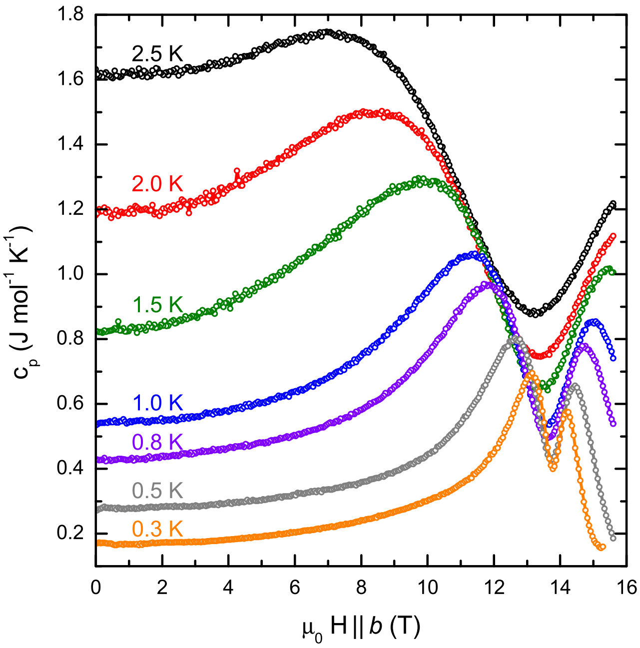

Figure 6.7: Specific heat of CuPzN as a function of the magnetic field applied along the *b* direction. Around 14 T a double peak structure evolves.

restricted the experiments to a single dewar with a suitable superconducting magnet that easily reaches up to 15 T. However, this magnet shows unwanted superconducting flux jumps below about 2 T. They induce non-continuous jumps of the magnetic field at the sample position, which in turn excessively heat the sample platform due to induction. These jumps are also reflected in the magnetocaloric raw data, shown in Fig. 6.8. In the field range shaded in gray, the power P applied to the heater strongly fluctuates. In the inset an exemplary oscillation of P close to 2 T is shown. Here, upon decreasing the field a flux jump occurs and the power is reduced to compensate the inductive heating, followed by the typical oscillations of a PID control loop. Although these effects are completely unwanted, they cannot be avoided in this magnet. Yet, the fast recovery of P and the shape of the oscillations indicate that the control parameters are well tuned.

Above 3 T the magnet does not show discontinuities. Up to 13 T the temperature stability, indicated by the relative change $(T_{\text{sample}} - T)/T$ in Fig. 6.8 (b), is below 0.2 %, which is about the noise level of the temperature acquisition. In the power P small kinks are found at 4 and 6 T. They stem from the interpolation of the magnetoresistance of the sample thermometer and cancel by anti-symmetrizing during the data analysis. Above 10 T the power shows a dependence on the field sweep direction. In this range, the sample temperature is slightly less stable. Still, the deviations are below 1 % and, thus, safely negligible. Due to the sudden change of the sweep direction at the maximum field at about 15.5 T the temperature control starts to oscillate, but recovers quite fast at about 15.3 T.

In the analysis of the raw data the low-field and the high-field region where experimental artifacts arise, are excluded. Using Eqns. (3.16) and (3.17) the entropy change $\Delta S = S(H) - S(4\,\text{T})$ with respect to the entropy at 4 T and the magnetic Grüneisen ratio $\Gamma_H(H)$ is calculated from the antisymmetric contribution of $P(H)$. The obtained ΔS curves, shown in Fig. 6.9 (a), are shifted with respect to each other according to the

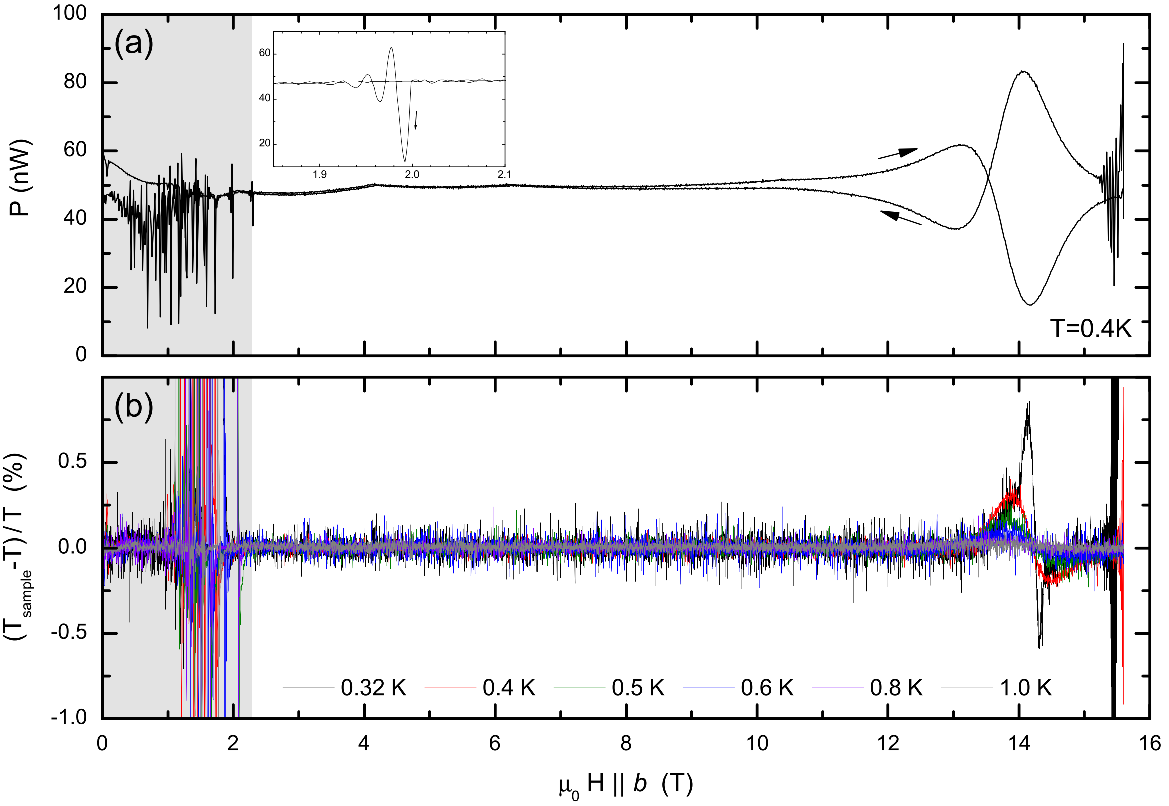

Figure 6.8: Raw data of the magnetocaloric-effect measurements. In (a) the power P applied to the heater as a function of the magnetic field is shown both for increasing and decreasing the field. Arrows indicate the sweep direction. In (b) the relative deviation of the sample temperature from the target temperature is shown.

linear low-temperature dependence of the entropy change $S(T, 4\,\mathrm{T}) - S(0.32\,\mathrm{K}, 4\,\mathrm{T})$, obtained from the specific heat at 4 T by integration and plotted in the inset (1) of Fig. 6.9 (a). Such, a single entropy offset remains for all data, which here is chosen such that $\Delta S(0.32\,\mathrm{K}, 0) = 0$. The overall temperature and field dependence of ΔS reveals some irregularities that are probably of experimental origin. For example, $\Delta S(0.32\,\mathrm{K})$ intersects $\Delta S(0.4\,\mathrm{K})$ twice. Also the curve at 0.8 K does not follow the general trend of the others. These deviations may arise from small experimental uncertainties in the raw data that come to light due to integrating the data. While the sample temperature of 0.32 K marks the lower border of the possible temperature range in the experimental setup, the data at 0.8 K are possibly influenced by other experimental issues. Thus, the absolute values at these two temperatures are not very reliable. Nevertheless, all measurements consistently show a maximum of the entropy between 13 and 14 T. Decreasing the temperature, the maximum narrows and shifts to larger fields. Below 0.6 K the shift of the maximum is well described by a linear fit, shown in the inset (2) of Fig. 6.9 (a), which extrapolates to a zero-temperature critical field of about 13.8 T.

The magnetic Grüneisen ratio Γ_H, plotted in Fig. 6.9 (b) versus the magnetic field, apart from constants, relates to ΔS via derivation. At small fields $H \lesssim 10\,\mathrm{T}$ it takes small negative values of about $-0.1\,\mathrm{T}^{-1}$, indicating a positive temperature dependence

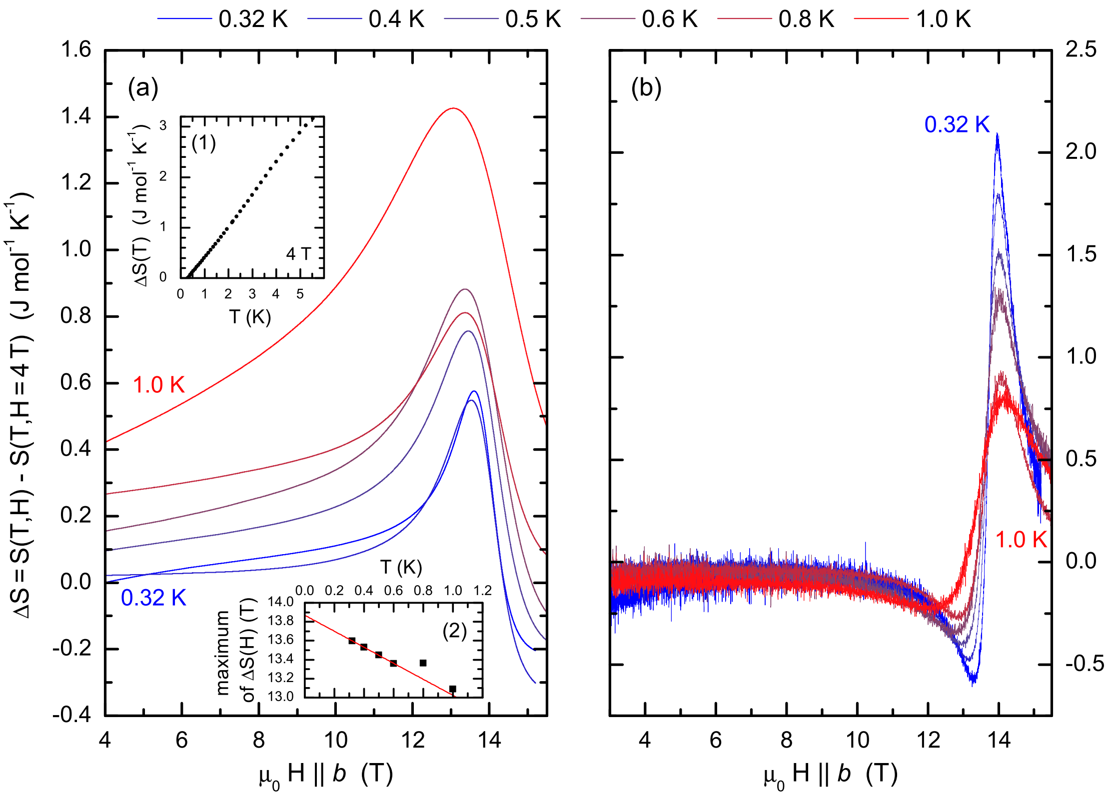

Figure 6.9: Entropy change ΔS (a) and the magnetic Grüneisen ratio Γ_H (b) as a function of the magnetic field applied along *b*. The entropy change is given in relation to the entropy at 0.32 K and 4 T, based on the temperature-dependent change of the entropy (inset 1). Inset 2 displays the temperature dependence of the peak of $\Delta S(H)$.

of the magnetization $\partial M/\partial T$. At high fields $\Gamma_H > 0$ reflects the thermal reduction of the saturated magnetization similar to a free ion's magnetism. Approaching a field of about 13.8 T, the data become increasingly temperature dependent and remind of a broadened pole. Both below and above the critical field the absolute values of $|\Gamma_H(T \to 0)|$ seem to diverge with decreasing the temperature. Consistent with the maximum of ΔS in between Γ_H becomes zero.

6.2.4 Magnetization

The magnetization as a function of the magnetic field is shown in Fig. 6.10. The Faraday magnetometer used for these measurements requires a sizable magnetic moment of the sample and a field gradient to obtain significant data. Below about 3 T the magnetic moment of the sample is comparably small. Thus, the magnetization cannot be determined with high precision in this field range. The most structure in the data arises at larger fields, anyway. Up to 10 T the magnetization increases with a rising slope. Depending on the temperature an inflection point is found between 13 and 14 T that is reflected in a maximum of the derivative dM/dH, shown on the right scale of Fig. 6.10. At 0.3 K a maximum of dM/dH at 13.6 T is found. Increasing the temperature, the data broaden and the inflection point shifts to larger fields as plotted in the inset of

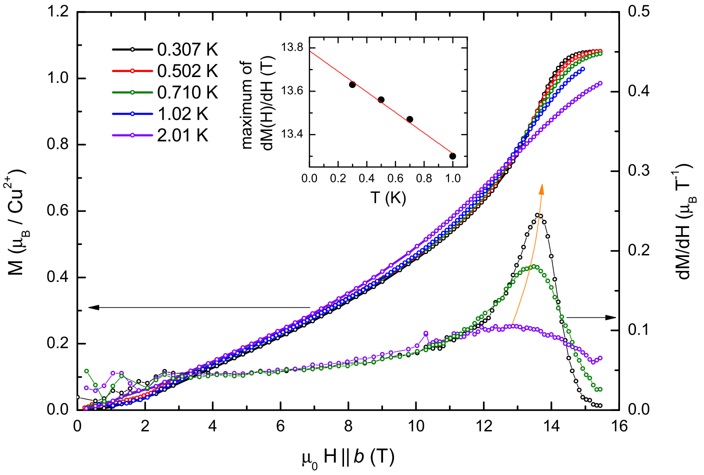

Figure 6.10: Magnetization of CuPzN measured as a function of the magnetic field applied along b at different constant temperature. For two selected temperatures the derivative dM/dH is shown (right scale).

Fig. 6.10. A linear fit of the temperature dependence yields a zero-temperature critical field of about 13.8 T, similar to the critical fields observed in the other quantities.

6.3 Comparison to the Heisenberg model

During the long history of the Heisenberg spin-chain model in the field of condensed matter physics, a large number of theoretical and experimental works have concerned its fundamental properties and manifestations in model crystals. Despite the simple form of the Hamiltonian,

$$\mathcal{H} = J \sum_{i} \mathbf{S}_i \cdot \mathbf{S}_j - g\mu_{\mathrm{B}}\mu_0 H S_i^z, \tag{6.3}$$

and the exact solubility based on the Bethe ansatz [40], the calculation of thermodynamic properties of the model at arbitrary temperature for a long time pose a challenge for theory. Especially at low-temperature ($T \ll J$), significant corrections arise, which for example are reflected in a large slope of the susceptibility. In this chapter the experimental data are compared to calculations that are based on a formalism laid out in Ref. 46 which yields high-precision results for thermodynamic quantities based on the exact solution. The author A. Klümper has provided a Fortran code that calculates the free energy F and its derivatives S (entropy), C (heat capacity), M (magnetization), as well as the spin-spin correlator $\langle \mathbf{S}_i \cdot \mathbf{S}_{i+1} \rangle$ for fixed values of the temperature and the magnetic field h. The calculations have been repeated in a dense mesh for temperatures T/J from 0.001 to 10 with 250 steps and for magnetic fields h/J from 0 to 6 with 600 steps. Using a standard desktop computer the total of 150.000 calculations completed in about one week. In Fig. 6.11 selected computation results are shown as density plots, where blue (yellow) colors indicate small (large) values. The heat capacity at zero field has a maximum at about $0.5\,T/J$ and shows the typical minimum around the critical field $2\,h/J$. At the critical field the low-temperature weight of the entropy is significantly increased. The magnetization saturates at $2\,h/J$ and continuously broadens with increasing the temperature. In case of the spin-spin correlation $\langle S_i S_{i+1} \rangle$ blue colors do

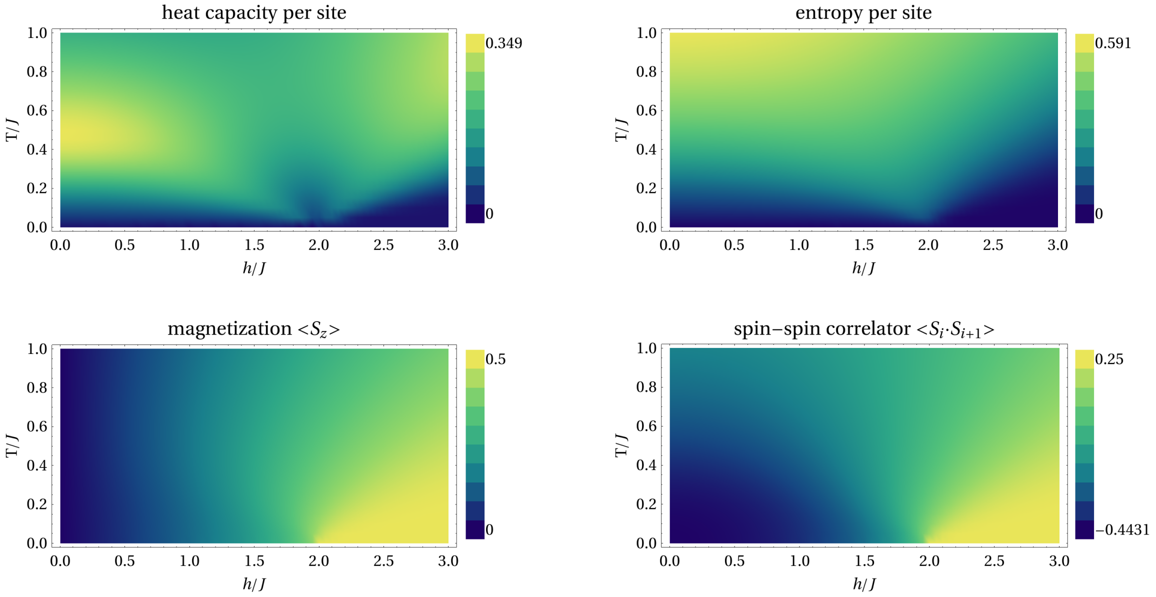

Figure 6.11: Calculated thermodynamic quantities of the spin-1/2 Heisenberg chain as a function of the reduced magnetic field h/J and temperature T/J. The colors indicates the value of the respective quantity from low (blue) to high (yellow).

not indicate 0 as in case of the previous quantities, but the zero-field low-temperature limit of the correlator of about −0.4431, while yellow indicates the value of 0.25 in the fully polarized state.

For comparisons to experimental data at arbitrary temperature and magnetic field, the calculated thermodynamic quantities at fixed temperature and field are interpolated by multivariate splines of third order using MATHEMATICA [23]. This allows to obtain any experimental quantity Ω for an arbitrary coupling constant J and a magnetic field H by interpolating and scaling the calculated ω,

$$\Omega = A \cdot \omega(\frac{T}{J}, g\frac{\mu_\mathrm{B}}{k_\mathrm{B}}\frac{H}{J}). \tag{6.4}$$

Here, the factor $\frac{\mu_\mathrm{B}}{k_\mathrm{B}} \approx 0.671$ is introduced and takes into account that J is given in units of Kelvin and H in units of Tesla. Further constants A are required to convert to the experimental units. For example in case of the specific heat, $A = N_\mathrm{A} k_\mathrm{B}$ converts from the heat capacity per site to $\mathrm{J\,mol^{-1}\,K^{-1}}$.

In the following the experimental data are compared to the Heisenberg model. For each thermodynamic quantity the experimental data $x(T_i, H_i)$ are fitted simultaneously by numerically minimizing the cost function

$$\Delta(\xi_1, \xi_2, ..) = \sum \left[x(T_i, H_i) - \Omega(T_i, H_i, \xi_1, \xi_2, ..)\right]^2 \tag{6.5}$$

with respect to the model parameters ξ_i using a metropolis-like algorithm that converges within a few hundred steps. As the field dependence of the Heisenberg model (Eqn. 6.3) depends on the ratio g/J, both quantities are hardly obtained simultane-

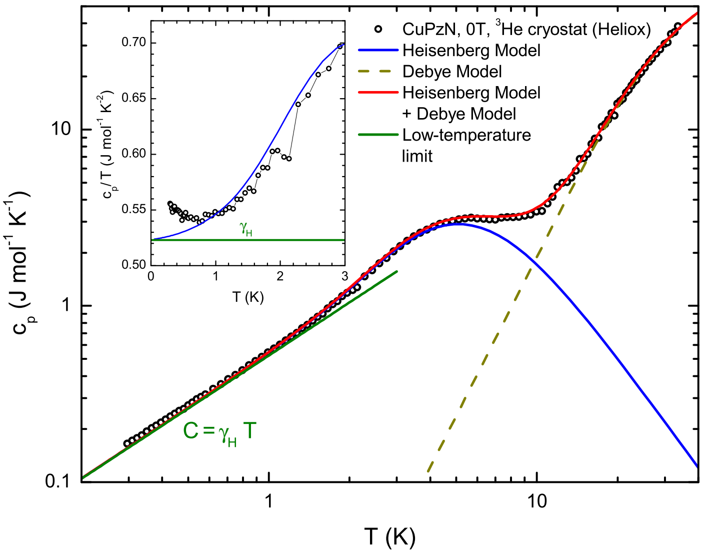

Figure 6.12: Zero-field specific heat of CuPzN in comparison to theory. The dashed yellow line represents the phonon contribution approximated from a Debye model. The blue line is the specific heat of the Heisenberg model using $J/k_\mathrm{B} = 10.6\,\mathrm{K}$, the green line represents the expected low-temperature limit. The sum of both contributions (red line) matches with the experimental data (open symbols). In the inset the low-temperature data are shown divided by temperature.

ously from the data. Thus, in all fits the g factor was fixed to the established literature value for the b axis of $g_b = 2.27$ [207, 210].

6.3.1 Specific heat

At zero field, the measured specific heat is well described by a sum of a Debye model and the calculated specific heat of the Heisenberg model. Although the applicability of the Debye model above 20 K might be questioned, a phenomenological description of the data is possible in this temperature range using a Debye temperature of 153 K and a scaling constant of 3.5, as shown by the dashed yellow line in Fig. 6.12. Below 10 K the extrapolation of the model essentially follows a T^3 dependence and provides an estimate of the phonon background for the fit of the magnetic low-temperature contribution by the Heisenberg model. The blue line represents the specific heat of the Heisenberg model using an exchange constant $J/k_\mathrm{B} = 10.6\,\mathrm{K}$. At low temperature the model calculation approaches the linear temperature dependence

$$C_H = \gamma_H \cdot T = \frac{\pi}{3} R \frac{k_\mathrm{B} T}{v_s(H)}, \tag{6.6}$$

with the spinon velocity $v_s(H)$, as expected for the Heisenberg spin chain in the limit of low temperature $T \ll J$ from the Bethe ansatz [43, 226, 227]. The linear temperature dependence of the specific heat arises from the linear dispersion $\epsilon(k)$ of spinons at low energy. At zero field the velocity $v_s = \frac{\partial \epsilon}{\partial k} = \pi J/2$ is determined by the coupling constant J. The green line in Fig. 6.12 represents $C_H(T)$ assuming $J/k_\mathrm{B} = 10.59\,\mathrm{K}$. The match of the model calculations with the exact result on the low-temperature limit confirms the high precision of the calculations. The sum of the magnetic contribution of the Heisenberg model and of the approximated phonon contribution, shown as a red line, matches the experimental data within a few percent in the whole temperature range. Yet, there are small deviations in the low-temperature tail as seen in the specific heat

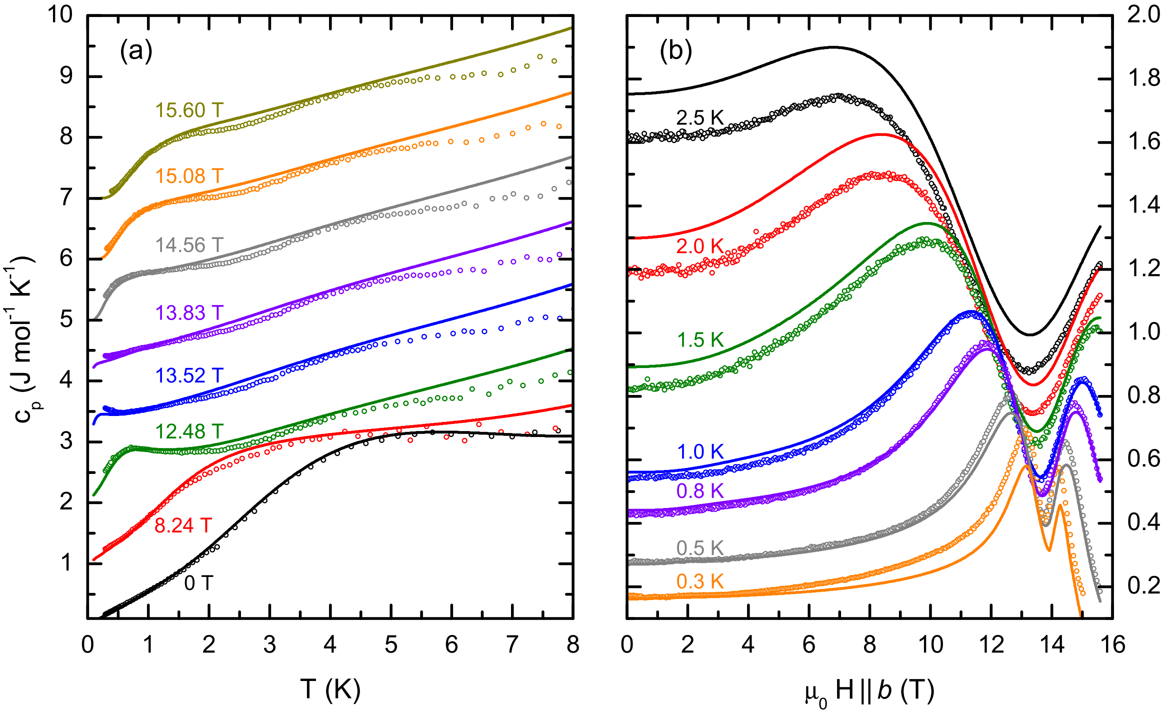

Figure 6.13: Temperature (a) and field (b) dependence of the specific heat in comparison to the Heisenberg model. Open symbols are the experimental data, solid lines are fits to the data. Curves in (a) are offset from each other by 1 $\mathrm{J\,mol^{-1}K^{-1}}$.

divided by temperature, plotted in the inset of Fig. 6.12. In this representation the slope of the linear temperature dependence is represented by a finite y intersect. The green line marks the value $\gamma_H \simeq 0.522\,\mathrm{J\,mol^{-1}\,K^{-2}}$ expected from Eqn. (6.6). While the calculations continuously decrease with decreasing temperature and approach γ_H, the experimental data increase below about 1 K. In a plot of $c_p(T)$ this deviation is reflected in a mismatch of the absolute values of about 5 %. Below 1 K the typical error of the specific heat measurements is of the same order. A true physical origin for the deviation therefore cannot be stated from this comparison.

Extending the comparison to include the specific heat at finite magnetic fields, the simultaneous fit of all data results in a very similar coupling constant

$$J/k_\mathrm{B} = 10.59\,\mathrm{K} \tag{6.7}$$

and a somewhat larger Debye temperature of 178 K. As shown in Fig. 6.13 (a), the overall field dependence at low temperature is well reproduced by the calculations. The suppression of the zero-field maximum from about 5 K to lower temperature as well as the high-field exponential temperature dependence are consistently found in the calculations. However, at fields larger than about 8 T the calculations do not reproduce the reduced values of the experimental data between 2 K and 4 K. Also, starting at about 6 K the specific heat is overestimated by the theory. In this temperature range the specific heat is possibly dominated by phonons, which suggest that the Debye model fails here. Yet, in the zero-field data these issues do not arise. In principle, the phonon specific heat might also depend on the magnetic field, but typically these effects are reasonably smaller.

Similarly, the field dependence of c_p is well described by the Heisenberg model, but only on a semi-quantitative level, see Fig. 6.13 (b). The double peak structure and its broadening by temperature are fully reflected by the calculations. However, the absolute values are not described by a single set of model parameters in the full temperature and field range. While at small fields only the high-temperature calculations are offset form the data, increasing the field the deviations increase further. Close to the critical field the calculations differ from the experimental data by about 10 %. This result is not due to a wrong modeling of the phonon background. Below 1 K the phonon specific heat, extrapolated from the high-temperature data, is smaller by about two orders of magnitude than the magnetic contribution. For example at 0.3 K phonons are fully negligible, but nevertheless the Heisenberg model cannot account for the absolute value of c_p around 14 T at that temperature.

A strict consequence of the mismatch would be to question the applicability of the Heisenberg model to CuPzN. In analogy to the discussion of possibly different anisotropies in Cs_2CoCl_4, one may ask whether the deviations arise from a magnetism of CuPzN that is not fully isotropic as assumed in the Heisenberg model. As seen from the slight anisotropy of the g factor for different crystallographic axes, the magnetism apparently is influenced by a finite angular momentum. Due to spin-orbit coupling in second order a small fraction of the quenched orbital moment in a crystal field may be recovered, leading to a factual anisotropy of the magnetism. A rough estimate of the anisotropy is obtained from the difference of the g factors $g_a = 2.05$ and $g_c = 2.07$ in comparison to $g_b = 2.27$. The two smaller g factors in comparison to the single larger one suggest an easy axis anisotropy. In analogy to the square dependence of the anisotropy parameter Δ in the XXZ Hamiltonian on the ratio of the g factors [3], one may estimate that $Cu(C_4H_4N_2)(NO_3)_2$ in fact has a small Ising anisotropy $\Delta \approx 1.01$. In consequence a small, yet finite gap of the order of $0.01\,J \approx 0.1\,\mathrm{K}$ in the excitation spectrum would follow and the low-temperature specific heat should be strongly influenced. The temperature range of the experiment, however, exceeds the estimated gap size by a factor of three. Thus, even if there is a finite gap, it hardly contributes to the present data. Only the zero-field specific heat divided by temperature (inset of Fig. 6.12) vaguely suggests the onset of a low-temperature feature below about 0.8 K. Yet, from the present data the scenario of a finite anisotropy of the magnetism of CuPzN cannot be quantified. To observe an eventually exponential temperature dependence of the specific heat measurements well below 100 mK are required, which is not only an experimental challenge, but finally also magnetic order occurs in this temperature range.

Several other possible influences on the specific heat in magnetic fields that could explain the deviations have been analyzed. Due to the imperfect sample shape, demagnetization effects could play a role. Yet, even assuming a demagnetization factor of 1, they are safely negligible in the full field range due to the small magnetization density of $Cu(C_4H_4N_2)(NO_3)_2$. The coupling constant may depend on temperature and on the magnetic field due to magnetoelastic coupling. To test this hypothesis, in the fits a coupling constant $J(T, H) = J_0 + \delta \cdot \langle S_i S_{i+1} \rangle$ changing as a function of the spin-spin

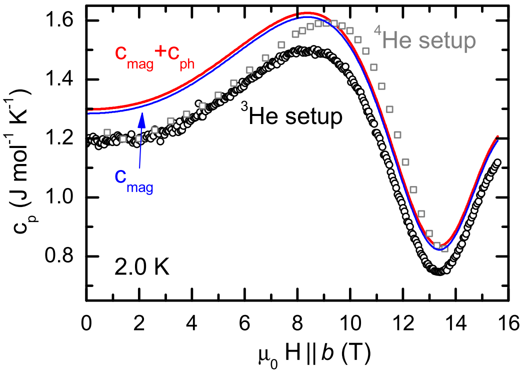

Figure 6.14: Zero-field specific heat of CuPzN measured at a temperature of 2 K using a home-built calorimeter with a ^{3}He cryostat (black circles) and a commercial setup based on a ^{4}He cryostat (gray squares) in comparison to theory. The blue line indicates c_{mag} of the Heisenberg model. An additional phonon background c_{ph} contributes to the red line.

correlator was assumed, where δ is a tunable parameter. However, the fits do not indicate a systematic field dependence of J. Due to the presence of two non-equivalent copper sites and the small anisotropy of the g factor also staggered field effects could be taken into account. A difference of the g factor by a small value Δg between two types of spin chains translates into a difference of the effective field from the external field H by $\Delta H = \Delta g \cdot H$. Thus, the total specific heat can be modeled as a superposition,

$$c_p(T, H) = \frac{c_p(T, H + \Delta H) + c_p(T, H - \Delta H)}{2}. \tag{6.8}$$

The calculations for various Δg, however, only differ from the non-staggered specific heat in a small rounding of the field-dependent maxima at low temperature and do not give an improved description of the data.

Another explanation of the inconsistencies is given by experimental issues at high fields. For comparison the specific heat has been measured as a function of the magnetic field also using the heat capacity option of a commercial setup based on a ^{4}He cryostat (PPMS, Quantum Design). The drawback of this setup is the restricted temperature range of 1.8 K lowest and the maximum field of 14 T. At zero field both setups yield a consistent temperature dependence of the specific heat, see Fig. 6.6. In Fig. 6.14 the field dependence of c_p at 2 K, obtained with the home-built ^{3}He setup (black symbols), is compared to that measured with the commercial ^{4}He setup (gray symbols). Up to 5 T the data match each other within the noise level, but not with the calculated specific heat. The phonon contribution is negligible at that temperature, as seen by comparing the very similar purely magnetic contribution c_{mag} of the Heisenberg model, shown as a blue line. Even fully neglecting phonons, the zero-field data are significantly lower. Around the critical field, the experimental data additionally differ from each other by about 10 %. In this field range, the absolute values of the ^{4}He setup data are slightly closer to the model calculations. However, the field range in this experiment is too small, respectively the temperature too high to resolve the double peak structure of $c_p(H)$ and to perform a meaningful fit. From the fact that the experimental data differ by up to 10 % between the two setups and that the deviations from the theory are of the same order, a physical origin of the discrepancies is hard to argue for. Instead, they might be induced by an imperfect calibration of the temperature sensors in large magnetic fields. Other quantities like the magnetization or the magnetostriction are less sensitive to the sample thermometer's calibration. Using the relaxation or the quasi-adiabatic method

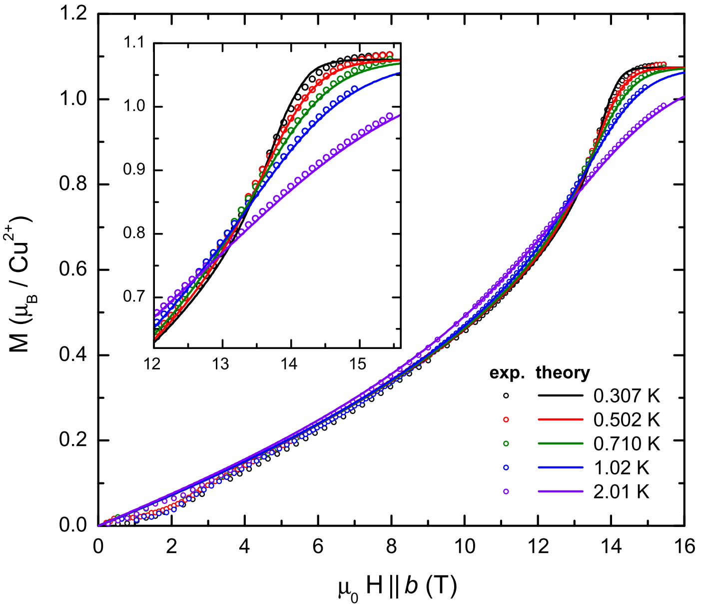

Figure 6.15: Magnetization of CuPzN measured with the magnetic field along b (symbols) in comparison to the Heisenberg model (solid lines). In the inset a zoom of the high-field range is shown.

the absolute value of the specific heat, however, directly relates to the temperature derivative of the temperature sensor's calibration curve $T(R)$. Improving the magnetic field calibration of the sensors may help to resolve these issues. At zero field, where the sensor calibration is straightforward and the present data agree with each other, nevertheless, the absolute value of c_p cannot be explained by the Heisenberg model.

6.3.2 Magnetization

Above 14 T the magnetization saturates to a value of $1.08\,\mu_\mathrm{B}$. For the spin-$1/2$ of Cu2+ this saturation value translates into a g factor of 2.16, which is slightly smaller than the established literature value of 2.27. The slightly larger saturation value of $1.15\,\mu_\mathrm{B}$ found in Ref. 17, instead would consistently yield $g_b = 2.3$. This deviation of about 6 % lies within the experimental uncertainty of the present experiment.

From the model calculations the thermal expectation value of S_z is obtained. It relates to the experimental magnetization along the b axis via

$$M = a \cdot g_b\,\mu_\mathrm{B} \langle S_z \rangle. \tag{6.9}$$

Here, the experimental factor a compensates for experimental uncertainties of the sample weighing and the magnetometer calibration. Fixing the g factor to the literature value of $g_b = 2.27$ a simultaneous fit of all data yields a coupling constant

$$J/k_\mathrm{B} = 10.58\,\mathrm{K} \quad \text{and} \quad a = 0.95. \tag{6.10}$$

The factor of 0.95 is of the same order than the deviation of the saturation value from that reported in Ref. 17. In contrast to the data of Ref. 17 that are scaled to high-temperature SQUID data, here the pristine data are presented as obtained directly from the low-temperature measurements. Figure 6.15 displays the fits of the magnetization versus the field at temperatures from 0.3 to 2.0 K. In the inset a zoom of the high-field range is shown. The saturation moment and the thermal broadening of the data is well described by the model calculations. The coupling constant closely resembles that obtained from the other thermodynamic quantities.

6.3.3 Thermal expansion

In the thermal expansion not only the one-dimensional magnetism of the spin chain is seen, but also phonons contribute, scaled by the pressure dependence of the Debye temperature, as understood from the Grüneisen scaling [102]. Above 15 K the phonon contribution to $\alpha(T)$ exceeds the magnetic contribution of the Heisenberg chain. Thus, only the low-temperature data for $T < 6\,\mathrm{K}$ are considered for a comparison to the model calculations. The thermal expansion and the magnetostriction are calculated from the spin-spin correlator $\langle S_i S_{i+1} \rangle$ as described in Chapter 2.3.3. The value of the coupling constant is mainly fixed by the peaks of the magnetostrictive coefficient λ at the critical field. Besides J the only other fit parameter is the uniaxial pressure dependence $\partial J/\partial p_b$. Simultaneously fitting all temperature and field dependent data of $\alpha(T < 6\,\mathrm{K})$ and $\lambda(H)$ yields

$$J/k_\mathrm{B} = 10.60\,\mathrm{K}, \quad \frac{\partial J}{\partial p_b} = 0.25\,\mathrm{K\,GPa^{-1}}, \quad \frac{\partial \ln J}{\partial p_b} = 2.3\,\%\,\mathrm{GPa^{-1}}. \tag{6.11}$$

In Fig. 6.16 the calculations are shown as solid lines. The relative length change $\Delta L/L_0$, shown in Fig. 6.16 (a) for different magnetic fields, compares well to the Heisenberg model. A single constant was used to shift all calculations such that the the zero-field data at the lowest temperature are matched. The field-induced change of the low-temperature slope as well as the overall curvature is well reproduced by the model. Yet, there are deviations at 0 and 5 T of about 10 to 15 %. As seen by comparing the thermal expansion coefficient, they are not described by a simple shift of ΔL by a constant. While the broad maximum of the experimental $\alpha(T)$, shown in Fig. 6.16 (b) is well reproduced, the absolute value is overestimated by about 10 %. Yet, in this low-field and low-temperature range, the measurements seem to be influenced by experimental issues. This is reflected in a crossing of the 0 T and the 5 T data at about 7 K, inconsistent with the monotonic increase of the magnetostriction at low temperature (cf. Fig. 6.5). Increasing the field the deviations reduce. At 12 and 13 T the calculations are in excellent agreement with the data and consistently yield a sign change of α by increasing the field to 14 T. Concerning the magnetostriction the agreement between experiment and theory is even more striking. The calculated length change $\Delta L(H)$, shown in Fig. 6.16 (c) for selected temperatures, lies on top of the data. Consistently, the magnetostrictive coefficient is also in quantitative agreement with the model calculations, see Fig. 6.16 (d). Both the position and the absolute value of the peak close to 14 T, as well as the broadening by temperature is captured by the Heisenberg model. Below 4 T the measurements vaguely suggest an additional small anomaly. However, from the Heisenberg spin chain no unique features are expected in this field range.

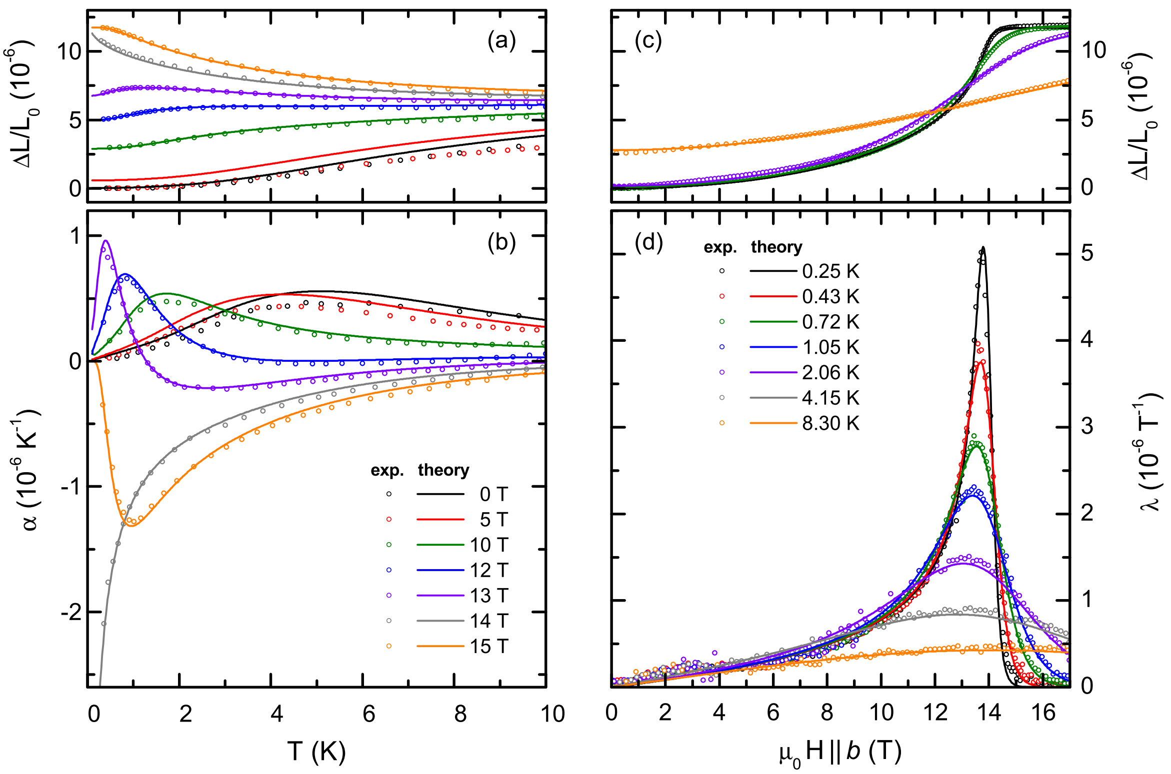

Figure 6.16: Thermal expansion and magnetostriction of CuPzN (symbols) in comparison to the Heisenberg model (solid lines).

6.3.4 Magnetocaloric effect

The absolute value of the entropy $S(T,H)$ at arbitrary temperature and field is obtained directly from the calculations. However, in experiment only the change of the entropy with respect to a certain temperature and magnetic field can be measured, but not the absolute value of the entropy. Comparing the experimental data to the calculations, therefore, an offset has to be considered for each measurement at a constant temperature. If in addition to the field dependence of S also the temperature dependence is known, the number of offsets reduces to a single overall constant. Due to the inconsistencies encountered above when comparing $\Delta S(H)$ obtained from the magnetocaloric effect to $\Delta S(T)$ extracted from the specific heat, here, the model calculations are taken as a reference of the entropy's temperature dependence. The experimental data are shifted according to the calculated maximum entropy close to the critical field of about 14 T. This allows to plot the absolute value of the entropy, shown in Fig. 6.17 (a) for a coupling constant $J/k_\mathrm{B} = 10.59\,\mathrm{K}$, obtained by fitting the experimental magnetocaloric-effect data.

At high fields the experimentally observed entropy change and the model calculations agree within few percent. Above 15 T and at low temperature S becomes zero due to the non-degenerate ground state selected by the magnetic field. The data obtained at 0.8 K might be influenced by experimental issues and solely deviate from the theory in this field range. Below 10 T some of the measured entropy changes significantly differ from the model results and even cross each other. Most possibly, these are experimental

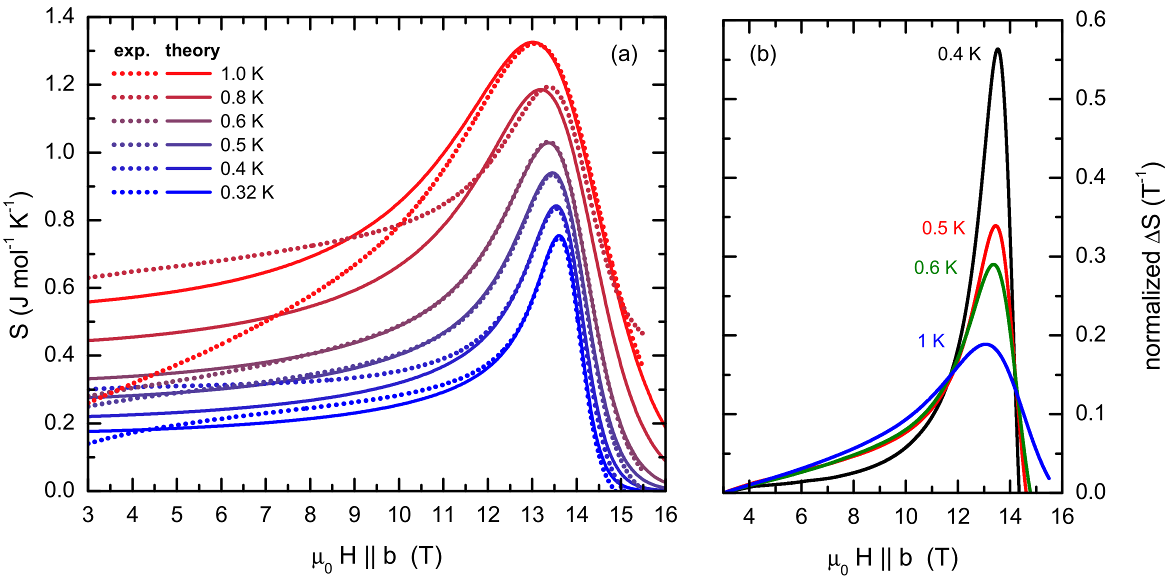

Figure 6.17: (a) Entropy of CuPzN as a function of the magnetic field applied along *b* in comparison to the Heisenberg model. Dotted lines are the experimental data, shifted by a constant each. Solid lines represent the calculated entropy of a Heisenberg spin chain. (b) Entropy change ΔS with respect to the entropy at 3 T normalized to $\int \Delta S(H)\,dH$

artifacts. The lowest sample temperature of 0.32 K is at the verge of the possible experimental range. At the highest temperature of 1.0 K the experimental signal comes close to the noise level and small errors increasingly contribute due to the integration of the data. Nevertheless, these data confirm that the developed experimental procedure in fact gives direct access to the entropy as a function of the magnetic field. Yet, further effort may be put into the optimization of the temperature stability while sweeping the field and into improving the resolution of the power measurement.

The temperature dependence of the entropy is illustrated more clearly by normalizing the entropy change $\Delta S = S(H) - S(3\,\mathrm{T})$ to the total entropy change $\int_{3\,\mathrm{T}}^{16\,\mathrm{T}} \Delta S(H)\,dH$ in the experimental field range. The resulting distribution function can be understood as the entropy weight as a function of the magnetic field. As shown in Fig. 6.17 (b), decreasing the temperature the entropy accumulates close to the critical field of the spin chain, as expected close to quantum critical points based on very general statements [103].

Besides the entropy change also the magnetic Grüneisen ratio Γ_H has been measured. It mainly relates to the entropy change via derivation with respect to the magnetic field. Thus, no offsets like in case of the entropy have to be considered. According to Eqn. (3.9) the magnetic Grüneisen ratio relates to the magnetization and the specific heat as

$$\Gamma_H = -\frac{\left.\frac{\partial M}{\partial T}\right|_H}{C_H}. \tag{6.12}$$

Both the temperature dependence of the magnetization as well as the specific heat at a constant magnetic field are obtained from the output of the model calculations either

Figure 6.18: Magnetic Grüneisen ratio Γ_H of CuPzN at different temperatures from 0.32 K (thin blue line) to 1.0 K (thin red line) in comparison to calculations for the Heisenberg chain (bold lines from blue to red). The black lines represent the expected zero-temperature field dependence of Γ_H. The dashed orange line marks the critical field $\mu_0 H_c = 13.90\,\mathrm{T}$.

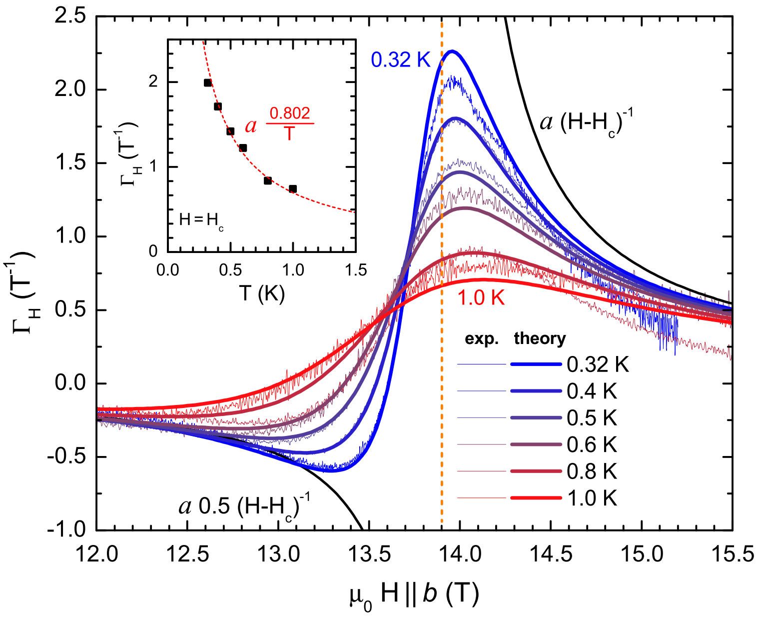

by numerical derivation of the calculated magnetization or directly in case of the heat capacity. Converting to the experimental units, the data can be compared quantitatively to the Heisenberg model. The experimental data, shown as thin lines in Fig. 6.18, are well described by including an overall constant $a \cdot \Gamma_H$ to compensate for systematic experimental errors like the weighing of the sample, offsets in the measurements of the heater power and other deviations from the ideal isothermal conditions assumed in the derivation of Γ_H from the experimental raw data. Similar to the entropy data the curve for 0.8 K stands out and possibly is influenced by experimental issues. From the fit of the data $a = 0.87$ and a coupling constant $J/k_\mathrm{B} = 10.59\,\mathrm{K}$ is deduced that translates into a critical field of the Heisenberg spin chain of

$$\mu_0 H_c = \frac{2J}{g\mu_\mathrm{B}} \simeq 13.90\,\mathrm{T}. \tag{6.13}$$

In Fig. 6.18 this field is marked by a vertical orange line. Far from the critical field $H \ll H_c$ both the experimental and the calculated Grüneisen ratio come close to zero. Approaching the critical field from below the temperature dependence increases and extrapolates to a divergence with a pole at H_c as described by $\Gamma_H \propto \frac{1}{H-H_c}$. Above the critical field Γ_H increases to large positive values with decreasing the temperature. At 0.32 K a maximum value of $2\,\mathrm{T}^{-1}$ is obtained. This value indicates a large magnetocaloric effect of the Heisenberg chain, similar to that of *XXZ* spin chains [228]. It can be pictured as a change of the system's temperature by 200 %/Tesla. However, this is true only in a small field range, and Γ_H rapidly drops with increasing the field further. The temperature dependence of $\Gamma_H(H > H_c)$ extrapolates to a zero-temperature scaling similar to that for $H < H_c$, but with a constant twice as large.

The measured value of Γ_H at the critical field is plotted in the inset of Fig. 6.18 versus the temperature. The data can be described by $\Gamma_H(T, H = H_c) = \frac{0.7}{T}$, shown as a dashed line. Both the field dependence of Γ_H, as well as the divergence for $T \to 0$ are expected close to quantum critical points as will be discussed in the next section.

6.4 Quantum criticality

One remarkable property of the Heisenberg spin-$1/2$ chain is the emergence of a quantum phase transition as a function of the magnetic field. In literature a quantum critical behavior of copper pyrazine dinitrate has been suggested based on various experimental techniques [13–17, 212, 229]. However, only few studies concern the thermodynamic properties up to the critical field of the spin chain or above it. In the previous chapter several measurements of thermodynamic properties were compared to calculations of the Heisenberg model. The generally good agreement between the data and the calculations is in favor of a quantum phase transition in CuPzN at a critical field of about 13.90 T. Further evidence is given by the analysis of the data with respect to the critical behavior in the following.

Finite-temperature signatures

The critical field is also reflected in the finite-temperature scaling of the signatures in the thermodynamic quantities. In Fig. 6.19 all specific heat data are combined in a temperature versus magnetic field color plot. Close to 14 T the minimum of $c_p(H)$ is seen as a green to yellow area extending to finite temperatures of up to 3 K. On top the temperature and field dependent extrema of all previously discussed thermodynamic properties are plotted by symbols. With a high precision they all follow linear field dependences,

$$T_{\mathrm{max,min}} \propto |H - H_c| \; , \tag{6.14}$$

with slightly varying slopes. Fits to the data, shown as dashed lines, extrapolate to a common critical field $\mu_0 H_c = 13.87(12)$ T. This representation strongly resembles the typical phase diagrams and the characteristic finite-temperature scaling of thermodynamic quantities close to quantum critical points [81, 82].

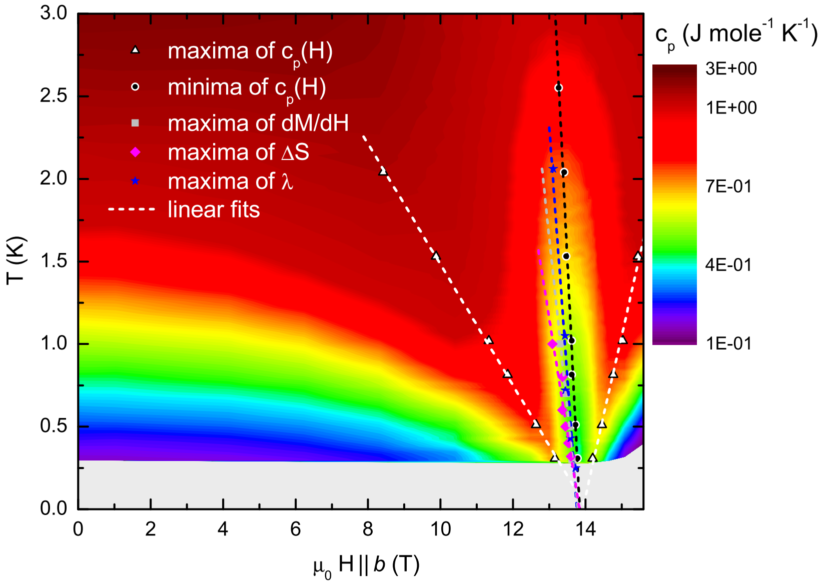

Figure 6.19: Density plot of the specific heat of CuPzN. Symbols represent the extrema of the specific heat $c_p(H)$, the magnetization, the entropy change ΔS and the magnetostriction λ. Dashed lines are linear fits to the extrema. The shaded gray area marks the temperature range that is not accessible in the experiment.

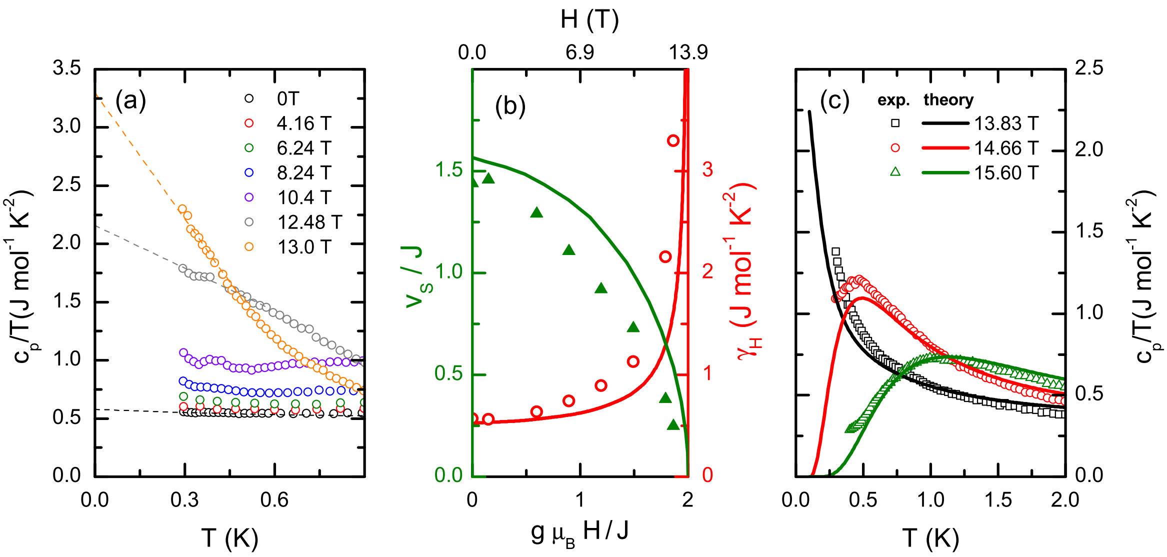

Figure 6.20: (a) Specific heat of CuPzN divided by temperature as a function of temperature at different constant magnetic fields below the critical field. Dashed lines are linear fits to the data. (b) Comparison of the extrapolated γ values and the spinon velocity v_s at different fields to the expectations for the Heisenberg model, calculated in Ref. 13. In (c) the divergence of c_p/T close to the critical field and the high-field behavior is compared to the Heisenberg model.

Low-temperature behavior of the specific heat

Another drastic change of the magnetism of CuPzN as a function of the magnetic field arises in the low-temperature specific heat. Approaching the critical field the low-temperature asymptotics of c_p strongly changes. According to Eqn. (6.6) the low-temperature slope γ_H of the specific heat changes at finite magnetic field and is inversely proportional to the spinon velocity $v_s(H)$ which is renormalized when by increasing the field. In Ref. 13 the velocity v_s is calculated from the Bethe ansatz by a set of integral equations for magnetic fields up to the critical field and is compared to experimental data extracted from the specific heat. However, only magnetic fields up to 9 T are applied. Here, the calculations are compared to the experimental γ values obtained from c_p/T by extrapolating the data below 0.6 K. Magnetic fields up to the critical field are included. In Fig. 6.20 (a) the fits of c_p/T at low temperature are shown as dashed lines for selected magnetic fields. At small fields the linear low-temperature dependence of c_p is reflected in an almost constant value of c_p/T below 1 K and the extrapolation of the fit to zero temperature yields γ_H with a high precision. The corresponding values of γ_H and the spinon velocity v_s/J, related via Eqn. (6.6), are shown in Fig. 6.20 (b). At zero field they are very close to the expected theory results from Ref. 13 of $\gamma_H \approx 0.52\,\mathrm{J\,mol^{-1}\,K^{-2}}$ and $v_s/J = \pi/2$. Increasing the field γ_H is expected to increase and v_s to approach zero at the critical field, as shown by solid lines in Fig. 6.20 (b). Although the overall field dependence of both quantities in fact follows the expectation, there are quantitative deviations between the calculations and the data. Partly, this originates from the non-linear temperature dependence of the specific heat which develops below about 0.6 T when approaching the critical field and from the restricted temperature range of the

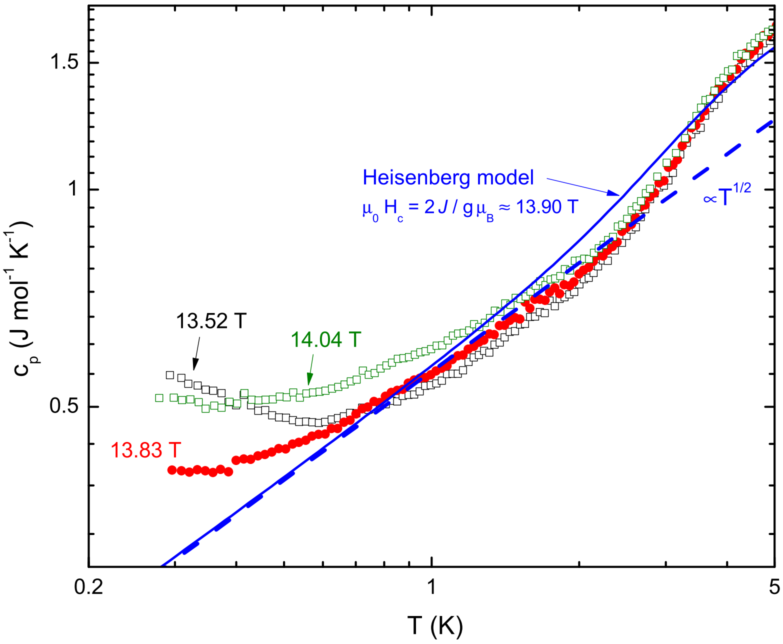

Figure 6.21: Low-temperature specific heat of CuPzN close to the critical field (symbols) in comparison to the Heisenberg model (solid line) and the low-temperature power-law dependence $c_p \propto T^{\frac{1}{2}}$ at the critical field (dashed line).

experiment. While the data for fields below about 10 T are reasonably extrapolated to zero temperature by a linear function, the extrapolation of the data above 10 T becomes more questionable. In fact, at the critical field a non-linear temperature dependence of $c_p \propto T^{\frac{1}{2}}$ of the specific heat is expected due to the quadratic dispersion of $\epsilon(k) \propto \cos k \approx k^2$ for small energies [13]. In consequence, at the critical field, $c_p/T \propto T^{-0.5}$ diverges and the extrapolation of γ_H from the data involves an increasing uncertainty in the vicinity of the critical field.

Therefore, the data close to the critical field are compared to the finite-temperature results for the Heisenberg model instead, see Fig. 6.20 (c). Here, a coupling constant $J/k_\mathrm{B} = 10.6\,\mathrm{K}$ and $g = 2.27$ are assumed as consistently derived from the thermodynamic data above. At 13.83 T, very close to the critical field, the experimental data as well as the calculations strongly increase with decreasing the temperature, reflecting the expected divergence of c_p/T at the critical field. In the high-field phase ($H > H_c$) a gapped behavior is represented by a strong suppression of the calculated c_p/T below 0.25 K, in agreement with the data.

The temperature dependence of the specific heat in the close vicinity of the critical field is analyzed in further detail in Fig. 6.21. In this double-logarithmic plot the power-law dependence $c_p \propto T^{\frac{1}{2}}$ is represented by a straight dashed line. The finite-temperature calculations of the Heisenberg model for $H = H_c$ (solid line) follow this power-law dependence for $T < 1\,\mathrm{K}$. At high temperature $T > 2\,\mathrm{K}$ the data for three selected fields close to the critical field agree with each other, and are in coarse agreement with the Heisenberg model (cf. previous discussion of the deviations in Chapter 6.3.1). Yet, below 1 K the specific heat strongly disperses. Both the experimental data acquired at 13.52 T and at 14.04 T, i. e., away from the critical field by about 3 % each, do not follow the power law of $c_p \propto T^{\frac{1}{2}}$ at low temperature, but show strongly increased values. Indeed, this behavior is expected and relates to the minimum of $c_p(H)$ close to the critical field. At 13.83 T, which is the data set closest to the critical field of 13.90 T available, the expected power law holds in a broader temperature range. Still, there are deviations, which can be explained by the finite distance to the critical field. Thus, it seems likely that upon tuning the magnetic field more precisely, the critical behavior of the specific heat can be observed.

Divergence of the magnetocaloric effect

Besides the quantitative agreement of several thermodynamic properties to the model calculations also other more general features are found in the data that confirm the quantum critical behavior of CuPzN. Close to magnetic-field-induced quantum critical points certain properties are expected to show critical behavior [103, 152]. For example, the magnetic analogon to the Grüneisen ratio, i. e., the magnetocaloric effect Γ_H is expected to change its sign at finite temperature above the quantum critical point. The zero temperature limit

$$\Gamma_{H,cr}(T \to 0, H) = -G_r \frac{1}{H - H_c}, \quad G_r = \frac{\nu(d - y_0 z)}{y_0} \tag{6.15}$$

is universal in the sense that the dimensionless G_r does not depend on model parameters like the coupling constant or on details of the crystal structure, but only on the nature of the system. Here, $\nu = 0.5$ is the exponent that describes the divergence of the correlation length $\xi \propto |(H - H_c)/H_c|^{-\nu}$ when approaching the critical field, d is the dimension of the system and y_0 is the exponent of the power-law behavior of the specific heat $C \propto T^{y_0}$. The parameter z is the “dynamical critical exponent” that relates the correlation time $\xi_\tau \propto \xi^z$ to that of the correlation length. In the present case of a one-dimensional antiferromagnet these constants add up to $G_r = -0.5$ for the free-fermion case $(d = 1, z = 2, y_0 = 1)$ at fields $H < H_c$ and to $G_r = -1$ in the polarized phase $(y_0 \to \infty)$ for $H > H_c$ [149].

At the critical field H_c, the temperature dependence of Γ_H is determined by $\nu z = 1$ and by another prefactor G_T that depends on nonuniversal parameters and evaluates to $G_T \simeq 0.527043 \frac{g\mu_\mathrm{B}}{k_\mathrm{B}}$ [103, 149]. Using $g = 2.27$ the expected temperature dependence of the magnetocaloric effect at the critical field is given by

$$\Gamma_{H,cr}(T, H = H_c) = -G_T T^{-\frac{1}{\nu z}} \simeq \frac{0.802}{T}. \tag{6.16}$$

In Fig. 6.18 the expected field dependence of $\Gamma_{H,cr}(T \to 0, H)$ is compared to the experimental data using the critical field $H_c \simeq 13.90\,\mathrm{T}$, consistently obtained from all thermodynamic quantities above. In analogy to the scaling of the model calculations $\Gamma_{H,cr}$ is multiplied by a constant $a = 0.87$ to compensate for small errors in the normalization of the data. The zero-temperature $\Gamma_{H,cr}$ is consistent with the model calculations and the experimental data. At fields $H \lesssim 13\,\mathrm{T}$ the calculated Γ_H and the experimental data at the lowest temperature of $0.32\,\mathrm{K}$ match with $\Gamma_{H,cr}$. Also at high fields $H \gtrsim 15\,\mathrm{T}$ the temperature dependence of the calculated and the experimental Γ_H extrapolates to $\Gamma_{H,cr}$. In the inset of Fig. 6.18 the experimental values at the critical field are plotted versus the temperature. The data follow an inverse temperature dependence as suggested by Eqn. (6.16) upon correcting the prefactor $G_T = 0.802$ with the same experimental constant a. This illustrates the expected divergence of Γ_H when approaching the quantum critical point.

Universality

The consistent description of both the magnetic field and the temperature dependence of Γ_H arises from the universality close to quantum critical points. Universality refers to the fact that the scaling of system properties does not depend on the microscopic details of the model. In the vicinity of the quantum critical point, where the universality holds, the properties of the system can be written in terms of a universal scaling function that only depends on dimensionless parameters [79]. In case of the magnetocaloric effect Γ_H that depends on the inverse distance $(H-H_c)^{-1}$ from the critical point the temperature dependence is expected to be described by a universal function $\Phi\left(\frac{H-H_c}{T}\right)$ which only depends on the ratio of the field and the temperature and allows to rewrite Γ_H in terms of a scaling law [103, 149],

$$\Gamma_H = \frac{1}{H-H_c}\Phi\left(\frac{H-H_c}{T}\right) . \tag{6.17}$$

Here, Φ is a function that describes the evolution of Γ_H for finite temperatures and magnetic fields away from the quantum critical point. Plotting $\Gamma_H \cdot (H-H_c)$, thus all experimental data are expected to collapse to the scaling function Φ. In fact the experimental data confirm the universal scaling. In Fig. 6.22 a plot of $\Phi = \Gamma_H \cdot \mu_0(H-H_c)$ versus the dimensionless ratio of field and temperature $\delta = \mu_B\mu_0(H-H_c)/(k_\mathrm{B}T)$ is shown. Here the constants μ_0 and k_B are introduced to take into account the experimental units of Tesla and Kelvin. Apart from the data for $T = 0.8\,\mathrm{K}$ that are possibly influenced by experimental issues, all curves collapse and for $-0.2 < \delta < 0.4$ are described by a straight line with a slope of 1. This dependence illustrates that Γ_H is suppressed for large temperatures T due to $\Phi(\delta \to 0) = 0$. In the limit of low temperature and at large negative fields, i. e., $\delta \to -\infty$, the data approximately approach

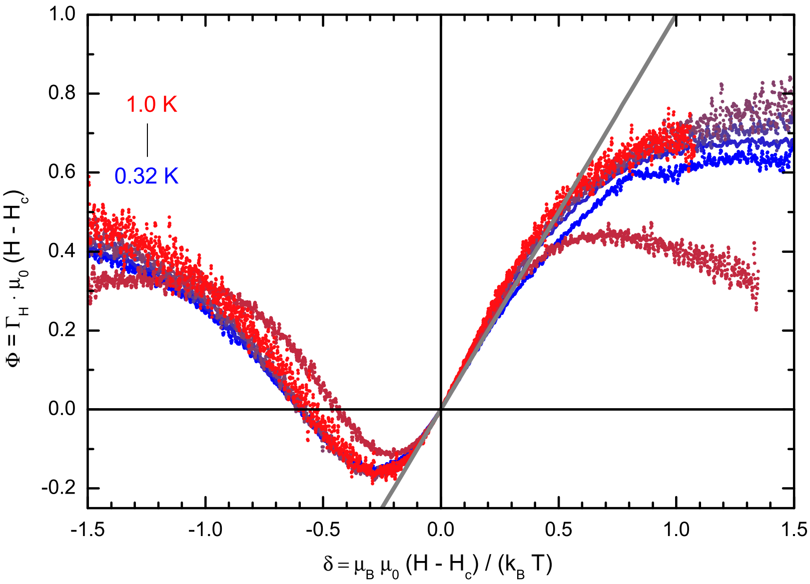

Figure 6.22: Universal scaling of the magnetocaloric effect Γ_H of CuPzN at temperatures $T = 0.32, 0.4, 0.5, 0.6, 0.7, 1.0\,\mathrm{K}$ (from blue to red). The experimental data of Γ_H multiplied by the reduced field $H-H_c$ are shown versus the ratio δ of temperature and magnetic field. The gray line represents $\Phi(\delta) = \delta$.

the value of 0.5 expected from the prefactor G_r in Eqn. (6.15). For the high field range $\delta \to \infty$ one expects $\Phi = 1$ instead. In fact the data seem to approach this value, however it is not reached within the range of the experiment and the experimental noise strongly increases for $|\delta| > 1$. Nevertheless, the expected asymmetry of Φ is clearly resolved and the obeyed universal scaling law once more confirms that a quantum phase transition arises in CuPzN as a function of the magnetic field.

6.5 Conclusion

The spin-$1/2$ chain compound copper pyrazine dinitrate was analyzed with respect to its thermodynamic properties in a temperature range from 0.25 to 30 K and in magnetic fields up to about 16 T applied along the b axis. The specific heat, the magnetization, the length change and the magnetocaloric effect were compared to analytical calculations of the one-dimensional antiferromagnetic Heisenberg model. The coupling constants J, individually obtained from fits to the experimental data of each quantity, match with a high precision, see Tab. 6.2. The mean value of

$$J/k_\mathrm{B} = 10.59\,\mathrm{K} \tag{6.18}$$

translates into a critical field $H_c = 2J/g_b\mu_B\mu_0$ of the spin chain of $H_c = 13.89\,\mathrm{T}$, assuming $g_b = 2.27$. The specific heat at zero field agrees with the model calculations on a quantitative level. The low-temperature slope of c_p increases as a function of the magnetic field and the related spinon velocity in consistence with theory is strongly reduced when approaching the critical field. At low temperature the specific heat shows a double peak structure as a function of the magnetic field. Due to experimental issues with the thermometry at high fields a quantitative comparison of the specific heat to the calculations is possible only within the experimental error of about 10 %. The measured magnetization as well as the thermal expansion are described by the Heisenberg model with a high accuracy. From the fit of the thermal expansion an increasing coupling constant $\partial \ln J/\partial p_b = 2.3\,\%\,\mathrm{GPa}^{-1}$ under uniaxial pressure is derived, which is significantly smaller than in Cs_2CoCl_4, where a value of $77\,\%\,\mathrm{GPa}^{-1}$ is found, and than in other spin chain systems [77, 154]. In CuPzN the magnetic exchange is mediated by pyrazine ($C_4H_4N_2$) rings along the chain direction a. In contrast to the superexchange,

	specific heat	magnetization	thermal expansion	MCE
J/k_B	10.59 K	10.58 K	10.60 K	10.59 K
g	2.27	2.27	2.27	2.27
Θ_D	178 K			
$\partial J/\partial p_b$			$0.25\,\mathrm{K\,GPa}^{-1}$	
$\partial \ln J/\partial p_b$			$2.3\,\%\,\mathrm{GPa}^{-1}$	
scaling factor		0.95		0.87

Table 6.2: Parameters of the Heisenberg model obtained from fits of the experimental data of different methods. The g factor was fixed during the fits.

e. g., in Cs_2CoCl_4 via ionic bonds cobalt and chlorine, here one may expect a different dependence on pressure due to the covalent π bonds in the organic pyrazine. A small dependence of J on the inter-atomic distance actually explains why CuPzN does not form a non-magnetic ground state via a Spin-Peierls transition.

All thermodynamic quantities show finite-temperature signatures of a quantum phase transition. They linearly depend on the magnetic field $|H - H_c|$ and consistently extrapolate to the critical field H_c. Further evidence for the quantum criticality of CuPzN is given by the magnetocaloric effect that conforms with the Heisenberg model and shows the typical field and temperature dependence expected in the vicinity of quantum critical points. Reducing the temperature an increasing relative weight of the entropy at the critical field is evidenced by the measurements of the entropy. The temperature dependence of the magnetic Grüneisen ratio extrapolates to a divergence described by $G_r\,|H - H_c|^{-1}$, where G_r is a universal prefactor. The finite temperature scaling of the magnetocaloric effect is described by a universal scaling law. The simultaneous agreement of various thermodynamic properties of copper pyrazine dinitrate to the numerical results, clearly reveals that the Heisenberg model is realized in this compound to a high degree. The wide temperature and field range where the model is applicable renders the compound a textbook example for one-dimensional magnetism and quantum criticality. Part of this success originates from the small interchain couplings in comparison to the dominant magnetic exchange via the organic constituents in the compound. Also the elastic properties of the organics in the compound may play an important role for its macroscopic properties. In other fields of physics the input of organic chemistry gave birth to exciting developments like organic light emitting diodes [230, 231] or organic superconductors [232]. As demonstrated by the unique properties of CuPzN, combining the complex physics of the magnetic transition metals with an organic component potentially yields systems with intriguing properties, extending those found in the classical field of inorganic compounds.

7 Summary

In this thesis the low-temperature magnetism of the two spin-chain compounds Cs_2CoCl_4 and $Cu(C_4H_4N_2)(NO_3)_2$ was investigated. In both cases the thermodynamic properties of single crystals were measured and compared to calculations of the spin-$1/2$ XXZ model and the isotropic spin-$1/2$ Heisenberg model, respectively. Special emphasis was put on signatures of quantum critical behavior that is expected from both model systems. In case of Cs_2CoCl_4, the influence of magnetic fields on the magnetically ordered phases was examined. Further, the change of the crystal structure and of the thermodynamic properties when partly substituting chlorine by bromine were studied.

The crystal structure of Cs_2CoCl_4 consists of distorted $CoCl_4$ tetrahedra that form chains along the b axis. The spin-$3/2$ states of the magnetic Co^{2+} are split by the anisotropic crystal field and at low temperatures an effective spin-$1/2$ chain model is applicable. In literature, commonly an anisotropy parameter $\Delta = 1/4$ is assumed [3–5, 7]. In this thesis, the influence of a symmetry-breaking magnetic field on the one-dimensional magnetism of Cs_2CoCl_4 has been investigated for the first time. The thermal expansion, the specific heat and the thermal conductivity of Cs_2CoCl_4 were measured in a temperature range from 0.05 to 30 K and in magnetic fields up to 4 T using different cryostats and custom setups. Numerical simulations of spin chains were performed using exact diagonalization and Quantum Monte Carlo methods for finite rings of spins. From the comparison of the data to the numerical results of the XXZ model it was found that significant corrections apply to the effective spin-$1/2$ XXZ model. A consistent and precise description of the thermodynamics of Cs_2CoCl_4 at temperatures above the magnetic order temperature is possible only upon the inclusion of virtual excitations of the parent spin-$3/2$ states in the mapping of the coupling constants to the effective spin-$1/2$ system. By virtue of the contributing higher-order terms, the anisotropy of the spin chain is determined from the full temperature dependence of the specific heat and the thermal expansion including the Schottky anomaly around 5 K that is characteristic for the crystal field strength. The results can be generalized to spin-$3/2$ systems with an easy-plane type magnetism, where the parent spin-$3/2$ coupling is not more than one order of magnitude smaller than the crystal field anisotropy. From a fit of the experimental data, it was found that the anisotropic magnetism of Cs_2CoCl_4 approaches the XY limit even further than previously believed. This is reflected in an anisotropy $\Delta \approx 0.12$ of the spin chain that is reasonably smaller than the value of $1/4$ assumed in literature. Among others, the constants extracted from the data are the spin-$3/2$ coupling constant $J_\mathrm{H} = 0.743\,\mathrm{K}$, the g factor of 3.27, the crystal field anisotropy $\mathcal{D} \simeq 7\,\mathrm{K}$ and the respective uniaxial pressure dependences $\frac{\partial \ln J_\mathrm{H}}{\partial p_b} = 0.77\,\mathrm{GPa}^{-1}$, $\frac{\partial \ln \mathcal{D}}{\partial p_b} = -0.63\,\mathrm{GPa}^{-1}$ and $\frac{\partial \ln \Theta_\mathrm{D}}{\partial p_b} = 0.01\,\mathrm{GPa}^{-1}$. The specific heat as well as the thermal expansion are described by the XXZ model in a transverse magnetic field with a high precision. The range where the description holds, is limited by the thermal population of excited crystal field states starting at about 2 K and by a field-induced entanglement of them for magnetic fields larger than 3 T. Magnetic fields induce a quantum phase transition, reflected in a sign change of the thermal expansion coefficient and in finite-temperature signatures that linearly scale to a critical field of about 2 T.

The one-dimensional magnetism of Cs_2CoCl_4 is also evident in the low-temperature thermal conductivity. Below about 1 K a magnetic contribution to the heat transport along the spin chains has been identified. A comparison to the intrinsic thermal conductivity of the *XXZ* spin-$1/2$ chain yields a large mean free path in the micrometer range below 0.3 K and a strong suppression of the magnetic heat transport with increasing temperature due to a scattering process that is characterized by an energy scale of about 3 K. In applied magnetic fields the magnetic contribution to the heat transport is suppressed due to the opening of a gap by the transverse field. At fields larger than the saturation field of about 2 T, the thermal conductivity along the spin chains again strongly increases. Both the zero-field low-temperature heat transport as well as the magnetic field dependence may relate to the contribution of spin-$3/2$ states. Yet, a quantification of these results requires a calculation of the transport properties of the spin-$3/2$ and the spin-$1/2$ chain in a transverse magnetic field.

Due to finite interactions between spin chains antiferromagnetic order arises at $T_\mathrm{N} \simeq 0.22\,\mathrm{K}$. A field-induced spin-liquid state has been proposed in literature [8]. Magnetic fields applied along other directions than a have not been considered previously. In this thesis, the magnetic order of Cs_2CoCl_4 was studied by measuring the thermal expansion and the specific heat in magnetic fields applied along different crystallographic and non-principal directions. The emerging low-temperature phases were discussed based on classical microscopic models. The zero-field magnetic order pattern with non-collinear moments tilted out of their respective magnetic easy planes could be explained by Dzyaloshinskii-Moriya interactions, but only in case of a sizable in-plane anisotropy of the magnetism of about 2 K. The absence of signatures of a finite in-plane anisotropy in the thermodynamic properties of the one-dimensional magnetism suggests that the magnetic order in Cs_2CoCl_4 could be accompanied by a small structural distortion.
In magnetic fields the antiferromagnetic order is suppressed. Before saturation an additional phase (II) emerges in a field range from about 2 to 2.4 T, bordering the antiferromagnetic phase. The revealed indications for a thermodynamic phase transition in this field range strongly suggest that this phase is not a spin-liquid phase as previously proposed in literature. While phase II arises irrespective of the field direction, in case of magnetic fields along b a more complex phase diagram was found that differs from those for other field directions in a widely extending phase II and in additional low-field transitions at 0.25 T and 0.7 T. These transitions can be understood as a two-stage spin-flop transition that is stabilized by Dzyaloshinskii-Moriya interactions between spin chains.
The thermodynamics of the one-dimensional *XXZ* magnetism suggest a quantum critical point in Cs_2CoCl_4. However, the associated critical field is not reflected in the low-temperature phases. Instead, reducing the temperature at the critical field of the spin chain, phase II arises. Two possible scenarios for phase II, an incommensurate magnetic order and nematicity, were discussed. In analogy to the formation of novel states as a consequence of competing interactions in other systems, the physics of phase II may be of general interest and a study of its properties by a microscopic method are asked for.

Mixed systems of the $Cs_2CoCl_{4-x}Br_x$ series were synthesized to investigate the influence of an exchange of chlorine by bromine on the crystal structure and on the magnetism. X-ray diffraction and thermodynamic data suggest that the exchange of ions is site-selective, reflected in a non-trivial change of the lattice constants and the magnetism as a function of the doping level x. Up to $x = 1$ only the crystal field anisotropy is influenced, whereas for larger x the dominant coupling constant additionally increases. For nominal $x \geq 2$ the crystal growth resulted in large single crystals of another series, $Cs_3CoCl_{5-y}Br_y$. The replacement of bromine by chlorine in this system most likely is site-selective as well and the magnetism is of the Ising type, evidenced by magnetic order peaks in the specific heat at about 0.3 K and a strong anisotropy with respect to the magnetic-field direction. As a function of y the magnetism non-continuously evolves from two-dimensional in Cs_3CoBr_5 to three-dimensional in Cs_3CoCl_5. Crystals with an intermediate doping level of $y = 2.5$ stand out due to a comparably large Néel temperature of about 1.2 K and a critical field of 4 T where magnetic order is suppressed. Crystals of this series open the field for further studies of a possible quantum phase transition as a function of the transverse magnetic field in an Ising system with tunable dimension.

The second system investigated in this thesis, $Cu(C_4H_4N_2)(NO_3)_2$, is an established example for a spin-$1/2$ Heisenberg chain. The crystal structure consists of copper ions linked along the a axis via pyrazine rings. Due to a very small interaction between the spin chains, magnetic order arises far below the common experimental range at about 0.1 K. From the Heisenberg model a quantum phase transition is expected as a function of an external field. However, comparably little has been known about the thermodynamics of the compound in the vicinity of the critical field. In this thesis, several thermodynamic properties of $Cu(C_4H_4N_2)(NO_3)_2$ were measured at temperatures down to 0.25 K and in magnetic fields up to 17 T. They were compared to exact results of the Heisenberg model including magnetic fields up to and above the critical field of the spin chain. Within the experimental resolution all data are well described by the Heisenberg model in the full temperature- and magnetic-field range. A coupling constant of 10.6 K and a critical field of 13.90 T are consistently derived from the specific heat, the magnetization, the thermal expansion and the magnetocaloric effect. The magnetocaloric effect was measured using a novel approach, which allows to acquire the data in a continuous way using a single setup. Several indications for a quantum criticality were found. All investigated quantities show finite-temperature signatures that linearly extrapolate to the critical field. The specific heat approaches the expected power-law dependence of $c_p \propto T^{0.5}$ close to the critical field. The magnetocaloric effect shows the temperature and field dependence that is expected in the vicinity of quantum critical points and it obeys a scaling law, confirming the universality in the quantum critical regime. These results illustrate that $Cu(C_4H_4N_2)(NO_3)_2$ is a textbook example of a model system for a quantum phase transition, where the finite-temperature properties are in a quantitative agreement with theory.

A Models, lattices and code written for the Alps project

Anisotropic spin model with in- and out-of-plane terms

In the standard library of the ALPS code a spin model already is included. Yet, it neither includes arbitrary magnetic field directions and couplings of spins along x, y and z, nor anisotropy terms other than along z. The following model definition realizes the hamiltonian

$$\mathcal{H} = \sum_i J_x S_x^i S_x^j + J_y S_y^i S_y^j + J_z S_z^i S_z^j - \left(h_x S_x^i + h_y S_y^i + h_z S_z^i\right) + D_z \left(S_z^i\right)^2 + E_x \left(\left(S_x^i\right)^2 - \left(S_y^i\right)^2\right)$$

for arbitrary spin by introducing further terms in addition to the standard spin model. All calculations shown in Chapter 4 were performed based on this model.

```
<MODELS>
<SITEBASIS name="spin">
  <PARAMETER name="local_spin" default="local_S"/>
  <PARAMETER name="local_S" default="1/2"/>
  <QUANTUMNUMBER name="S" min="local_spin" max="local_spin"/>
  <QUANTUMNUMBER name="Sz" min="-S" max="S"/>
  <OPERATOR name="Splus" matrixelement="sqrt(S*(S+1)-Sz*(Sz+1))">
    <CHANGE quantumnumber="Sz" change="1"/>
  </OPERATOR>
  <OPERATOR name="Sminus" matrixelement="sqrt(S*(S+1)-Sz*(Sz-1))">
    <CHANGE quantumnumber="Sz" change="-1"/>
  </OPERATOR>
  <OPERATOR name="Sz" matrixelement="Sz"/>
</SITEBASIS>

<BASIS name="spin">
  <SITEBASIS ref="spin">
    <PARAMETER name="local_spin" value="local_S#"/>
    <PARAMETER name="local_S#" value="local_S"/>
    <PARAMETER name="local_S" value="1/2"/>
  </SITEBASIS>
  <CONSTRAINT quantumnumber="Sz" value="Sz_total"/>
</BASIS>

<SITEOPERATOR name="Sx" site="x">
  1/2*(Splus(x)+Sminus(x))
</SITEOPERATOR>

<SITEOPERATOR name="Sy" site="x">
  -(I/2)*(Splus(x)-Sminus(x))
</SITEOPERATOR>

<BONDOPERATOR name="exchange_x" source="x" target="y">
  1/2*(Splus(x)+Sminus(x))*1/2*(Splus(y)+Sminus(y))
</BONDOPERATOR>

<BONDOPERATOR name="exchange_y" source="x" target="y">
  -(1/2)*(Splus(x)-Sminus(x))*(1/2)*(Splus(y)-Sminus(y))
</BONDOPERATOR>

<BONDOPERATOR name="exchange_xy" source="x" target="y">
  1/2*(Splus(x)*Sminus(y)+Sminus(x)*Splus(y))
</BONDOPERATOR>

<BONDOPERATOR name="biquadratic" source="i" target="j">
  (exchange_xy(i,j)+Sz(i)*Sz(j))*(exchange_xy(i,j)+Sz(i)*Sz(j))
</BONDOPERATOR>

<HAMILTONIAN name="spin">
  <PARAMETER name="J0" default="0"/>
  <PARAMETER name="J" default="J0"/>
  <PARAMETER name="Jz" default="J"/>
  <PARAMETER name="Jy" default="J"/>
  <PARAMETER name="Jx" default="J"/>
  <PARAMETER name="Jz0" default="Jz"/>
  <PARAMETER name="Jx0" default="Jx"/>
  <PARAMETER name="Jy0" default="Jy"/>
  <PARAMETER name="J1" default="0"/>
  <PARAMETER name="J'" default="J1"/>
  <PARAMETER name="Jz'" default="J'"/>
  <PARAMETER name="Jx'" default="J'"/>
  <PARAMETER name="Jy'" default="J'"/>
  <PARAMETER name="Jz1" default="Jz'"/>
  <PARAMETER name="Jx1" default="Jx'"/>
  <PARAMETER name="Jy1" default="Jy'"/>
  <PARAMETER name="hz" default="0"/>
  <PARAMETER name="hy" default="0"/>
  <PARAMETER name="hx" default="0"/>
  <PARAMETER name="Dz" default="0"/>
  <PARAMETER name="Ex" default="0"/>
  <PARAMETER name="K" default="0"/>
  <BASIS ref="spin"/>
  <SITETERM site="i">
  <PARAMETER name="hz#" default="hz"/>
  <PARAMETER name="hy#" default="hy"/>
  <PARAMETER name="hx#" default="hx"/>
  <PARAMETER name="Ex#" default="Ex"/>
  <PARAMETER name="Dz#" default="Dz"/>
    -hz#*Sz(i)-hx#*Sx(i)-hy#*Sy(i)+Dz#*Sz(i)*Sz(i)+Ex#*(Sx(i)*Sx(i)-Sy(i)*Sy(i))
  </SITETERM>
  <BONDTERM source="i" target="j">
    <PARAMETER name="J#" default="0"/>
    <PARAMETER name="Jz#" default="J#"/>
    <PARAMETER name="Jx#" default="J#"/>
    <PARAMETER name="Jy#" default="J#"/>
    <PARAMETER name="K#" default="0"/>
    Jz#*Sz(i)*Sz(j)+Jx#*exchange_x(i,j)+Jy#*exchange_y(i,j)+K#*biquadratic(i,j)
  </BONDTERM>
</HAMILTONIAN>
</MODELS>
```

Definition of the full lattice of Cs_2CoCl_4

The magnetic lattice of Cs_2CoCl_4 is described as stacked anisotropic triangular layers. For testing of algorithms it has been implemented in the ALPS code [57] using the following definition.

```
<LATTICEGRAPH name = "ccc">
  <FINITELATTICE>
    <LATTICE ref="simple cubic lattice"/>
    <PARAMETER name="W" default="L"/>
    <PARAMETER name="H" default="W"/>
    <EXTENT dimension="1" size="L"/>
    <EXTENT dimension="2" size="W"/>
    <EXTENT dimension="3" size="H"/>
    <BOUNDARY type="periodic"/>
  </FINITELATTICE>
  <UNITCELL name="ccc unitcell" dimension="3" vertices="4">
   <VERTEX id="1" type="0"><COORDINATE> 0.5 0 0</COORDINATE></VERTEX>
   <VERTEX id="3" type="0"><COORDINATE> 0 0.5 0.5</COORDINATE></VERTEX>
   <VERTEX id="2" type="1"><COORDINATE> 0 0 0.5</COORDINATE></VERTEX>
   <VERTEX id="4" type="1"><COORDINATE> 0.5 0.5 0</COORDINATE></VERTEX>

   <EDGE type="0"><SOURCE vertex="1" offset="0 0 0"/><TARGET vertex="1" offset="1 0 0"/></EDGE>
   <EDGE type="0"><SOURCE vertex="4" offset="0 0 0"/><TARGET vertex="4" offset="1 0 0"/></EDGE>
   <EDGE type="0"><SOURCE vertex="2" offset="0 0 0"/><TARGET vertex="2" offset="1 0 0"/></EDGE>
   <EDGE type="0"><SOURCE vertex="3" offset="0 0 0"/><TARGET vertex="3" offset="1 0 0"/></EDGE>

   <EDGE type="1"><SOURCE vertex="1"/><TARGET vertex="4"/></EDGE>
   <EDGE type="1"><SOURCE vertex="4" offset="0 0 0"/><TARGET vertex="1" offset="0 1 0"/></EDGE>
   <EDGE type="1"><SOURCE vertex="2" /><TARGET vertex="3" /></EDGE>
   <EDGE type="1"><SOURCE vertex="3" offset="0 0 0"/><TARGET vertex="2" offset="0 1 0"/></EDGE>

   <EDGE type="2"><SOURCE vertex="1"/><TARGET vertex="2"/></EDGE>
   <EDGE type="2"><SOURCE vertex="1" offset="0 0 0"/><TARGET vertex="2" offset="1 0 0"/></EDGE>
   <EDGE type="2"><SOURCE vertex="1" offset="0 0 0"/><TARGET vertex="2" offset="0 0 -1"/></EDGE>
   <EDGE type="2"><SOURCE vertex="1" offset="0 0 0"/><TARGET vertex="2" offset="1 0 -1"/></EDGE>
   <EDGE type="2"><SOURCE vertex="4"/><TARGET vertex="3"/></EDGE>
   <EDGE type="2"><SOURCE vertex="4" offset="0 0 0"/><TARGET vertex="3" offset="1 0 0"/></EDGE>
   <EDGE type="2"><SOURCE vertex="4" offset="0 0 0"/><TARGET vertex="3" offset="0 0 -1"/></EDGE>
   <EDGE type="2"><SOURCE vertex="4" offset="0 0 0"/><TARGET vertex="3" offset="1 0 -1"/></EDGE>
  </UNITCELL>
</LATTICEGRAPH>
```

Exact diagonalization

The following code implements a full diagonalization of a spin-3/2 chain with 8 sites, a coupling constant $J = 0.743\,\mathrm{K}$ and an out-of-plane anisotropy $Dz = 7\,\mathrm{K}$. The calculation is repeated for values of the in-plane anisotropy Ex from 0 to 4. The previously listed definition of the model is referenced via the parameter "MODEL_LIBRARY" in line 5. After the exact diagonalization algorithm has completed, the thermodynamic quantities have to be evaluated by the command given in line 27. Using the command line tool *plot2text* selected quantities are extracted from the XML output files.

```
1   import os
2   import pyalps
3   import matplotlib.pyplot as plt
4   import pyalps.plot
5   from pylab import *
6
7   ExVals=[0,1,2,3,4]
8   for Ex in ExVals:
9    parms = []
10   parms.append(
11    {
12      'MODEL_LIBRARY'   : "inplanemodel.xml",
13      'LATTICE'         : "chain lattice",
14      'MODEL'           : "spin",
15      'local_S'         : 1.5,
16      'J'               : 0.743 ,
17      'L'               : 8,
18      'Dz'              : 7,
19      'Ex'              : Ex,
20    }
21    )
22    # write parameter file and run the
          simulation
23   parmfile="parm_Ex%f" % (Ex)
24   input_file = pyalps.writeInputFiles(
         parmfile,parms)
25   res = pyalps.runApplication('fulldiag',
         input_file,Tmin=5)
26
27   # evaluate the results
28   data = pyalps.evaluateFulldiagVersusT(
         pyalps.getResultFiles(prefix=parmfile
         ),DELTA_T=0.01, T_MIN=0.01, T_MAX=20)
29
30   #extract the entropy, the free energy and
          the specific heat
31   cmd = 'plot2text '+parmfile+'.task1.plot.
         entropy.xml | awk "{print \$1,\$2}" >
          ' + "S_Ex%f" % (Ex)
32   os.system(cmd)
33
34   cmd = 'plot2text '+parmfile+'.task1.plot.
         free_energy.xml | awk "{print \$1,\$2
         }" > ' + "F_Ex%f" % (Ex)
35   os.system(cmd)
36
37   cmd = 'plot2text '+parmfile+'.task1.plot.
         specific_heat.xml | awk "{print \$1,\
         $2}" > '+"cp-per-site_Ex%f" % (Ex)
38   os.system(cmd)
```

Quantum Monte Carlo

The susceptibility and the specific heat of Heisenberg spin chains with large spin numbers has been calculated using the looper code [59]. These calculations are motivated by the isotropic susceptibility of $SrMn_2V_2O_8$ [233]. The following code runs a simulation of a spin-$5/2$ Heisenberg chain with 80 sites. In contrast to exact diagonalization, the calculation has to be repeated for every temperature, as performed here in logarithmically spaced steps. After completion of all simulations the temperature dependence of the susceptibility and the specific heat is collected and written to the output files *susceptibility* and *cp* as a tab-separated file. The typical computing time using a desktop computer for the full temperature range lies in the range of one or two days with the thermalization and sweep parameters given below.

```
import pyalps
import matplotlib.pyplot as plt
import pyalps.plot
from pylab import *

parms = []
for t in logspace(log10(0.001),log10(80),500):
 parms.append(
  {
    'LATTICE'        : "chain lattice",
    'MODEL'          : "spin",
    'local_S'        : 2.5,
    'T'              : t,
    'J'              : 1 ,
    'THERMALIZATION' : 15000,
    'SWEEPS'         : 70000,
    'L'              : 80,
    'ALGORITHM'      : "loop"
  }
 )

input_file = pyalps.writeInputFiles('parmH',parms)
pyalps.runApplication('loop',input_file)

data = pyalps.loadMeasurements(pyalps.getResultFiles(prefix='parmH'),'Susceptibility')
susceptibility = pyalps.collectXY(data,x='T',y='Susceptibility')
f=open('susceptibility','w')
for index in range(len(susceptibility[0].x)):
 f.write(str(susceptibility[0].x[index]) + "\t" + str(susceptibility[0].y[index]) + "\n")
data = pyalps.loadMeasurements(pyalps.getResultFiles(prefix='parmH'),'Specific Heat')
cp = pyalps.collectXY(data,x='T',y='Specific Heat')
f=open('cp','w')
for index in range(len(cp[0].x)):
 f.write(str(cp[0].x[index]) + "\t" + str(cp[0].y[index]) + "\n")
```

Custom measurements in exact diagonalization

In the Ising-like effective spin-1/2 systems $A\mathrm{Co}_2\mathrm{V}_2\mathrm{O}_8$ the high-temperature susceptibility is anisotropic [72, 73]. To investigate the relation of the anisotropy to the crystal-field influence on the parent $S = 3/2$ system, the magnetization of the spin system was calculated by exact diagonalization. Here, the definition of the parameter "MEASURE_AVERAGE" is essential to measure the thermal expectation value of an operator. Using command line tools, the susceptibility is calculated numerically by dividing the thermal average expectation values of S_z and S_x by the applied small field. The Quantum Monte Carlo codes could not be applied to this model as in the present implementation they cannot measure the expectation value of off-diagonal matrix elements. The susceptibilities calculated with the following code are discussed in Chapter 2.3.3.

Longitudinal ($\chi_{\parallel}$)

```
import pyalps
import matplotlib.pyplot as plt
import pyalps.plot
from pylab import *
import os

for D in linspace(-15,-10,6):
 parms = []
 h = 0.01
 Gamma=0
 parms.append(
 {
   'LATTICE'          : "chain lattice",
   'MODEL'            : "spin",
   'local_S'          : 1.5,
   'D'                : D,
   'J'              : 1  ,
   'L'                : 8,
   'h'          : h,
   'Gamma' : Gamma,
   'MEASURE_AVERAGE[Sz]' : 'Sz',
   'MEASURE_AVERAGE[Sx]' : 'Sx',
 }
 )
 title = 'para-D_%f-J_%f-L_%f' % (D,J,L
        )
 input_file = pyalps.writeInputFiles(
        title,parms)
 pyalps.runApplication('fulldiag',
        input_file)
 data = pyalps.evaluateFulldiagVersusT(
        pyalps.getResultFiles(prefix=
        title),DELTA_T=0.01, T_MIN=0.1,
       T_MAX=200.0)
 os.system('plot2text '+title+'.task1.
        plot.specific_heat.xml | awk "(NF
        ==2) {print \$1,\$2*8.314}" > '+
        title+'.cp')
 os.system('plot2text '+title+'.task1.
        measurements.Sz.plot.xml | awk "(
        NF==2) {print \$1,\$2/' + str(h)
        +'}" > '+title+'.chi')
```

Transverse ($\chi_{\perp}$)

```
import pyalps
import matplotlib.pyplot as plt
import pyalps.plot
from pylab import *
import os

for D in linspace(-15,-10,6):
 parms = []
 h = 0
 Gamma=0.01
 parms.append(
 {
   'LATTICE'          : "chain lattice",
   'MODEL'            : "spin",
   'local_S'          : 1.5,
   'D'                : D,
   'J'              : 1  ,
   'L'                : 8,
   'h'          : h,
   'Gamma' : Gamma,
   'MEASURE_AVERAGE[Sz]' : 'Sz',
   'MEASURE_AVERAGE[Sx]' : 'Sx',
 }
 )
 title = 'perp-D_%f-J_%f-L_%f' % (D,J,L
        )
 input_file = pyalps.writeInputFiles(
        title,parms)
 pyalps.runApplication('fulldiag',
        input_file)
 data = pyalps.evaluateFulldiagVersusT(
        pyalps.getResultFiles(prefix=
        title),DELTA_T=0.01, T_MIN=0.1,
       T_MAX=200.0)
 os.system('plot2text '+title+'.task1.
        plot.specific_heat.xml | awk "(NF
        ==2) {print \$1,\$2*8.314}" > '+
        title+'.cp')
 os.system('plot2text '+title+'.task1.
        measurements.Sx.plot.xml | awk "(
        NF==2) {print \$1,\$2/' + str(
        Gamma) +'}" > '+title+'.chi')
```

B Complete data sets

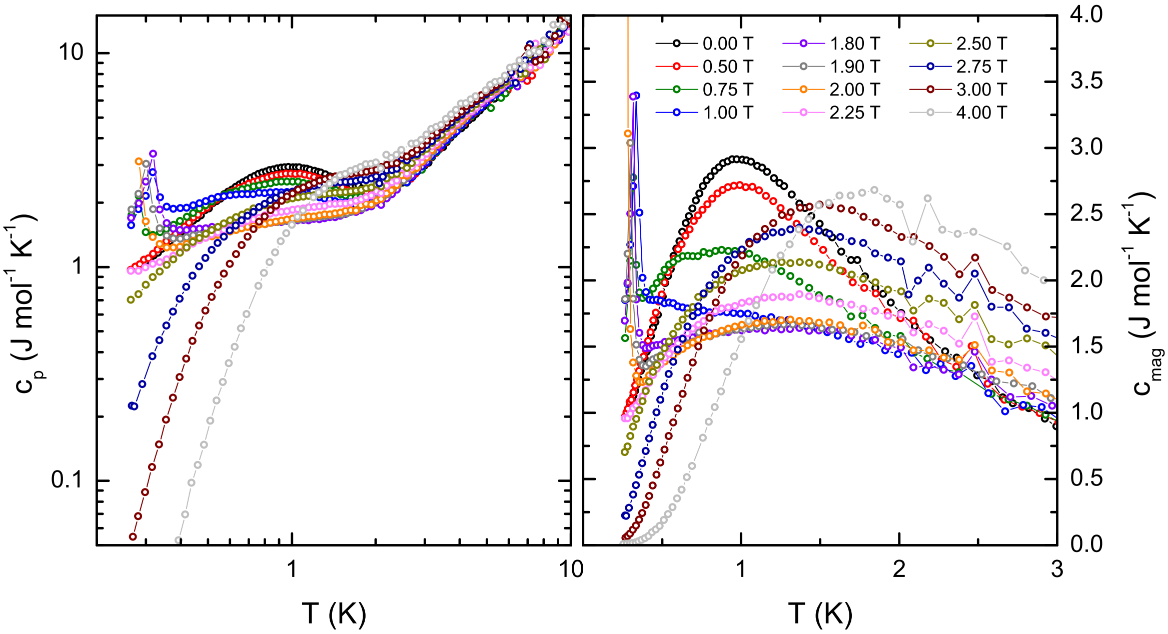

Figure B.1: Specific heat of Cs_2CoCl_4 measured in applied magnetic field $H \parallel b$ at $T > T_N$. The magnetic heat capacity was estimated by subtracting a field-independent phononic background ($\theta_D = 67\,K$) and a Schottky anomaly with an energy gap $\Delta E = 13.9\,K$.

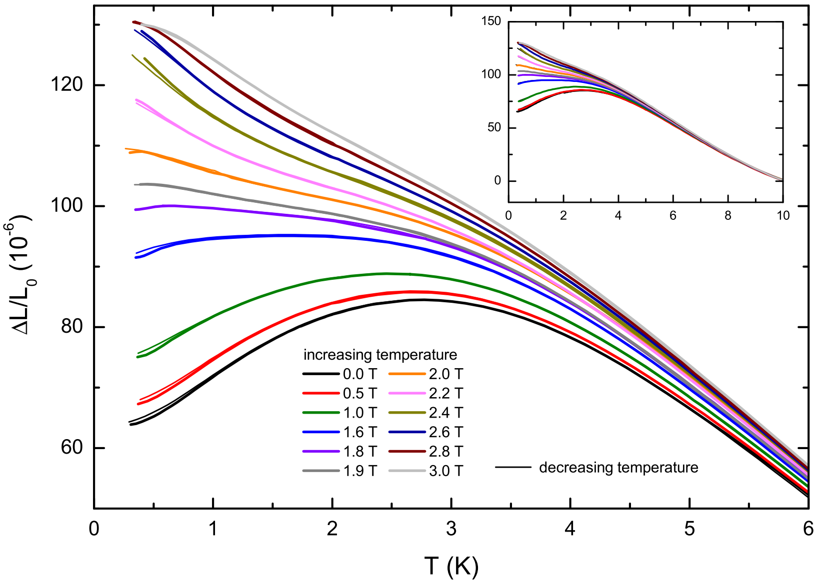

Figure B.2: Thermal expansion of Cs_2CoCl_4 in the one-dimensional temperature regime. Bold (thin) lines represent measurements with increasing (decreasing) temperature.

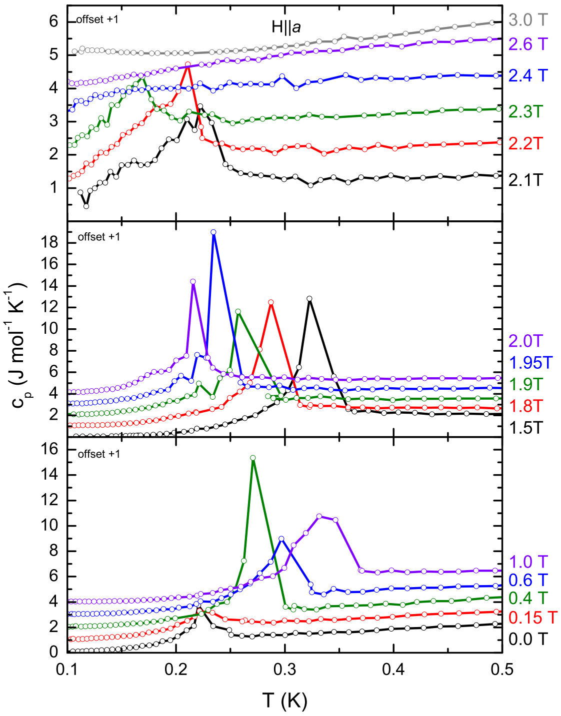

Figure B.3: Specific heat of Cs_2CoCl_4 for $H \parallel a$ and $T \leq 0.5\,K$.

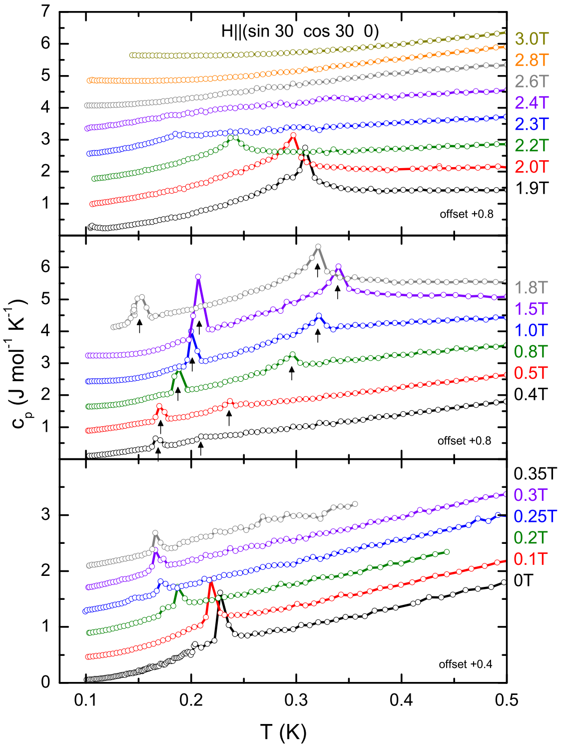

Figure B.4: Specific heat of Cs_2CoCl_4 for $H \parallel (\sin 30, \cos 30, 0)$ and $T \leq 0.5\,K$.

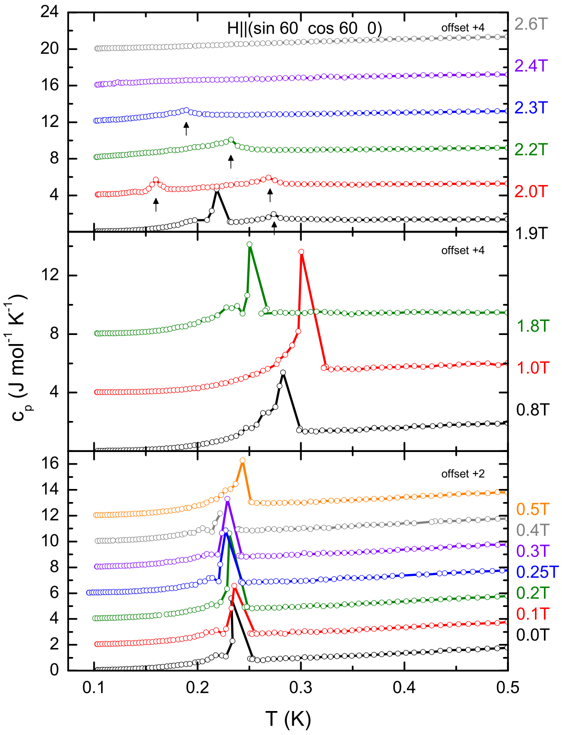

Figure B.5: Specific heat of Cs_2CoCl_4 for $H \parallel (\sin 60, \cos 60, 0)$ and $T \leq 0.5\,K$.

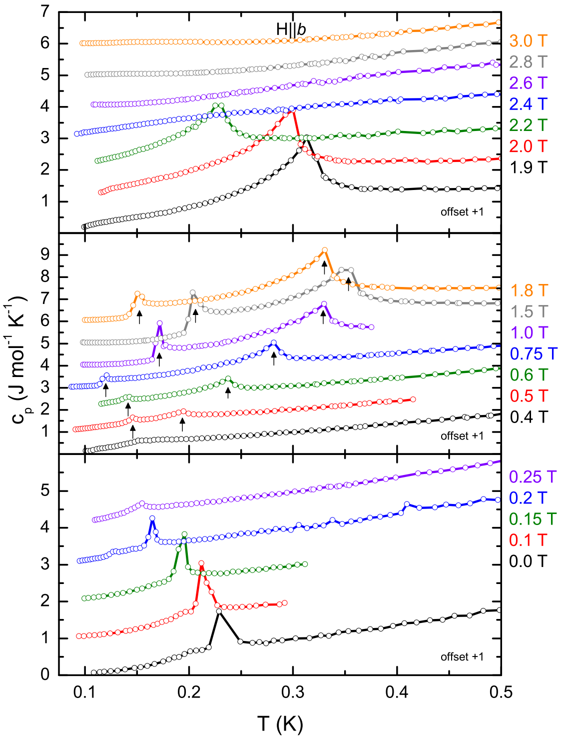

Figure B.6: Specific heat of Cs_2CoCl_4 for $H \parallel b$ and $T \leq 0.5\,K$.

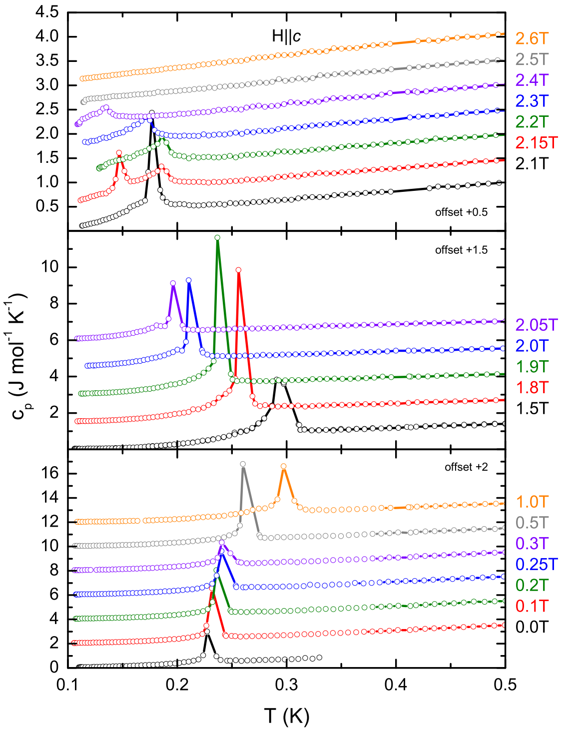

Figure B.7: Specific heat of Cs_2CoCl_4 for $H \parallel c$ and $T \leq 0.5\,K$.

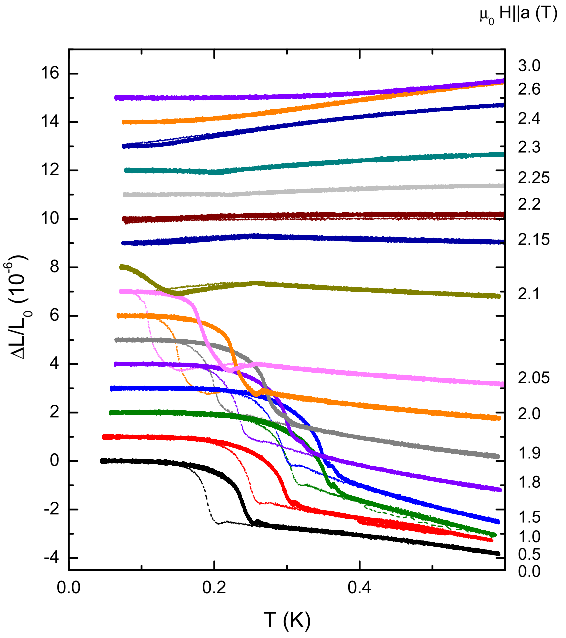

Figure B.8: Thermal expansion of Cs_2CoCl_4 for $H \parallel a$ and $T \leq 0.6\,K$. Bold (thin) lines represent measurements with increasing (decreasing) temperature.

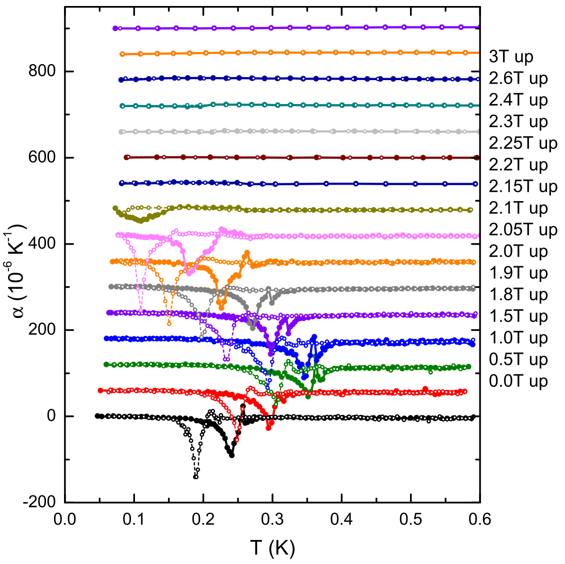

Figure B.9: Thermal expansion coefficient of Cs_2CoCl_4 for $H \parallel a$ and $T \leq 0.6\,K$. Full (open) symbols represent data acquired with increasing (decreasing) temperature. Curves are offset by $60\,K^{-1}$.

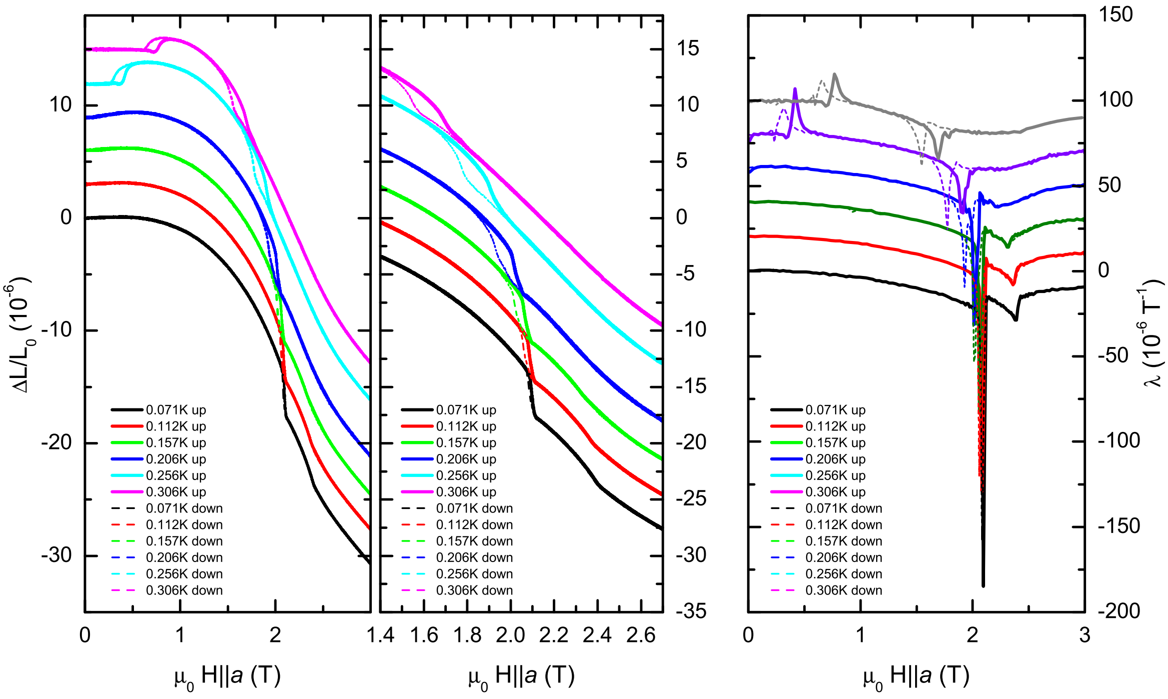

Figure B.10: Magnetostriction of Cs_2CoCl_4 for $H \parallel a$ and $T \lesssim T_N$. The magnetostrictive coefficient λ was numerically obtained from the data. Bold (thin/dashed) lines represent data acquired with increasing (decreasing) field.

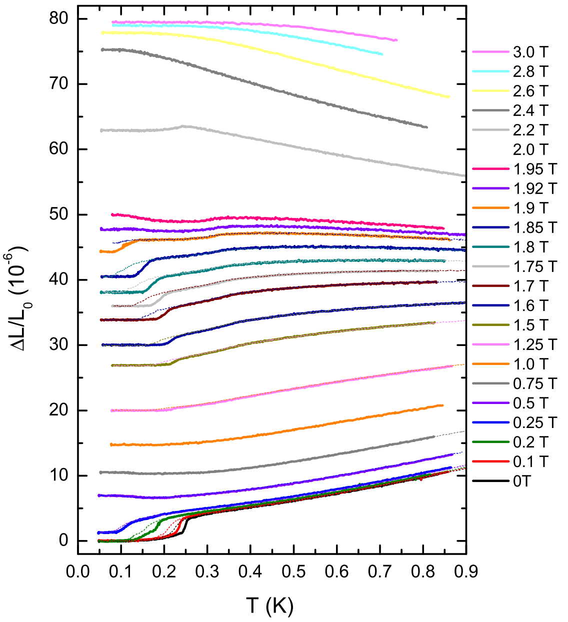

Figure B.11: Thermal expansion of Cs_2CoCl_4 for $H \parallel b$ and $T \lesssim 0.8\,K$. The data are shifted according to the magnetostriction. Solid (dashed) lines represent data acquired with increasing (decreasing) temperature.

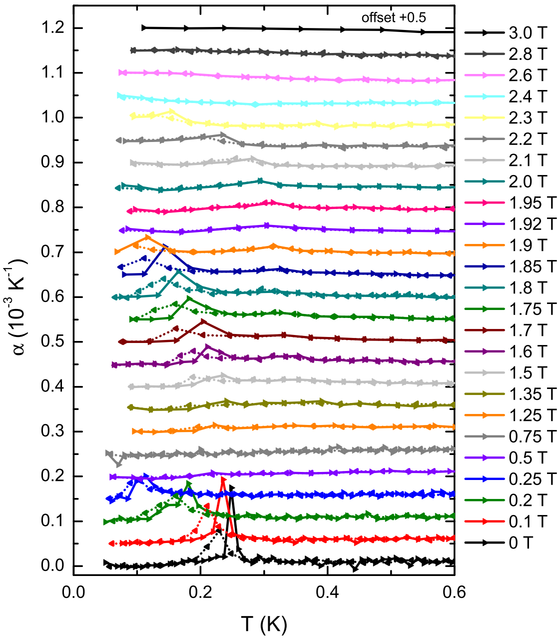

Figure B.12: Thermal expansion coefficient of Cs_2CoCl_4 for $H \parallel b$ and $T \leq 0.6\,K$. Full symbols (dashed lines) represent data acquired with increasing (decreasing) temperature. The data are offset by $5 \times 10^{-4}\,K^{-1}$.

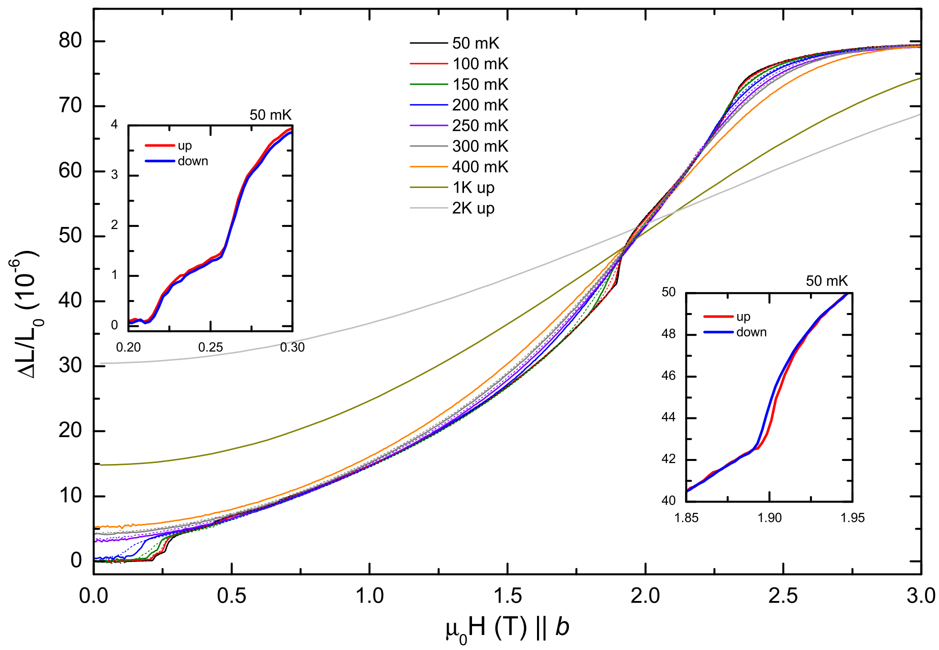

Figure B.13: Magnetostriction of Cs_2CoCl_4 for $H \parallel b$ and $T \lesssim T_N$. In the insets the low-temperature data close to 0.25 T and 1.9 T are shown.

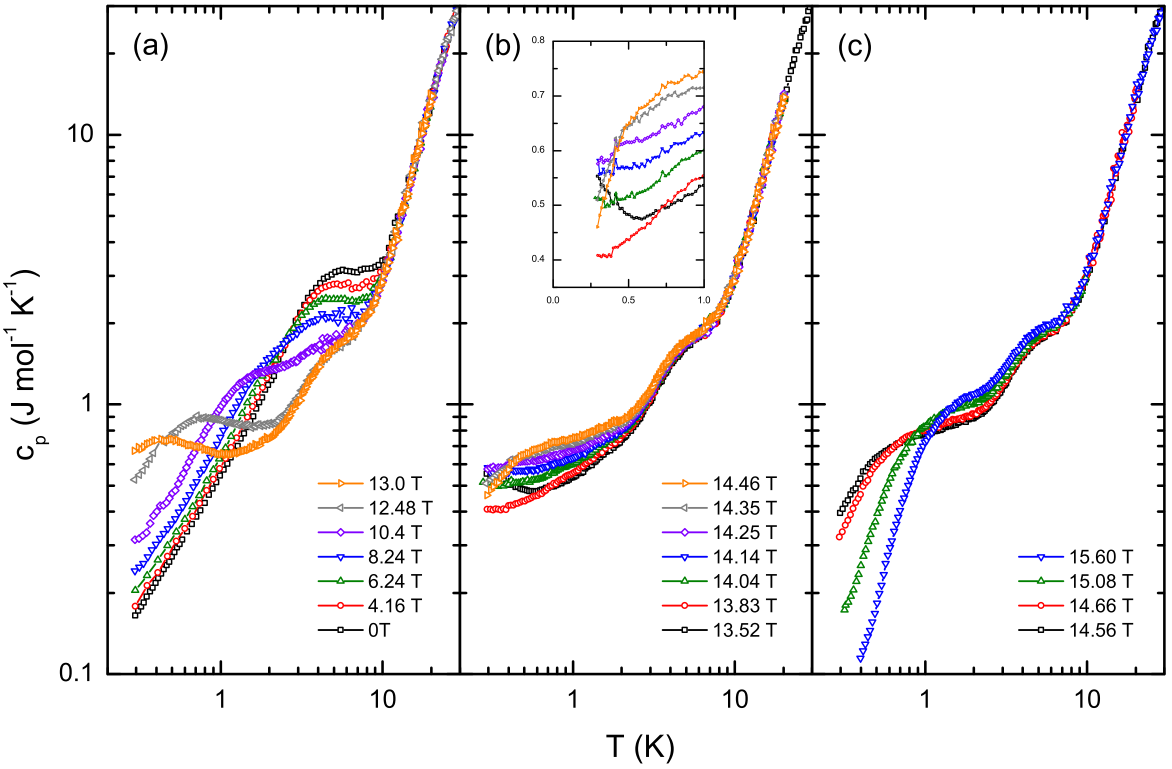

Figure B.14: Specific heat of copper pyrazine dinitrate measured as a function of temperature at various constant magnetic fields. In the inset of (b) the low-temperature range of c_p close to the critical field of ≈ 14 T is shown.

Bibliography

[1] D. Bitko, T. F. Rosenbaum, and G. Aeppli, Physical Review Letters **77**, 940 (1996).

[2] R. Coldea, D. A. Tennant, E. M. Wheeler, E. Wawrzynska, D. Prabhakaran, M. Telling, K. Habicht, P. Smeibidl, and K. Kiefer, Science **327**, 177 (2010).

[3] H. A. Algra, L. J. de Jongh, H. W. J. Blöte, W. J. Huiskamp, and R. L. Carlin, Physica B+C **82**, 239 (1976).

[4] J. N. McElearney, S. Merchant, G. E. Shankle, and R. L. Carlin, The Journal of Chemical Physics **66**, 450 (1977).

[5] J. Smit and L. De Jongh, Physica B+C **97**, 224 (1979).

[6] P. Duxbury, J. Oitmaa, M. Barber, A. Van Der Bilt, K. Joung, and R. Carlin, Physical Review B **24**, 5149 (1981).

[7] I. Chatterjee, Journal of Magnetism and Magnetic Materials **265**, 363 (2003).

[8] M. Kenzelmann, R. Coldea, D. A. Tennant, D. Visser, M. Hofmann, P. Smeibidl, and Z. Tylczynski, Physical Review B **65**, 144432 (2002).

[9] P. T. Cong, B. Wolf, M. de Souza, N. Krüger, A. A. Haghighirad, S. Gottlieb-Schoenmeyer, F. Ritter, W. Assmus, I. Opahle, K. Foyevtsova, H. O. Jeschke, R. Valentí, L. Wiehl, and M. Lang, Physical Review B **83**, 064425 (2011).

[10] G. Mennenga, L. de Jongh, W. Huiskamp, and J. Reedijk, Journal of Magnetism and Magnetic Materials **44**, 89 (1984).

[11] T. Lancaster, S. Blundell, M. Brooks, P. Baker, F. Pratt, J. Manson, C. Landee, and C. Baines, Physical Review B **73**, 020410 (2006).

[12] M. Mourigal, M. Enderle, A. Klöpperpieper, J.-S. Caux, A. Stunault, and H. M. Ronnow, Nature Physics **9**, 435 (2013).

[13] P. Hammar, M. Stone, D. Reich, C. Broholm, P. Gibson, M. Turnbull, C. Landee, and M. Oshikawa, Physical Review B **59**, 1008 (1999).

[14] H. Kühne, A. A. Zvyagin, M. Günther, A. P. Reyes, P. L. Kuhns, M. M. Turnbull, C. P. Landee, and H.-H. Klauss, Physical Review B **83**, 100407 (2011).

[15] M. Stone, D. Reich, C. Broholm, K. Lefmann, C. Rischel, C. Landee, and M. Turnbull, Physical Review Letters **91**, 037205 (2003).

[16] A. A. Validov, E. M. Lavrentyeva, M. Ozerov, S. A. Zvyagin, M. M. Turnbull, C. P. Landee, and G. B. Teitel'baum, Journal of Physics: Conference Series **200**, 022070 (2010).

[17] Y. Kono, T. Sakakibara, C. Aoyama, M. M. Turnbull, C. Landee, and Y. Takano, The Physical Society of Japan: Conference Proceedings **3**, 012015 (2014).

[18] H. Bethe, Annalen der Physik **3**, 133 (1929).

[19] B. N. Figgis and M. A. Hitchman, *Ligand Field Theory and Its Applications* (John Wiley And Sons, 2000).

[20] D. J. Newman, *Crystal Field Handbook* (Cambridge University Press, 2007).

[21] R. D. Cowan, *The Theory of Atomic Structure and Spectra* (Los Alamos Series in Basic and Applied Sciences, 1981).

[22] M. W. Haverkort, Ph.D. thesis, University of Cologne (2005).

[23] *Mathematica*, Wolfram Research Inc. (2014).

[24] A. P. Ramirez, A. Hayashi, R. J. Cava, R. Siddharthan, and B. S. Shastry, Nature **399**, 333 (1999).

[25] S. T. Bramwell, M. J. Harris, B. C. den Hertog, M. J. P. Gingras, J. S. Gardner, D. F. Mcmorrow, A. R. Wildes, A. L. Cornelius, J. D. M. Champion, R. G. Melko, and T. Fennell, Physical Review Letters **87**, 047205 (2001).

[26] B. C. den Hertog and M. J. P. Gingras, Physical Review Letters **84**, 3430 (2000).

[27] W. Heitler and F. London, Zeitschrift für Physik **44**, 455 (1927).

[28] J. B. Goodenough, *Magnetism And The Chemical Bond* (John Wiley And Sons, 1963).

[29] D. Khomskii, in *Spin Electronics*, Lecture Notes in Physics, Vol. 569, edited by M. Ziese and M. Thornton (Springer Berlin Heidelberg, 2001) pp. 89–116.

[30] H. Kramers, Proceedings of the Royal Academy of Sciences at Amsterdam **33**, 959 (1930).

[31] S. Bravyi, D. P. DiVincenzo, and D. Loss, Annals of Physics **326**, 2793 (2011).

[32] J. Schrieffer and P. Wolff, Physical Review **149**, 491 (1966).

[33] P. Jordan and E. Wigner, Zeitschrift für Physik **47**, 631 (1928).

[34] E. Lieb, T. Schultz, and D. Mattis, Annals of Physics **16**, 407 (1961).

[35] R. Basak and I. Chatterjee, Journal of Physics: Condensed Matter **1**, 1475 (1989).

[36] A. K. Kolezhuk, H.-J. Mikeska, K. Maisinger, and U. Schollwöck, Physical Review B **59**, 13565 (1999).

[37] J. des Cloizeaux and J. J. Pearson, Physical Review **128**, 2131 (1962).

[38] L. Faddeev and L. Takhtajan, Physics Letters A **85**, 375 (1981).

[39] R. Coldea, D. Tennant, and Z. Tylczynski, Physical Review B **68** (2003).

[40] H. Bethe, Zeitschrift für Physik **71**, 205 (1931).

[41] M. Takahashi, Progress of Theoretical Physics **46**, 401 (1971).

[42] K. Nomura, Physical Review B **48**, 16814 (1993).

[43] I. Affleck, Physical Review Letters **56**, 746 (1986).

[44] A. Klümper, European Physical Journal B **5**, 677 (1998).

[45] S. Eggert, I. Affleck, and M. Takahashi, Physical Review Letters **73**, 332 (1994).

[46] A. Klümper and D. C. Johnston, Physical Review Letters **84**, 4701 (2000).

[47] N. Ishimura and H. Shiba, Progress of Theoretical Physics **63**, 743 (1980).

[48] E. Ising, Zeitschrift für Physik **31**, 253 (1925).

[49] H. Kramers and G. Wannier, Physical Review **60**, 252 (1941).

[50] S. Katsura, Physical Review **127**, 1508 (1962).

[51] T. Tohyama, Japanese Journal of Applied Physics **51**, 010004 (2012).

[52] D. Khomskii, Physics **2**, 20 (2009).

[53] C. Hess, The European Physical Journal Special Topics **151**, 73 (2007).

[54] S. T. Bramwell and M. J. Gingras, Science **294**, 1495 (2001).

[55] R. G. Melko and M. J. P. Gingras, Journal of Physics: Condensed Matter **16**, R1277 (2004).

[56] L. J. de Jongh and A. R. Miedema, Advances in Physics **50**, 947 (2001).

[57] B. Bauer, L. D. Carr, H. G. Evertz, A. Feiguin, J. Freire, S. Fuchs, L. Gamper, J. Gukelberger, E. Gull, S. Guertler, A. Hehn, R. Igarashi, S. V. Isakov, D. Koop, P. N. Ma, P. Mates, H. Matsuo, O. Parcollet, G. Pawłowski, J. D. Picon, L. Pollet, E. Santos, V. W. Scarola, U. Schollwöck, C. Silva, B. Surer, S. Todo, S. Trebst, M. Troyer, M. L. Wall, P. Werner, and S. Wessel, Journal of Statistical Mechanics: Theory and Experiment **2011**, P05001 (2011).

[58] *Alps Project Web Page*, http://alps.comp-phys.org (2015).

[59] S. Todo and K. Kato, Physical Review Letters **87**, 047203 (2001).

[60] F. Alet, S. Wessel, and M. Troyer, Physical Review E **71**, 036706 (2005).

[61] M. Troyer, S. Wessel, and F. Alet, Physical Review Letters **90**, 120201 (2003).

[62] S. R. White, Physical Review Letters **69**, 2863 (1992).

[63] C. Lanczos, Journal of Research of the National Bureau of Standards **49**, 33 (1952).

[64] V. H. Privman, *Finite size scaling and numerical simulation of statistical systems* (World Scientific, 1990).

[65] J. Schnack and P. Shchelokovskyy, Journal of Magnetism and Magnetic Materials **306**, 79 (2006).

[66] M. Siahatgar and A. Langari, Physical Review B **77**, 54435 (2008).

[67] J.-S. Caux, F. Essler, and U. Löw, Physical Review B **68** (2003).

[68] S. Kimura, H. Yashiro, M. Hagiwara, K. Okunishi, K. Kindo, Z. He, T. Taniyama, and M. Itoh, Journal of Physics: Conference Series **51**, 99 (2006).

[69] Z. He, T. Taniyama, and M. Itoh, Journal of Crystal Growth **293**, 458 (2006).

[70] S. Kimura, T. Takeuchi, K. Okunishi, M. Hagiwara, Z. He, K. Kindo, T. Taniyama, and M. Itoh, Physical Review Letters **100**, 4 (2008).

[71] S. Kimura, T. Takeuchi, M. Hagiwara, K. Okunishi, Z. He, T. Taniyama, and M. Itoh, Journal of Physics: Conference Series **150**, 042090 (2009).

[72] S. K. Niesen, G. Kolland, M. Seher, O. Breunig, M. Valldor, M. Braden, B. Grenier, and T. Lorenz, Physical Review B **87**, 224413 (2013).

[73] S. K. Niesen, O. Breunig, S. Salm, M. Seher, M. Valldor, P. Warzanowski, and T. Lorenz, Physical Review B **90**, 104419 (2014).

[74] S. K. Niesen, Ph.D. thesis, University of Cologne (2015).

[75] Z. He and D. Fu, Chemistry of Materials **17**, 2924 (2005).

[76] S. Kimura, K. Okunishi, M. Hagiwara, K. Kindo, Z. He, T. Taniyama, M. Itoh, K. Koyama, and K. Watanabe, Journal of the Physical Society of Japan **82**, 033706 (2013).

[77] F. Anfuso, M. Garst, A. Rosch, O. Heyer, T. Lorenz, C. Rüegg, and K. Krämer, Physical Review B **77**, 235113 (2008).

[78] V. Zapf, V. Correa, P. Sengupta, C. Batista, M. Tsukamoto, N. Kawashima, P. Egan, C. Pantea, A. Migliori, J. Betts, M. Jaime, and A. Paduan-Filho, Physical Review B **77**, 020404 (2008).

[79] S. Sachdev, *Quantum Phase Transitions* (Cambridge University Press, 2001).

[80] S. Sachdev and N. Haven, in *Encyclopedia of Mathematical Physics*, edited by J.-P. Françoise, G. Naber, and S. Tsou (Elsevier, Oxford, 2006).

[81] M. Vojta, Reports on Progress in Physics **66**, 2069 (2003).

[82] S. Sachdev and B. Keimer, Physics Today **64**, 29 (2011).

[83] N. D. Mermin and H. Wagner, Physical Review Letters **17**, 1133 (1966).

[84] S. Sachdev, Physica Status Solidi B **247**, 537 (2010).

[85] A. W. Kinross, M. Fu, T. J. Munsie, H. A. Dabkowska, G. M. Luke, S. Sachdev, and T. Imai, Physical Review X **4**, 1 (2014).

[86] F. Pobell, *Matter and Methods at Low Temperatures* (Springer, 2007).

[87] C. Elliott, V. Vijayakumar, W. Zink, and R. Hansen, Journal of the Association for Laboratory Automation **12**, 17 (2007).

[88] K. Kiefer, Ph.D. thesis, University of Saarbrücken (2004).

[89] G. Kolland, O. Breunig, M. Valldor, M. Hiertz, J. Frielingsdorf, and T. Lorenz, Physical Review B **86**, 060402(R) (2012).

[90] E. Gmelin, Thermochimica Acta **110**, 183 (1987).

[91] J. S. Hwang, K. J. Lin, and C. Tien, Review of Scientific Instruments **68**, 94 (1997).

[92] *Temperature Measurement and Control Catalog*, Lake Shore Cryotronics (2004).

[93] O. Breunig, Diploma thesis, University of Cologne (2011).

[94] G. Kolland, Ph.D. thesis, University of Cologne (2013).

[95] C. A. Swenson, Review of Scientific Instruments **70**, 2728 (1999).

[96] W. Schnelle, J. Engelhardt, and E. Gmelin, Cryogenics **39**, 271 (1999).

[97] E. Warburg, Annalen der Physik **249**, 141 (1881).

[98] A. Kitanovski and P. W. Egolf, International Journal of Refrigeration **29**, 3 (2006).

[99] B. Yu, Q. Gao, B. Zhang, X. Meng, and Z. Chen, International Journal of Refrigeration **26**, 622 (2003).

[100] J. Romero Gómez, R. Ferreiro Garcia, A. De Miguel Catoira, and M. Romero Gómez, Renewable and Sustainable Energy Reviews **17**, 74 (2013).

[101] V. K. Pecharsky and K. A. Gschneidner Jr, Journal of Magnetism and Magnetic Materials **200**, 44 (1999).

[102] E. Grüneisen, Annalen der Physik **344**, 257 (1912).

[103] L. Zhu, M. Garst, A. Rosch, and Q. Si, Physical Review Letters **91**, 066404 (2003).

[104] G. Brändli and R. Griessen, Cryogenics **13**, 299 (1973).

[105] O. Heyer, Diploma thesis, University of Cologne (2005).

[106] D. Löwen, Diploma thesis, University of Cologne (2011).

[107] S. Orbe, Diploma thesis, University of Cologne (2011).

[108] M. A. Porai-Koshits, Kristallografiya **1**, 291 (1956).

[109] M. A. Porai-Koshits, Journal of Structural Chemistry **2**, 207 (1961).

[110] B. N. Figgis, M. Gerloch, and R. Mason, Proceedings of the Royal Society of London Series A **279**, 210 (1964).

[111] H. Blöte, Physica B+C **79**, 427 (1975).

[112] B. N. Figgis, P. A. Reynolds, and A. H. White, Journal of the Chemical Society, Dalton Transactions, 1737 (1987).

[113] J. H. Hubbell, *Tables of X-ray mass attenuation coefficients and mass energy-absorption coefficients 1 keV to 20 MeV for elements Z=1 to 92 and 48 additional substances of dosimetric interest*, edited by S. M. Seltzer (National Institute of Standards and Technology, Gaithersburg, 1996).

[114] R. Coldea, D. A. Tennant, A. M. Tsvelik, and Z. Tylczynski, Physical Review Letters **86**, 1335 (2001).

[115] T. Radu, H. Wilhelm, V. Yushankhai, D. Kovrizhin, R. Coldea, Z. Tylczynski, T. Lühmann, and F. Steglich, Physical Review Letters **95**, 127202 (2005).

[116] O. A. Starykh, H. Katsura, and L. Balents, Physical Review B **82**, 014421 (2010).

[117] M. Y. Veillette, J. T. Chalker, and R. Coldea, Physical Review B **71**, 214426 (2005).

[118] Y. Tokiwa, T. Radu, R. Coldea, H. Wilhelm, Z. Tylczynski, and F. Steglich, Physical Review B **73**, 2 (2006).

[119] R. Coldea, D. Tennant, K. Habicht, P. Smeibidl, C. Wolters, and Z. Tylczynski, Physical Review Letters **88**, 137203 (2002).

[120] H. Yoshizawa, G. Shirane, H. Shiba, and K. Hirakawa, Physical Review B **28**, 3904 (1983).

[121] A. Abragam and B. Bleaney, *Electron paramagnetic resonance of transition ions* (Clarendon Press, 1970).

[122] N. F. Henry and K. Lonsdale, eds., *International Tables for Crystallography*, Vol. A (Springer, 2005).

[123] F. A. Cotton, D. M. L. Goodgame, and M. Goodgame, Journal of the American Chemical Society **83**, 4690 (1961).

[124] L. I. Katzin, Journal of the American Chemical Society **76**, 3089 (1954).

[125] T. P. Melia and R. Merrifield, Journal of the Chemical Society A, 1166 (1970).

[126] T. P. Melia and R. Merrifield, Journal of the Chemical Society A, 1258 (1971).

[127] R. J. Bursill, T. Xiang, and G. A. Gehring, Journal of Physics: Condensed Matter **8**, L583 (1996).

[128] R. Potts, Physical Review **88**, 352 (1952).

[129] C. Yang, Physical Review **85**, 808 (1952).

[130] T. Giamarchi, *Quantum Physics in One Dimension* (Oxford University Press, 2004).

[131] U. Schollwöck, J. Richter, D. J. J. Farnell, and R. F. Bishop, eds., *Quantum Magnetism*, Lecture Notes in Physics, Vol. 645 (Springer Berlin Heidelberg, Berlin, Heidelberg, 2004).

[132] X. Zotos, Physical Review Letters **82**, 1764 (1999).

[133] X. Zotos, F. Naef, and P. Prelovsek, Physical Review B **55**, 11029 (1997).

[134] A. Klümper and K. Sakai, Journal of Physics A: Mathematical and General **35**, 2173 (2002).

[135] F. Heidrich-Meisner, A. Honecker, D. Cabra, and W. Brenig, Physical Review B **68**, 134436 (2003).

[136] A. V. Sologubenko, T. Lorenz, H. R. Ott, and A. Freimuth, Journal of Low Temperature Physics **147**, 387 (2007).

[137] F. Heidrich-Meisner, A. Honecker, D. C. Cabra, and W. Brenig, Physical Review B **66**, 140406 (2002).

[138] K. Sakai and A. Klümper, Journal of Physics A: Mathematical and General **36**, 11617 (2003).

[139] O. Breunig, M. Garst, E. Sela, B. Buldmann, P. Becker, L. Bohatý, R. Müller, and T. Lorenz, Physical Review Letters **111**, 187202 (2013).

[140] P. Jung, R. W. Helmes, and A. Rosch, Physical Review Letters **96**, 67202 (2006).

[141] X. Zotos, Physical Review Letters **92**, 67202 (2004).

[142] C. Hess, H. ElHaes, A. Waske, B. Büchner, C. Sekar, G. Krabbes, F. Heidrich-Meisner, and W. Brenig, Physical Review Letters **98**, 027201 (2007).

[143] N. Hlubek, X. Zotos, S. Singh, R. Saint-Martin, A. Revcolevschi, B. Büchner, and C. Hess, Journal of Statistical Mechanics: Theory and Experiment **2012**, P03006 (2012).

[144] N. Hlubek, P. Ribeiro, R. Saint-Martin, S. Nishimoto, A. Revcolevschi, S.-L. Drechsler, G. Behr, J. Trinckauf, J. E. Hamann-Borrero, J. Geck, B. Büchner, and C. Hess, Physical Review B **84**, 214419 (2011).

[145] A. Mohan, N. S. Beesetty, N. Hlubek, R. Saint-Martin, A. Revcolevschi, B. Büchner, and C. Hess, Physical Review B **89**, 104302 (2014).

[146] N. Prasai, A. Rebello, A. B. Christian, J. J. Neumeier, and J. L. Cohn, Physical Review B **91**, 054403 (2015).

[147] A. V. Sologubenko, K. Giannò, H. R. Ott, A. Vietkine, and A. Revcolevschi, Physical Review B **64**, 054412 (2001).

[148] A. V. Sologubenko, E. Felder, K. Giannò, H. R. Ott, A. Vietkine, and A. Revcolevschi, Physical Review B **62**, R6108 (2000).

[149] M. Garst, *Private Communication* (2015).

[150] D. V. Dmitriev, V. Y. A. Krivnov, and A. A. Ovchinnikov, Journal of Physics: Condensed Matter **19**, 4 (2001).

[151] D. V. Dmitriev, V. Y. Krivnov, A. A. Ovchinnikov, and A. Langari, Journal of Experimental and Theoretical Physics **95**, 538 (2002).

[152] M. Garst and A. Rosch, Physical Review B **72** (2005).

[153] F. Weickert, M. Brando, F. Steglich, P. Gegenwart, and M. Garst, Physical Review B **81**, 134438 (2010).

[154] T. Lorenz, O. Heyer, M. Garst, F. Anfuso, A. Rosch, C. Rüegg, and K. Krämer, Physical Review Letters **100**, 067208 (2008).

[155] T. Lorenz, S. Stark, O. Heyer, N. Hollmann, A. Vasiliev, A. Oosawa, and H. Tanaka, Journal of Magnetism and Magnetic Materials **316**, 291 (2007).

[156] I. Dzyaloshinsky, Journal of Physics and Chemistry of Solids **4**, 241 (1958).

[157] V. V. Mazurenko and V. I. Anisimov, Physical Review B **71**, 184434 (2005).

[158] N. Terada, S. Mitsuda, H. Ohsumi, and K. Tajima, Journal of the Physical Society of Japan **75**, 023602 (2006).

[159] O. Tchernyshyov, R. Moessner, and S. Sondhi, Physical Review Letters **88**, 067203 (2002).

[160] J. P. Shepherd, Review of Scientific Instruments **56**, 273 (1985).

[161] S. Katsura, T. Horiguchi, and M. Suzuki, Physica **46**, 67 (1970).

[162] O. Lounasmaa, Physical Review **126**, 1352 (1962).

[163] M. Dixon, F. E. Hoare, T. M. Holden, and D. E. Moody, Proceedings of the Royal Society of London Series A **285**, 561 (1965).

[164] O. Breunig, M. Garst, A. Rosch, E. Sela, B. Buldmann, P. Becker, L. Bohaty, R. Müller, and T. Lorenz, Physical Review B **91**, 024423 (2015).

[165] I. Tsukada, J. Takeya, T. Masuda, and K. Uchinokura, Physical Review Letters **87**, 127203 (2001).

[166] L. Balents, Nature **464**, 199 (2010).

[167] J. Nasu, T. Kaji, K. Matsuura, M. Udagawa, and Y. Motome, Physical Review B **89**, 115125 (2014).

[168] R. M. Fernandes, A. V. Chubukov, and J. Schmalian, Nature Physics **10**, 97 (2014).

[169] T. Tonegawa, Solid State Communications **40**, 983 (1981).

[170] P. Gegenwart, J. Custers, C. Geibel, K. Neumaier, T. Tayama, K. Tenya, O. Trovarelli, and F. Steglich, Physical Review Letters **89**, 056402 (2002).

[171] J. Kurmann, G. Müller, H. Thomas, M. W. Puga, and H. Beck, Journal of Applied Physics **52**, 1968 (1981).

[172] J. Kurmann, H. Thomas, and G. Müller, Physica A **112**, 235 (1982).

[173] C. Niedermayer, C. Bernhard, T. Blasius, A. Golnik, A. Moodenbaugh, and J. I. Budnick, Physical Review Letters **80**, 3843 (1998).

[174] H. Luetkens, H.-H. Klauss, M. Kraken, F. J. Litterst, T. Dellmann, R. Klingeler, C. Hess, R. Khasanov, A. Amato, C. Baines, M. Kosmala, O. J. Schumann, M. Braden, J. Hamann-Borrero, N. Leps, A. Kondrat, G. Behr, J. Werner, and B. Buchner, Nature Materials **8**, 305 (2009).

[175] Y. Kamihara, T. Watanabe, M. Hirano, and H. Hosono, Journal of the American Chemical Society **130**, 3296 (2008).

[176] H. Takahashi, K. Igawa, K. Arii, Y. Kamihara, M. Hirano, and H. Hosono, Nature **453**, 376 (2008).

[177] X. H. Chen, T. Wu, G. Wu, R. H. Liu, H. Chen, and D. F. Fang, Nature **453**, 761 (2008).

[178] C. de la Cruz, Q. Huang, J. W. Lynn, J. Li, W. Ratcliff II, J. L. Zarestky, H. A. Mook, G. F. Chen, J. L. Luo, N. L. Wang, and P. Dai, Nature **453**, 899 (2008).

[179] N. D. Mathur, F. M. Grosche, S. R. Julian, I. R. Walker, D. M. Freye, R. K. W. Haselwimmer, and G. G. Lonzarich, Nature **394**, 39 (1998).

[180] B. J. Powell and R. H. McKenzie, Physical Review Letters **94**, 47004 (2005).

[181] K. Foyevtsova, Y. Zhang, H. O. Jeschke, and R. Valentí, Journal of Physics: Conference Series **145**, 012038 (2009).

[182] R. Coldea, D. A. Tennant, R. A. Cowley, D. F. McMorrow, B. Dorner, and Z. Tylczynski, Journal of Physics: Condensed Matter **8**, 7473 (1996).

[183] N. Krüger, S. Belz, F. Schossau, A. A. Haghighirad, P. T. Cong, B. Wolf, S. Gottlieb-Schoenmeyer, F. Ritter, and W. Assmus, Crystal Growth and Design **10**, 4456 (2010).

[184] M. Musa, Physica Status Solidi **16**, 771 (1966).

[185] H. J. Seifert and I. Al-Khudair, Journal of Inorganic and Nuclear Chemistry **37**, 1625 (1975).

[186] V. A. Zasukha and S. V. Volkov, Theoretical and Experimental Chemistry **19**, 131 (1983).

[187] V. Petricek, M. Dusek, and L. Palatinus, Zeitschrift für Kristallographie **229**, 345 (2014).

[188] R. Wielinga, H. Blöte, J. Roest, and W. Huiskamp, Physica **34**, 223 (1967).

[189] B. Figgis and P. Reynolds, Australian Journal of Chemistry **34**, 2495 (1981).

[190] P. A. Reynolds, B. N. Figgis, and A. H. White, Acta Crystallographica Section B Structural Crystallography and Crystal Chemistry **37**, 508 (1981).

[191] H. M. Powell and A. F. Wells, Journal of the Chemical Society, 359 (1935).

[192] V. L. Berezinskii, Zhurnal Eksperimentalnoi i Teoreticheskoi Fiziki [Soviet Physics–JETP] **61**, 1144 (1972).

[193] J. M. Kosterlitz and D. J. Thouless, Journal of Physics C: Solid State Physics **6**, 1181 (1973).

[194] L. A. Mól, A. R. Pereira, H. Chamati, and S. Romano, The European Physical Journal B **50**, 541 (2006).

[195] K. Harada and N. Kawashima, Journal of the Physical Society of Japan **67**, 2768 (1998).

[196] C. Biagini, A. Cuccoli, V. Tognetti, R. Vaia, and P. Verrucchi, Journal of Applied Physics **79**, 4638 (1996).

[197] Y.-B. Deng and Q. Gu, Chinese Physics Letters **31**, 020504 (2014).

[198] B. N. Figgis, M. Gerloch, and R. Mason, Acta Crystallographica **17**, 506 (1964).

[199] S. Misra and J. Felsteiner, Physical Review B **8**, 5326 (1973).

[200] H. Beljers, P. Bongers, R. van Stapele, and H. Zulstra, Physics Letters **12**, 81 (1964).

[201] K. Mess, E. Lagendijk, D. Curtis, and W. Huiskamp, Physica **34**, 126 (1967).

[202] J. Hammann, Physica **43**, 277 (1969).

[203] C.-H. Chern, Physical Review B **78**, 020403 (2008).

[204] S. Leonel, P. Coura, B. Costa, and A. Pires, Solid State Communications **123**, 201 (2002).

[205] W. E. Hatfield and J. F. Villa, Journal of the American Chemical Society **93**, 4081 (1971).

[206] D. B. Losee, The Journal of Chemical Physics **59**, 3600 (1973).

[207] K. T. McGregor, The Journal of Chemical Physics **64**, 2506 (1976).

[208] A. V. Sologubenko, K. Berggold, T. Lorenz, A. Rosch, E. Shimshoni, M. Phillips, and M. Turnbull, Physical Review Letters **98**, 107201 (2007).

[209] A. Santoro, A. D. Mighell, and C. W. Reimann, Acta Crystallographica Section B Structural Crystallography and Crystal Chemistry **26**, 979 (1970).

[210] G. Kokoszka and C. Reimann, Journal of Inorganic and Nuclear Chemistry **32**, 3229 (1970).

[211] C. Yasuda, S. Todo, K. Hukushima, F. Alet, M. Keller, M. Troyer, and H. Takayama, Physical Review Letters **94**, 217201 (2005).

[212] Y. Kono, T. Sakakibara, C. P. Aoyama, C. Hotta, M. M. Turnbull, C. P. Landee, and Y. Takano, Physical Review Letters **114**, 037202 (2015).

[213] V. Kiryukhin, Y. J. Kim, K. J. Thomas, F. C. Chou, R. W. Erwin, Q. Huang, M. A. Kastner, and R. J. Birgeneau, Physical Review B **63**, 144418 (2001).

[214] S. Hayden, G. Aeppli, R. Osborn, A. Taylor, T. Perring, S.-W. Cheong, and Z. Fisk, Physical Review Letters **67**, 3622 (1991).

[215] S. Scharffe, Diploma thesis, University of Cologne (2012).

[216] J. Rohrkamp, M. D. Phillips, M. M. Turnbull, and T. Lorenz, Journal of Physics: Conference Series **200**, 012169 (2010).

[217] J. Rohrkamp, *Private Communication* (2014).

[218] R. E. Peierls, *Quantum Theory of Solids* (Oxford: Clarendon Press, 1955).

[219] A. I. Buzdin and L. N. Bulaevskii, Soviet Physics Uspekhi **23**, 409 (1980).

[220] M. Hase, I. Terasaki, and K. Uchinokura, Physical Review Letters **70**, 3651 (1993).

[221] A. N. Vasil'ev, R. Z. Levitin, L. I. Leonyuk, L. A. Ponomarenko, and V. V. Snegirev, Czechoslovak Journal of Physics **46**, 1955 (1996).

[222] U. Ammerahl, T. Lorenz, B. Büchner, A. Revcolevschi, and G. Dhalenne, Zeitschrift für Physik B Condensed Matter **102**, 71 (1996).

[223] B. van Bodegom, B. C. Larson, and H. A. Mook, Physical Review B **24**, 1520 (1981).

[224] I. S. Jacobs, J. W. Bray, H. R. Hart, L. V. Interrante, J. S. Kasper, G. D. Watkins, D. E. Prober, and J. C. Bonner, Physical Review B **14**, 3036 (1976).

[225] J. W. Bray, H. R. Hart, L. V. Interrante, I. S. Jacobs, J. S. Kasper, G. D. Watkins, S. H. Wee, and J. C. Bonner, Physical Review Letters **35**, 744 (1975).

[226] H. W. J. Blöte, J. L. Cardy, and M. P. Nightingale, Physical Review Letters **56**, 742 (1986).

[227] J. D. Johnson and B. M. McCoy, Physical Review A **6**, 1613 (1972).

[228] B. Wolf, Y. Tsui, D. Jaiswal-Nagar, U. Tutsch, A. Honecker, K. Removic-Langer, G. Hofmann, A. Prokofiev, W. Asmuss, G. Donath, and M. Lang, Proceedings of the National Academy of Sciences **108**, 6862 (2011).

[229] M. Stone, D. Reich, C. Broholm, K. Lefmann, C. Rischel, C. Landee, and M. Turnbull, Physical Review Letters **91**, 037205 (2003).

[230] Nature Photonics **7**, 761 (2013).

[231] J. Shinar and R. Shinar, Journal of Physics D: Applied Physics **41**, 133001 (2008).

[232] G. Saito and Y. Yoshida, Chemical Record **11**, 124 (2011).

[233] S. K. Niesen, O. Heyer, T. Lorenz, and M. Valldor, Journal of Magnetism and Magnetic Materials **323**, 2575 (2011).

List of Figures

List of Tables

Kurzzusammenfassung

In dieser Arbeit werden die thermodynamischen Eigenschaften der Spin-1/2-Ketten Systeme Cs_2CoCl_4 und $Cu(C_4H_4N_2)(NO_3)_2$ untersucht. Messungen der spezifischen Wärme, thermischen Ausdehnung, Magnetisierung und des magnetokalorischen Effektes in einem Temperaturbereich von 0.25 bis 30 K und in Magnetfeldern von bis zu 17 T werden mit Modellrechnungen verglichen. In Cs_2CoCl_4 führt eine Kristallfeldanisotropie von etwa 7 K zu einer Aufspaltung der Spin-3/2 Zustände der magnetischen Co^{2+} Ionen in Kramers Doubletts. Es wird gezeigt, dass die höherliegenden Kristallfeldzustände bei der Anwendung eines effektiven Spin-1/2 *XXZ* Modells notwendigerweise berücksichtigt werden müssen, um die Thermodynamik von Cs_2CoCl_4 konsistent beschreiben zu können. Die Anisotropie $\Delta \approx 0.12$ der Spinkette ist kleiner als zuvor in der Literatur angenommen. Unterhalb von 2 K und in Magnetfeldern von bis zu 4 T ist der Magnetismus von Cs_2CoCl_4 in guter Übereinstimmung mit dem *XXZ* Modell in einem transversalen Magnetfeld. Die thermodynamischen Messgrößen zeigen ein Quantenphasenübergang bei einem Feld von 2.0 T an.

Unter $T_N \simeq 0.22$ K tritt magnetische Ordnung auf. Aus den experimentellen Daten werden Phasendiagramme für verschiedene Magnetfeldrichtungen abgeleitet und die mikroskopischen Ursprünge der beobachteten Phasen diskutiert. An die antiferromagnetische Phase grenzt eine weitere Tieftemperaturphase, die vermutlich keine Spinflüssigkeitsphase ist, wie zuvor in der Literatur vermutet. In einem Magnetfeld entlang der kristallographischen *b* Achse tritt zudem ein zweistufiger Spin-Flop Übergang auf.

Für die gemischten Systeme $Cs_2CoCl_{4-x}Br_x$ und $Cs_3CoCl_{5-y}Br_y$ deuten strukturelle und thermodynamische Untersuchungen auf einen platz-selektiven Austausch der Ionen hin. In der ersten Dotierungsreihe weist der Magnetismus, ähnlich zur Muttersubstanz, eine *XY*-artige Anisotropie auf. In $Cs_3CoCl_{5-y}Br_y$ herrscht eine Ising-Anisotropie vor und die Tieftemperatureigenschaften entwickeln sich unstetig als Funktion von y.

Der Magnetismus von $Cu(C_4H_4N_2)(NO_3)_2$ ist in hohem Maße isotrop und sehr gut durch eine Spin-1/2 Heisenberg Kette beschrieben, die einen Quantenphasenübergang als Funktion des Magnetfeldes aufweist. In dieser Arbeit werden thermodynamische Eigenschaften von $Cu(C_4H_4N_2)(NO_3)_2$ mit exakten Ergebnissen für das Heisenberg Modell verglichen, unter Berücksichtigung von Magnetfeldern bis über das kritische Feld hinaus. Alle untersuchten Eigenschaften sind mit hoher Genauigkeit durch das Modell beschrieben und lassen eindeutig auf einen Quantenphasenübergang schließen. Es ergibt sich eine Kopplungskonstante von 10.60 K und ein kritisches Feld von 13.90 T. Nahe des kritischen Feldes zeigt die spezifische Wärme das erwartete Potenzgesetz, der magnetokalorische Effekt divergiert und ein universelles Skalierungsverhalten ist erfüllt.

Abstract

In this thesis the thermodynamic properties of the spin-$^1/_2$ chain compounds Cs_2CoCl_4 and $Cu(C_4H_4N_2)(NO_3)_2$ (CuPzN) are investigated. Measurements of the specific heat, the thermal expanison, the magnetization and the magnetocaloric effect in a temperature range from 0.25 to 30 K and in magnetic fields up to 17 T are compared to model calculations. In Cs_2CoCl_4 a crystal field anisotropy of about 7 K leads to a splitting of the orbital spin-$^3/_2$ states of the magnetic Co^{2+} into Kramers doublets. It is shown that the inclusion of excited crystal field states in the application of a spin-$^1/_2$ *XXZ* model to the system is essential for a consistent description of the thermodynamics of Cs_2CoCl_4. The anisotropy $\Delta \approx 0.12$ of the spin chain is smaller than previously assumed in literature. Below 2 K and for magnetic fields smaller than 4 T the magnetism of Cs_2CoCl_4 is well described by the *XXZ* model in a transverse magnetic field. Signatures of a quantum phase transition at 2.0 T are found in the thermodynamic data.

Below $T_N \simeq 0.22$ K magnetic order arises. The magnetic phase diagrams for different field directions are derived from the experimental data and the microscopic origins of the appearing phases are discussed. Bordering antiferromagnetism a low-temperature phase is identified that possibly is not a spin-liquid phase as previously suggested in literature. For fields along the crystallographic b axis an additional two-stage spin-flop transition arises.

In the mixed compounds $Cs_2CoCl_{4-x}Br_x$ and $Cs_3CoCl_{5-y}Br_y$ a site-selective doping is indicated by structural and thermodynamic investigations. While in the first system an easy-plane type magnetism, similar to the parent compound is found, the latter shows an easy-axis anisotropy and a non-continuous evolution of the low-temperature magnetism.

The magnetism of $Cu(C_4H_4N_2)(NO_3)_2$ is highly isotropic and well described by the spin-$^1/_2$ Heisenberg chain, which shows a quantum phase transition as a function of an external field. In the thesis, the thermodynamics of $Cu(C_4H_4N_2)(NO_3)_2$ are compared to exact results of the Heisenberg model including magnetic fields up to and above the critical field of the spin chain. All investigated thermodynamic quantities are described by the model with a high precision and show clear signatures of a quantum phase transition. A coupling constant of 10.60 K is found and all data consistently indicate a critical field of the spin chain of 13.90 T. Approaching the critical field, the specific heat acquires the expected power law, the magnetocaloric effect diverges and a universal scaling law is obeyed.

Teilpublikationen

- *Low-temperature ordered phases of the spin-$\frac{1}{2}$ XXZ chain system Cs_2CoCl_4*
  O. Breunig, M. Garst, A. Rosch, E. Sela, B. Buldmann, P. Becker, L. Bohatý, R. Müller, and T. Lorenz
  Physical Review B **91**, 024423 (2015)
- *Spin-$\frac{1}{2}$ XXZ Chain System Cs_2CoCl_4 in a Transverse Magnetic Field*
  O. Breunig, M. Garst, E. Sela, B. Buldmann, P. Becker, L. Bohatý, R. Müller, and T. Lorenz
  Physical Review Letters **111**, 187202 (2013)

Offizielle Erklärung

Ich versichere, dass ich die von mir vorgelegte Dissertation selbständig angefertigt, die benutzten Quellen und Hilfsmittel vollständig angegeben und die Stellen der Arbeit – einschließlich Tabellen, Karten und Abbildungen –, die anderen Werken im Wortlaut oder dem Sinn nach entnommen sind, in jedem Einzelfall als Entlehnung kenntlich gemacht habe; dass diese Dissertation noch keiner anderen Fakultät oder Universität zur Prüfung vorgelegen hat; dass sie - abgesehen von oben angegebenen Teilpublikationen - noch nicht veröffentlicht worden ist sowie, dass ich eine solche Veröffentlichung vor Abschluss des Promotionsverfahrens nicht vornehmen werde. Die Bestimmungen der Promotionsordnung sind mir bekannt. Die von mir vorgelegte Dissertation ist von Prof. Dr. T. Lorenz betreut worden.

Köln, den 27.4.2015

Oliver Breunig